Optimising Production of High Energy Radiation Using Laser Wakefield Acceleration

Christopher Isaac Donald Underwood

Doctor of Philosophy

University of York

Physics

November 2020

Abstract

This thesis presents work from experiments and simulations on characterising and optimising electron and X-ray sources created using laser wakefield accelerators.

The flux, critical energy of the spectrum, source size and divergence of a laser wakefield accelerator driven bremsstrahlung X-ray source were characterised experimentally and through simulation. The source had the highest energy photon spectrum measured from a laser wakefield bremsstrahlung source, with critical energies over 100 MeV. The source is shown to be tunable over the measured characteristics with changes in the plasma density and converter parameters.

A 5% energy spread 1.2 GeV electron beam was experimentally created using a density profile injection mechanism, the highest energy recorded using this injection technique. The density profile formation was investigated using fluid simulations, and the effect of the profile on electron generation was explored using particle-in-cell simulations.

Optimisation of electron beams using a machine learning technique was deployed experimentally in the form of a Bayesian optimisation algorithm. The algorithm was shown to be an effective method of finding a global optimum, and for creating electron beams with different characteristics. Comparisons between optimising the total beam energy and optimising for the energy in a narrow divergence were made. This difference in optimal position in parameter space was shown to be based on pulse evolution. This approach found the global optimum, in a four input parameter space for accelerated charge, in $\lesssim 20$ data points. This efficient optimisation of a laser wakefield accelerator will increase the usable time of future devices using this approach.

A new design for a high repetition rate plasma mirror was characterised. The mirror was created from a flowing liquid which refreshes the surface at a rate suitable for operation at $\sim$1 kHz, compared with other liquid based plasma mirrors operating at $\sim$1 Hz. The injection of subsequent laser pulses into a staged wakefield accelerator operating at high repetition rate could be achieved with this plasma mirror.

Contents

List of Figures

List of Tables

Acknowledgements

My four years based in York working towards my PhD has been highly enjoyable. Being part of the Fusion CDT brought me into York with a cohort of wonderful people. Travelling around the different universities in my first year was great fun, and I am sure I learnt something on the way. Our Christmas weekends away have been epic, and it's a shame that the four year tradition looks like it is going to be ruined by Covid-19. When talking of writing my thesis, it is hard not to think about the effect of the Covid pandemic. Spending the last 6 months only interacting via Zoom calls, especially with the 'rural' wifi connection, was not quite the fun, low-stress writing up period I had imagined. Then again, writing up is supposed to be something miserable to look fondly back on, so maybe this was the best time for me to experience a worldwide pandemic.

I would like to thank the CDT and funders for all the wonderful travel opportunities I have had during the PhD. With conferences, collaborations and summer schools I feel well travelled, even if in some places I did spend all my time in dark, underground rooms. Saying that, working on laser wakefield experiments has mainly been highly enjoyable, but I am glad that no-one had mentioned the ridiculous hours that are worked beforehand, I may not have been so keen... I would like to thank and acknowledge all the people I have worked with over these years. My supervisor Dr Chris Murphy has been super supportive of my work, a great source of information when I have been trying to work out what is going on, and always keen for a meeting that ends at a pub. I have enjoyed being part of your group, even though it means mainly working with people also called Chris, and no nickname system in operation! Thank you to Matt and Rob, who made the last few experiments more enjoyable and from whom I learnt a lot.

Thank you to my parents, Nicky and Graham, whose house and garden has provided me with a relaxing environment for the Covid write up, and the opportunity for many beach trips. I cannot thank you enough, along with my sister Jessica and partner Rachel, for helping with the first, and many more, decipherings of what I have written. Without all of you, this would be far less comprehensible.

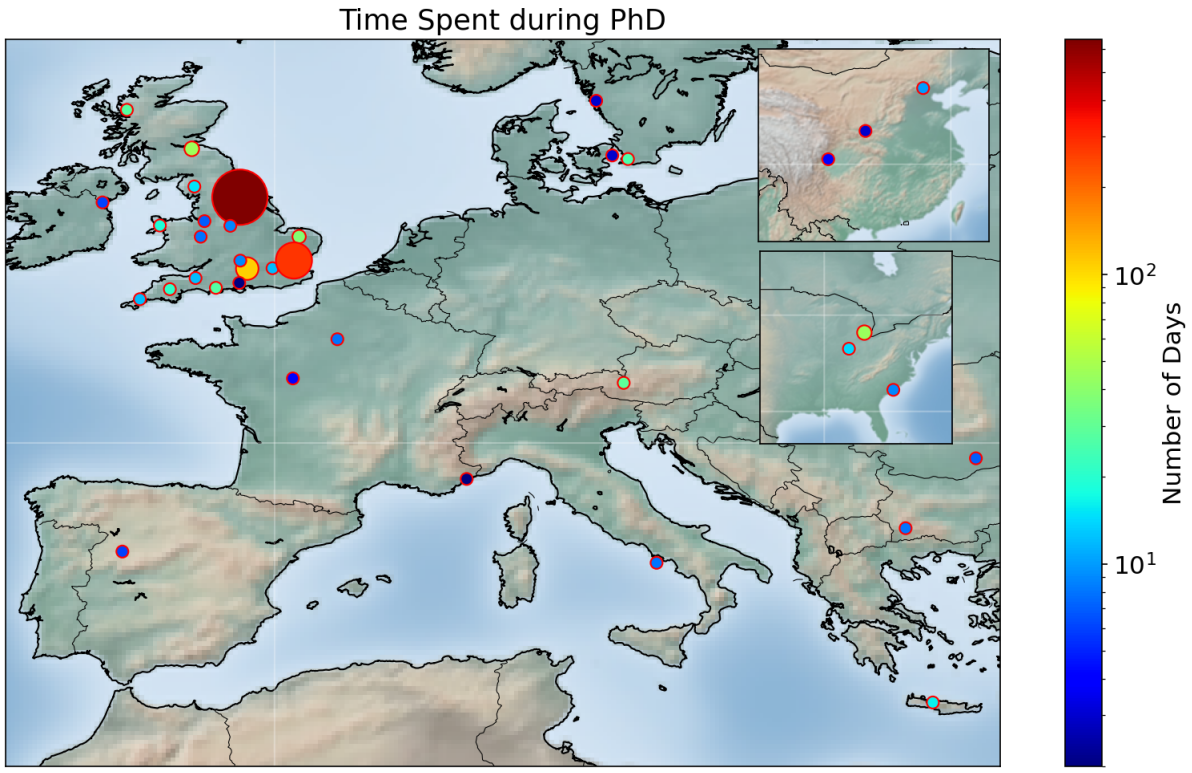

Figure 1: My nomadic existence during the PhD.

Declaration

I declare that this thesis is a presentation of original work and I am the sole author. This work has not previously been presented for an award at this, or any other, University. All sources are acknowledged as References.

Role of the author

All the experiments based around laser wakefield acceleration are large collaborations. The experiments presented here are no exception. For the data in this thesis, the author was involved in the setup of the experiment and some, if not all, of the data collection. The analysis of these experiments has been a collaboration, with some results provide to the author by other members of the experimental team. For the data extracted by, or with the help of, some other person, this has been flagged in the text where it is presented.

List of peer-reviewed publications

Published

Development of control mechanisms for a laser wakefield accelerator-driven bremsstrahlung X-ray source for advanced radiographic imaging

C. I. D. Underwood *et al.*

Plasma Physics and Controlled Fusion, Vol 62, October 2020

DOI 10.1088/1361-6587/abbebe

Characterization of flowing liquid films as a regenerating plasma mirror for high repetition-rate laser contrast enhancement

C. I. D. Underwood *et al.*

Laser and Particle Beams, Vol 38, Issue 2 June 2020

DOI 10.1017/S0263034620000129

Coded apertures with scatter and partial attenuation for high-energy high-resolution imaging

M. P. Selwood ; **C. I. D. Underwood** ; R. Heathcote and C. D. Murphy

Plasma Physics and Controlled Fusion, Vol 62, June 2020

DOI 10.1088/1361-6587/ab8ca4

Application of Compact Laser-Driven Accelerator X-Ray Sources for Industrial Imaging

J.-N. Gruse, ... **C.I.D. Underwood** *et al.*

Nuclear Instruments and Methods in Physics Research Section A: Accelerators, Spectrometers, Detectors and Associated Equipment Vol 983 July 2020

DOI 10.1016/j.nima.2020.164369

Automation and control of laser-plasma accelerators using Bayesian optimisation

R.J. Shalloo; S.J.D. Dann; J.-N. Gruse; **C.I.D. Underwood** *et al.*

Nature Communications 11(1), 6355. 2020

DOI 10.1038/s41467-020-20245-6

1 Introduction

The laser wakefield accelerator (LWFA) was proposed by Tajima and Dawson in 1979 [1], with the first experimentally accelerated electrons produced in the 1990s [2]. The first quasi mono-energetic electrons were produced in the 2004 [3–5], and since then the maximum energy [6], the energy spread and the repeatability [7] of the electron bunches have been improved. LWFAs are still in the proof-of-concept stage of their development, with all LWFAs to date produced in experimental facilities. The work in this thesis investigates the optimisation of sources, both electron and X-ray, that can be produced from a LWFA. It is necessary to understand the processes behind these optimisations to allow the implementation of LWFAs to real-life applications.

1.1 Uses of a particle accelerator

A particle accelerator produces a high energy beam of charged particles, normally electrons or ions. From these high energy particles secondary sources can be produced, such as X-rays. There are a wide range of applications of the high energy sources that are produced by particle accelerators: medical, industrial, security and scientific. As of 2014, there is estimated to be over 40 000 particle accelerators in use worldwide [8]. For medical accelerators the two main roles are the production of radioisotopes (used for tracers, radiotherapy and sterilisation [9]), and to produce high energy particle beams for medical treatment. Industrial uses include the characterisation and modification of material properties [10]. Their uses in security include: cargo inspection, nuclear waste management

and materials characterisation [11]. Particle accelerators have also led to many scientific discoveries, such as the discovery of the Higgs Boson by the Large Hadron Collider [12].

1.2 Particle accelerator history

The useful application of high energy particles beams to probe matter became apparent with Rutherford's discovery of the atomic nucleus. A beam of alpha particles, produced through nuclear decay, was used to probe a thin gold foil, and the nucleus was proposed to explain the large scattering angles (>90°) of some of the alpha particles [13]. However, relying on nuclear decay to produce energetic particles does not give any control over the interactions, as the particle energy will be determined by the decay path. Particle accelerators are machines that were developed to provide on demand access to particles of a given energy.

Figure 1.1 shows the first purpose built particle accelerator (1930), invented by Cockcroft and Walton, which used a direct current (DC). The other particle generator at this time was a Van de Graaff generator (1931) [15]. Both these DC machines had maximum electric fields of around 1 MV/m, and only accelerate particles in one field region [14].

The next step in particle accelerator development, which involved using alternating current (AC), was invented by Rolf Wideröe in 1928. Using Wideröe's idea, the first linear accelerator (linac) was build in America in 1931 [16]. A charged particle in an oscillating electric field sees an accelerating field for one half of an oscillation period and a de-accelerating field for the other. A particle gains energy in the accelerating field, and to prevent this energy being lost, the particle must be shielded from the de-accelerating field. The linac was created by lining up multiple accelerating regions, which are known as radio frequency (RF) cavities, and the electric field in these cavities oscillates so that the electric field in each cavity is accelerating the particle while the particle is travelling through it. The discharge of voltage of one gap, which was the limiting factor for DC accelerators, is overcome by using multiple accelerating regions allowing the acceleration of particles to a higher energy. By using circular structures such as storage rings, the energy of particles was further increased [14].

Figure 1.1: The author by a Cockcroft and Walton particle accelerator, the first purpose build particle accelerator, in the National Museum of Scotland. This device transformed an AC voltage using a voltage multiplier (zigzag structure in image) into a DC potential in which particles were accelerated [14].

Development of these machines to accelerate particles to higher and higher energies has led to the construction of some of the largest machines in the world, such as the 27 km circumference Large Hadron Collider (LHC) at CERN [17]. Conventional particle accelerators are normally built in one of two geometries: linear (known as a linac) or circular (known as a synchrotron). The power lost by synchrotron radiation is $P \propto E^4/(m^4R^2)$ where m is the particles mass, E the particles energy and R the radius of the trajectory [18]. Electrons, due to their small mass compared with ions, emit a lot more of their energy in a synchrotron putting a comparatively lower limit on the energy that they

can be accelerated to. Therefore, linacs are the preferred acceleration geometry for the production of high energy electrons, as they do not suffer this power loss. To increase the energy of the particles in a linac, either the accelerating field or the length of acceleration has to increase. RF cavities, that create the accelerating electric field, have a maximum field gradient in the region of $\lesssim$100 MV/m, above which sparking and breakdown of the electric field can occur [19]. This results in a minimum length of machines for a given energy. As linacs become longer the cost of building the machines also increases, with the machines now being around 3 km in length, and energies of the order of 10 GeV [20].

The next technological leap has been to use plasmas to support the accelerating electric field. This method is called plasma wakefield acceleration, and is the acceleration method that has been used in this thesis. A plasma is a quasi-neutral gas of charged and neutral particles which exhibits collective behaviour [21]. The name wakefield comes from the acceleration structure which forms in the wake of the laser pulse (or bunch of charged particles for beam driven wakefield acceleration) that drives the waves in the plasma [1]. As plasmas are already ionised they can support extremely high electric fields, 10 to 100 GV/m, which allows acceleration to the same energies in a thousandth of the distance compared with the fields produced in RF cavities. The maximum electric field strength in a plasma wave is of the order of the 'cold wave-breaking limit' [2] (Equation 2.65). The accelerators in this work range between 100 µm and 15 mm in length. A benefit of the acceleration medium already being ionised, is that there is no-longer the problem of the field arcing and causing damage to the accelerator. Another advantage of plasma acceleration is that the maximum size of the electron bunches produced is of the order of the plasma wavelength, $\sim$10 µm which is smaller than most linac produced electron bunches. This means that the peak brightness of the source is very high, as the bunch length duration is of the order of femtoseconds (a pulse duration that only a few conventional accelerators can match).

LWFA are still in the proof of concept stage of development with their applicability currently constrained by: the low laser driver repetition rate ($<$ 1 Hz for a petawatt-class laser); the low wall-plug efficiency ($<$ 0.1%) of the Ti:Sapphire lasers used [22]. However,

lasers are now coming on-line at the petawatt (PW) level operating at ∼Hz [23, 24], and LWFA MeV electrons have been produced at kHz [25]. Working at high repetition rate makes these devices competitive with linacs that can work at a repetition rate of >10 Hz.

1.3 Laser wakefield accelerators

The idea of using an intense electromagnetic (EM) pulse to drive a wake through a plasma to accelerate electrons was first proposed by T.Tajima and J. M. Dawson [1], who predicted fields of GV/cm.

Figure 1.2 shows a schematic of a laser pulse setting up a wakefield. The high intensity laser is focused onto a gas target, which is ionised and forms a plasma. As the laser pulse

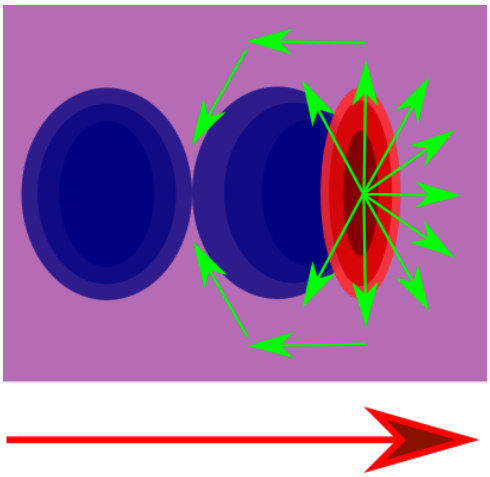

Figure 1.2: Cartoon of the ponderomotive force driving a wakefield through plasma (purple). The laser pulse (red) is travelling from left to right, which is most intense at its centre. The electrons (green arrows) are pushed down the intensity gradient leaving behind the positive charge of the ions (dark blue). The structures length scale is on the order of 10 µm.

propagates through the plasma the electrons are pushed down the intensity gradient of the EM field (laser pulse), away from the high intensity peak of the laser. This force, down the intensity gradient of the laser, is known as the ponderomotive force. The ions, due to their large mass relative to electrons, are effectively stationary on the timescale

of the electrons' expulsion from the path of the laser pulse, creating a large space charge in the wake of the laser. The electrons are accelerated back by the electric field created by the charge separation and overshoot creating a harmonic oscillator. This oscillating structure follows in the wake of the laser pulse, with the oscillation length being the plasma wavelength. The displacement of the electrons and ions creates large electric fields in the wake, $\sim$100 GV/m, which allows the electrons to be accelerated to high energies, with an energy gain per distance of $\sim$0.1 MeV/µm.

The plasma wake forms the acceleration structure, but for electrons to be accelerated they have to be in the correct region of phase space (position and momentum) to be trapped by the wake. This process is known as injection and can occur by several different methods, such as: self-injection, ionisation injection, dual laser beam injection and density transition injection. These different methods all have advantages and disadvantage and are discussed more in Section 2.8.

1.3.1 Lasers to drive a plasma accelerator

Laser stands for "light amplification by stimulated emission of radiation". In a laser, energy is stored in a medium, known as the gain medium. The energy is then emitted as a photon when another photon (in the correct energy range) passes through the medium. The photon emitted has the same properties as the photon that caused the stimulation, effectively cloning the initial photon. When this process has occurred many times, a temporally and spatially coherent pulse of light is produced, creating the output to the laser.

In this thesis the plasma wakefield accelerators were driven by high-intensity solid state lasers ($>5 \times 10^{17}\,\mathrm{Wcm^{-2}}$). The lasers used a Ti:sapphire crystal as their gain medium. Ti:sapphire is a laser gain material that produces radiation around 800 nm and can produce pulse durations of the order of 10 fs. The energy of the lasers pulses used in this thesis were in the range of 100 mJ to 10's J, with a peak power $\gtrsim$ 1 TW. These systems make use of chirped pulse amplification (CPA), the development of which was awarded the 2018 Nobel prize [26]. CPA stretches the pulse in time with respect to its frequencies,

which decreases the intensity of the pulse. The pulse is amplified and then re-compressed with respect to its frequency to produce a short intense pulse.

1.4 Plasma versus conventional acceleration

Plasma accelerators have both advantages and disadvantages compared with RF cavities. The properties of the electron beams LWFAs produce will complement those of current linacs. Table 1.1 compares some of their characteristics. The short pulse duration of LWFA allows X-ray sources to be produced that can image on ultra-fast time scales with a high intensity photon flux. The reduction in size of a LWFA compared to a linac means the cost of the LWFA will be drastically less, as well as the geographical space demands.

	XFEL Designed [27]	XFEL Commissioned [28]	Short bunch LWFA [29]	Maximum energy LWFA [6]
Beam Energy	10-20 GeV	12 GeV	84 ± 21 MeV	7.8(6) GeV
Emittance	1.4 mrad × mm	-	-	-
Divergence FWHM (mrad)	-	-	6.0 ± 1.6	0.20 ± 0.05
Bunch Charge	1 nC	100-500 pC	15 ± 7 pC	5(62) pC
Bunch Length	80fs	240 fs (res. limited)	1.4-1.8fs	-
Energy spread FWHM (MeV)	<2.5	-	21 ± 17	-
Beam Current (Max)	5mA	-	3-4kA	-
Field Gradient	23 MV/m	-	∼30 GV/m	∼40 GV/m
Accelerator size	∼1.5 km	1.46 km	3 mm	20 cm

Table 1.1: A comparison of the electron beams produced by the superconducting conventional accelerator for the European XFEL and two reported laser driven particle accelerators.

1.5 X-ray sources

There are several methods that generate high-brightness, ultra-short pulse duration X-ray (hard-photon) pulses from the electrons produced in a LWFA. These include betatron oscillations [30], inverse Compton scattering (ICS) [31], and bremsstrahlung radiation [32]. Betatron radiation is produced by the oscillations of the electrons in the wake, in the direction normal to the propagation direction. These oscillations generate X-ray radiation with a very small source size (∼µm). ICS is an effective way to produce MeV-

scale, narrow energy spread X-rays [33, 34] but has a low photon flux compared to other methods. The simplest method is via bremsstrahlung radiation [32], and can be achieved by placing a foil in the path of the beam. The de-acceleration of the electrons through the interaction with the atomic nuclei in the foil emits X-rays.

These X-ray sources are highly competitive with current methods used in industry. They can produce small sources with a large transverse coherence length, allowing high resolution phase-contrast imaging. They can produce high energy ($>1\,\mathrm{MeV}$) small source size ($<50\,\mu\mathrm{m}$) X-ray sources.

1.6 Outline of thesis work

This thesis focuses on the optimisation of LWFA sources, both the electrons produced, and the sources made with those electrons. This work was undertaken via experiments at the Central Laser Facility at the Rutherford Appleton Laboratory, and through simulation work using particle-in-cell (PIC), fluid and Monte-Carlo codes. The four data chapters present the following work.

Chapter 4 describes how a LWFA produced bremsstrahlung X-ray source was characterised in unparalleled detail with the highest energy photon spectrum recorded to date. Tunability of the source characteristics is shown through changes in the accelerated electron properties, and changes in the X-ray converter target. A tunable LWFA X-ray source has the potential to become a key new tool for industrial X-ray imaging. This work is published in Underwood *et al.* [35].

Chapter 5 describes the investigation of the density profile injection method with PIC simulations. Experimental data is presented with $\sim$1.2 GeV electron bunches produced using density transition injection, with supporting fluid simulations of the density profile. This is the highest energy produced via the density profile injection method to date. Controlling the injection of electrons into a LWFA improves the stability of the electron bunches, and stable electron bunches are important for the creation of predictable sources for applications.

Chapter 6 describes the Bayesian optimisation technique applied to the electrons produced from a LWFA. This is the first time a Bayesian optimisation algorithm has been experimental deployed on a LWFA. Electron beams with different properties (maximised accelerated charge or energy, and narrow divergence electron beams) were found by optimising over five input parameters simultaneously. Using this optimisation approach, the performance of the LWFA is improved compared to the standard, human led, optimisation. This work is an extension to the work published in Shalloo *et al.* [36].

The final data chapter, Chapter 7, describes the development of a new high repetition rate (HRR) plasma mirror, which is published in Underwood et al. [37]. The plasma mirror was formed from a flowing liquid, creating a regenerative surface. The properties of this surface were characterised. Current experimental designs for LWFA do not require plasma mirrors for the drive pulse, with their main use being the extraction of the leftover laser beam energy after the interaction. The HRR plasma mirror will have uses for applications where laser interactions require a high contrast ratio, such as ion acceleration by radiation pressure [38]. Creating a thin mirror could have applications in a staged laser wakefield accelerator [39], where the laser pulses will need to be inserted into the later accelerator stages with a mirror that does not cause large perturbations to the electron bunch as it propagates through the mirror. This HRR plasma mirror may be a candidate for such a mirror.

This work adds to the community's understanding of LWFAs and the X-ray sources they can produce. Along with the development of high repetition rate lasers, this work and the work of others aims to move LWFAs beyond being a proof-of-principle scientific device, to becoming a widely used tool.

2 | Background and theory

This chapter describes the relevant theory for understanding how a laser wakefield accelerator (LWFA) works. Optimising a LWFA requires knowledge of how the laser interacts with the plasma, and then how the electrons are accelerated by the wake structure.

2.1 Definition of plasma

Plasma is often described as the 4^{th} state of matter, a quasi-neutral ionised gas [21]. The three factors that define a plasma are:

1. **Being quasi-neutral** meaning the number of positive and negative charges roughly balance.

2. **Being able to effectively shield external electric field** which means that once beyond one Debye length from a charge, it is effectively shielded. This requires the Debye length to be smaller than the total size of the plasma.

3. **Exhibiting bulk properties** meaning that the plasma behaves like a fluid.

4. **Electrostatic interactions dominate over collisions**, hence the plasma frequency is greater than the collision frequency.

Where the Debye length (λ_D) is the measure of the charge shielding. For each λ_D further away from a charge the electric potential will decrease in magnitude by $1/e$ [21].

2.2 Plasma frequency

When a ultra-short pulse laser interacts with a plasma, it does so on a time scale where the electrons move but the ions remain effectively stationary (due to their larger mass). As with so much of physics, this creates a simple harmonic oscillator, where the electric field created between the stationary ions and the mobile electrons produces a restoring force on the electrons. The restoring force leads to oscillations in the plasma, with a characteristic

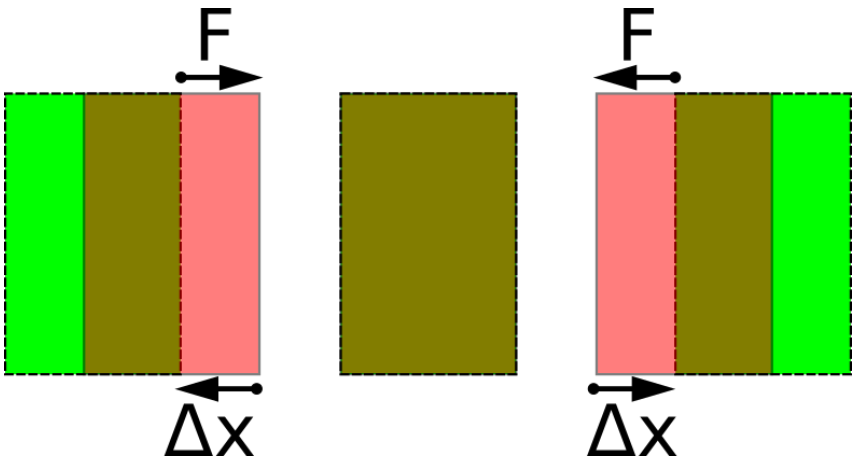

Figure 2.1: The simple harmonic oscillator caused by the displacement of a slab of electrons (green) by Δx from the ions (red), and the restoring force on the slab F.

frequency known as the plasma frequency (ω_p). This frequency can be calculated from this restoring force. Making the assumption that the plasma is: fully ionised, infinite, uniform, and ignoring thermal motion, then it is possible to consider a 2D slab of plasma where the electron and ion densities overlap perfectly [40]. The region of non-overlapping charge is then a function of how far the electrons are displaced from their initial position Δx (Figure 2.1). The electric field (E) that forms in the gap is given by [41]:

$$\begin{aligned} E &= \frac{\sigma}{\epsilon_0} \\ &= \frac{en_e}{\epsilon_0}\Delta x \end{aligned} \tag{2.1}$$

where σ is the charge density, n_e is the electron density, e the charge of an electron, ϵ_0 is the vacuum permittivity, and Δx the displacement of the electrons. The force (F) on the

electrons is:

$$\begin{aligned} F &= ma = qE \\ &= \frac{e^2 n_e \Delta x}{\epsilon_0} \end{aligned} \tag{2.2}$$

where m is the particle's mass, a the acceleration of the particle and q is the particle's charge. This gives a second order linear ordinary differential equation:

$$\ddot{\Delta x} = \frac{e^2 n_e}{m_e \epsilon_0} \Delta x \tag{2.3}$$

where m_e is the mass of an electron. This gives the frequency of the oscillation as:

$$\omega_p = \sqrt{\frac{e^2 n_e}{m_e \epsilon_0}} \tag{2.4}$$

LWFA operate in the under-dense plasma regime, $n_e < n_c$, where n_c is the critical density (the density at which the plasma frequency matches the laser frequency):

$$n_c = \frac{\omega^2 m_e \epsilon_0}{e^2} \tag{2.5}$$

This means that the laser frequency is greater than the plasma frequency, $\omega_0 > \omega_p$, and therefore, the laser pulse can propagate through the plasma.

2.3 Motion of electrons in electromagnetic fields

Considering the electromagnetic field created by a linearly polarised plane wave travelling in the $\hat{z}$ direction and the electric field in the $\hat{x}$, the electric and magnetic fields are described in Cartesian coordinates by the following equations [42]:

$$\begin{aligned} \vec{E} &= E_0 \cos(\omega t - kz)\hat{x} \\ \vec{B} &= B_0 \cos(\omega t - kz)\hat{y} \end{aligned} \tag{2.6}$$

where E_0 the electric field amplitude, B_0 the magnetic field amplitude, k is the wave vector, and ω is the angular frequency. Using the dipole approximation $\omega t - kz \approx \omega t$ [43], the particle at rest responds only to the electric field $E = E_0 \cos(\omega t)$. The force on an electron will be given by the Lorentz force:

$$\vec{F} = q(\vec{E} + \vec{v} \times \vec{B}) \tag{2.7}$$

where q is the charge of the electron and $\vec{v}$ is the velocity of the electron. Assuming the electron is non-relativistic, the motion in the x direction is calculated from $\ddot{x} = qE_x/m$:

$$\begin{aligned} a_x(t) &= -\frac{eE_0}{m}\cos(\omega t) \\ v_x(t) &= -\frac{eE_0}{m\omega}\sin(\omega t) \\ x(t) &= -\frac{eE_0}{m\omega^2}(\cos(\omega t) - 1) \end{aligned} \tag{2.8}$$

where the magnetic force component can be neglected as $|v \times B| = \frac{v}{c}E_0 << E_0$. The instantaneous kinetic energy of the quivering electron is given by $\frac{1}{2}mv^2$:

$$U = \frac{1}{2}m\left(-\frac{eE_0}{m\omega}\sin(\omega t)\right)^2 \tag{2.9}$$

And using the time average ($\langle\cos^2(\theta)\rangle = \frac{1}{2}$), the average quiver energy is:

$$\begin{aligned} \langle U\rangle &= \frac{e^2E_0^2}{4m\omega^2} \\ &\approx 4\frac{I_{14}\lambda_{\mu m}^2}{10^{14}}\text{eV} \end{aligned} \tag{2.10}$$

where I_{14} is the intensity in units of $10^{14}\,\text{W/cm}^{-2}$, and $\lambda_{\mu m}$ is the laser wavelength in microns. This average quiver energy is often referred to as the "ponderomotive" energy.

The motion in the z direction is calculated from $q\vec{v} \times \vec{B}/m$ giving $\ddot{z} = qv_xB_y/m$. The magnetic field is related to the electric field by $B_0 = E_0/c$:

$$\begin{aligned} a_z(t) &= \frac{q}{m}v_xB \\ &= -\frac{e}{m}\left(-\frac{eE_0}{m\omega}\sin(\omega t)\right)\frac{E_0}{c}\cos(\omega t) \\ &= \frac{e^2E_0^2}{m^2\omega c}\sin(\omega t)\cos(\omega t) \end{aligned} \tag{2.11}$$

Integrating to give the velocity at time t:

$$\begin{aligned} v_z(t) = \int_0^t a_z(t)dt \qquad &= -\frac{e^2E_0^2}{4m^2\omega^2c}\cos(\omega t)|_0^t \\ = \frac{e^2E_0^2}{2m^2\omega^2c}\sin^2(\omega t) \end{aligned} \tag{2.12}$$

And then for position using $\int \sin^2(ax)dx = \frac{x}{2}\frac{\sin(2ax)}{4a}$:

$$\begin{aligned} z(t) = \int_0^t v_z(t)dt \qquad &= \frac{1}{2}\frac{e^2E_0^2}{m^2\omega^2c}\left(\frac{t}{2} - \frac{\sin(2\omega t)}{4\omega}\right) \\ = -\frac{1}{8}\frac{e^2E_0^2}{m^2\omega^3c}\sin(2\omega t) + \frac{1}{4}\frac{e^2E_0^2}{m^2\omega^2c}t \end{aligned} \tag{2.13}$$

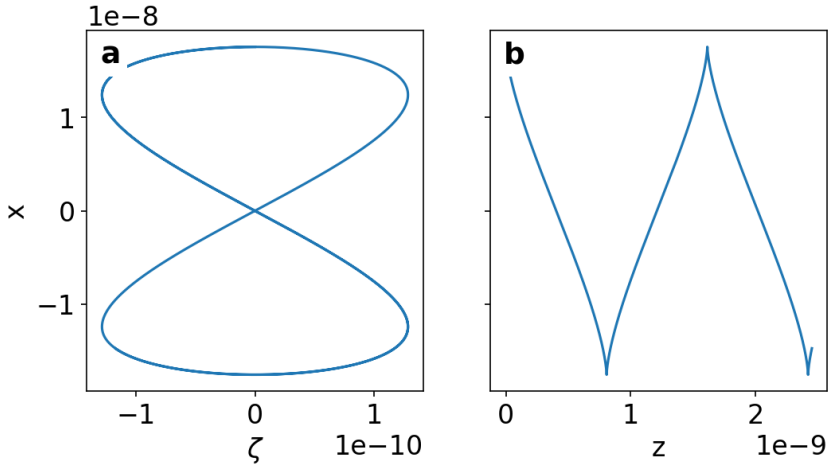

Figure 2.2: The motion of the electron in a plane EM wave. (a) Electron motion in reference frame ζ, moving at the drift velocity (v_d) from Equation 2.14. (b) The motion in the rest frame (z).

Figure 2.2 shows Equations 2.8 and 2.13 plotted. In Figure 2.2 (a) the electron moves in a figure of eight loop in the x-ζ reference frame, moving at the drift velocity. The motion in the rest (x-z) reference frame is shown in Figure 2.2 (b) with the translation in the positive z direction with respect to time being shown:

$$\begin{aligned} v_d &= \frac{1}{4}\frac{e^2 E_0^2}{m^2\omega^2 c} \\ &= \frac{1}{4} c a_0^2 \end{aligned} \tag{2.14}$$

Where the normalised vector potential is defined as:

$$\begin{aligned} a_0 &= \frac{eE_0}{m_e c\omega} \\ &= \sqrt{\frac{I[W cm^{-2}]\lambda_0[\mu m]}{1.37\times 10^{18}}} \end{aligned} \tag{2.15}$$

where I is the laser intensity, and λ_0 is the laser wavelength [42].

The drift momentum mv_d of an electron is given by the average quiver energy divided by the speed of light, $\langle U\rangle/c$.

2.3.1 Non-uniform electric field

A laser pulse is not an infinitely uniform electromagnetic (EM) field, but varies spatially. This means that the ponderomotive potential (Equation 2.10) varies spatially. For a scalar potential field Φ, there will be a force $\vec{F} = -\nabla\Phi$ [41]. For a spatially varying ponderomotive potential the time averaged force on an electron is:

$$\begin{aligned} \vec{F_p} &= -\frac{e^2}{4m\omega^2}\nabla E_0^2 \\ &= -\frac{mc^2}{4}\nabla a_0^2 \end{aligned} \tag{2.16}$$

assuming the relativistic mass increase is small [42]. At the laser focus there is a gradient in a_0 away from the centre of the focus. At the centre of the laser pulse the electrons are quivering with more energy compared with electrons away from the focus. This sets up a potential gradient, which pushes the electrons down the intensity gradient of the pulse, driving the electrons away from the high intensity region.

2.4 Lasers

A laser, standing for "light amplification by stimulated emission of radiation", is a device that produces a beam of EM radiation which can be tailored to have properties such as coherence, collimated, and narrow bandwidth.

To drive a LWFA, a high intensity laser is required. For the LWFA to be operating in the regime where all the electrons have been expelled from the region directly behind the laser pulse (blow-out or bubble regime), the laser's normalised vector potential (Equation 2.15) has to be $a_0 >> 1$ [2]. This is now possible due to the advances in laser technology since their invention. Stimulated emission was predicted by Albert Einstein [44], and occurs when an excited atomic state decay is triggered by an external photon, and produces a photon identical in energy, frequency and wave vector [45]. Charles H. Townes came up with the idea of a maser (microwave amplification by stimulated emission of radiation) in the 1950s, and towards the end of the decade showed that it is possible for amplification to work in the optical spectrum [46]. The first laser was then built by

Theodore H. Maiman in 1960 [47]. The early lasers created continuous beams, but soon pulsed laser came along, utilising Q-switching [48] and then mode-locking [49]. Another important development was that of Chirped Pulse Amplification (CPA) [50], for which the 2018 Nobel prize was awarded [26]. CPA works by stretching the temporal duration of the initial pulse, by dispersion with respect to frequency. The pulse length increase is by a couple of orders of magnitude, which decreases the intensity of the pulse. The decrease in intensity prevents damage to the amplification crystals (the gain medium for the lasers used), allows smaller crystals to be used and stops non-linear effects such as B-integral [51]. B-integral occurs due to the non-linear refractive index at high intensities:

$$B = \frac{2\pi}{\lambda} \int (n_2 I(z))\, dz \tag{2.17}$$

where n_2 is the second order refractive index. Once the amplification has occurred the pulse is re-compressed to create a short pulse duration, high intensity laser pulse.

A laser works on the principle that light can be amplified if the stimulated emission occurs more rapidly than absorption inside the gain medium. For a gain medium to exist, it requires a large population of excited states known as a population inversion. As the light, with initial flux F propagates through the medium in the z direction, the radiation will increase as:

$$\begin{aligned} dF &= (\sigma_{21} F N_2 - \sigma_{12} F N_1) dz \\ dF &= \alpha F dz \end{aligned} \tag{2.18}$$

where σ_{ij} is the proportionality constant for the transition from state i to j, N_i is the population density of state i. As Einstein showed:

$$\sigma_{21} = \sigma_{12} \frac{g_1}{g_2} \tag{2.19}$$

where g_i is the degeneracy of the quantum state i. This results in the gain coefficient being:

$$\alpha = \sigma_{21}(N_2 - \frac{g_2}{g_1}) \tag{2.20}$$

The radiation flux increases as it passes through a gain medium of length L if $\alpha > 0$:

$$F_{\text{out}} = F_{\text{in}} \exp(\alpha L) \tag{2.21}$$

The excitation of the atomic states in the gain medium is often achieved by photo-excitation, and the creation of the population inversion is called pumping. The production of a population inversion requires 3 or more energy levels, otherwise the pump light would cause stimulated emission and prevent the inversion. For maximum efficiency the gain medium energy levels should be such that the energy of the lasing decay is a large fraction of the pump energy.

2.4.1 Gaussian beam focusing

The intensity of the laser light during the amplification stages is kept low to stop damage to the optical components and non-linear refractive index effects, such as B-integral Equation 2.17. The laser beam produced needs to be focused, usually with a parabolic mirror, to create the high intensity required to drive a LWFA. Assuming that the radial profile of the laser beam is Gaussian, then the beam propagation can be calculated from the paraxial wave equation (cylindrically symmetric) [45]. Note that high-powered lasers normally have a top-hat or super-Gaussian beam profile, but this approach is a good approximation and explains the region around focus. The focal spots produced by the high-powered lasers used (Gemini TA2 & TA3) had a Gaussian shape. The normal wave equation is:

$$\nabla^2 \vec{E} - \frac{n^2}{c^2}\frac{\partial^2}{\partial t^2}\vec{E} = 0 \tag{2.22}$$

where n is the refractive index ($n = 1$ for a vacuum) and c is the speed of light. Assuming that the wave is propagating in the z direction, the solution takes the form:

$$E(x, y, z, t) = E_0 \psi(x, y, z) \exp(i(\omega t - kz)) \tag{2.23}$$

The electric field is (Derivation in Appendix A.1):

$$\begin{aligned} E(z, r) = E_0 & \left(\frac{w_0}{w(z)} \exp\left(-\frac{r^2}{w^2(z)} \right) \right) \\ & \times \exp\left(-i \left(kz - \arctan\left(\frac{z}{z_0} \right) \right) \right) \\ & \times \exp\left(-i \frac{kr^2}{2R(z)} \right) \\ & \times \exp(i\omega t) \end{aligned} \tag{2.24}$$

where $R(z)$ is the radius of curvature:

$$\begin{aligned} R(z) &= \frac{1}{z}\left(z^2 + \mathcal{Z}_r^2\right) \\ &= z\left(1 + \left(\frac{\mathcal{Z}_r}{z}\right)^2\right) \end{aligned} \tag{2.25}$$

In Equation 2.24 each line of the equation corresponds to the: amplitude factor, longitudinal phase, radial phase and temporal phase respectively. The beam radius is described by:

$$w^2(z) = w_0^2\left(1 + \left(\frac{z}{\mathcal{Z}_r}\right)^2\right) \tag{2.26}$$

The beam is tightly focused (defined as the electric field remaining above $1/e$ of the maximum value) for a Rayleigh length either side of the focal plane. The Rayleigh length describes the distance from the focus to the point where the beam electric field amplitude decreases to the $1/e$ of the maximum, and the intensity to $1/e^2$:

$$\mathcal{Z}_R = \frac{n\pi w_0^2}{\lambda_0} \tag{2.27}$$

The beam radius at focus is w_0, and for distances far from focus, $|z| >> |\mathcal{Z}_r|$, the beam radius changes linearly with respect to z, $w(z) \approx w_0 z/\mathcal{Z}_r$ as the constant term in Equation 2.26 becomes insignificant. Figure 2.3 shows the electric field of a Gaussian beam focused at $z = 0$. The minimum spread of a beam with radius w_0 is given by:

$$\theta = \frac{2\lambda}{\pi n w_0} \tag{2.28}$$

From this, and using the f-number of the lens, $f_\# = \frac{f}{D}$, where f is the focal length and D the diameter of the lens, the size of the beam focus can be calculated:

$$\text{Diameter} = 2w_0 = \frac{4\lambda}{n\pi} f_\# \tag{2.29}$$

and the Rayleigh length:

$$\mathcal{Z}_R = \frac{4\lambda_0}{n\pi} f_\#^2 \tag{2.30}$$

The focusing optics used on the experiments described in this thesis are $f_\# \sim 15 - 40$. The focused properties for these different focusing optics are shown in Table 2.1. A

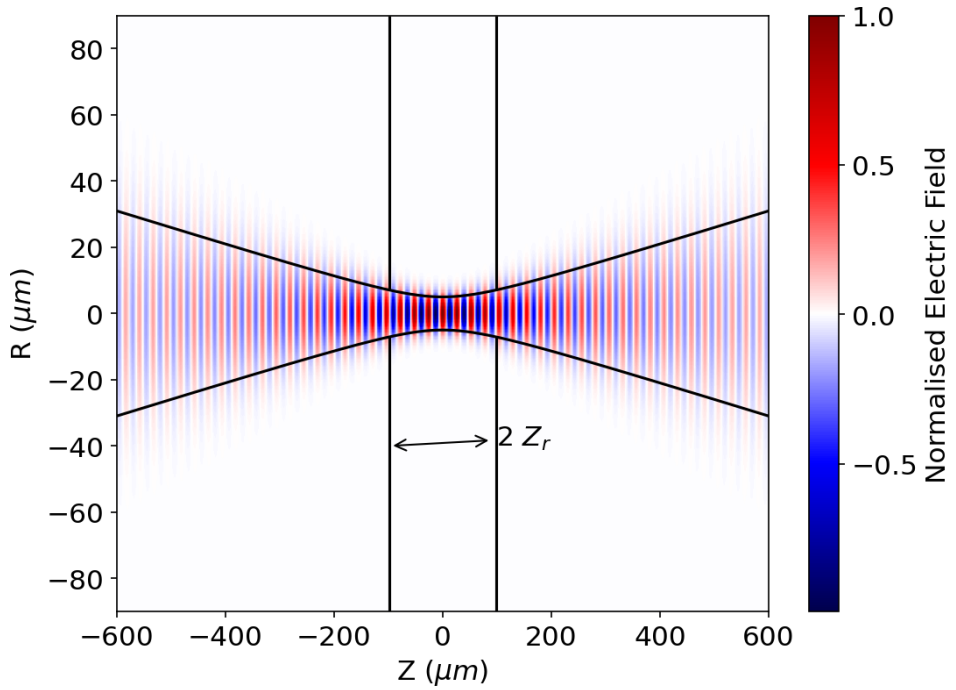

Figure 2.3: A Gaussian beam focusing at $Z = 0$, showing the finite width the beam reaches. The size of the focus does not change rapidly inside one Rayleigh length of the focal plane, after which the beam width increase follows a linear relation with distance. The beam width is marked with the black lines, which have a constant gradient until close to the focus (Equation 2.26) where they do not come to a point, but keep a finite width.

f-number $f_{\#}$	Diameter $2w_0$ $[\mu m]$	Rayleigh length $\mathcal{Z}_r$ $[\mu m]$
5	5.09	25.5
10	10.2	101
20	20.4	407
40	40.7	1630

Table 2.1: Gaussian beam properties when focused with a focusing optics with different f-numbers for 800 nm light, characteristic of Ti:sapphire laser systems.

compromise has to be made between the intensity required, and therefore the focal spot size, and the distance that the pulse remains highly focused. Therefore, a more powerful laser allows the use of a larger the $f_{\#}$ focusing optic, as the required intensity can still be reached but the interaction length is increased.

2.4.2 Self-focusing

The Rayleigh length describes the range in which the laser beam is highly focussed (within $1/e$ of maximum value) in a vacuum. Due to interactions between the laser pulse and the plasma it is possible for the beam to remain highly focused for longer, due to the self-focusing of the laser pulse. This effect is particularly important when using lower power laser pulses, as smaller $f_{\#}$ focusing optics are normally required to create high enough intensities to drive a LWFA. Table 2.1 and Equation 2.30 show that the Rayleigh length increases quadraticly with increasing $f_{\#}$.

Self focusing in plasma is described by W. Mori [52], starting from an unmagnetised plasma with the index of refraction being:

$$\eta = \sqrt{1 - \frac{\omega_p^2}{\gamma_\perp \omega_0^2}} \tag{2.31}$$

where ω_p is the plasma frequency, ω_0 is the laser frequency and $\gamma_\perp = \sqrt{1 + 1/2a_0^2}$. Considering only small modulations, and weakly relativistic pumps the index of refraction can be expanded as:

$$\eta = 1 - \frac{1}{2}\frac{\omega_p^2}{\omega_0^2}\left(1 + \frac{\delta n}{n} - \frac{a_0^2}{2} - 2\frac{\delta\omega_0}{\omega_0}\right) \tag{2.32}$$

The group and phase velocity are:

$$\begin{aligned} v_\phi &= c\eta^{-1} \\ &= c\left(1 + \frac{1}{2}\frac{\omega_p^2}{\omega_0^2}\left(1 + \frac{\delta n}{n} - \frac{a_0^2}{2} - 2\frac{\delta\omega_0}{\omega_0}\right)\right) \end{aligned} \tag{2.33}$$

$$v_g = c\left(1 - \frac{1}{2}\frac{\omega_p^2}{\omega_0^2}\left(1 + \frac{\delta n}{n} - \frac{a_0^2}{4} - 2\frac{\delta\omega_0}{\omega_0}\right)\right) \tag{2.34}$$

The classical action assumption is that within a local volume the photon number is conversed:

$$a_0^2 \omega_0 w^2 L = \text{constant} \tag{2.35}$$

Therefore, changes in the laser's vector potential can occur by: longitudinal bunching (changes in L), transverse focusing (changes in w) and photon acceleration (changes in ω_0). The index of refraction must be stationary in the frame of the light.

Longitudinal bunching

The laser pulse can undergo longitudinal bunching due to changes in the group velocity. The distance between two points (L) may change with respect to time (Δt):

$$\begin{aligned} \Delta L &= (v_{g1} - v_{g2})\Delta t \\ \frac{1}{L}\frac{\partial L}{\partial \tau} &= -\frac{1}{c}\frac{\partial v_g}{\partial \psi} \end{aligned} \tag{2.36}$$

where $\psi = t - x/c$ and $\tau = t$.

A change in the laser's vector potential can occur due to longitudinal compression or through photon acceleration, from Equation 2.35 for a fixed focal spot size:

$$\Delta a_0^2 = -\frac{\Delta L}{L} a_0^2 = \frac{\Delta \omega_0}{\omega_0} a_0^2 \tag{2.37}$$

Photon acceleration occurs when photons gain energy from the wake, and photon deceleration when they lose energy to the wake. The frequency of the photons increases when the refractive index (plasma density) increases with propagation direction will result in an increase in photon frequency:

$$\frac{1}{\omega_0}\frac{\partial \omega_0}{\partial \tau} = \frac{1}{c}\frac{1}{\omega_0}\frac{\partial v_\phi}{\partial \psi} \tag{2.38}$$

Using Equation 2.36 and the equation for photon acceleration (Equation 2.38) the following equation is formed:

$$\begin{aligned} \frac{\partial a_0^2}{\partial \tau} &= \frac{1}{c}\left(\frac{\partial v_g}{\partial \psi} - \frac{\partial v_\phi}{\partial \psi}\right) a_0^2 \\ &= -\left(\frac{\omega_p}{\omega_0}\right)^2 a_0^2 \frac{\partial}{\partial \psi}\frac{\delta n}{n} \end{aligned} \tag{2.39}$$

The longitudinal bunching and photon acceleration cause modulation to the vector potential. The bunching is caused by the plasma density variation's effect on the group velocity, as photons will travel slower in higher density plasma. In the classical action

description no photons are created or destroyed, so for the plasma to take energy from the laser pulse the photons must red-shift. The laser light that is in the accelerating region of the wake experience a time-dependent increase in the plasma density, and are blue-shifted (increase in frequency) [53].

Photon acceleration also agrees with Heisenberg's uncertainty principle $\Delta E \Delta t \geq \hbar/2$ [54]. Assuming the pulse on entering the plasma was fully compressed, i.e. the shortest possible duration, then as the pulse duration shortens the spectral range of the pulse must increase.

Transverse focusing

The focal spot size will change due to the angle of the wavefront, which occurs due to differences in the phase velocity, where $\phi_{\mathrm{OffAxis}} = \phi_1$ and $\phi_{\mathrm{OnAxis}} = \phi_0$:

$$\theta = \left(\frac{v_{\phi 1} - v_{\phi 0}}{w} \right) \Delta t \tag{2.40}$$

Focusing occurs when $\phi_1 > \phi_0$, corresponding to the refractive index decreasing with increased radial distance. The change in spot size with respect to time is:

$$\frac{\partial w}{\partial \tau} = -c\theta = -c \left(\frac{v_{\phi 1} - v_{\phi 0}}{w} \right) \Delta t \tag{2.41}$$

The acceleration in the spot size is:

$$\frac{\partial^2 w}{\partial \tau^2} = - \left(\frac{v_{\phi 1} - v_{\phi 0}}{w} \right) c \tag{2.42}$$

The laser pulse's phase velocity experiences changes in the direction normal to the propagation direction due to a:

1. Non-linear refractive index, with higher intensity on the laser axis (on-axis).
2. Lower electron density on-axis, due to the ponderomotive force expelling electrons.
3. Larger relativistic mass increase on-axis, due to a larger a_0 driving the acceleration.

Relativistic self-focusing occurs due to the mass increase of the electrons travelling close to c. Assuming that v_ϕ varies only due to the a_0 term, the self-focusing described by

Equation 2.42 becomes:

$$\frac{\partial^2 w}{\partial \tau^2} = -\frac{1}{8}\left(\frac{\omega_p}{\omega_0}\right)^2 \frac{c^2}{w} a_0^2 \tag{2.43}$$

A Gaussian optics produced focal spot would be diffracting after the focal plane:

$$\begin{aligned} w &= w_0 \sqrt{1 + \left(\frac{\tau}{\tau_R}\right)^2} \\ \tau_R &= \frac{1}{2}\frac{k_0}{c} w_0^2 \end{aligned} \tag{2.44}$$

where τ_R is the Rayleigh or diffraction time. The double differentiation of this is $\frac{\partial^2 w}{\partial \tau^2} \approx \frac{4}{k_0^2 w_0^3}$. The acceleration of the spot size is:

$$\frac{\partial^2 w}{\partial \tau^2} = \frac{4}{k_0^2 w_0^3}\left(1 - \frac{a_0^2}{32} w_0^2 \left(\frac{\omega_p}{\omega_0}\right)^2\right) \tag{2.45}$$

Therefore, the condition for self focusing is:

$$1 < \frac{a_0^2}{32} w_0^2 \left(\frac{\omega_p}{\omega_0}\right)^2 \tag{2.46}$$

This gives a critical power required for relativistic self-focusing [55]:

$$P_{\text{crit}}[GW] \simeq 17 \frac{n_c}{n_e} \tag{2.47}$$

where n_c is the critical density, the density where the plasma frequency is equal to the laser frequency. For 800 nm light it is $n_c = 1.72 \times 10^{21}\,\text{cm}^{-3}$.

2.5 Ionisation of gas targets

For laser wakefield experiments a laser is focused onto a gas target with a length of the order of 1 mm. The gas is ionised by the strong laser fields, and there are two mechanisms that dominate, multi-photon and barrier-suppression ionisation. Multi-photon ionisation occurs when the laser field is so intense that an electron can absorb multiple photons and gain enough energy to be above the ionisation threshold [56]. This occurs when $eE_{\text{ion}} < n\hbar\omega_l$ where n is the number of photons absorbed.

Barrier-suppression ionisation, or field ionisation [57], occurs when the electric field of the laser is so strong that the potential of the ion is no longer large enough to contain the

electron. Tunnel ionisation occurs for electric field strengths below this value, where the electron escapes the potential well via quantum tunnelling.

Ion	Ionization potential E_{ion}(eV)	Intensity threshold I_L (W/cm^2)
He^+	24.6	3.7×10^{14}
He^{2+}	54.4	8.8×10^{15}
N^{4+}	77.5	3.9×10^{15}
N^{5+}	97.9	7.5×10^{15}
N^{6+}	552.1	7.6×10^{18}
N^{7+}	667.0	1.6×10^{19}

Table 2.2: Ionization potential [58] and intensity threshold for barrier-suppression ionization for elements used in the plasma targets [59].

For the LWFA experiments in this thesis, the laser intensity were of the order 10^{18} W/cm^2. This intensity meant that when a helium gas was used as the plasma target it was fully ionised. For this thesis fully ionised is defined as all electrons being ionised.

2.6 Analytical 1D laser wakefield model

To fully understand wakefield generation and injection, simulations using particle-in-cell codes are required, Section 3.5.1. However, it is possible to create an analytical 1D model to aid the understanding of processes that occur.

To create the model, a Hamiltonian ($\mathcal{H}(q, \vec{p}, t)$) is constructed that satisfies the following equations:

$$\begin{aligned} \frac{d\vec{p}}{dt} &= -\frac{\partial \mathcal{H}}{\partial q} \\ \frac{dq}{dt} &= \frac{\partial \mathcal{H}}{\partial \vec{p}} \end{aligned} \tag{2.48}$$

where $\vec{p}$ is the momentum, q is the generalised coordinates and t is time. The time evolution of the system is uniquely defined by these equations.

For the 1D wakefield model, two unit-less values are used, momentum $\pi \equiv \beta\gamma = p/mc = \sqrt{\gamma^2 - 1}$ and position $\zeta \equiv (z - v_p t)/c$. Here v_p is the velocity of the wakefield, and ζ is the co-moving coordinate of the wakefield. The equations in these coordinates are:

$$\frac{d\pi}{dt} = -\frac{\partial \mathcal{H}}{\partial \zeta} \tag{2.49}$$

$$\frac{d\zeta}{dt} = \frac{\partial \mathcal{H}}{\partial \pi} \tag{2.50}$$

Using the Lorentz factor (γ) and the ratio of the velocity to the speed of light (β):

$$\begin{aligned} \beta &= v/c \\ \gamma &= \frac{1}{\sqrt{1-\beta^2}} \\ \beta &= \frac{\sqrt{\gamma^2 - 1}}{\gamma} \end{aligned} \tag{2.51}$$

The terms relating to the wakefield are:

$$\begin{aligned} \beta_p &= \sqrt{1 - \left(\frac{\omega_p}{\omega_0}\right)^2} \\ \gamma_p &= \frac{\omega_0}{\omega_p} \end{aligned} \tag{2.52}$$

where γ_p is the Lorentz factor of the wake, ω_0 and ω_p the frequency of the laser and the plasma respectively.

The first of the components comes from the potential energy:

$$\frac{dp}{dt} = qE_z \tag{2.53}$$

Where the electric field can be described by the electric potential in terms of the co-moving frame $E_z = -\frac{\partial V(\zeta)}{\partial z}$:

$$\frac{dP}{dt} = mc\frac{d\pi}{dt} = qE_z \tag{2.54}$$

$$\frac{d\pi}{dt} = -\frac{q}{mc}\frac{\partial V(\zeta)}{\partial z} \tag{2.55}$$

Integrating Equation 2.49 and Equation 2.55 the Hamiltonian has the form:

$$\mathcal{H} = \frac{q}{mc^2}V(\zeta) + C \tag{2.56}$$

where C is a term to be found. The normalised potential is:

$$\Phi = \frac{q}{mc^2} V(\zeta) \tag{2.57}$$

The C term in Equation 2.56 comes from the kinetic energy term, from Equation 2.50. Using the co-moving coordinate:

$$\frac{\partial \zeta}{\partial t} = \frac{\partial_t z - v_p}{c} = \frac{v - v_p}{c} = \beta - \beta_p \tag{2.58}$$

and comparing with Equation 2.50 to get:

$$\begin{aligned} \frac{\partial \mathcal{H}}{\partial \pi} &= \beta - \beta_p \\ &= \frac{\pi}{\gamma} - \beta_p \\ &= \frac{\pi}{\sqrt{\pi^2 - 1}} - \beta_p \end{aligned} \tag{2.59}$$

Integrating the above gives:

$$\begin{aligned} \mathcal{H} &= \sqrt{\pi^2 + 1} - \pi\beta_p + C \\ &= \gamma - \gamma\beta\beta_p + C \\ &= \gamma(1 - \beta\beta_p) + C \end{aligned} \tag{2.60}$$

Comparing Equations 2.55 and 2.60 the Hamiltonian is:

$$\mathcal{H} = \gamma(1 - \beta\beta_p) - \Phi(\zeta) \tag{2.61}$$

An equation for the plasma potential ($\Phi(\zeta)$) is required which is given in Section 2.6.1.

2.6.1 1D plasma potential

Following the method of Bingham and Trines [60], the 1D plasma potential can be calculated from the following starting information and assumptions: one fluid; cold relativistic hydrodynamics; Maxwell's equations; and the quasi-static approximation.

Equation of motion:

$$\frac{D\vec{p}}{Dt} = m_e \left(\frac{\partial \vec{v}}{\partial t} + (\vec{v} \cdot \nabla)\vec{v} \right) = -e(\vec{E} + \vec{v} \times \vec{B}) \tag{2.62}$$

Continuity equation:

$$\frac{\partial n_e}{\partial t} + \nabla \cdot (n_e \vec{v}) = 0 \tag{2.63}$$

Gauss' Law:

$$\nabla \cdot \vec{E} = \frac{-e(n_e - n_i)}{\epsilon_0} \tag{2.64}$$

where n_e is the plasma density, n_i the ion density, m_e the mass of the electron, ϵ_0 the vacuum permittivity, $\vec{E}$ the electric field and $\vec{B}$ the magnetic field.

From this a linear plasma potential can be derived (see Appendix A.2). For different driver (laser pulse) shapes the resonance pulse length has been found [18, 55, 61] (Table 2.3), with an optimum driver pulse length of the order of the plasma wavelength. The magnitude of the electric field that forms in the wake can reach the order of the 'cold

Driver shape	Pulse length for resonance
Top Hat	$L = \lambda_p/2$
$\sin^2(\pi\zeta/L)$	$L = \lambda_p$
$\exp\left(-(\zeta/L)^2\right)$	$L = \lambda_p/(\pi\sqrt{2})$

Table 2.3: The temporal length of the driver (laser pulse) of a 1D LWFA in the linear regime that resonantly drives the wake for some characteristic shapes of laser pulses [18, 55, 61].

wave-breaking limit', which is defined as [2]:

$$E_{wb} = \frac{m_e c \omega_p}{e} \tag{2.65}$$

A non-linear plasma potential description is required for large values of a_0 ($a_0 > 1$). The equation is [55]:

$$\frac{1}{k_p^2}\frac{\partial^2 \phi}{\partial \zeta^2} = \gamma^2 \left(\beta_p \left[1 - \frac{\gamma_\perp^2}{\gamma^2 (1+\phi)^2} \right]^{-\frac{1}{2}} - 1 \right) \tag{2.66}$$

where $\gamma_\perp^2 = 1 + u_\perp^2 = 1 + a_0^2$, $\gamma = (1-\beta^2)^{-\frac{1}{2}}$. This simplifies in the limit of $\gamma_p >> 1$ to:

$$\frac{1}{k_p^2}\frac{\partial^2 \phi}{\partial \zeta^2} = \frac{1}{2}\left(\frac{1+a_0^2}{(1+\phi)^2} - 1 \right) \tag{2.67}$$

2.6.2 1D wakefield results

Figure 2.4 shows the numerically solved plasma potential (blue dashed line), electric field (orange line) and number density (navy line) for three different a_0 values of drive pulse (red). For a low a_0 drive pulse, a sinusoidal wake follows the laser pulse. As a_0 increases to around 1 the wake starts to become non-linear. Once $a_0 > 1$ the electron density starts to show sharp peaks, and the fields develop a saw-toothed shape. For the $a_0 = 3$ case

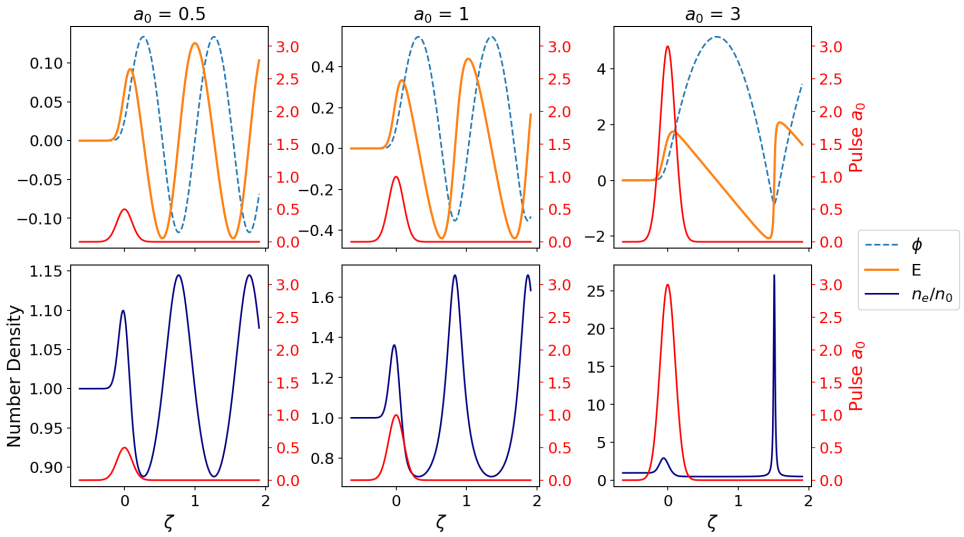

Figure 2.4: Numerical solutions to the 1D wakefield model. The solutions are sinusoidal for $a_0 < 1$. As the laser intensity increases the wake starts to become non-linear. For large a_0 the electric field becomes saw-toothed, and the electron density highly peaked.

the wavelength of the oscillations has increased, and this is due to the relativistic mass increase as the velocity of particles in the wake approach the speed of light ($\beta \to 1$).

Using the Hamiltonian Equations 2.61 and 2.67 the phase space between the co-moving coordinates for position and momentum is plotted in Figure 2.5. If the initial momentum (γ) of a particle is either too low or high, then it will form part of the oscillating structure but will not gain any energy from the wakefield. However, if the particle is within the dashed lines (the seperatrix) it will be trapped in the accelerating structure and will gain energy.

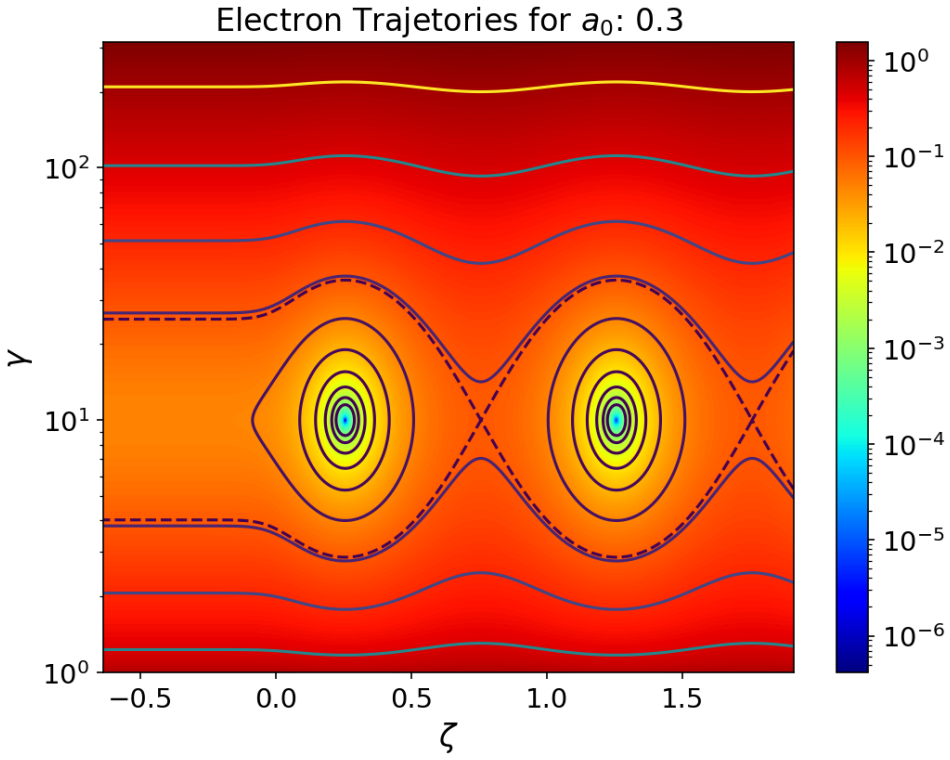

Figure 2.5: The phase space, between position and momentum, of the electrons in a wakefield. The separatrix (dashed line) is the separation between closed and open orbits.

The seperatrix allows the calculation of the minimum energy a particle requires to be trapped, and also the maximum energy gain of the particle [62]:

$$\begin{aligned} \mathcal{H}(\gamma, \zeta_{max}) &= \mathcal{H}_s \\ \gamma(1 - \beta\beta_p) - \phi_{max} &= \frac{1}{\gamma_p} - \phi_{min} \end{aligned} \tag{2.68}$$

Now let $\Delta = \frac{1}{\gamma_p} + \phi_{max} - \phi_{min}$ which describes the ease with which a particle is trapped in the wake, and using $\beta\gamma = \sqrt{\gamma^2 - 1}$, Equation 2.68 becomes a quadratic:

$$\begin{aligned} \gamma - \beta_p\sqrt{\gamma^2 - 1} &= \Delta \\ \beta_p^2(\gamma^2 - 1) &= \gamma^2 + \Delta^2 - 2\Delta\gamma \\ 0 &= \gamma^2 - 2\Delta\gamma_p^2\gamma + \gamma_p^2(\beta_p^2\Delta^2) \end{aligned} \tag{2.69}$$

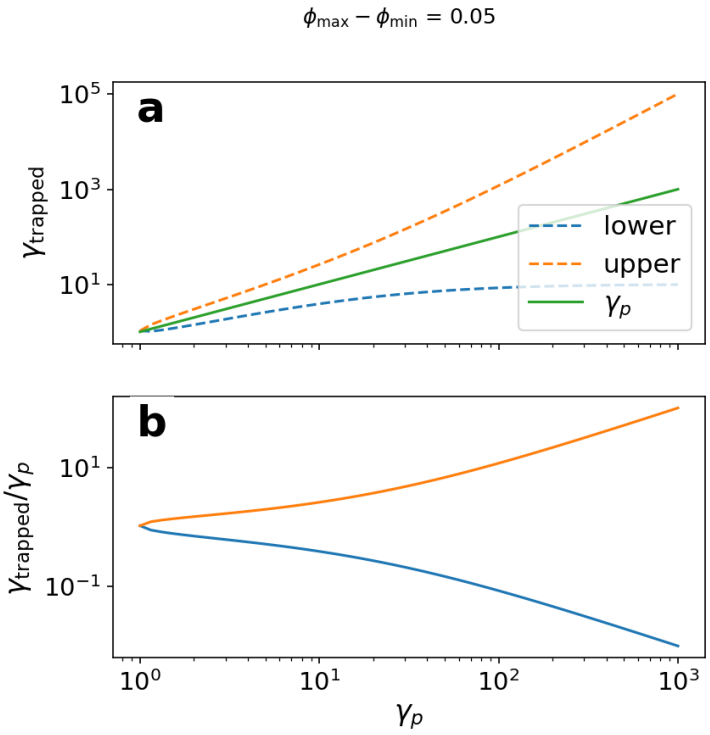

Figure 2.6: a) The minimum and maximum trapping energies of the wake is related to the energy of the wake. These both increase proportionally to the energy of the wake. b) The maximum energy gain of particles increases with energy of the wake.

The roots of this equation corresponded to the trapped particle range:

$$\begin{aligned}\gamma_{trapped} &= \gamma_p\Delta \pm \sqrt{\gamma_p^4\Delta^2 - \gamma_p^2(\beta_p^2 + \Delta^2)} \\ &= \gamma_p\Delta \pm \gamma_p\sqrt{\Delta^2(\gamma_p^2 - 1) - \beta_p^2} \\ &= \gamma_p\Delta \pm \gamma_p\beta_p\sqrt{\Delta^2\gamma_p^2 - 1}\end{aligned} \tag{2.70}$$

From Equation 2.70, the following physical effects are shown. Firstly if there is no wake, ie. $\phi_{min} = \phi_{max}$ then $\Delta = \gamma_p^{-1}$. This means that the only particles that are trapped are particles travelling at the speed of the wake, $\gamma_{trapped} = \gamma_p$, as ought to be expected as there is no field acting on them. The next is if $\delta = \gamma_p\Delta = 1 + \gamma_p(\phi_{max} - \phi_{min})$ the trapped particle's Lorentz factor is:

$$\gamma_{trapped} = \delta \pm \beta_p\gamma_p\sqrt{\delta^2 - 1} \tag{2.71}$$

The doubly normalised potential from Equation 2.57 is:

$$\widetilde{\phi} = -\frac{\gamma_p q V}{mc^2} = -\frac{\omega_0}{\omega_p}\frac{qV}{mc^2} \tag{2.72}$$

$\widetilde{\phi}$ shows that the same wake potential (V) can trap a larger range of particle energies when γ_p is larger. This happens at lower densities, as $\gamma_p = \omega_0/\omega_p = \sqrt{\frac{n_{crit}}{n_e}}$. Finally, Figure 2.6 shows the particle energy against the gamma of the wakefield. An increase in γ_p both lowers the minimum energy required for trapping, and increases the maximum energy gain that is possible.

2.6.3 Divergence model

The divergence of the electron beam produced by a plasma target created by a gas cell is often smaller than that produced by a gas jet plasma target. Here this is explored using a simple model, where the restoring force on the electrons oscillating around the laser beam axis has been modelled as a simple harmonic (SHM) oscillator. The electric field E in the plasma provides the restoring force, and maximum field strength (non-relativistic wavebreaking limit) is $E_{wb} = mc\omega_p/e$ [63], showing that $E \propto \sqrt{n_e}$. Therefore, the spring constant k is $\propto \sqrt{n_e}$. The SHM model is shown Figure 2.7. Both plasma targets have a notional edge at $z = 50$. The density profile of a gas jet is approximately flat-topped, whereas a gas cell has been approximated with an exponentially decaying profile after this point. This is due to the exit holes of the gas cell acting as a gas jet along the propagation direction of the laser. The gas jet profile does not damp the radial velocity of the particles as they exit the wake, whereas the gas cell exponentially decaying profile does. Therefore, due to the shape of the density profile gas cells are more likely to produce low divergence electron beams.

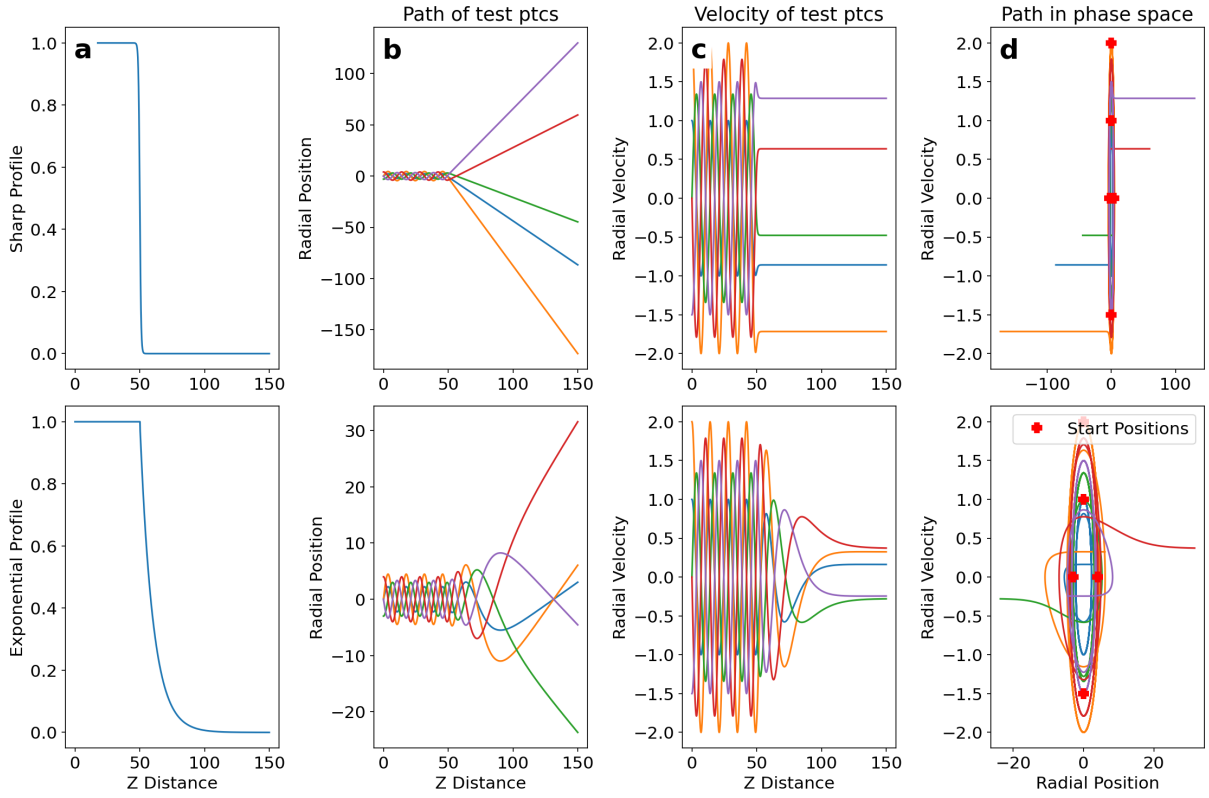

Figure 2.7: Longitudinal density profile on electron divergence using a SHM model. The columns are: a) The longitudinal density profile. b) The radial position of the particles. c) The velocity of the particles. d) The path of the particles in the position-velocity space.

2.7 Limits on acceleration

Particle accelerators produce high energy particles by having the particles in an accelerating field over a given distance. The output energy is related to the integrated field by distance the particle travels. LWFA have large fields, but there are three fundamental issues to overcome when increasing the length of the acceleration region. These relate to the driving laser pulse, and are: depletion, dephasing and diffraction.

2.7.1 Depletion

A high intensity gradient is required to drive the wake, which is set up using the ponderomotive force. The laser pulse loses energy to the wake in order to drive it, and this will decrease the intensity of the pulse as it propagates forward [64]:

$$\begin{aligned} k_p L_{pd} &\simeq (\omega_0/\omega_p)^2 \frac{\omega_p \tau}{a_0^2} \quad a_0 < 1 \\ &\simeq \frac{1}{3}(\omega_0/\omega_p)^2 \omega_p \tau \quad a_0 > 1 \\ &\simeq (\omega_0/\omega_p)^2 \omega_p \tau \quad a_0 > 2 \end{aligned} \tag{2.73}$$

One approach to solving this issue it to use multiple laser pulses, and have acceleration regions joined together [39], not unlike radio frequency (RF) cavities. This is known as "staging" and is thought to be required to reach energies much greater than 10 GeV [22].

2.7.2 Diffraction

To achieve the high intensity required to drive the wake, laser pulses are required to be focused down to small focal spots. This often requires focusing with a reasonably small $f_\#$ optic (~ 10) to reach the required intensity ($a_0 \sim 1$). Therefore, the length over which the laser pulse is highly focused, the Rayleigh length, is proportional to $f_\#^2$ (Equation 2.30). Therefore, the stronger the focusing of the laser the shorter the interaction length will be. This effect is mitigated to some extent by the self-focusing of the laser. Another method is to use plasma channels to guide the laser [65].

2.7.3 Dephasing

The laser pulse travels at the speed of light in the plasma, which is slower than in a vacuum due to the refractive index. The electrons that are accelerated quickly become relativistic, moving close to the speed of light in vacuum. In the plasma the electrons are actually travelling faster than the laser pulse, which results in the electron bunch catching up with the laser pulse. This means that the electrons move out of the accelerating phase and into the de-accelerating phase of the plasma wave. In the frame of the wake, this occurs

when the electrons have travelled $\sim \frac{1}{2}\lambda_p$. In addition to being in the correct accelerating region of the wake, there are focusing and defocusing transverse fields which need to be considered. For a simple 1D description these focusing fields reduce the usable accelerator by another factor of $\frac{1}{2}$. However, for the 3D case the distance the electrons can slip with respect to the wake is between $\frac{1}{4}\lambda_p \rightarrow \frac{1}{2}\lambda_p$. Depending on the a_0 of the laser the dephasing length is [64]:

$$\begin{aligned} L_\phi &\simeq \frac{\lambda_p}{2\pi}(\omega_0/\omega_p)^2 && a_0 < 1 \\ &\simeq 2a_0^2\frac{\lambda_p}{\pi}(\omega_0/\omega_p)^2 && a_0 > 1 \\ &\simeq (4/6\pi)\sqrt{a_0}\lambda_p(\omega_0/\omega_p)^2 && a_0 > 2 \end{aligned} \tag{2.74}$$

To reach higher energies without dephasing, a lower electron density is required. However, self-focusing effect on the laser pulse increase with electron density, so a balance of these three effects dictates the experimental design.

2.8 Injection of electrons into the wakefield

The high intensity laser pulse propagation through the plasma sets up the wake, but the formation of this structure in itself does not create high energy electrons. To produce high energy electrons, electrons have to become separate from the electrons forming the wave, and be injected into the accelerating region of the wave. Figure 2.5 shows this: electrons have to be inside the seperatrix to gain energy from the wake. Electron beams with a large energy spread occur when the injection into the accelerating structure happens in a large region of the phase space (γ, ζ), which described the electrons seen prior to 2004. In 2004 three groups independently observed narrow energy spread (quasi mono-energetic) electron bunches [3–5]. This was possible due to the injection being in a localised region of phase space, and work has since been done on improving the production of quasi mono-energetic electrons and therefore, injection methods. One of the reasons for the mono-energetic electron production in 2004 was the short laser pulse duration that was now possible due to Ti:sapphire lasers [51]. Ti:sapphire laser pulse lengths of ~30 fs allow

$\lambda_p \approx c\tau$ in plasma densities used (10^{18} to $10^{19}\,\mathrm{cm}^{-3}$) and therefore, resonant driving of the wake. Ti:sapphire based lasers are now the main driver of LWFAs.

The next paragraphs outline the different methods that have been used and developed for injecting electrons into the wake. The more advanced mechanisms can lead to a more stable electron beam which is useful for the realisation of applications.

2.8.1 Self injection

Self injection created the first mono-energetic electron beam seen in 2004 [3–5]. Mono-energetic beams were seen at the lowest plasma density that produces electron beams. This is due to the laser pulse energy being just above the threshold for trapping. Once electrons are injected, the beam loading effect prevents further injection. As the electrons in the accelerated region all start at the same time and position, they see the same accelerating forces [5]. Another reason was using a lower density plasma, resulting in the dephasing length of the accelerated electrons being longer than the length of the plasma target. If the electron bunch dephases and then interacts with the laser pulse, the low divergence and mono-energeticness of the beam is degraded [3].

2.8.2 Ionisation injection

Ionisation injection occurs when an impurity, usually nitrogen, is present in the gas used. Table 2.2 shows that the inner electron shells of nitrogen require an intensity of the order $10^{19}\,\mathrm{Wcm}^{-2}$ to be ionised. By designing the experiment such that the intensity required to ionise these electrons only occurs for one small location in space and time, then all the electrons will see the same accelerating forces. Laser ionisation injection was first accomplished by C. McGuffey *et al.* [66] and Pak *et al.* [67] in 2010. They found that the electron trapping initiated by ionisation increased the amount of charge injected by an order of magnitude and also decreased the beam emittance.

Narrow energy spread beams have been created with this method by using a gas cell with two internal regions. The first region, the injector, is filled with a mixed gas. The second, the accelerator, is filled with a pure gas, meaning the injection only occurs in the

first region. All electrons that are trapped in the first region are then accelerated for the same length, the second region of the gas cell, producing quasi mono-energetic beams [68].

2.8.3 Density transition injection

A plasma density transition can also be used to induce injection in a LWFA. Injection of electrons at a sharp density jump was first shown by K. Schmid *et at* [69] in 2010. The laser pulse enters a region of high plasma density, which then transitions to a low density region. The injection occurs because the wavelength of the plasma is proportional to $\lambda_p \propto \sqrt{n_e}$. Therefore, the structure of the plasma wave is suddenly altered at the transition point. The sudden transition causes some of the electrons from the high density wake oscillations to end up in the trapped region of phase space of the low density plasma wave. For this injection method to work the density transition must be of the order of the plasma wavelength [69, 70], which for the plasma densities of 10^{18} to $10^{19}\,\mathrm{cm}^{-3}$ is $\sim 10\,\mu\mathrm{m}$. These profiles have been made experimentally by using a supersonic gas flow and an obstruction (razor blade) [69, 71], coupling a gas jet and capillary [72]. It has also been investigated through simulations for multi-region gas cells [73]. Experimentally multi-region gas cells have been used, and they have also been combined with ionisation injection [68, 74]. Using a two region gas cell allows the first 'injector' region to be filled with a mixed gas, and the second 'accelerator' region filled a pure gas.

2.8.4 Dual laser pulse injection

J. Faure *et al* [75] in 2006 used two counter-propagating lasers to create mono-energetic electron beams. One beam was used to drive the wakefield, and the other to cause electron injection. When the two pulses overlapped a laser beatwave pattern was formed. This has a large local ponderomotive force, $F_{bw} \propto 2a_d a_i/\lambda_0$, where a_d and a_i are the a_0s of the drive laser and injection laser respectively. This beatwave force (F_{bw}) locally accelerates some of the background electrons, giving them enough energy to be trapped by the wake. This gives a good level of control of the electron energy, as by changing the delay between

the two pulses, the interaction in z position is moved through the plasma target, changing the acceleration length region.

Dual laser pulse injection can also be achieved with co-propagating laser pulses [76], where one is used to drive the wakefield, and the other to guide it.

2.9 X-ray sources

One application that has been of great interest is the development of compact X-ray sources, which could compliment the current sources driven by an X-ray tube, or by linacs. X-rays can be produced from the highly energetic electrons produced in a LWFA in several different ways, shown in Figure 2.8. Such LWFA light sources have been studied extensively and reviewed by Corde *et al.* [77] and Albert and Thomas [78].

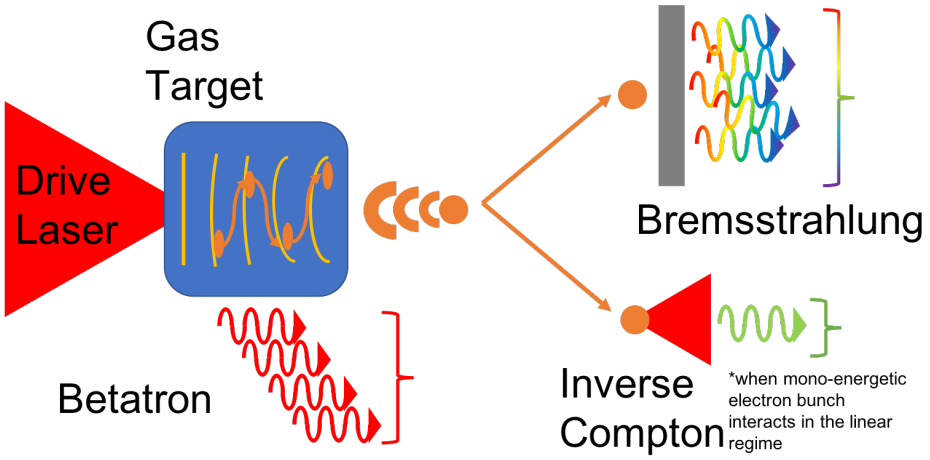

Figure 2.8: The potential X-ray sources produced using a LWFA. The inherent electron oscillations (orange arrows) in the wake cause betatron radiation (red photons). Once the energetic electrons exit the LWFA they can be used to create other sources. The electrons are propagated into a dense material to produce bremsstrahlung radiation which is bright and broadband. Inverse Compton scattering can create narrow band photons under the correct conditions. The electrons can pass through an undulator (not shown) to produce X-rays through synchrotron radiation or free-electron laser (FEL).

2.9.1 Betatron

The acceleration structure in the wake has electric fields accelerating in the laser propagation direction, and focusing fields in the transverse directions due to the curvature of the plasma buckets. This means that electrons that are injected into the wake off axis will oscillate in the wake. This inherent transverse motion of the electrons is known as betatron oscillations, and will generate X-ray radiation (10-100keV) [30] which, due to its micron-scale source size and high-spatial coherence, is ideal for phase-contrast imaging [79–82]. This radiation is very similar to synchrotron radiation, but due to the plasma wavelength being significantly shorter, the size of the undulator created by the wake is orders of magnitude smaller and requires electron beams with lower energy (MeV instead of GeV). An undulator/wiggler is a device that has a periodic field structure that causes the electrons to oscillate, and is used in synchrotrons and free electron lasers.

2.9.2 Inverse Compton scattering

Inverse Compton scattering (ICS) is the up-shifting in energy of photons by scattering from the electrons. The energy of the scattered photons scales (in the linear regime for a head on collision, $\phi = 180°$ where ϕ is the scattering angle) as $E_\gamma = 4\gamma^2 E_l$, where E_γ is the X-ray energy, E_L is the incoming laser energy and γ is the gamma factor of the electrons. ICS is an effective way to produce MeV-scale, narrow energy spread X-rays [33, 34], but due to the small cross-section and the number of electrons from the LWFA the X-ray flux is low. As the scattering laser photons become more intense then the scattering becomes non-linear. The photon spectrum changes from its narrowband spectrum to include higher harmonics, and tends towards a synchrotron-like broad spectrum [83]. The resulting energy of the photons also depends on the angle of the interaction, ϕ, with a head-on collision producing a $4\gamma^2$ up-shift in photon energy. Therefore, to produce mono-energetic photons the angle of the interaction has to be limited to a scattering angle $\phi \approx 180$.

2.9.3 Bremsstrahlung

Bremsstrahlung radiation [32] can be used to create an X-ray source by placing a foil in the path of the energetic electron beam. The de-acceleration of the electrons through the interaction with the positive ions emits X-rays. Compact LWFA X-ray sources for imaging have also been demonstrated using bremsstrahlung radiation [35, 84–87]. Electrons incident on a high-Z material produce a cone angle beam of radiation with a broad energy spread extending up to the maximum electron energy.

The radiated power per unit energy per unit solid angle is given by [78]:

$$\frac{d^2P}{dEd\Omega} = \frac{1}{\hbar}\frac{dP}{d\omega}\left[\frac{3}{16\pi}\frac{1}{\gamma^2(1-\beta\cos(\theta))^2}\left(2+\frac{\cos^2(\theta)-1}{\gamma^2(1-\beta\cos(\theta))^2}\right)\right] \tag{2.75}$$

where:

$$\frac{dP}{d\omega} = \frac{16}{3}Z^2 n_i e^2\left(\frac{e^2}{m_e c^2}\right)^2\frac{1}{\beta}\ln\left(\frac{Q_{max}}{Q_{min}}\right) \tag{2.76}$$

Where Z is the atomic number of the converter, n_i is the density of ions in the converter and Q is the momentum transfer.

2.9.4 Applications

A LWFA based light source has been shown to be a useful tool for radiography, using betatron, ICS and bremsstrahlung, with potential uses in port security and large industry [88]. Phase contrast imaging has been shown for LWFA betatron radiation sources [79–82, 89], and for bremsstrahlung sources created through laser solid interactions [90]. One radiographic application currently in high demand is *non-destructive testing* (NDT), where rapid high resolution ($<$0.1 mm) tomography of large, dense objects is required. To image small features in high density material samples a highly penetrative spectrum and small source size are required. For projectional radiography the smallest features that can be measured is defined by the geometry of the imaging and the source size. The most challenging objects in aerospace, automotive and nuclear sectors are additively manufactured structures with fine internal features composed of materials such as steel or nickel, which need to be inspected for failure indicators and quality control. It is advantageous to use a

LWFA X-ray source for these cases, due to its small divergence source resulting in a lower overall radiation dose for the investigated object, and small source size for high spatial resolution [78]. Commercial linac driven sources are often limited to source sizes in the millimetre range [91].

These LWFA light sources have uses in nuclear medicine, such as the photo-nuclear reactions to produce ^{99}Mo which then decays into the technetium isomer $^{99}Tc_m$ [78] that is used in over 80% of medical procedures using radioactive sources [92].

LWFA sources can also be used for: backscattered x-ray and gamma-ray inspection (useful for remote sensing of objects); isotope-specific detection with nuclear resonance fluorescence (important for homeland security, stockpile stewardship, or nuclear waste assay); nuclear waste transmutation (reducing the long lived waste to shorter half-life isotopes) [78].

LWFAs have the potential to produce these X-ray sources in a compact and relatively inexpensive manner, complementing the current sources that exist.

3 | Methodology

The work presented in this thesis is based on both experimental and simulation results. Three pre-built simulation codes were used, which are described below. The experiments described in this thesis took place at the Central Laser Facility (CLF) at the Rutherford Appleton Laboratory (RAL), UK, and at the Gérard Mourou Center for Ultrafast Optical Science (CUOS) at the University of Michigan, USA. The systems and diagnostics used on these experiments are described here.

3.1 High power lasers

For the laser wakefield accelerator (LWFA) experiments in this thesis, high powered (>1 TW) lasers were required. In order to create ultra-short pulses solid state lasers were used, with Ti:sapphire [93] as their gain medium. The energy in the laser pulses ranged from the order of 100 mJ to 10 J with pulse durations of ∼40 fs, corresponding to a peak laser power of the order TW to PW.

3.1.1 Basic layout of a laser

The layout of all the high powered lasers used was the master oscillator power amplifier (MOPA) arrangement. In a MOPA laser, the laser pulse is initiated in the front end, or oscillator. The oscillator creates ultra-short pulses, using a mode-locking technique in the laser cavity [49]. An individual pulse is selected from the pulse chain produced in the oscillator, using Pockels cells [49] and polarisers, and is known as the seed pulse. The seed pulse is then temporally stretched with respect to its spectral frequencies using dispersive

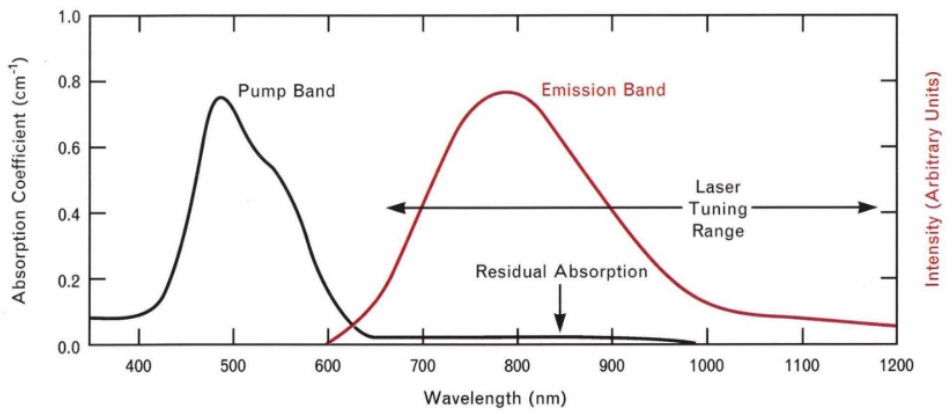

Figure 3.1: The pump and emission bands of the Ti:sapphire gain material. The full width half maximum (FWHM) of the emission band is 210 nm. Copied from [94].

gratings, creating a lower intensity chirped pulse for passing through the gain medium, in a process called chirped pulse amplification (CPA) [50]. The gain medium Ti:sapphire has a peak emission wavelength of 800 nm (Figure 3.1) and amplifies a spectrum with a bandwidth corresponding to a minimum pulse duration of ∼10 fs [93]. Ti:sapphire is pumped with green light (Figure 3.1). The pumping of the crystal at the experimental facilities used was carried out by a laser, with a wavelength chosen to efficiently pump the material. The narrow bandwidth of the pump laser means the pump light is only in a region of the spectrum that is efficiently absorbed, reducing the heating of the crystal which is detrimental to the performance of the laser system. The pulse is then amplified, normally in stages, by either a regenerative amplifier (lower energy pulses) or a multi-pass amplifier (normally in the final amplification stage(s)).

During amplification the spectrum of the laser can be modified, which for a Ti:sapphire crystal based laser is primarily through gain-narrowing and gain-shifting of the central wavelength [95]. Gain saturation is crucial to these processes, and means that very intense parts of the spectrum are no-longer linearly amplified by the emission spectrum but see a reduced gain. Gain shifting occurs when the pulse has been spectrally stretched, normally with a positive chirp. This means that the low frequency end of the pulse (red end of the

spectrum) passes through the crystal first. Gain saturation is reached by the temporal front edge of the pulse first, as it has been seeing a higher gain [95]. Gain narrowing occurs during the unsaturated amplification of the beam. The spectrum of the emission band is peaked at 800 nm (Figure 3.1) [94] . Each time the pulse being amplified passes through the gain medium, the part of the spectrum corresponding to this peak is amplified at a faster rate compared with the rest of the pulse. These effects mean that the pulse properties of the amplified beam are usually different to the seed pulse.

After each amplifier stage the beam is normally expanded, to reduce the intensity of the beam on the next optical component, so it both remains below the damage threshold intensity and reduces the non-linear refractive index effects that are detrimental to the pulse. This beam expansion also allows the use of small crystals in the initial amplification stages. This both reduces the cost of the gain crystals and reduces the amplified spontaneous emission (ASE), which occurs when a spontaneously emitted photon travels through the gain medium and is amplified by the stimulated emission. ASE becomes a real issue with the highest powered Ti:sapphire lasers, where the beam size is of the order 10 cm, where ASE along the crystal axis saps energy from the crystal, which is detrimental to the amplified pulse [96].

The final stage of the laser is a compressor, again comprised of dispersive gratings, which reduce the pulse duration back to, approximately, the input value. The Gemini laser at the Central Laser Facility uses a double pass compressor to remove the spatial chirp from the pulse.

3.1.2 Control over the pulse properties

The temporal shape of the pulse can be altered using a pulse shaper. At the Astra-Gemini laser facility the pulse shaping is performed by an Acousto-optic Modulator [97], with the specific device being a Fastlite Dazzler [98]. This is a device that modifies the refractive index of a material using the oscillation in mechanical strain produced by a sound wave [99]. A refractive grating is formed from the propagation of the sound wave through the crystal. The frequency and direction of the scattered beam depend on the frequency of the

sound wave, and the acoustic power controls the diffracted optical power. This approach allows for pre-compensation of gain-narrowing [49], and can compensate for high order phase distortions, creating cleaner and shorter pulses [98].

The wavefront can be altered using an adaptive optic (AO), which is a mirror with an adaptable curvature. Using the AO on the Astra-Gemini laser it was possible to modify the wavefront to shift the focal plane by $\sim\pm 1\,\mathrm{mm}$.

For the work in this thesis, the laser pulse was optimised at the beginning of each period of data collection by flattening the wavefront and reducing the pulse duration. Normally the LWFA is then optimised with 1D scans in the focal plane and changing the pulse properties with the Dazzler. For Chapter 6 these scans were computer controlled for multidimensional optimisations.

3.2 Laser diagnostics

The shape of the laser pulse, both spatial and temporal, has a large effect on a LWFA. Therefore, to understand the effect of the pulse shape on the interaction it is important to have a well diagnosed laser pulse.

3.2.1 Wavefront

The quality of the laser focus from the focusing optic depends on the wavefront. To reach the minimum focal spot size from the standard focusing optic for LWFA, an off-axis parabola, a flat wavefront is required. This can be improved by using an AO coupled with a wavefront sensor (WFS). For the experiments at the CLF a HASO WFS [100] was used, which is based on the Shack-Hartmann design [101]. This WFS has an array of lenslets (small lenses) mounted such that the lenses image a parallel beam onto the plane of the detector. Each lenslet focuses the light incident on it to a point on the sensor depended on the average orientation of wavefront on the lenslet. Increasing the number of lenslets in the array improves the resolution of the measurement. A 1D example case is shown in Figure 3.2. If the incoming wavefront is flat (Figure 3.2 (a)), then the focus position is at

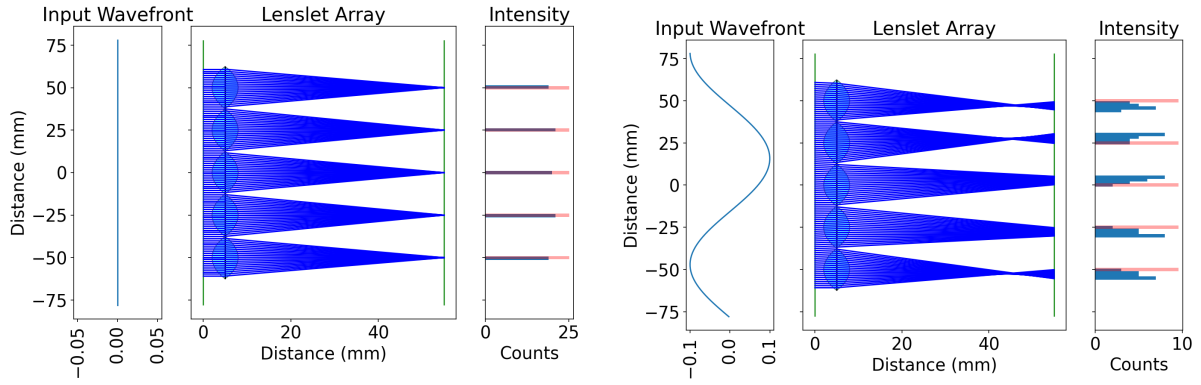

(a) (b)

Figure 3.2: The principles behind a Shack-Hartmann WFS shown for a 1D test case. (a) For a flat wavefront the focus points occur where expected, marked by the red lines. (b) When a non-flat wavefront is introduced, the points no longer match. The wavefront can be calculated from these shifts.

the expected positions. For a non-uniform wavefront (Figure 3.2 (b)), the focus point of each lens changes, and from this change the wavefront can be calculated.

The WFS and AO are run in a iterative loop at the beginning of data collection shots to flatten the wavefront.

3.2.2 Pulse characterisation

Measurement of the pulse duration of the ultra-short pulses was carried out using a Spectral Phase Interferometry for Direct Electric-field Reconstruction (SPIDER) [102], which is a specific implementation of spectral shearing interferometry. The specific device used was an APE Compact LX Spider [103]. A portion of the main laser pulse can be taken to the SPIDER for an on-shot pulse duration measurement.

On-shot measurements of the laser energy and pointing can be taken using the leakage through a dielectric mirror. By imaging the near-field of this leakage beam, the laser energy on target can calculated. There is a linear relation between sum of all the pixels and the laser energy. Imaging the far-field allows tracking of laser pointing fluctuations, and also observation of any change in shape of the focus spot.

3.3 Diagnostics for LWFA

When operating a LWFA it is important to be able to measure the inputs (laser pulse and plasma conditions) and outputs (electrons and photons) of the accelerator. The key diagnostics used for this are described below.

3.3.1 Electron diagnostics

For a LWFA, the most important element to diagnose are the properties of the electron beam, as these are the main output.

Electron spectrometer

The energy spectrum of the electrons is measured using a magnetic dipole spectrometer. This consists of a fixed permanent magnet, and a scintillating Lanex screen. The electrons are swept by the magnet onto the Lanex screen, and the energy is calculated from the amount of deflection to the electron trajectory. Figure 3.3 shows the energy to pixel position on a camera is not a linear relation. To calibrate the spectrometer the magnetic

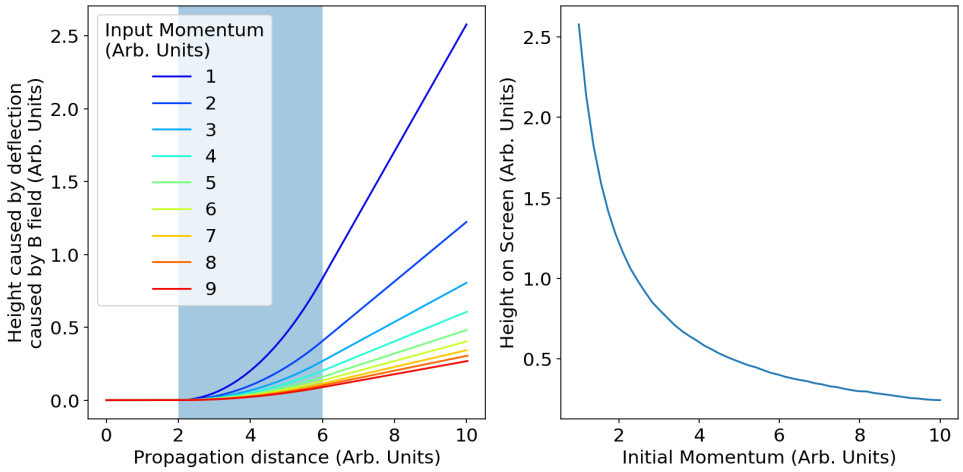

Figure 3.3: Schematic of electrons' trajectories through the fixed magnetic dipole. The magnetic field region, where the deflection occurs, is marked in blue. The resulting height on the screen is not linear with input momentum.

field must be mapped, and then the path of the electrons to the screen calculated. The magnet map is the measured magnetic field in a 2 dimensional (2D) plane around the midpoint of the magnet. The Lanex screen is positioned to detect the electrons of the expected or interesting energies. The light produced by the Lanex is at a wavelength of 546 nm [104] and is captured with an optical camera. An interference filter for 546 nm was often used experimentally to reduce the background signal.

The image that forms on the spectrometer camera relates to the electron energy for the axis the magnetic field has swept. The orthogonal axis corresponds to the integrated one dimensional (1D) divergence of the electron beam. To retrieve the energy spectrum the image has to be un-warped, as the range of energies being captured per pixel is not constant. The paths the electrons travel from their source to the Lanex screen is often not constant for the different energies, requiring this to be accounted for when calculating the divergence.

Electron profile

The electron spectrometer provides information about the spectrum and one dimension of the divergence. To look at the 2D divergence a measurement has to be performed before the electron beam passes through the magnet. To do this, a Lanex screen is used, and the light captured using an optical camera. This gives information about the beam pointing, and the 2D divergence.

3.3.2 Optical probe

Transverse optical probing is used to determine the conditions of the plasma that the main laser pulse interacts with. On experiments at the CLF the probe beam was created from the same laser as the main pulse which allows synchronization (∼1 fs) between the two pulses (probe and main beam) by altering the path length of the probe with a translation stage. The probe is normally timed such that it images the plasma within ∼ps of the main laser pulse interaction.

The probe can be setup to get spatial (shadowgraphy) or density (interferometry) information. Shadowgraphy is sensitive to second spatial derivative of the refractive index [18]. Interferometry is useful for measuring the phase shift caused by the plasma. When designing the probe for a shadowgraphy the main concern is the resolution of the image, and for interferometry it is the ability to measure the phase shift caused by the plasma.

Resolution

This is defined by the imaging system, but is normally set by the first lens after the interaction point, the collection optic. This is because only the light within a maximum angle is collected by this optic, which is determined by the $f_{\#}$ of the lens:

$$\theta_{max} = \arctan \frac{1}{2f_{\#}} \tag{3.1}$$

Optics transform information between the spatial domain $f(x, y)$ and the spatial frequency domain $F(u, v)$. A lens of finite diameter cannot capture all the information, with the high frequency components being lost first. Figure 3.4 shows the effect on the imaged profile as the number of high frequency components is decreased. The sharpness of the image decreases as less information is kept, and then finally the intensity of the image decreases.

The effect of imaging an object experimentally with a lens can be examined, as it is the same as numerically convolving the object's shape with an Airy disk, the focus of a perfect lens [105]. The focus diameter relates to the $f_{\#}$ of the lens and the wavelength of light (λ):

$$D_{\text{Airy Disk}} = 2.44\lambda f_{\#} \tag{3.2}$$

Investigating the effect of probing a hard-edged column of uniform density with different lenses is shown in Figure 3.5. Note that the phase shift profile is proportional to the amount of material the probing light would have to travel through. Using assumptions about the size of the object a maximum usable $f_{\#}$ is found. From Figure 3.5 it is clear that once the $f_{\#} > 20$, the measured values are no-longer a good match to the expected values.

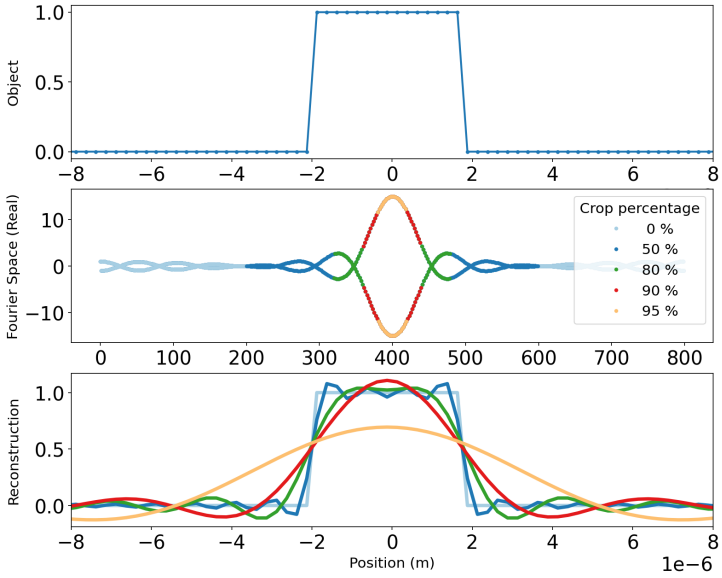

Figure 3.4: The effect of not capturing the whole Fourier domain on a top hat profile. The sharpness of the image decreases as less of the Fourier space is captured. The crop percentage colours are the same on middle and bottom plots.

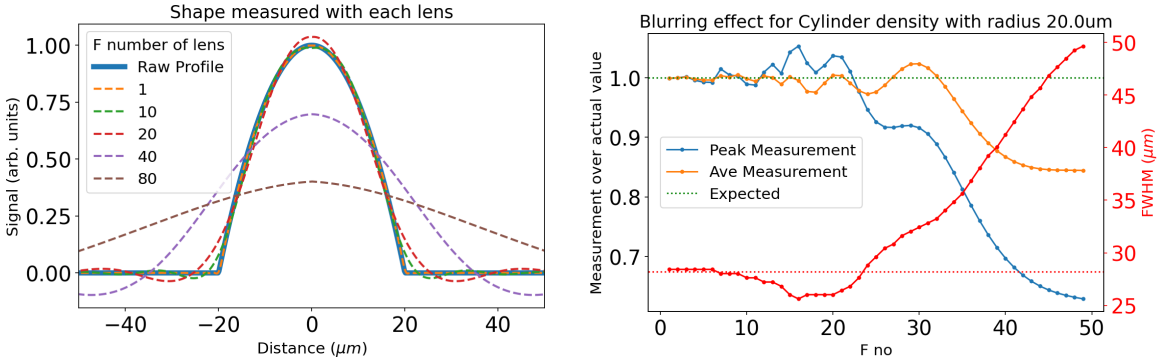

(a) (b)

Figure 3.5: The blurring effect of collection optic on the measured phase shift of a beam going through a hard-edged column with radius 20 µm. (a) Blurring of image caused by the $f_{\#}$ of the lens on the measured phase shift. (b) How the measured values change with $f_{\#}$. The average value is over the region ±20 µm.

Shadowgraphy

The simplest probing technique is shadowgraphy [106], where an image of the interaction region is taken with the probe. Shadowgraphy measures the 2^{nd} order effects of the change in density, and can be used to image the plasma channel and see shock features (for example, the density transition injection point).

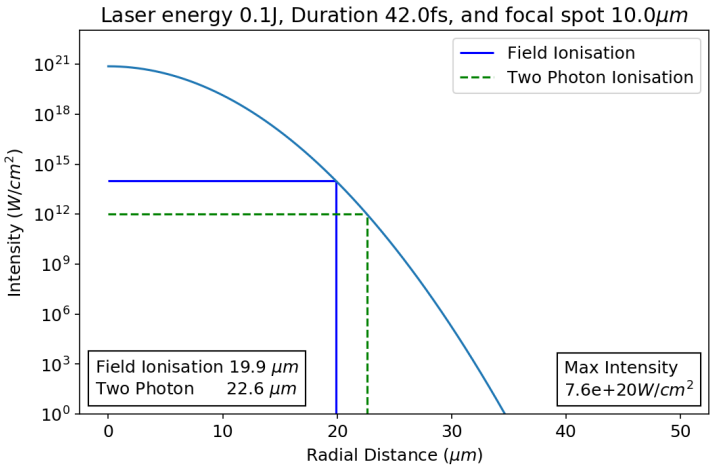

Figure 3.6: The plasma channel for the TA2 laser for a Gaussian focal spot of 10 µm.

For LWFA shadowgraphy is a useful diagnostic for checking laser alignment and checking the formation of plasma during the initial commissioning shots of an experiment. The expected size of the plasma channel generated by a given laser pulse can be calculated (Figure 3.6) so the experimental resolution of the probe required can be estimated.

Interferometry

The density of the plasma can be extracted from an interferogram. This is achieved by measuring the phase shift that occurs due to the beam passing through the plasma, compared with a reference beam. The refractive index of a plasma is:

$$\eta_p = \sqrt{1 - \frac{n_e e^2}{m_e \epsilon_0 \omega^2}} \tag{3.3}$$

where the critical density (the density at which the plasma frequency matches the laser frequency) is:

$$n_c = \frac{\omega^2 m_e \epsilon_0}{e^2} \tag{3.4}$$

which for 800 nm light is $1.75 \times 10^{21}\,\mathrm{cm}^{-3}$. In the case of LWFA accelerators where the plasma is underdense ($n_e << n_c$) the refractive index can be expanded as:

$$\eta \approx 1 - \frac{1}{2}\frac{n_e}{n_c} \tag{3.5}$$

The phase velocity of light in the plasma is $v_\phi = c/\eta_p$. Light that has not travelled through a plasma, but instead passed through vacuum ($\eta = 1$) can be used to measure the phase shift (ϕ_p) in v_ϕ and therefore, the n_e:

$$\phi_p = \frac{2\pi}{\lambda}\int \eta_p dz \tag{3.6}$$

$$\begin{aligned}\Delta\phi &= \frac{2\pi}{\lambda}\int (\eta_p - \eta_{\mathrm{vac}})dl \\ &= -r_e\lambda \int n_e dz\end{aligned} \tag{3.7}$$

where the classical electron radius $r_e = \frac{1}{4\pi\epsilon_0}\frac{e^2}{m_e c^2}$.

A device called an interferometer is used to create the two beams needed to measure the phase shift. The two designs used in this thesis work are shown in Figure 3.7. In an interferometer, one arm is used as the reference and the other is used to measure the plasma density. Due to space limitations on experiments these are normally setup as folded wavefront interferometers. This means that the beam travels through the chamber and interaction point as one beam. Inside the arms of the interferometer an offset between the two arms is introduced, such that the part of the beam that has the plasma information encoded within it is now overlapping with a region of the beam that has not passed through plasma. This is often a region of the gas target, but the phase shift introduced passing through the gas is negligible compared to the phase shift of the plasma, allowing the phase shift of the plasma to be measured accurately.

Considering the probe beam as a plane wave [107]:

$$E_{\mathrm{Probe}}(x, y, z, t) = E_0 \exp(i(kz - \omega t)) \tag{3.8}$$

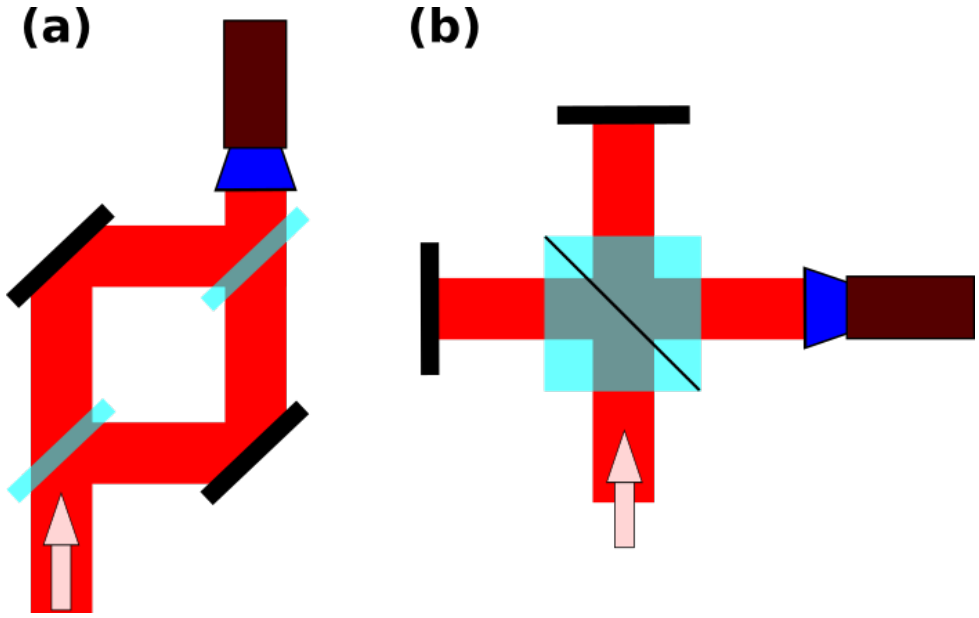

Figure 3.7: Interferometer setups used in this thesis. The arrows indicate the incoming light and the output is measured with an optical camera. (a) Mach-Zender, comprising of two beam splitters (cyan) and two mirrors (black). One of the mirrors is on a translation stage to allow timing of the arms. In this design it is easier to control the fringe angle, but is harder to align. (b) Michelson, comprising of one beam splitter, and two mirrors. Again, one mirror is on a translation stage for timing the arms. The design is simpler to align, but has less control over the field of view and fringe angles.

The arm that has travelled through the plasma acquires a phase shift:

$$E_{\text{Probe}}(x, y, z, t) = E_0 \exp(i(kz - \omega t + \Delta\phi(x, y))) \tag{3.9}$$

The reference beam is travelling in the x-y plane with an angle θ and an arbitrary phase offset χ:

$$E_{\text{ref}}(x, y, z, t) = E_0 \exp(i(kx \sin\theta + kz \cos\theta - \omega t - \chi)) \tag{3.10}$$

When the two beams are recombined the intensity pattern that occurs is:

$$I(x, y, z, t) \propto |E_{\text{Probe}} + E_{\text{ref}}|^2 \tag{3.11}$$

Observing the intensity at the camera plane ($z = 0$):

$$I(x, y) \propto 1 + \cos(kx \sin\theta - \Delta\phi(x, y) - \chi) \tag{3.12}$$

This means that in the absence of any phase shift, the camera will only see a set of interference fringes spaced by:

$$\lambda_f = \lambda / \sin(\theta) \tag{3.13}$$

The larger the fringes are on the camera, the higher the density resolution will be. The expected phase shift on an experimental can be calculated using (Equation 3.7) $\Delta\phi = -\frac{\omega_0}{2cn_c} n_e l$, from where l and n_e is the expected size of the plasma channel and plasma density respectively, giving a rough calculation of how many pixels per fringe will be required to measure the phase shift.

An additional issue arises with using ultra-short pulsed lasers. The temporal duration of the laser pulses is $\sim$40 fs, which means that to get the two pulses to overlap, the difference in arm length has to be small: $\Delta L_{\text{arms}} \lesssim 10\,\mu\text{m}$.

Extracting the plasma density from the phase shift is covered in Section 3.7.

3.4 X-ray source diagnostics

Novel photon sources are a useful product from a LWFA. Depending on the photon energy and flux regime, different techniques are deployed to diagnose the photons.

X-rays created through betatron radiation are often imaged with X-ray cameras, such as the Andor iKon [108]. These cameras can give the total energy of the X-rays, be used for imaging, or calculating spectral information using using single-hit detection. Spectral information extraction from the single-hit image is possible as the pixel brightness is linearly proportional to the photon energy. For this to work the flux on the camera has to be low so the odds of two photons being registered by a single pixel is small. These cameras work well for photon energies up to 20 keV. Above this energy the probability of a photon stopping in the sensitive region of the camera drops towards 0, and if a photon does stop it will saturate the pixel.

For high flux betatron beams with energies of ∼10 keV spectral information can be gained using filter packs, making use of the k-edges in absorption [109, 110]. Using the known absorption of these filters and the assumption that the spectrum is synchrotron-like a spectral energy measurement can be made [111].

Spectrometry of high flux X-ray beams beyond 100 MeV remains a challenge, with limited options including Compton-scattering spectrometers [112], photo-nuclear activation measurements [113] and differential filtering [114]. Imaging with these beams can be done either using image plate which is efficient up to 20 keV [115], or using scintillators.

Scintillators

Scintillators are materials that emit a small flash of light when struck by a high energy particle or radiation [116]. Their notable characteristics are the following. Firstly they exhibiting luminescence (the ability to absorb energy and re-emit it as visible light) and are transparent to the emitted light. Secondly, above a minimum energy, having an almost linear relationship between emitted light and energy deposited. And thirdly, they have a fast response time ($\lesssim$100 ns).

Two scintillating crystals were used on experiments in this thesis, thallium activated caesium iodide (CsI) [117] and cerium doped lutetium (LYSO) [118]. Both of these are inorganic crystals, and their scintillation method is characteristic of the electron band structure of crystals. Inorganic scintillators were used due to their larger stopping power, which is due to their high density and high atomic numbers [116]. In these scintillators there is a valance band and a conduction band separated by an energy band gap. In addition there is an exciton band, just below the conduction band. When a particle enters the crystal, there are two principle forms of energy absorption that occurs [116]:

1. An electron is ionised, moving from the valence band into the conduction band, creating a free electron and a free hole.

2. An exciton can be created, when an electron is ionised to the exciton band, so the electron and hole are still bound.

If an exciton is formed it is free to migrate through the crystal. Where there is an impurity in the crystal there are extra energy levels, so the impurity atom can be ionised by the exciton. This creates a free hole for another electron to fall into, emitting radiation if allowed.

These crystals scintillate when energy is deposited in them, and the brightness is linear in terms of energy deposition [116, 119, 120].

3.5 Code description

Several simulation codes were used throughout the PhD. These were used to model future experiments, understand experimental data, and to understand the physics that occurred experimentally.

3.5.1 Particle-in-cell code: EPOCH

To fully simulate a LWFA the following needs to be understood: the laser pulse evolution, the evolution of the wake structure, electron injection and acceleration of the electron bunch. To simplify the computational requirement of simulating continuous electromagnetic fields and the trajectories of all the particles, particle-in-cell (PIC) codes were created. For this thesis the PIC code EPOCH was used in 2D [121].

PIC simulations have a field grid structure (Cartesian in EPOCH) and pseudo-particles, therefore, simplifying the interaction between the laser fields and the particles, making the simulation computationally possible. The fields are calculated at the grid point vertices, and then are interpolated to calculate the force on the individual particles. This reduces the number of calculations from $O(N^2)$ for N particles to $O(N \log N_g)$ for N_g grid points. The fields and particles are propagated forward in time with two coupled solvers, the particle pusher and the field solver. The resolution of the grid structure is set by the smallest relevant features of the continuous space, of the real world, that the discrete grid is describing [122].

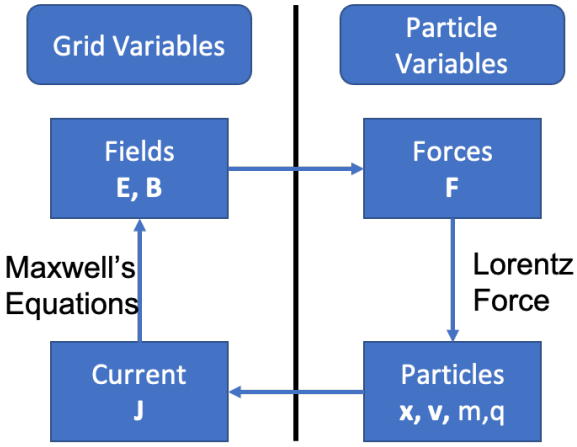

Figure 3.8: The PIC algorithm loop. The electromagnetic fields are calculated for the grid of the simulation. These fields are then interpolated to the particle positions to work out the force on each particle. The particles are then moved forward a time-step, with the new fields calculated at the grid points [121, 123].

The simulation propagates forward in time with the following four steps as shown in Figure 3.8:

1. The position of each particle is updated using the Lorentz force and the particle pusher.

2. The effect of the particles on the fields is calculated at the grid points.

3. The electromagnetic fields are calculated using Maxwell's equations and the field solver

4. The fields are interpolated to calculate the forces on each particle.

PIC codes make several assumptions which cause numerical issues [123]. Unlike real particles moving through space, PIC codes use a discrete grid to calculate fields and hence the forces on the pseudo-particles. However, if the grid is too course then fine scale physics can be missed. There are considerably fewer pseudo-particles than the number of real particles. How these particles mimic real particles will effect the result, and also the speed of the calculation. The simulation has a time-step when calculating the new fields

and particle positions. This time-step must be short enough to see the shortest process that can occur, and is a trade off between resolving physics and total runtime, giving rise to the Courant condition, $C \leq \frac{u\Delta t}{\Delta x}$ [123].

To increase the speed of the simulation a moving window is used, with a speed to match the propagation of the laser pulse. This means that the plasma which has not yet interacted with the laser does not get simulated, and for a LWFA the acceleration occurs in the first few plasma buckets of the wakefield. Therefore, the window only needs to be several plasma wavelengths around the laser pulse.

The speed, but also the accuracy, of the simulation is dependent on the number of grid points, and the number of pseudo-particles used. Therefore, for each set of simulations numerical convergence testing is required.

For the PIC simulations in this thesis, they were populated with pre-ionised electrons and no ions (EPOCH creates a neutralising background charge for quasi-neutrality). The boundary conditions (BC) for the inlet and outlet were 'simple laser' and 'simple outflow' respectively. The field BC in the transverse directions were open, and the particle BC were periodic.

Extracting data from EPOCH

Figure 3.9 shows a collection of simulation outputs. The PIC code allows tracking of the evolution of variables throughout the simulation which would be almost impossible to track experimentally, thus giving useful insight into the physical processes that occur. The self-focusing effects of the plasma on the laser pulse are shown in Figure 3.9 (b). Here, as the laser propagates in time it is initially focusing. If it followed Gaussian focusing (Section 2.4.1) the beam should only be tightly focused for a Rayleigh length either side of the focal plane. However, after 10 ps it remains focused to a spot size of $\sim$20 µm, indicating that self-focusing is occurring. Self-focusing will also shift the focal plane, and can increase the maximum intensity the laser pulse reaches. Figure 3.9 (c) shows an example of the evolution of the electron's energy with respect to time through the simulation. The top red line shows electrons accelerated up to and above 400 MeV,

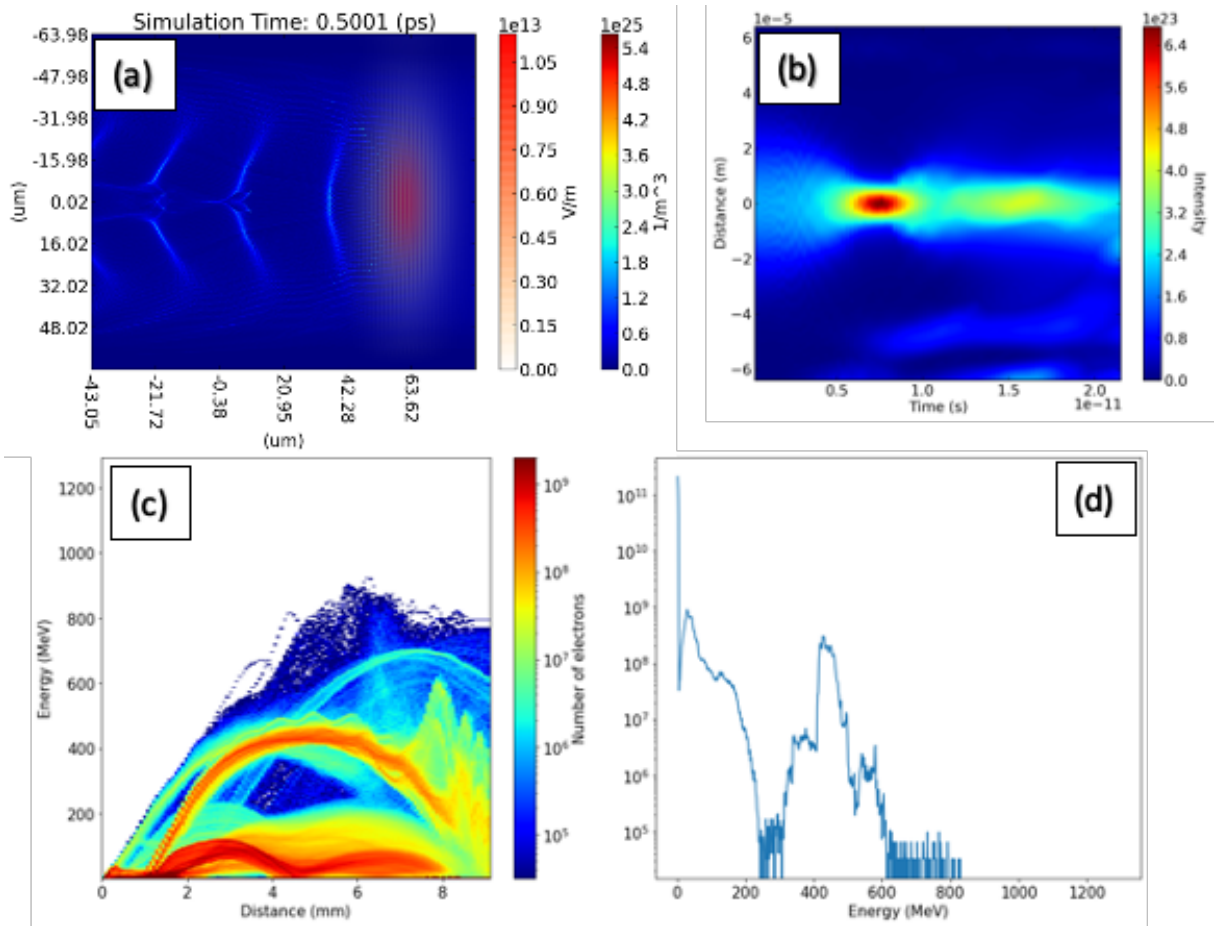

Figure 3.9: The extracted outputs of the PIC code. (a) The plasma density and the electric field (laser pulse) show the wake structure and accelerated electrons. (b) The evolution of the intensity through the simulation. Self-focusing is evident as the beam stays focused for a long duration through the simulation. (c) The evolution of the momentum of the electrons though the simulation. (d) The resulting electron spectrum at the end of the simulation.

where they then dephase and start to be decelerated. Figure 3.9 (d) shows an example spectrum produced by the PIC code.

3.5.2 Monte-Carlo simulations: Geant4

Monte-Carlo methods can be used to simulate processes that have an inherent randomness in them. By repeat random sampling the simulation results tends towards the continuous

distribution. When simulating the passage of high energy particles travelling through matter, depending on the conditions there are various physical processes that need to be considered. Each interaction has a probability distribution for possible different outcomes, meaning that Monte-Carlo methods are an ideal approach to simulate this situation. The simulation tool-kit Geant4 has been developed to tackle the problem of the passage of particles through matter [124]. This tool-kit relies on understanding the processes behind the interactions between the highly energetic particles, which comes from both experimental and theoretical physics. This tool-kit is used by many different research fields, so to include all the provided information in a given simulation is not required. The physics that is required is selected using physics lists. The uses of Geant4 in this thesis has been for simulating: bremsstrahlung emission from a high energy electron beam incident on a converter; and for the deposition of energy in scintillating crystals. These electromagnetic processes (bremsstrahlung, pair production, Compton scattering, photo-absorption and multiple scattering) are well understood in the intermediate energy range. Below the order of magnitude of keV the atomic properties of material become important, and for high energies complex particles can be produced. Positron-electron pairs were created in the experiments being conducted, as the incoming energy of particles produced was $\sim$100 MeV and the rest mass energy of these electrons and positrons is 0.511 $\mathrm{MeV/c^2}$. Muons have the next lowest rest mass at 105 $\mathrm{MeV/c^2}$ [125], and therefore, are not likely to be produced in large quantities. A comparison between a pre-built physics list "QBBC" and a specific list created for bremsstrahlung sources was made. The difference between these two was small, $\lesssim 1\%$, and the QBBC list ran around two times faster, so was used for all subsequent simulations. Another benefit of production physics lists is they are used by large user groups and because of their importance, they are well-maintained and tested [126].

Convergence testing

To create realistic results from a Monte-Carlo simulation enough events have to occur for the result to become apparent over the random nature of the input and probabilistic

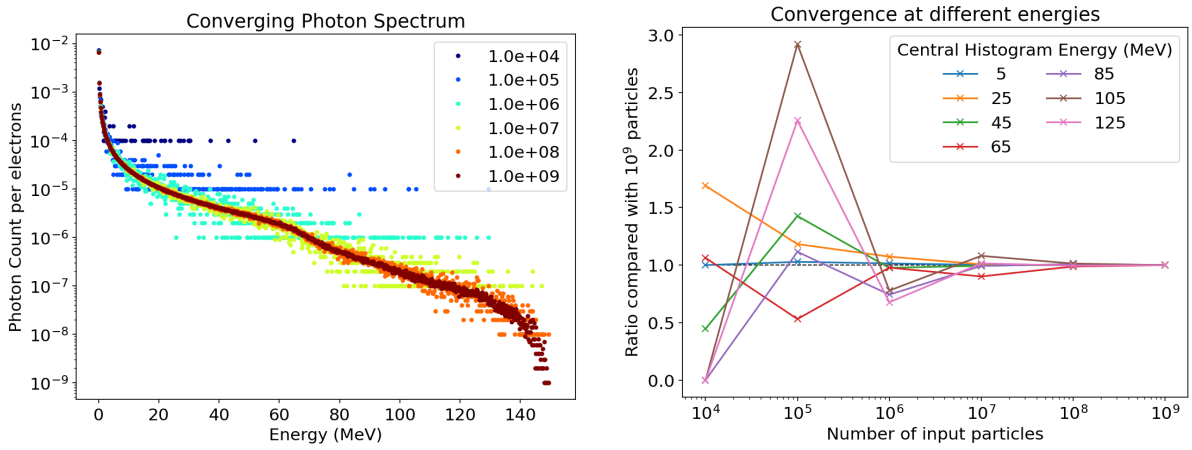

(a) (b)

Figure 3.10: Convergence testing the Geant4 simulation of energetic electrons onto a slab of material to produce photons via bremsstrahlung radiation. (a) The effect of increasing the number of particles in the simulation on the resulting spectrum shape. (b) Comparing the result at different energy bins with respect to the simulation with the most particles in, 1×10^9 electrons.

events. Therefore, for all simulations convergence testing is required, to show that the answer does not vary with a change in particle number.

An example of the convergence testing for the photon spectrum produced via bremsstrahlung radiation from an electron beam colliding with a converter is shown in Figure 3.10. Here Figure 3.10 (a) shows the normalised spectrum produced for different particle numbers. This convergence was quantified by looking at the difference in the number of photons in different energy bins, shown in Figure 3.10 (b). The low energy bin, 5 MeV, converges from the lowest number of input particles, whereas the highest bins, at 105 and 125 MeV, require 10^8 particles to converge. The reason for this is twofold: the probability of creating a given energy photon decreases with energy; and only the highest energy electrons can produce the highest energy photons. These two points mean that only at a large number of input particles are the number of particles produced in the highest energy bins statistically significant compared with the poison distribution counting error, $1/\sqrt{N}$, where

N is the number of counts. The final choice in particle number is chosen so the result fluctuation is less than above a given value (often chosen to be $< 1\%$).

3.5.3 Fluid simulations: OpenFOAM

Computational fluid dynamics (CFD) has become more useful since its creation in the 1960s with both code development and increased computing power. Using simulation codes for example, allows examination of fluid properties at a finer resolution than experimental measurements. CFD allows exploration into new setups without the cost of setting up an experiment for each new case.

In this thesis, the open source fluid code OpenFOAM (for "Open-source Field Operation And Manipulation") was used [127]. OpenFOAM has different solvers aimed at solving different problems. For the work looking at the formation of gas targets in Chapter 5, the solver "rhoCentralFoam" was used, due to its ability to work in the trans-sonic region.

3.6 Optimisation algorithm

A Bayesian optimisation (BO) method was used on the Streeter 2019 experiment at TA2 CLF's Astra-Gemini facility. BO is a form of machine learning optimisation that looks for the global maximum of an objective function, $f(x)$. It requires that f is continuous, and works with x being multi-dimensional, where the number of dimensions is typically $d \leq 20$. It is often used to optimise functions that are expensive to evaluate, and works with noisy data [128].

The BO process for a 1D test case is shown in Figure 3.11. Here the red dashed line is the "true" data, or objective function, about which noisy samples are taken, shown as black crosses. A model is created from the known data points via a technique called Gaussian Process Regression (GPR) [128]. A GPR model assumes that all points in space can be described by a normal distribution, with a covariance matrix defining how closely different regions in the space are linked. If some knowledge of the parameter space is already known then the initial "prior" can be given that shape in the multi-

dimensional space to speed up the optimisation process, or it can be initially uniform over the parameter space. The covariance matrix is constructed so that points close in parameter space are highly correlated. This encodes the belief that two points very close in space should give a similar result. The model is updated with each new data point and the next point to sample is chosen through the use of an acquisition function (right-hand column in Figure 3.11). Acquisition functions trade off between exploitation (sampling at the predicted maximum) and exploration (sampling where the uncertainty is high) of the surrogate model, and for each case the ratio between these two has to be tuned. This allows the next data point to provide the most information possible to the model.

The BO process for work in this thesis was carried out in Python using Scikit-learn [129]. The optimisation required the length scales of the different input parameters to be comparable for each, and therefore they were scaled to bring the values for each parameter to be in the range $-10 < x < 10$.

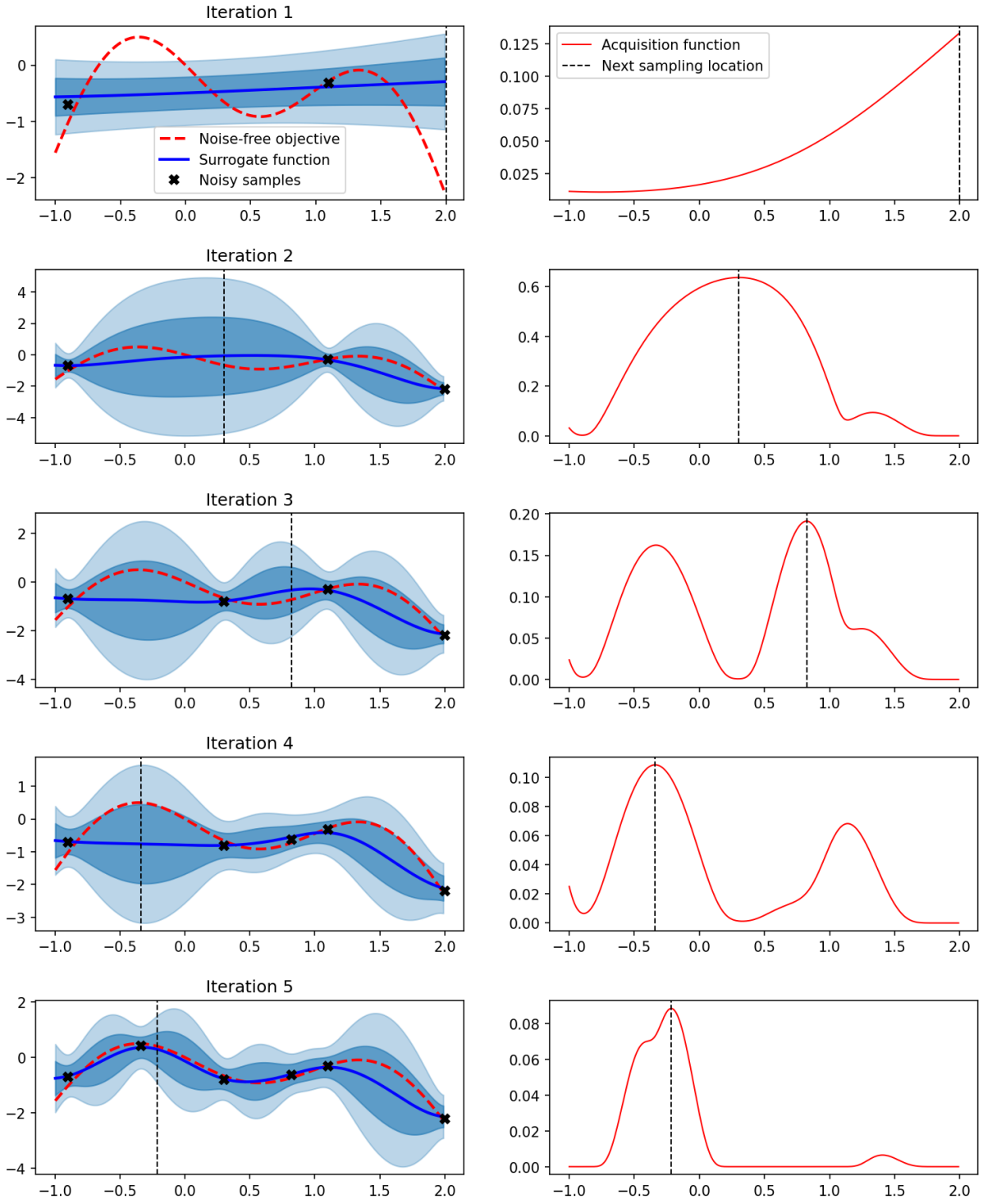

Figure 3.11: The Bayesian optimisation process for a 1D test case.

3.7 Interferometry extraction code

A code to extract the density from the interferometry images was written in Python [1]. The phase shift caused by the plasma can be calculated by several methods [18]. Here, the method used was a Fourier-based method developed by Takeda *et al.* [130]. The intensity pattern on the camera (Figure 3.12 (a)) is of the form:

$$\begin{aligned} I(x,y) &= a(x,y) + b(x,y)\cos(k_f x \sin\theta - \phi(x,y)) \\ &= a(x,y) + (c(x,y)\exp(ik_f x\sin\theta) + c^*(x,y)\exp(-ik_f x\sin\theta)) \end{aligned} \tag{3.14}$$

where $a(x,y), b(x,y)$ represent the non-uniformities in the probing beams, $k_f = \frac{2\pi}{\lambda_f}$, $c(x,y) = \frac{1}{2}b(x,y)\exp(-i(\phi(x,y)))$, * indicates the complex conjugate, and ϕ is the phase shift caused by the plasma. To speed up data processing, and to remove sources of noise, only the region of interest in the image (the plasma channel) is processed. This is selected by cropping with a window function (Figure 3.12 (b)) to prevent sharp edges in the image. The window function is used to create a smooth crop as the introduction of a sharp feature in real space will introduce high frequency components in Fourier space.

Fourier transforming Equation 3.14 gives:

$$\mathcal{F}(I(x,y)) = A(k_x,k_y) + C(k_x + k_f, k_y) + C^*(k_x - k_f, k_y) \tag{3.15}$$

where the Fourier transform of a function is indicated with a capital letter: $X = \mathcal{F}(x)$. Each of the three terms correspond to a different part of the image. The background of the image is taken into account in A and creates a peak in the centre of the Fourier image (Figure 3.12 (c)). Note that this peak is missing from Figure 3.12 (c) as it is a synthetic interferogram containing no noise. The C and C^* terms corresponds to the two remaining peaks. To extract the phase a crop is performed in Fourier space to one of these side peaks (Black box on Figure 3.12 (c)). For the code written the right-hand peak was chosen.

The phase shift extraction was performed using the comparison between the shifted fringes and the reference data of the unperturbed fringes. The image of the unperturbed fringes was found/created in one of three ways:

[1] https://bitbucket.org/Chris_Underwood/probe_interferometry_extraction/

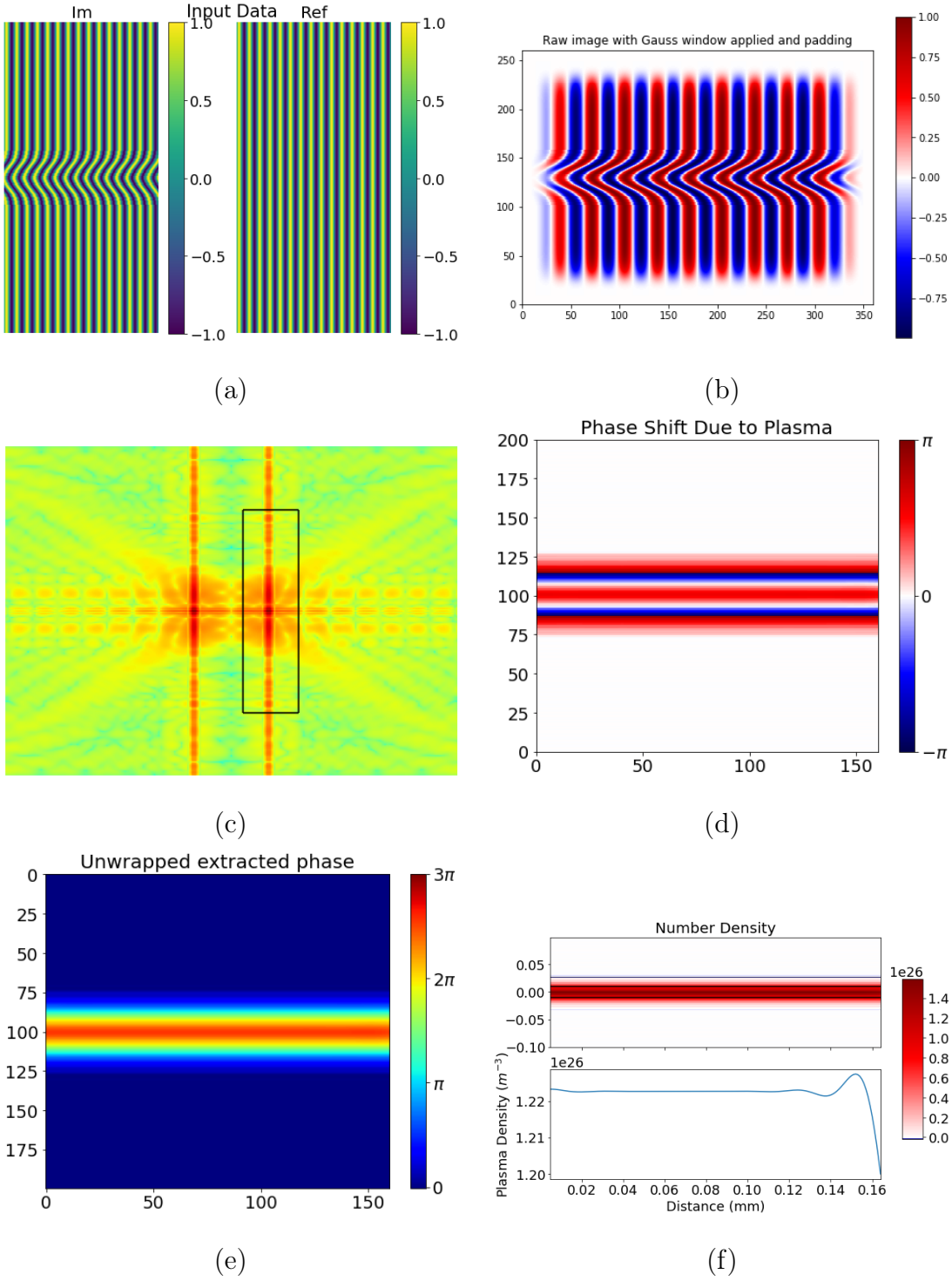

Figure 3.12: The stages of the interferometry extraction code. (a-f) in text.

1. A reference image was taken, with no plasma.

2. A region of the image with unperturbed fringes was used as the reference.

3. A 2D fit was used to fit fringes to the image. These fitted fringes were then used as the reference.

Cropping to the carrier frequency peak in Fourier space is also applied to the reference image (as just described).

The phase is then extracted by calculating the angle between the inverse Fourier transform of the image and the reference. However, the angle that is extracted will have a 2π range (Figure 3.12 (d)) meaning that the output image may have discontinuities of 2π in the data. The phase data will then require "unwrapping". Here a 2D unwrapping algorithm from "skimage" was used [131], with the region where no plasma existed having no phase shift (Figure 3.12 (e)).

The number density is extracted from the phase shift using an inverse Abel transform (Figure 3.12 (f)) which was performed by "PyAbel" [132]. An Abel transform describes the projection of a cylindrically symmetric 3D object onto a 2D plane. The inverse Abel transform reverses this, taking a 2D projection and creating a 3D cylindrically symmetric object. For the case of a LWFA plasma, the assumption is made that the plasma is cylindrically symmetric around the laser axis:

$$f_A(y) = 2\int_y^\infty \frac{\phi(r)r}{\sqrt{r^2 - y^2}}dr \tag{3.16}$$

The inverse Abel transform allows extraction of $\phi(r)$ from $f_A(y)$. The density is then retrieved from this using the result of the inverse Abel transform:

$$n_e = \frac{\phi(r)}{(r_e * \lambda_l * (\text{distance per pixel}))} \tag{3.17}$$

One thing to note is the Abel transform is very sensitive to the angle of the plasma channel, as it requires the axis of symmetry to be inputted correctly. The "PyAbel" package requires the plasma channel to be horizontal in the image, so the unwrapped phase may

have to be rotated before the transform. This code was successfully benchmarked against another code [2].

3.8 Response curves of CsI array X-ray diagnostic

A caesium iodide (CsI) array of scintillating crystals was used on the experiment describe in Chapter 4 as a detector of the properties of the energetic (>10 MeV) photon beams. In order to extract information about the spectrum of the photons from this detector, knowledge of how the detector responded to different energy photons was required. As there is no mono-energetic photon source at the energies required, creating the response matrix was simulation based and carried out using Geant4 [124] (See Section 3.5.2).

The CsI diagnostic array was built in Geant4 according to the following dimensions [133, 134]: the array was 33 crystals high and 47 crystals deep; each CsI crystal was $5 \times 5 \times 50$mm with the long axis perpendicular to the incoming beam; 1 mm thick aluminium spacers between the crystals; and a 9 mm stainless steel plate on the front surface, through which the X-ray beam entered the diagnostic.

3.8.1 Mono-energetic photon responses

Figure 3.13 shows the simulated response curves for the mono-energetic photons with increasing energy on the y axis, and increasing penetration into the array on the x axis. By using the simulated response for a well spaced set of energies a response matrix for the detector is generated. To convert from detector response to photon energy the following equation is used:

$$R_{En}\gamma_E = C_n \tag{3.18}$$

where R_{En} is the response matrix times γ_E, the column vector representing the number of photons at each energy, to give the crystal response per column of the array C_n. This, in an ideal situation, is all that is required to calculate the photon spectrum from the measured light response. However, the response curves for high energy photons become

[2] https://github.com/jasmcole/Interpret

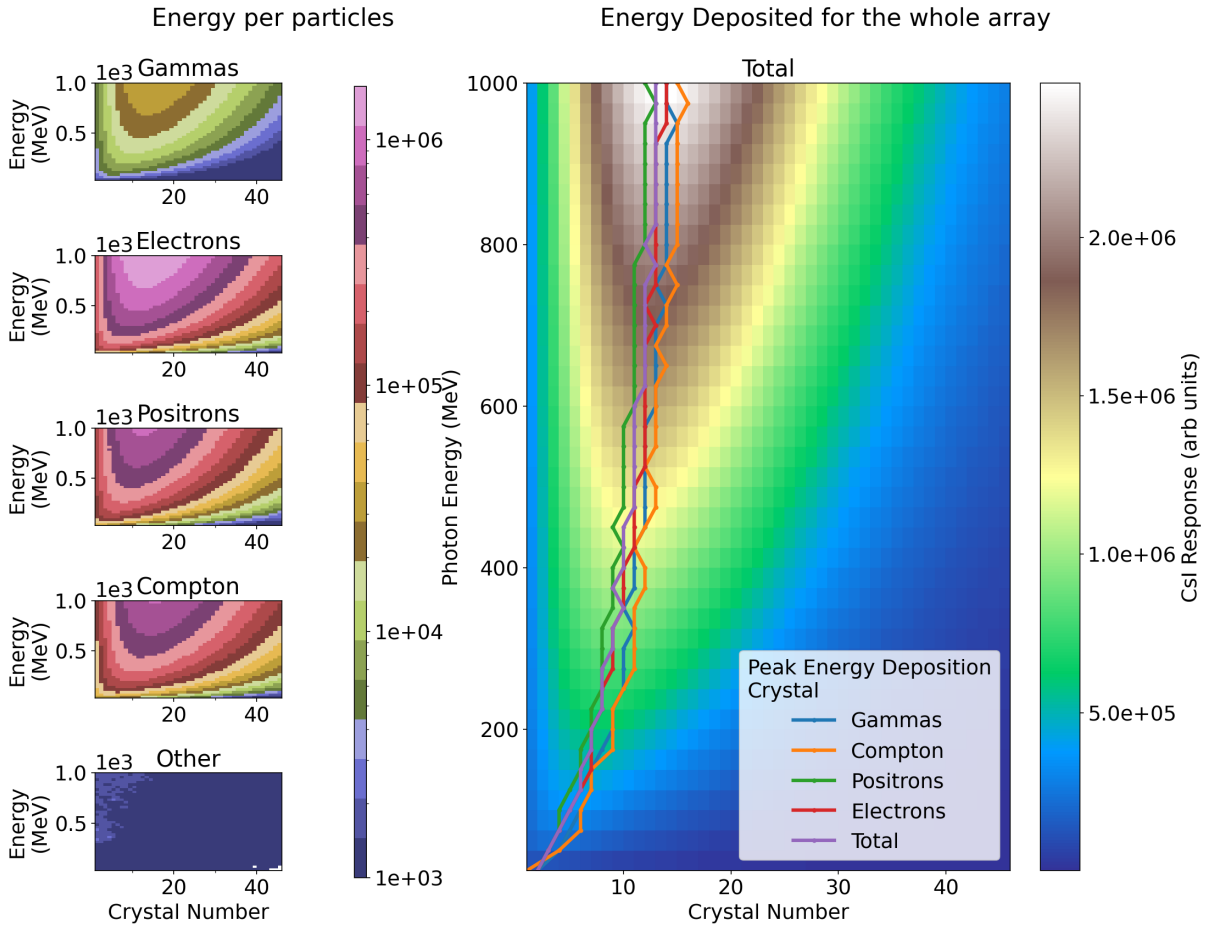

Figure 3.13: Response curves of the detector to mono-energetic photons. For a photon of a given energy (y-axis), the response of the CsI array per crystal (x-axis) is shown. The particles that deposit energy are displayed in the subplots to the left with a logarithmic colour scale. Direct energy deposition by high energy photons (gammas) is a small component of the energy deposition. The energy is mainly deposited by electrons and positrons. The assumed energy deposition by Compton scattering is calculated by subtracting the positron deposition from the electron deposition. Compton scattering and pair production are the main energy deposition processes that occur within this detector. The main plot shows the response with respect to increasing input photon energy, marking the crystal which has the maximum amount of energy deposited in it by each particle.

very similar in shape, with their peak occurring around the same crystal. This makes it impossible to distinguish between different spectra without an assumption about the photons spectral shape, as multiple lower energy photons can produce a similar response to a high energy photon.

The use of Geant4 allows an examination of the processes which are depositing the energy in the detector. The amount of energy deposited by the different particles: γ, e^-, e^+ and other particles is shown in the sub-plots of Figure 3.13. The amount of energy that was deposited from Compton scattering is calculated by subtracting the pair production electrons, $e^-_{\text{Pair Production}} = e^+$, from the total energy deposited by electrons. The processes that are most important for the energy deposition into the array were found to be: Compton scattering; pair production and direct photon absorption.

The side plots of Figure 3.13 show that the processes that deposit a large amount of energy into the crystals all follow a similar shape, and lines on the main plot show that the peak signal is in roughly the same crystal for each energy. To demonstrate more clearly whether the different processes varied from each other the response of the detector to a 300 MeV beam is normalised in Figure 3.14. This further shows that all processes that deposit a significant amount of energy do so in the same response shape. This could have been important as some scintillators produce different light with respect to the ionising radiation they are seeing, but this simulation result shows that in this case experimentally distinguishing the different light would not provide any more information. Figure 3.14 shows that the electrons from Compton scattering deposit their energy further into the array than the pair-produced electrons. This is because it is assumed that the pair-produced electrons deposit in the same crystals as the positrons. This was a good first approximation and if this work had returned a more promising result would have been investigated further.

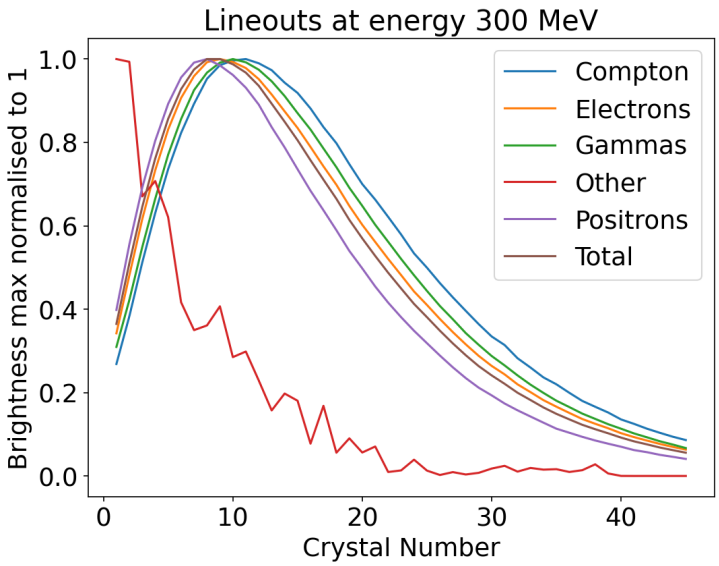

Figure 3.14: Comparison of processes that occur in the detector. These are also shown in the left hand side of Figure 3.13. The different processes that deposit a large amount of energy all do so in the same shape. The "other" particles deposit around three orders of magnitude less energy and therefore could not be used to improve the understanding of the detector.

CsI response curve convergence testing

Convergence of the CsI array response curve simulation is shown in Figure 3.15. The response is compared to the simulation with the most particles, which is assumed to be the true solution. Confidence in this is found by looking at Figure 3.15 (a), where the results of the lower particle number in the simulations fluctuate around the (true) high particle answer. This is quantified by looking at the difference with respect to the highest particle simulation. The average signal in groups of 10 crystals, marked by the average crystal position, is shown in Figure 3.15 (b). The convergence with particle number is characterised normalising the signal by the number of input particles in each simulation. This is then divided by the result from the highest particle number simulation. Figure 3.15 shows that the crystals further into the array converge only at higher particle numbers. This is because the probability of a given photon getting further and further through the

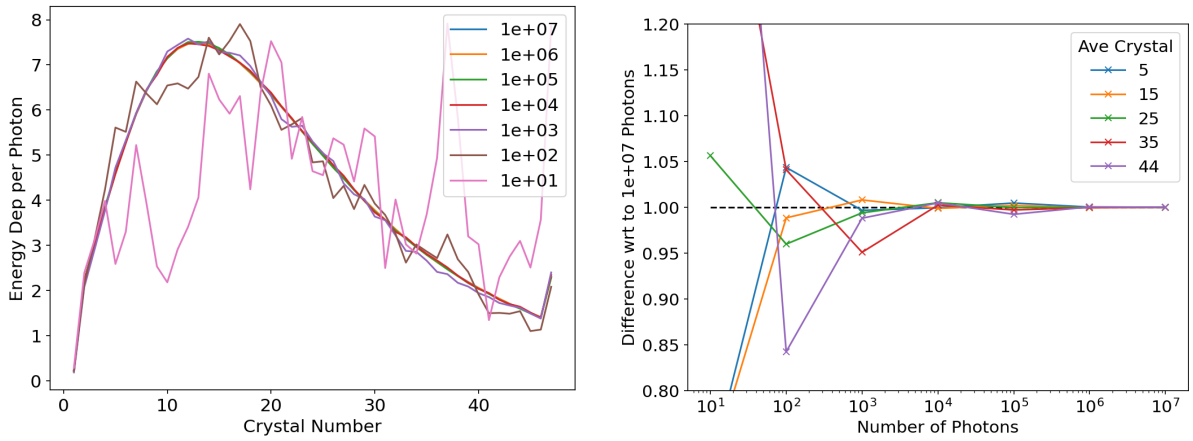

(a) (b)

Figure 3.15: Convergence testing of CsI detector response, showing that at least 10^4 are required.

array will drop exponentially. Therefore, to get a high enough count in these crystals, which reduces the fluctuations, more input particles are required. A convergence condition was applied, such as saying the maximum fluctuation is $< 1\%$, to find the minimum particle numbers required. For the production of the response matrix (Figure 3.13) 10^6 particles were used.

3.9 Conclusion

This chapter has described the general implementation of diagnostics, and the simulations tools used to understand the results, for the experiments in this thesis. For the actual implementation of these, further explanation is in the relevant data chapters.

4 | LWFA driven bremsstrahlung photons

In this chapter results are presented from an experiment carried out in December 2017 to January 2018 at the CLF's Gemini laser facility and the supporting simulations, and is published in Underwood *et al.* [35]. The experimental aim was to show to industrial partners that a laser wakefield accelerator (LWFA) produced X-ray source is competitive with other available sources. On this experiment a betatron source was also created, and this is published in Gruse *et al.* [89]. In this chapter the raw electron spectra were extracted and provided to the author by C. D. Baird, and the cell pressure to electron density relation was provided by O. J. Finlay. All Geant4 simulations were initially built by the author, and M. P. Selwood assisted in parallelising the electron beam to X-ray source simulation.

4.1 Background and motivation

To create an industrially relevant X-ray source, the following parameters need to be optimised:

1. Minimising image acquisition time by increasing:
   (a) The repetition rate of source.
   (b) The data acquisition.
2. Improving the resolution of imaging, by reducing the source size.
3. Increasing the flux so images can be created with a single X-ray pulse.

4. Versatility in the objects that can be imaged:

   (a) Different density changes, either absorption imaging or phase contrast imaging.
   (b) Penetration of the photons.

The next generation of petawatt class lasers (ELI Beamlines [135], ELI-ALPS [24], EPAC [136]) have a two order of magnitude improvement in repetition rate to ∼10 Hz, addressing 1a. The Gemini laser, used for this proof of principle experiment, has a maximum repetition rate of 0.05 Hz. Work on increasing the repetition rate of LWFA shows that the plasma targets can run in steady state [137] and have already be run at 5 Hz [138]. A stable electron beam has operated for 24 h with the variations seen related to the laser pulse variations [7]. On this experiment scintillator detectors and charge-coupled device (CCD) cameras were used. The scintillator crystals used have a very fast decay time, 45 ns [118], and the scientific camera used for X-ray imaging has a maximum frame rate of 100 fps [139]. Therefore, the data acquisition currently exceeds the laser repetition rate.

The resolution of the imaging system was investigated by looking at the smallest features that could be imaged. On the experiment the source size was inferred by imaging resolution grids, as image resolution is a combination of both the source size and the resolution of the imaging system. By setting up the geometry and detectors correctly the images were taken in a situation where the resolution was limited by the source size. There were no X-ray optics in the imaging system, which means a smaller X-ray source size enhances the spatial resolution by decreasing blurriness caused by the penumbra effect [140]. By measuring the smallest features resolved on a resolution grid experimentally source size had an upper limit 150 µm.

One advantage of using a LWFA driven source, is the ease with which one can change between two very different energy photon sources, betatron radiation and bremsstrahlung radiation. Betatron radiation, produced by the inherent transverse motion of the electrons in the wake generates X-ray radiation (10 - 100 keV) [30] which, due to its micron-scale source size and high-spatial coherence, is ideal for phase-contrast imaging (PCI) [79–82]. The betatron source from the experiment is described in Gruse *et al.* [89]. X-rays can

be produced using bremsstrahlung radiation (previously demonstrated using a LWFA by [84–87, 141, 142]), which is the radiation produced by the rapid deceleration of charged particles in the nuclear field. Electrons incident on a high-Z material produce a cone of radiation with a broad energy spread extending up to the maximum electron energy, ∼100 MeV for this experiment. Bremsstrahlung sources will be suitable for applications for which high photon energy and flux is required for penetration of dense materials, and a large divergence for wide field-of-view is required. The combination of these two X-ray sources makes a LWFA driven device highly competitive for potential industrial applications. The X-ray refractive index for the object is $n = 1 - \delta - i\beta$ [143]. LWFA X-rays sources can be in two imaging regimes, which can be chosen depending on the thickness of the object to be imaged and the changes in density that are expected. X-ray absorption imaging (projectional radiography) works by an X-ray beam propagating through an object onto a detector (difference in β). The more absorbing the object is to the X-rays, the darker the image on the detector. X-ray PCI uses the bending of the X-ray wavefront (difference in δ) as it propagates through the object [80]. For PCI the spatial coherence length is:

$$L_t = \frac{\lambda u}{2\pi w_{x,y}} \tag{4.1}$$

were u is the distance from the source, λ the radiation wavelength and $w_{x,y}$ the source size. The spatial coherence has to be larger than the feature being imaged [90]. Rapid changes in refractive indexes, which occur at boundaries between materials, result in sharp variations in intensity, even for polychromatic sources [143]. The spatial resolution of the imaging must be able to resolve these sharp variations.

The work presented here is on the characterisation of the bremsstrahlung source; divergence, flux, photon spectrum and source size. The energies of these bremsstrahlung photon beams (∼100 MeV) are higher than those reported previously using differential filtering (ten's of MeV) [144].

4.2 Experimental setup

A schematic of the experiment is shown in Figure 4.1. To generate the electron beam, the south beam of the Gemini laser was focused into a helium filled 11.8 mm long gas cell with an $f/40$ parabolic mirror, delivering (6.0 ± 0.7) J of energy in (49 ± 3) fs. The focal spot was measured to be an ellipse with major and minor axes of 50 µm × 40 µm, giving a peak intensity of $(2.9 \pm 0.4) \times 10^{18}\,\mathrm{W\,cm^{-2}}$ ($a_0 \simeq 1.2$). After passing through the gas cell, the laser pulse was diverted onto a beam dump by a thin polyimide tape acting as a plasma mirror. The accelerated electron bunch then propagated through a converter material mounted 50 mm behind the gas cell. After the converter there was a magnetic dipole spectrometer (total magnetic length $\int B(x)dx = 0.4\,\mathrm{T\,m}$). When the converter

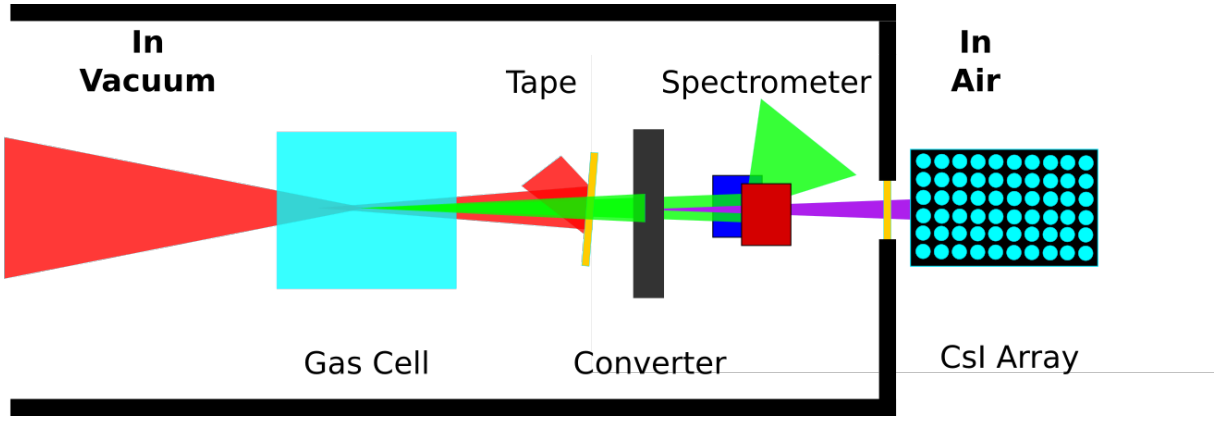

Figure 4.1: Experimental set-up showing the focusing laser beam (red) coming in from left to right, into the gas cell (cyan). The LWFA produces electrons (green) which are co-propagating with the laser beam. The laser beam is removed with a polyimide tape (yellow) and the electrons propagated into a bremsstrahlung converter (black), where X-ray photons (purple) are created. The electrons are swept away with a magnetic dipole spectrometer, and the photons leave the vacuum chamber through a polyimide window and propagate into the caesium iodide crystal array, 3500 mm from the gas cell. For X-ray imaging the sample was placed outside the chamber, 2600 mm from the gas cell, and the CsI array was replaced with a LYSO crystal and CCD camera.

was absent this was used to measure the electron spectrum with the second dimension of the spectrometer screen giving information about the divergence in the non-dispersive direction. When the converter was present it was used to disperse the electrons after the converter so that the samples were not irradiated by the electron beam, preventing the sample from becoming an additional bremsstrahlung source. The plasma target was diagnosed with a transverse probe, with a Mach-Zehnder interferometer (Section 3.3.2) used to measure the plasma density [145]. The X-ray beam was then propagated out of the vacuum chamber, where the attenuation of X-rays leaving was minimised by using a thin polyimide window ($\sim 100\,\mu m$). Outside of the chamber, the array of scintillating thallium activated caesium iodide (CsI) crystals [117] was positioned on the beam axis, and the light emitted from the scintillating crystals was imaged with a CCD camera (gigE Manta) [146]. The array was one crystal deep, 33 crystals high and 47 crystals long.

The spectral shape of photons produced by bremsstrahlung radiation is well known. However, spectrometry of high flux X-ray beams beyond 100 MeV remains a challenge. For particle accelerators, with very stable electron beams, it is possible to use particle tagging to calculate the energy of the photon beam [147]. However, the LWFA used was not stable enough, so the limited options available included Compton-scattering spectrometers [112], photo-nuclear activation measurements [113] and differential filtering [114]. In each case, the choice is based on experimental specifics, and involves compromising on spatial or energy resolution, repetition rate, or a combination of all three. In this study, a differential self-filtering diagnostic was utilised, in order to retain sub-centimetre spatial resolution while obtaining some spectral information with a data acquisition rate higher than our laser shot rate. The specific detector had been fielded elsewhere [133, 134], demonstrating its suitability in the relevant energy range. The incident photon spectrum on the detector can be calculated by unfolding the image of the scintillator light using the response matrix of the detector (Section 3.8). However, the diagnostic has a non-uniqueness problem, meaning that there are multiple solutions, or photon spectra, which may correspond to one detector response. This problem is explained in Section 3.8, but it means that an assumption is required about the spectral shape. The spectral shape is well approximated

by the following equation [133, 134]:

$$N_p(E) = AE^{-\frac{2}{3}} \exp(-E/E_{\text{crit}}) \tag{4.2}$$

where $N_p(E)$ is the number of photons per energy.

The two fitting parameters are: A is the amplitude of the photons and E_{crit} is the critical energy of the spectrum, with 49% of the photon energy radiated below this energy [133]. Figure 4.2 shows the simulated spectrum from an experimental electron beam in to a bremsstrahlung converter with the spectral shaped fitted with Equation 4.2. This equation does not account for the high energy cut off that occurs, due to no photons being created with more energy than the maximum electron energy. However, the number of photons that the equation predicts above this energy is small compared to the total number of photons.

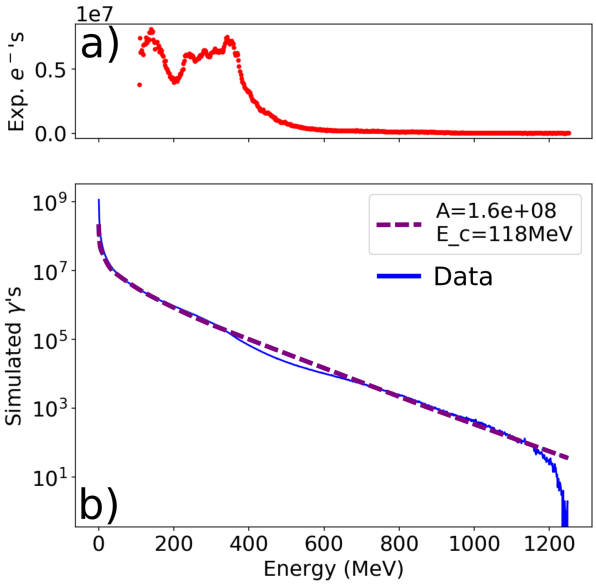

Figure 4.2: The simulated photon spectrum produced by a 10 mm thick iron bremsstrahlung converter. a) The experimental electron spectrum used as the input into the Geant4 simulation. b) The simulated photon spectrum and the fit of Equation 4.2. The cut off energy is seen here at 1.2 GeV which corresponds to the maximum energy in the electron spectrum.

4.3 Simulations setup

The required simulations for this chapter used Geant4, the Monte-Carlo toolkit for the simulation of the passage of particles through matter [124], described in Section 3.5.2.

The first was a simulation of the CsI diagnostic array, where photons were the incident particle. This simulation recorded the amount of energy deposited in each crystal for the incoming mono-energetic photon beam to build a detector response matrix. The particles that were depositing the energy were also noted, showing what processes are important in the diagnostic. This is described in Section 3.8.

The second was of an electron beam incident on a bremsstrahlung converter, recording information about the output photons. The photon flux, critical energy, divergence and source size was extracted from the simulation data.

The third was to track the angle of the emitted photons with radial position, showing the trend between radial position and the emitted angle.

4.4 Experimental electron beams

The tunability of the electron beam was examined by changing the plasma density (Figure 4.3) through changing the pressure of the pure helium gas into the gas cell. The electron spectra for each of the different plasma density are shown in Figure 4.3 (a), with the shaded region corresponding to 1 standard error. The maximum energy follows the inverse scaling estimate for maximum energy gain due to dephasing, $E_{max} = 2m_e c^2 n_c/n_e$ (Figure 4.3 (b)) where m_e is the rest mass of an electron, n_c is the critical plasma density [55]. The helium gas was fully ionised by the laser at this intensity (Section 2.5) so there was a linear relation between gas pressure and electron density. The data lies on the line when dephasing length (L_ϕ) of the electrons was shorter than the length of the gas cell, where $L_\phi \simeq (4/6\pi)\sqrt{a_0}\lambda_p(\omega_0/\omega_p)^2$, λ_p is the plasma wavelength, ω_0 the frequency of the laser and ω_p the plasma frequency [64]. The dashed navy line shows the point where L_ϕ is equal to the length of the gas cell. For the two data points for electron densities that have a dephasing length longer than the gas cell (3.6×10^{18} & $4.5 \times 10^{18}\,\mathrm{cm}^{-3}$), it would be ex-

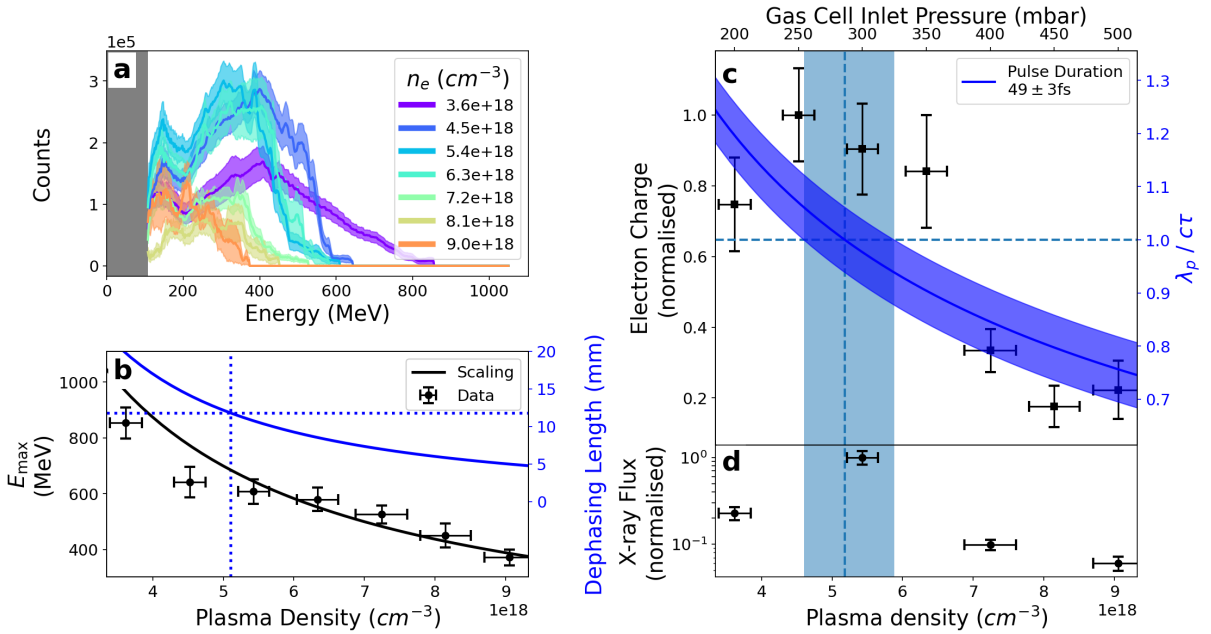

Figure 4.3: The electron beam characterisation [35]. (a) The average electron spectrum at the different plasma densities (Errors are 1 standard error), and their maximum energy scaling inversely with plasma density. (b) The maximum electron energy vs plasma density, and dephasing length vs plasma density. (c) The electron beam charge vs plasma density. (d) The bremsstrahlung X-ray flux vs plasma density.

pected that the $4.5 \times 10^{18}\,\mathrm{cm}^{-3}$ density plasma would produce a higher maximum energy electron as the electric field strength $E \propto \sqrt{n_e}$ [63]. One potential explanation for this could be the increased beam charge at this density (Figure 4.3 (c)) has reduced the acceleration fields through beam loading [148, 149]. By varying n_e between $3.6 \times 10^{18}\,\mathrm{cm}^{-3}$ and $9 \times 10^{18}\,\mathrm{cm}^{-3}$ the maximum energy was reduced from (850 ± 60) MeV to (370 ± 30) MeV.

In Figure 4.3 (c & d), the maximum electron charge and resulting X-ray flux did not coincide with the lowest plasma density, but at a higher density. This result is consistent with previous work including McGuffey *et al.* [150] who showed that there was a peak in accelerated charge with respect to plasma density that occurred above the threshold density for injection, and the decrease at high densities was due to the increasing divergence of the electrons. The solid blue line on Figure 4.3 (c) shows the value of $\lambda_p/c\tau$

for the measured pulse duration. Above this density, as the spatial length of the pulse is longer than the plasma wavelength, the laser energy will be split between multiple plasma buckets which is detrimental to the performance of the accelerator.

Gas cell pressure (mbar)	Electron density (cm^{-3})	Divergence (mrad)
200	3.6×10^{18}	2.7 ± 0.3
300	5.4×10^{18}	2.6 ± 0.3
400	7.2×10^{18}	4 ± 2

Table 4.1: The average divergence of the electron spectra used for Geant4 simulations, with the error in the full width at half maximum (FWHM) measurement, provide by C. D. Baird. Inlet pressure to plasma density relation provide by O. J. Finlay.

For the experimental converter scan, 3 gas cell densities were chosen, that were the result of the inlet pressure being 200, 300 and 400 mbar. Changing the electron density changes the properties of the wake that is driven in the plasma, as $\lambda_p \propto \sqrt{n_e}$ and therefore, the electron beam profile. The average divergence of these electron beams is shown in Table 4.1.

The assumption made while taking the data for the bremsstrahlung sources was that the electron spectra were stable, and therefore, it would be possible to average the 5 shots taken at these pressures. The 5 shots should then have similar incident electron bunches, which would allow processing of the data. Analysis of the fluctuations was examined afterwards by taking 5 random shots from the electron spectra data set. Figure 4.4 shows the fluctuations for the 3 different electron densities. The average is plotted with a thick blue line. 9 sub-datasets were created, for each pressure, by averaging 5 randomly selected shots from the full data set. This is to be representative of the experimental fluctuations that occurred. The shape of the $3.6 \times 10^{18}\,cm^{-3}$ spectrum is reasonably constant above 500 MeV. However, the electrons produced by the densities 5.4×10^{18} and $7.2 \times 10^{18}\,cm^{-3}$ show a large amount of fluctuation over the whole spectrum.

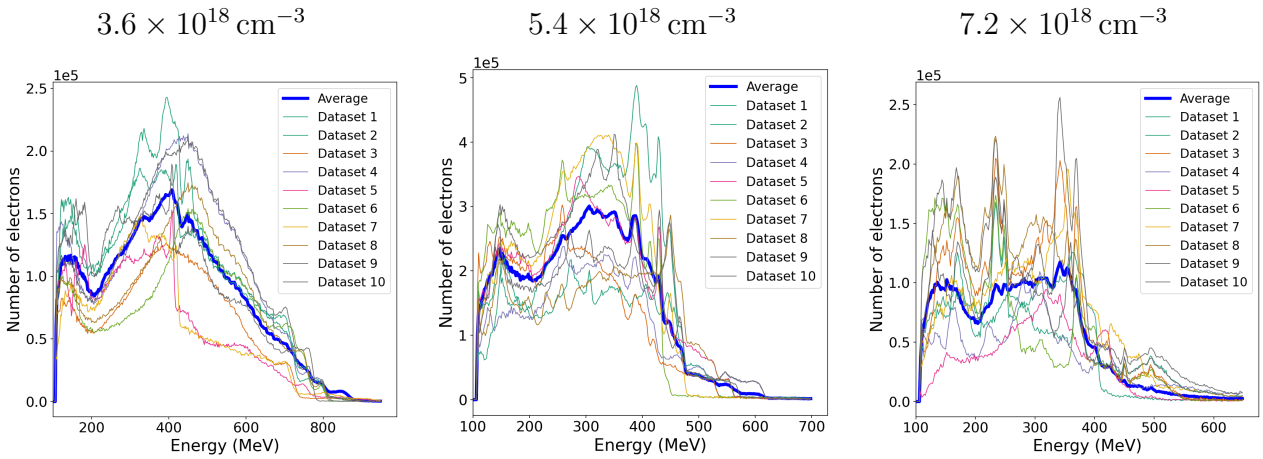

Figure 4.4: The experimental electron beam fluctuation expected for 10 measurements, calculated by averaging 5 random shots from the total data set for each electron density. The size of the fluctuations can be seen with respect to the average (thick blue line).

The effect of the electron beam fluctuation on the X-ray source was investigated through Geant4 simulations. The thinness and thickest converters that were used experimentally were chosen, 100 µm aluminium and 10 mm iron. A histogram and kernel density plot is shown of the critical energy for these two converter, Figure 4.5 (a & b). Figure 4.5 (c) the average error in the critical energy for the 3 different electron regimes. The error by assuming an average spectrum is largest for the highest density, as expected from the fluctuations Figure 4.4. Figure 4.5 (d) shows that the percentage error for the flux is also high for these two converters, that should be representative of the converters used. This helps explains the large errors seen in Section 4.6, but does not account for the experimentally unmeasured electrons (<100 MeV). Depending on their stability and number, the expected error could increase or decrease.

For this experiment the electrons were self-injected into the accelerator. Future work could use a controlled injection mechanism to improve the stability of the electron beams, such as ionisation injection [66], density profile injection (Chapter 5) [69] and dual laser pulses [75, 76]. Additional consideration should be given to retaining the simplicity of the

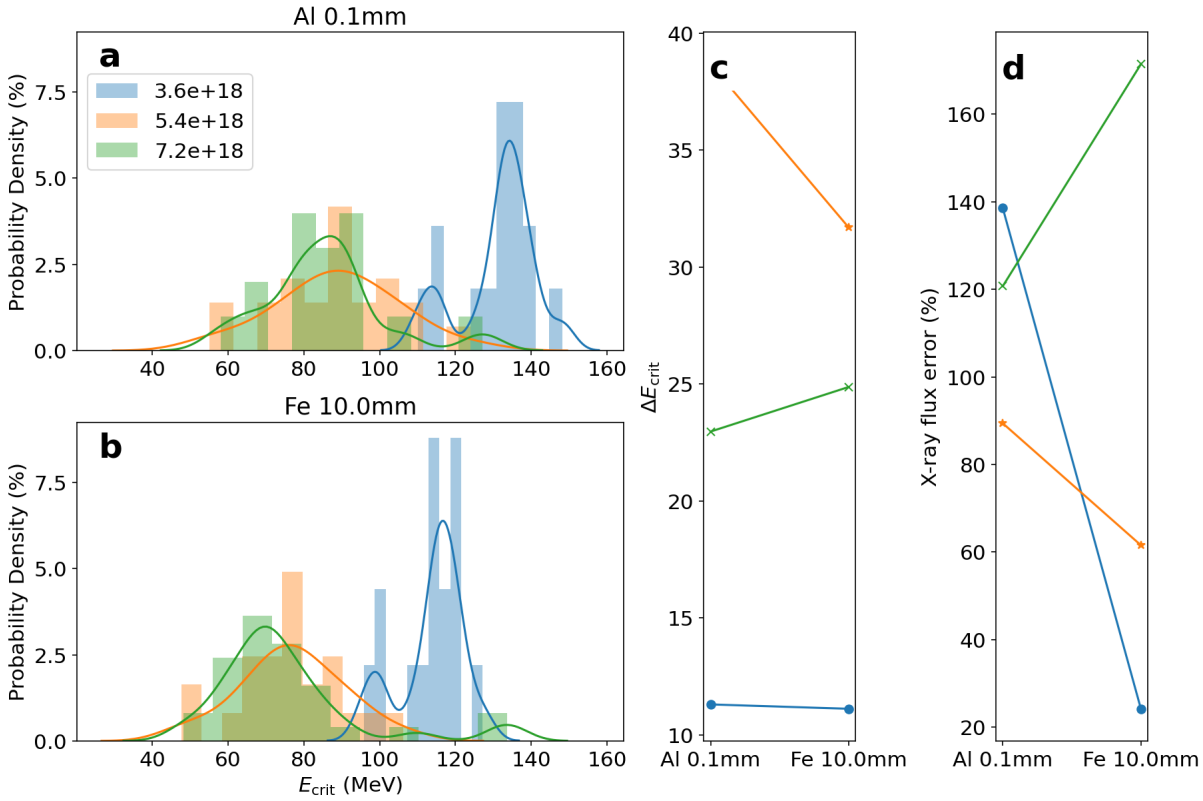

Figure 4.5: The effect of the fluctuating electron beams on simulated X-ray source properties. (a) The probability distribution of critical energies extracted from a 100 µm aluminium converter. (b) as before for a 10 mm iron converter. (c) The average critical energy spread for each electron regime for the two converters. (d) as before for the photon flux. The data in (c&d) is the FWHM of the kernel density estimation.

set-up since electron propagation distance must be small to minimise the source size. The controlled injection could be used to minimise the divergence, improving imaging quality by reducing the X-ray source size [151]. The optimisation of the electron beams could be done using a machine learning algorithm, such as in Chapter 6. The use of a machine learning algorithm would allow the global optimum for the beam parameters required to be efficiently found.

4.5 Extracting experimental data from the CsI array

The response of the CsI array was collected with a 12-bit gigE manta camera [146]. The detector response was calculated for each crystal row, so the camera pixels corresponding to each crystal were summed to calculate the response of the detector. The pixels that did not correspond to crystals had a background plane fitted to them, and this background was then subtracted from the crystal data, following the approach of Behm *et al.* [133].

The flux was calculated by the total brightness in the crystals. The divergence was calculated by fitting a Lorentzian to the first column of crystals. The critical energy was extracted using the response curves (Section 3.8).

4.5.1 Calibrating the imaging system

The imaging system's collection efficiency had to be calibrated. On previous experiments using this diagnostic, the calibration method was to use a thick, high Z, converter placed in the electron beam [133]. It is assumed that the spectrum produced is bremsstrahlung shaped, and all the energy of the electron beam is converted into photons. However, if the electron beam fluctuates from shot to shot there is no way to account for this as the electron spectra cannot be measured simultaneously. The electron beams, Figure 4.4, showed a large fluctuation. Therefore, an alternative approach had to be used for this data.

In this thesis a new method of calibration is presented which accounted for the vignetting, low performing crystals, camera viewing angles, $f_{\#}$ of lens, and spectral/angular response of optical components all at once. The new method involved using an on-shot measurement of both the electron beam and the detector response. For this to be possible, a converter that does not cause large perturbations to the electron beam has to be used. The electron spectrometer was designed for a low divergence electron beam coming in at the height of the interaction (Section 3.3.1). The spectrometer keeps one axis of spatial information (divergence) and the other axis becomes energy. For accurate measurement of the electron beam properties the electrons must enter the spectrometer as expected,

i.e. an unperturbed beam. The scattering in the converter will occur in both angles (θ and ϕ), so will appear on the spectrometer screen as a blurring in both axes. Therefore, a electron beam with a small divergence indicates that the electron beam was mainly unperturbed.

A comparison of the electron spectra that had propagated through the thinnest converters (the converters which should produce the smallest perturbation on the electrons) divergence was performed (Figure 4.6 (a)). It was found that the converter with the smallest electron beam divergence was the 100 µm Al, using the narrow beams produced by the plasma target with a electron destiny $3.6 \times 10^{18}\,\mathrm{cm}^{-3}$. Due to its low density and atomic number (Table 4.2) the Al converter perturbed the electron spectrum the least compared with the other thin foils, shown in Figure 4.6 (a). This is because bremsstrahlung emission energy is $\propto Z^2$ and $\propto n$, where Z is the atomic number of the converter, and n is the density of nuclei in the converter [152]. Therefore, the small perturbations to the electron beam was seen experimentally, by recording no measurable increase in electron divergence on the spectrometer (Figure 4.6 (a)). In addition, simulations showed an energy loss of less than 0.2% in the electron beam when passing through a 100 µm Al converter. These measurements of the electron spectrum and CsI response allowed comparison between the experimental results and simulated results (using the experimental beams as inputs), with the difference being the correction factor for the experimental results (Figure 4.8).

The electron spectrometer only measured energies $> 100\,\mathrm{MeV}$. This meant that the low energy electrons were not detected, and might still have had a considerable effect on the response. Another reason, as well as that explained above, for choosing the $3.6 \times 10^{18}\,\mathrm{cm}^{-3}$ density for the calibration was it produced the most stable spectra, and had the highest ratio of high energy electrons to low energy electrons. Therefore, it was the least likely to have large and changing numbers of unmeasured electrons and having more high energy electrons means the signal in the detector, after the first couple of crystals, will be dominated by the measured electrons.

Figure 4.7 shows the relation between the electron charge and the total counts on the X-ray detector for the 5 data shots that are used to create the calibration. The relation

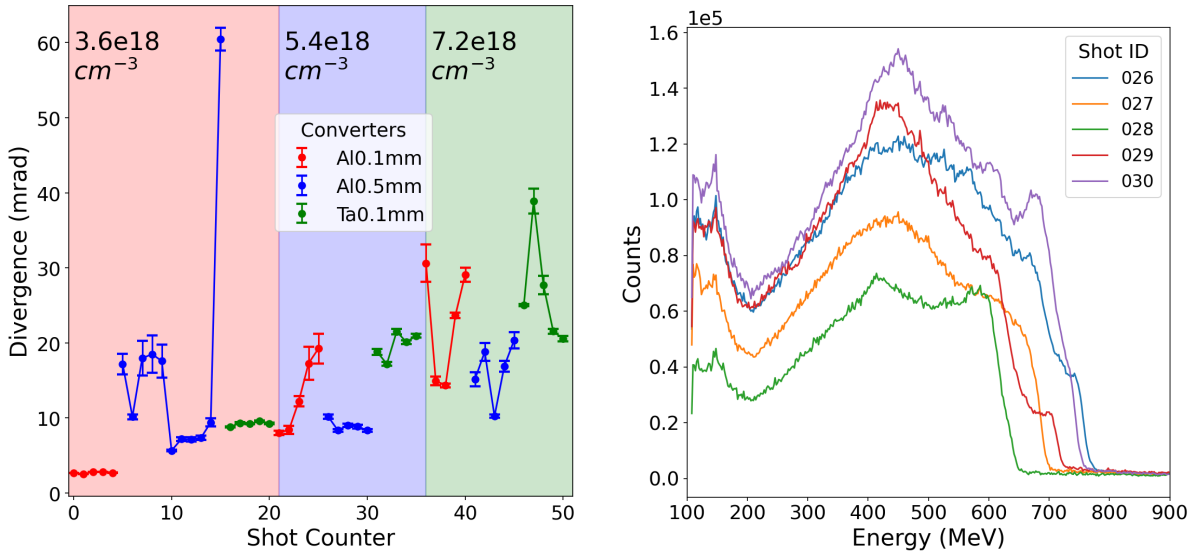

(a) (b)

Figure 4.6: Experimental electrons through thin foils (a) The divergence of the electron beams for the 3 thinnest foils. The different coloured regions correspond to the 3 electron densities selected by the gas cell pressure. The lowest divergence result was from the $3.6 \times 10^{18}\,\mathrm{cm}^{-3}$ plasma density produced spectrum into a Al 0.1 mm converter. (b) Electrons Spectra through foil for the $3.6 \times 10^{18}\,\mathrm{cm}^{-3}$ Al 0.1 mm converter. These are the 5 shots used for the calibration.

is expected to be linear [117] with no offset. The fitting of a line of best fit with the equation $mx + c$ and mx (Figure 4.7) shows that the offset is within error range of zero. The offset being positive is indicative of the unmeasured electrons contributing to the CsI signal (by producing >keV bremsstrahlung photons), but being in error of the expected answer showed that their effect does not dominate the response. The other reason for the data points not having a perfect linear relation is the detector was finite, meaning that some photons will not deposit their energy inside the detector.

Only the shape of the response of the CsI array can distinguish between the energies, as the amount of light produced by the scintillator is linear with energy deposited. This is shown in Section 3.8, and at energies >400 MeV the shape of the curve is effectively constant. However, for photons under 100 MeV the peak of the response occurs in the

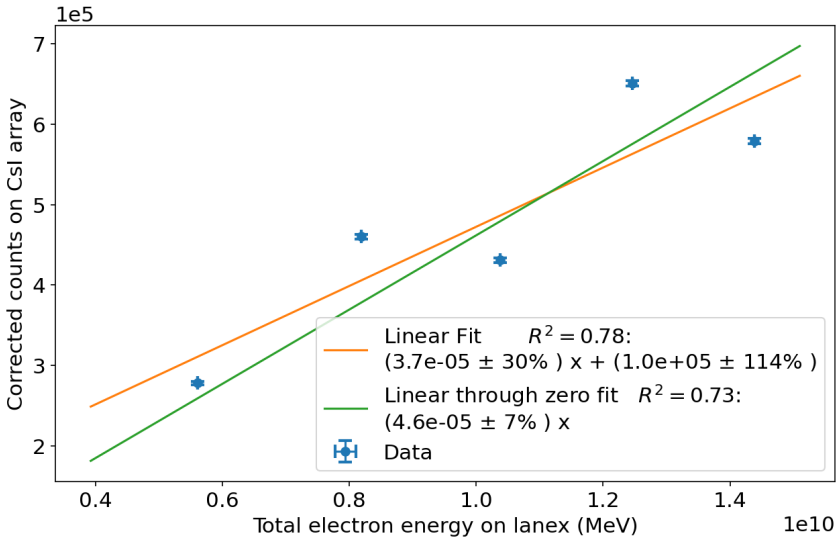

Figure 4.7: The total energy of the experimental electrons compared with the total energy deposited in the CsI array. The relation should be linear through zero [117], with unmeasured electrons likely being the reason for the variation.

first few crystals. The effect of not measuring the low energy electrons is not likely to affect the majority of the array, as the photon spectrum will be exponentially decaying spectrum up to their maximum energy. This means that the number of photons produced by these electrons that propagate past the first couple of crystals will be small. This linear relation between total electron energy and X-ray flux is important for the calibration, as Geant4 simulations are run for a given number of input particles and hence would not account for variation in electron numbers in the input. Total electron energy is linearly proportional to the total charge ($R^2 = 0.99$) so this relation is used to account for the variation in electron beam charge in the simulations.

The different electron spectra from Figure 4.6 (b) were used as the input into a bremsstrahlung Geant4 simulation. The photon spectra produced is shown in Figure 4.8 (a). These simulated photons were then propagated into a simulated CsI array. Figure 4.8 (b&c) shows the response of both simulation and experiment CsI array. The difference between them gives the correction factor Figure 4.8 (d). This correction factor has taken into account all the imaging system losses and vignetting.

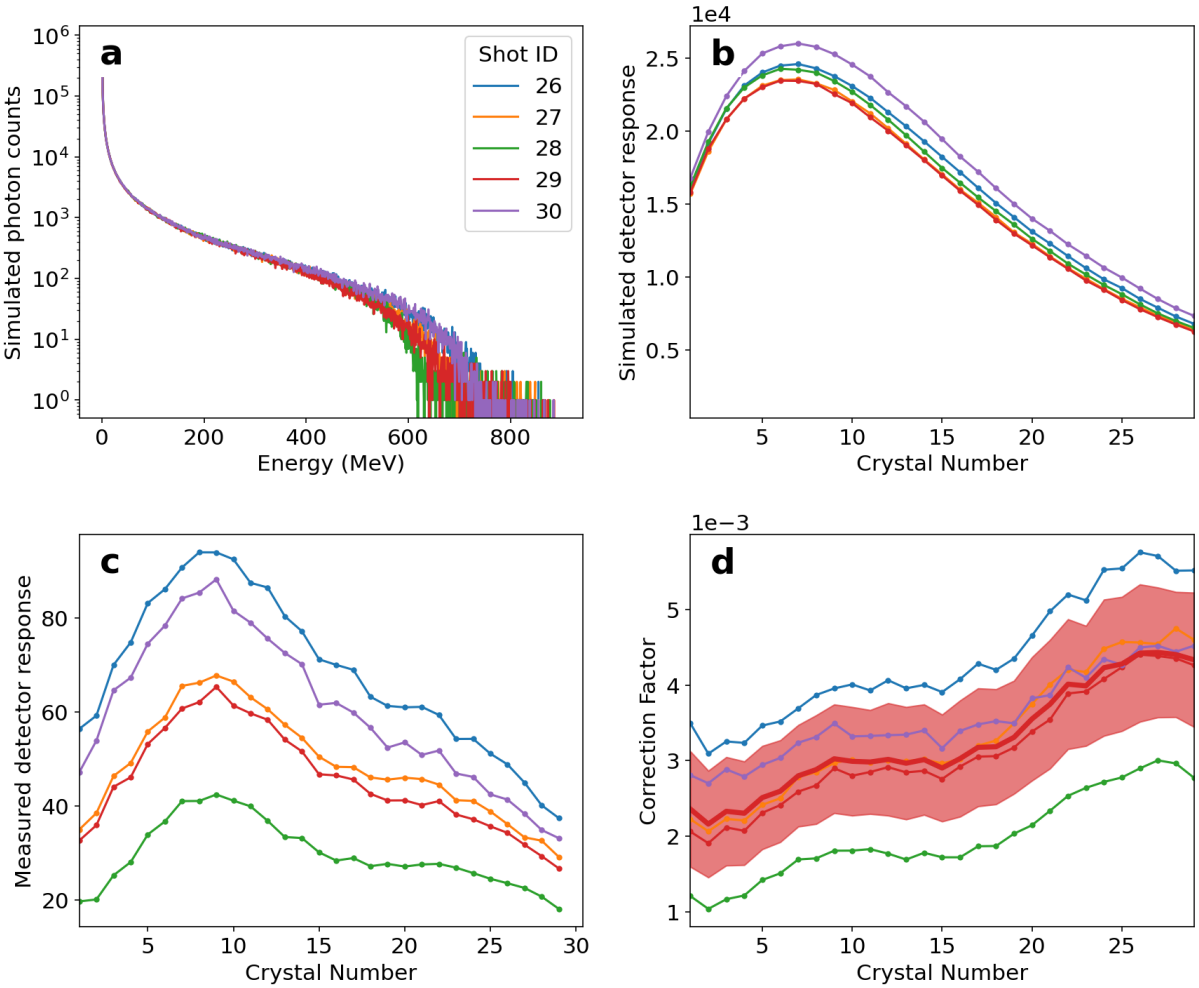

Figure 4.8: The Geant4 calibration simulations, using the experimental electron spectra Figure 4.6 (b) incident on a 100 µm aluminium foil. 10^8 particles were used and corrected for the number of counts seen on the electron spectrometer. (a) Simulated photon energy spectra from the experimental electron spectra. (b) The CsI simulated response for each shot. (c) The CsI measured response for each shot. (d) Correction Factor between the simulation and experimental results. The average is shown by the red line and the errors indicated by the red shaded region

4.6 Bremsstrahlung source properties

Using the experimental CsI X-ray diagnostic and Geant4 simulations, the source was characterised by measuring: conversion efficiency, divergence and spectral properties. The experimental data allowed: the extraction of the spectral shape of the photons; a measurement of the total flux (energy deposited in the detector); and a measurement of the divergence per source. These were also inferred from simulations; the simulation divergence was calculated by fitting a 2D Gaussian to the 2D image on the detector. The divergence was found to be the same in both axes, as expected. The source size was not measured experimentally for each converter. This measurement was done by imaging a resolution grid, which was only done using the converters and conditions that were perceived, at the time of the experiment, to produce the interesting sources (either narrow divergence or highest flux). This data was influenced by the detectors, which had a strong low energy ($< MeV$) dependence. The thickness of the experimental detector, for the scintillating crystals, also alters the energy that is detected. An upper limit on the source size was also inferred from using the resolution of the sample images, and simulations indicated the source size to be $\lesssim$140 µm. Three electron densities were used: 3.6, 5.4 and $7.2 \times 10^{18}\,\mathrm{cm}^{-3}$. The bremsstrahlung converters were made of iron and tantalum, and ranged in thickness from 500 µm to 10 mm.

Material	Atomic number	Density (gcm^{-3})
Al	13	2.7
Fe	26	7.87
Ta	73	16.4

Table 4.2: The properties of the bremsstrahlung converter materials used [153].

4.6.1 Divergence

The divergence of the photon source (Figure 4.9 (a)) shows that the smallest divergence was seen at $3.6 \times 10^{18}\,\mathrm{cm}^{-3}$ for the thinnest converters. The divergence angle of the X-rays

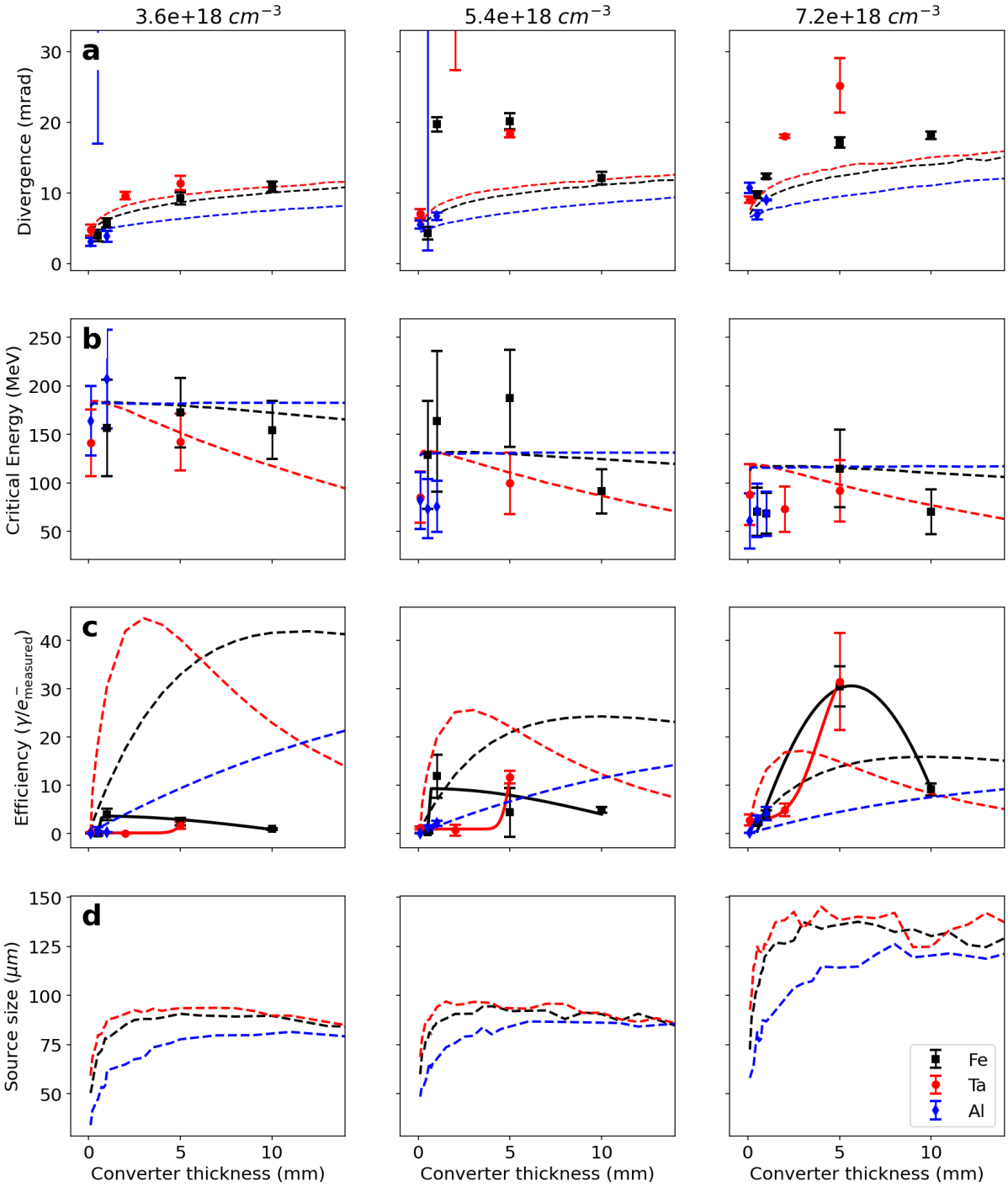

Figure 4.9: Effect of changing plasma density (n_e) and converter thickness on X-ray characteristics as measured experimentally (points) and inferred from simulations (dashed lines). Each row correspond to an X-ray source parameter. (a) Divergence. (b) Critical Energy. (c) X-ray conversion efficiency, with the experimental data is fitted with a skewed Gaussian (solid line). (d) Source size

increased with n_e. This is for two reasons, firstly the opening angle of the bremsstrahlung beam scales with $1/\gamma_e$ due to relativistic beaming [154] and γ_e decreases with increased plasma density (Figure 4.3 (a & b)) where γ_e is the Lorentz factor of the electron beam. Secondly the experimentally measured divergence of the beam of electrons increased with plasma density (Table 4.1). In this case the increased divergence of the electron beam for $7.2 \times 10^{18}\,\mathrm{cm}^{-3}$ plasma density is the dominating factor. The divergence of the X-rays increases with converter thickness, due to more scattering events occurring, described in Section 4.6.4.

For the electrons at higher plasma density, the simulations underestimate the divergence seen in the experiment. This is likely due to the lower γ_e electrons which were not measured, but more likely to be generated at higher plasma density.

A 2D Gaussian was fitted to the X-ray beam profiles for each of the different plasma densities, measured on the 8 mm LYSO (Figure 4.15 (a)). Comparing the ratio of orthogonal axes of this fit gave a ratio of 1.0 ± 0.1 indicating that the beam is circular.

4.6.2 Spectrum

Figure 4.9 (b) shows that increasing the electron density reduces the critical energy of the X-ray beam. This is due to the higher electron density accelerator producing a lower energy electron beam (Figure 4.3 (a & b)) and the maximum photon energy produced is equal to the maximum electron energy. Therefore, reducing the energy of the input electron reduces the energy of the photons produced.

The lowering of E_{crit} with increasing areal density (thickness $\times$ density) and atomic number is due to the higher number of scattering events in the converter [152]. The areal density increases more rapidly for the denser converter materials (Table 4.2) hence a larger drop in E_{crit} for the Ta converter. After an emission event, the electron will have a lower energy, resulting in a lower energy radiation in subsequent events. Multiple scattering from a single electron, results in the production of more photons overall, increases the flux of the source. The energies in these bremsstrahlung photon beams are higher than those reported previously using differential filtering ($\sim$10 MeV) [144].

Therefore, by tuning the incident electron beam by changing the plasma density with the control of the gas cell pressure, and changing the converter material, the spectral properties of the photons are altered. Spectral tuning is highly beneficial for optimising absorption contrast and decreasing noise in imaging, and allows the X-ray technology performance to be matched to an individual object, thus increasing image acquisition efficiency.

4.6.3 Conversion efficiency

Figure 4.3 (d) demonstrates that the X-ray flux is highest when the accelerated electron charge is also highest in keeping with expectations. Figure 4.9 (c) shows that the experimental data generally supports the simulation result for conversion efficiency, showing that there is an optimal thickness in generating X-ray conversion efficiency, shown by the solid lines. Initially, an increase in thickness leads to an increase in photon conversion efficiency. Further increase in thickness results in the material acting to absorb the radiation and so the X-ray conversion efficiency decreases. The other reason for a decrease in conversion efficiency would be if the emitted photon is not into the solid angle the detector subtends (Figure 4.12) which is discussed in the Section 4.6.4. The experimental measurement appears to peak at a smaller thickness (solid lines) compared to simulations (dashed lines). This may be understood as a consequence of the unmeasured electrons with energies of $< 100\,\mathrm{MeV}$. The poorer agreement observed at the highest electron density may be attributed to the greater fluctuations in the electron spectrum.

The results presented here agreed with the previous work of S. Cipiccia *et al.* [151] in terms of the divergence increasing with atomic number, Z. Agreement is also found in terms of flux (conversion efficiency) increasing with both Z and thickness, R, up to a point. The reduction in flux at the highest Z and R values correspond to materials that are beyond the scope of the study by S. Cipiccia *et al.* [151].

4.6.4 Source size

Due to the small pixel size required to resolve this source size an additional simulation was parallelised by M. P. Selwood to allow particle numbers up to 10^{10}. This showed that the results converged at 10^9 particles, and the source size was calculated by using the FWHM of the line spread function gradient.

Figure 4.9 (d) shows the simulated source size, measured using penumbral imaging [155]. The source size increases with increasing the electron density, due to the divergence of the electron beam increasing (Table 4.1). This means that the area of the electron beam increases on the converter, increasing the source size. This is in agreement with S. Cipiccia *et al.* [151]. Simulations show a source size of $\lesssim$50 µm for the thinness converters at all plasma densities. Increasing the converter thickness, does increase the source size, but only up to a limit of around 100 µm for 3.6 and $5.4 \times 10^{18}\,\mathrm{cm}^{-3}$, and 140 µm for $7.2 \times 10^{18}\,\mathrm{cm}^{-3}$.

The plateauing of the source size was a surprising result required additional simulations to explain. The result was investigated by comparing the source size measure by penumbral imaging (line spread function of an edge), to a direct measurement on the rear side of the converter. Figure 4.10 shows the two different methods used in the simulation. The difference between the source size measured for the two techniques is shown Figure 4.10 (b), with the penumbral imaging technique showing source sizes $\lesssim$50 µm compared with source sizes of up to 1.5 mm from the direct method.

The disagreement in result of these two methods was investigated through additional simulations, Figure 4.11. The directly measured source will increase as more photons leave the converter with a larger distance from the beam axis (r) as the thickness increases. The discrepancy between the two results can be seen however, as the photons leaving at a larger r also leave with a larger angle. As for the source size measured with penumbral imaging, only the photons that hit the detector ($\theta \approx 0$) will add to the source size (Figure 4.12). If these scattering events are in the small angle limit ($\theta_i \to 0$), the source size is not increased significantly, but the divergence increases linearly with number of scattering events. If the first scattering event is into a large angle, θ_1, (increasing the source size on the rear

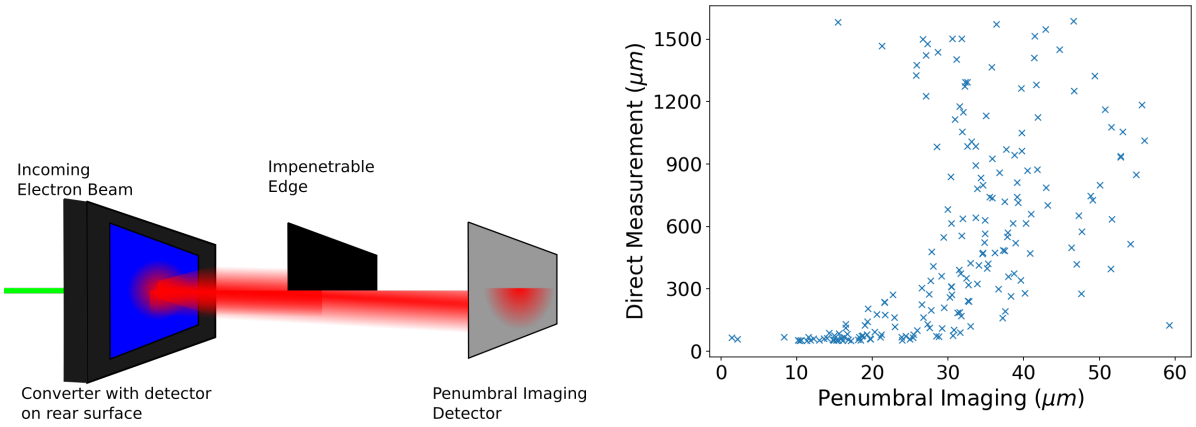

(a) (b)

Figure 4.10: The two methods used in Geant4 simulations to measure the source size. (a) Diagram of simulations. The electrons (green) propagate into the converter target. The photons produced (red) are measured by the two detectors. The direct measurement (y-axis) is done by the detector (blue) is placed directly on the back surface of the converter. An impenetrable edge is placed halfway between the converter and a second detector (grey) and the blurring of the edge gives the source size (x-axis). (b) The difference between the two methods of measuring source size for a pencil beam. The direct method is an order of magnitude larger.

of the converter) the second scattering event will only contribute to an increase in the detected source size at a distance if the second photon produced by this electron strikes the detector. That is, $\theta_2 \sim \theta_1$. The chance of this becomes vanishingly small as the first scatter angle increases, as the detector subtends a smaller azimuthal angle as the required polar angle increases (Figure 4.12). The preservation of source size is, in a sense, empirical since it results from the detector being a finite distance away (10 cm for simulations, 3.5 m for experiment). Therefore, increasing the thickness, and thus areal density, does not lead to an increase in the effective source size as the additionally generated photons do not contribute to the final image. This will also contribute to the reduction in flux as the areal density increases.

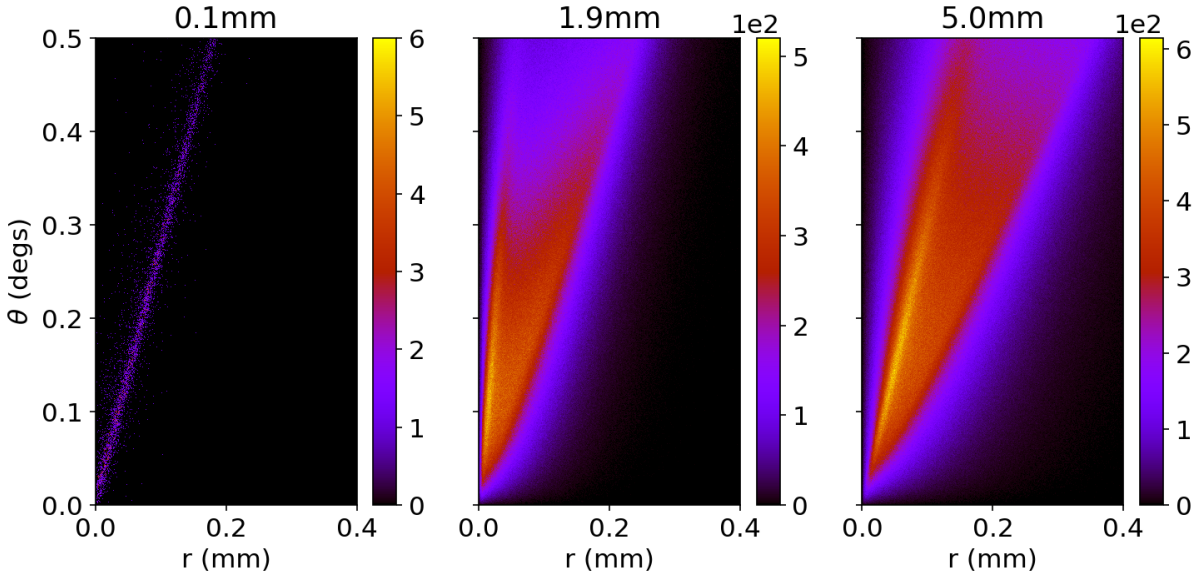

Figure 4.11: The simulated angle of photons leaving the detector with respect to the distance from the beam axis, for an iron converter in the $3.6 \times 10^{18}\,\mathrm{cm}^{-3}$ electron beam. Simulation conducted in Geant4. The thickness of the converter is marked above each plot. The colour map is the number of photons in each 2D histogram bin.

A small source size of 150 µm was seen experimentally (Figure 4.13) by imaging resolution grids. The different detectors have different abilities to image photons of different energies. For the image plate the response will be dominated by photons in the keV range[115], whereas the LYSO scintillator is able to detect photons up to the MeV range [110]. Experimentally, the significant difference in the contrast between the detector types (image plate, 8 mm and 2 mm LYSO) demonstrates that the imaging quality in our setup is limited by the detector itself, and not by the source size. Therefore, the experimental source was $\lesssim$ 150 µm. High repetition rate detectors of multi MeVs will have to be improved to capitalise fully on the resolution offered by these sources.

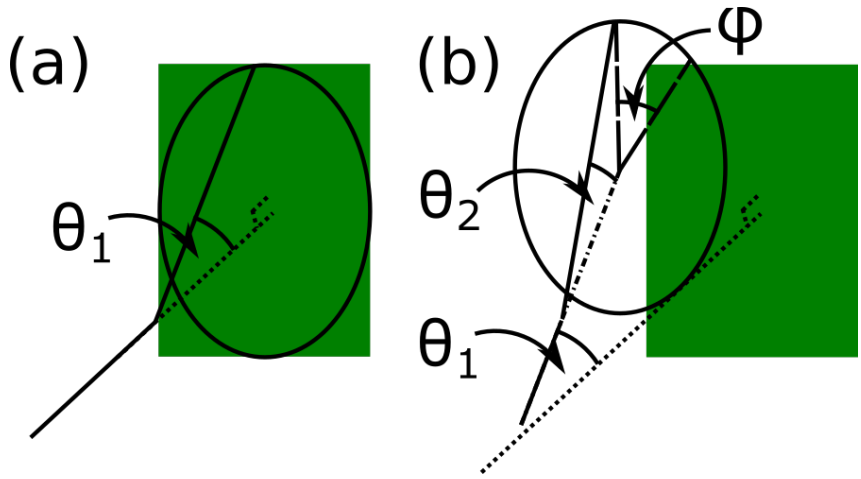

Figure 4.12: Schematic showing whether a emission event reaches the detector [35]. (a) An on-axis event has a maximum acceptance angle θ_1 for a given detector. (b) For a scattering event from an off-axis electron for a given θ_2 there is only a small range of ϕ that subtends the detector.

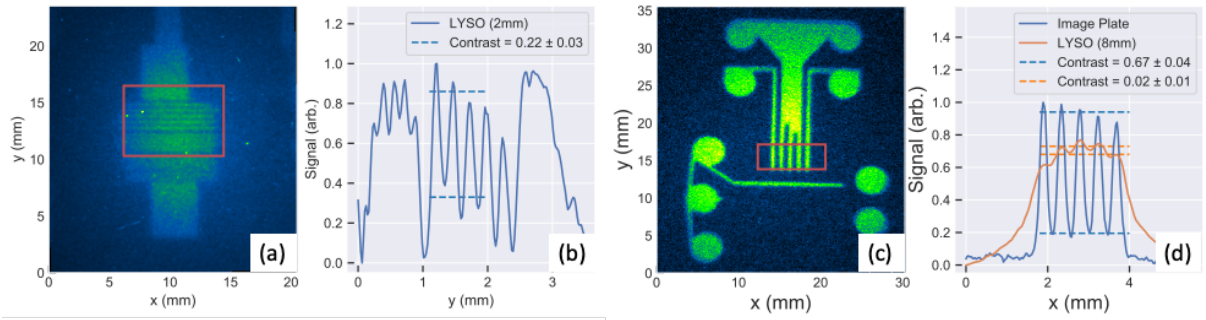

Figure 4.13: Images of resolution grids captured with the experimental bremsstrahlung source, produced by C. D. Baird for [35]. (a) Single shot image of small (150 µm) features on a 2 mm thick LYSO crystal. (b) A contrast of 0.22 ± 0.03 was measured for a line-out perpendicular to the features in the highlighted region in (a). (c) 10 shot image plate scan of resolution grid. Features in the red box are 200 µm. (d) Contrast of a perpendicular line-out to the 200 µm features shown in (c), as measured with image plate, and a 8 mm thick LYSO crystal. The scintillator material causes significant blurring due to its thickness.

4.7 Sample imaging

To test the imaging capability of the source a variety of samples from industrial collaborators were used. Figure 4.14 (a) shows one example, an additively-manufactured star-based prism artefact composed of the nickel alloy Inconel718, which is around 5 cm in each dimension. This was placed outside the target chamber (magnification M=1.6), and imaged using bremsstrahlung from a 2 mm tantalum converter.

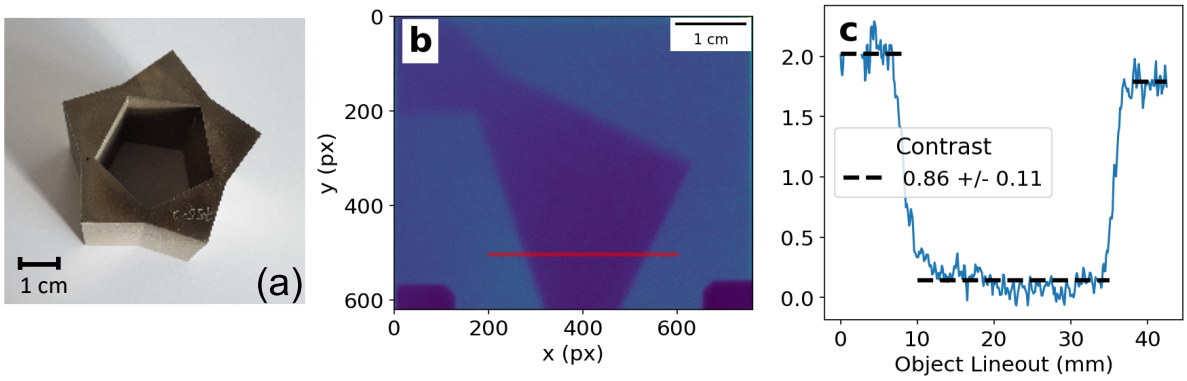

Figure 4.14: Image of test object with X-ray source [35]. (a) Photograph of Inconel star object. (b) Experimental image of star from 2 mm LYSO. The X-ray beam profile has been removed, and the image is the result of a pixel-wise median of 10 shots. (c) Contrast of 0.9 ± 0.1 of Inconel star object measured on the 2 mm LYSO for line-out marked on (b).

Figure 4.14 (b) shows the shadow of the object (Figure 4.14 (a)) projected onto 2 mm LYSO, where the scintillation light is collected by a CCD camera. The use of the thinner scintillator allows higher spatial resolution (due to reduced optical blurring) but also results in the image being dominated by lower energy x-rays. The detector (40x50 mm) corresponds to a field of view at the object of (25x31 mm). The 2 mm LYSO results in a larger field of view than the 8 mm LYSO as the highest energy bremsstrahlung emission appears closest to the axis, in agreement with [156]. This is apparent when comparing the beam profile on the thick 8 mm LYSO crystal compared with the thin 2 mm (Figure 4.15) which absorbs more high energy photons [118] and therefore, shows a more sharply peaked

beam profile. Figure 4.14 (c) shows a contrast of 0.9 ± 0.1 across the line-out indicated in Figure 4.14 (b) where the object is 5 cm thick Inconel (areal density 45 gcm^{-2}).

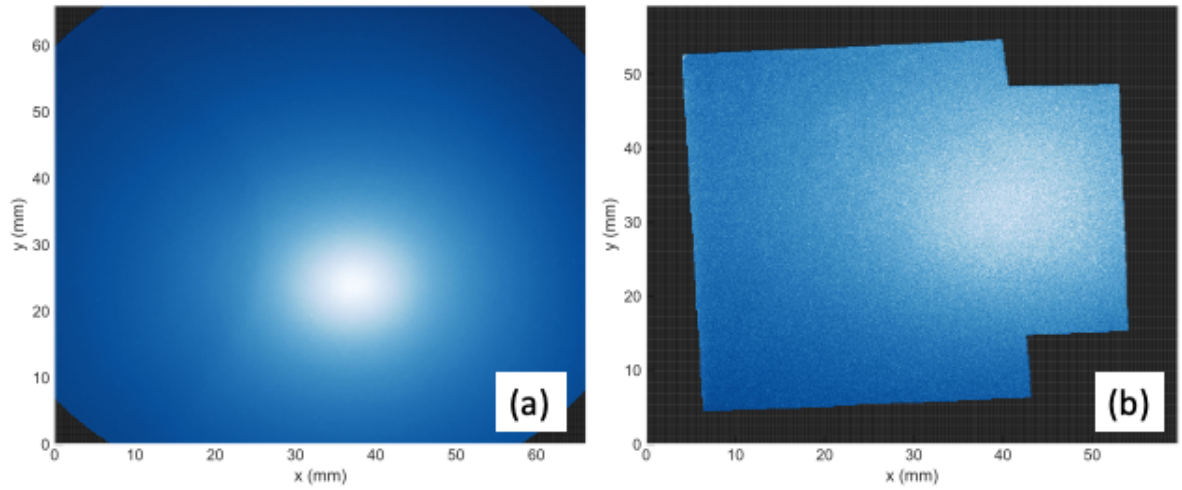

Figure 4.15: Experimental X-ray beam profile for (a) 8 mm LYSO crystal. (b) 2 mm LYSO crystal. The thicker crystal displays a sharper peak. Plots produced by C. D. Baird for [35].

The incomplete obscuration of the X-ray signal (Figure 4.14 (b)) demonstrates the penetrative ability of the source. However, the region on the detector that is obscured by the object appears uniform instead of having the shape of the X-ray beam profile. This suggests that the X-rays that have propagated through the sample and are detected have been scattered, homogenising the signal. The attenuation coefficient for nickel for 10 MeV photons is $\sim 0.03\,/\mathrm{cm}$, but for 0.1 MeV photons is $\sim 0.44\,/\mathrm{cm}$ [109], so penetration of the sample is expected for the highest energy component of our source. As the energy of the photons increase, the probability of the detector detecting the photon decreases [118], resulting in the photons that propagated through are not efficiently detected. As with the detection of the source size, the detector is currently the limiting factor when using these sources. When new detectors are designed that only detect the high energy photons (>1 MeV) it will be possible to use the penetrative effect of this photon source to the best of its potential.

4.8 Source characteristic scalings

For broad utility of this source, and a given LWFA electron beam, the user may wish to select the area radiated, penetrative capability, and speed of acquisition to suit the specific application. This will require independent control of the divergence, critical energy and conversion efficiency (or flux) respectively.

Simulating the source generated from an electron beam (the experimental electron spectrum from $n_e = 3.6 \times 10^{18}\,\mathrm{cm}^{-3}$ for this data) showed the changes in the X-ray source result from changes in converter parameters. This result (Figure 4.16 (a)) showed that the shape of the response was universal for a scaling parameter based on a unique combination of converter parameters: thickness (R); atomic number (Z); and density (ρ):

$$\begin{aligned} \theta &= R^{0.03\pm0.01}\rho^{0.008\pm0.004}Z^{0.01\pm0.003} \\ \eta &= R^{1.63\pm0.02}\rho^{1.07\pm0.04}Z^{1.16\pm0.03} \\ E &= R^{0.20\pm0.004}\rho^{0.29\pm0.002}Z^{0.08\pm0.001} \end{aligned} \tag{4.3}$$

where θ, η and E are the scaling parameters for divergence, conversion efficiency, and critical energy, respectively. The scaling axes were found by minimising the difference between converters. The curves for divergence and critical energy are seen to only scale with this parameter, whereas the amplitude of the conversion efficiency also increases with Z, so the data was normalised for the calculation.

Using the scaling axes, converters made of different materials can be evaluated, Figure 4.16(b). The different properties scale with axes that are not parallel (θ, η, E), which allows tuning of the different source properties with choice of material (Z, ρ) and thickness (R). The density of the materials could also be reduced if required by using structures such as aerogels [157]. For example, a tantalum converter could produce a high flux, low critical energy beam with a small divergence at a thickness of 3 mm, whereas using a thick converter of a lower atomic number material such as aluminium would allow a source with a higher critical energy to be produced with similar divergence.

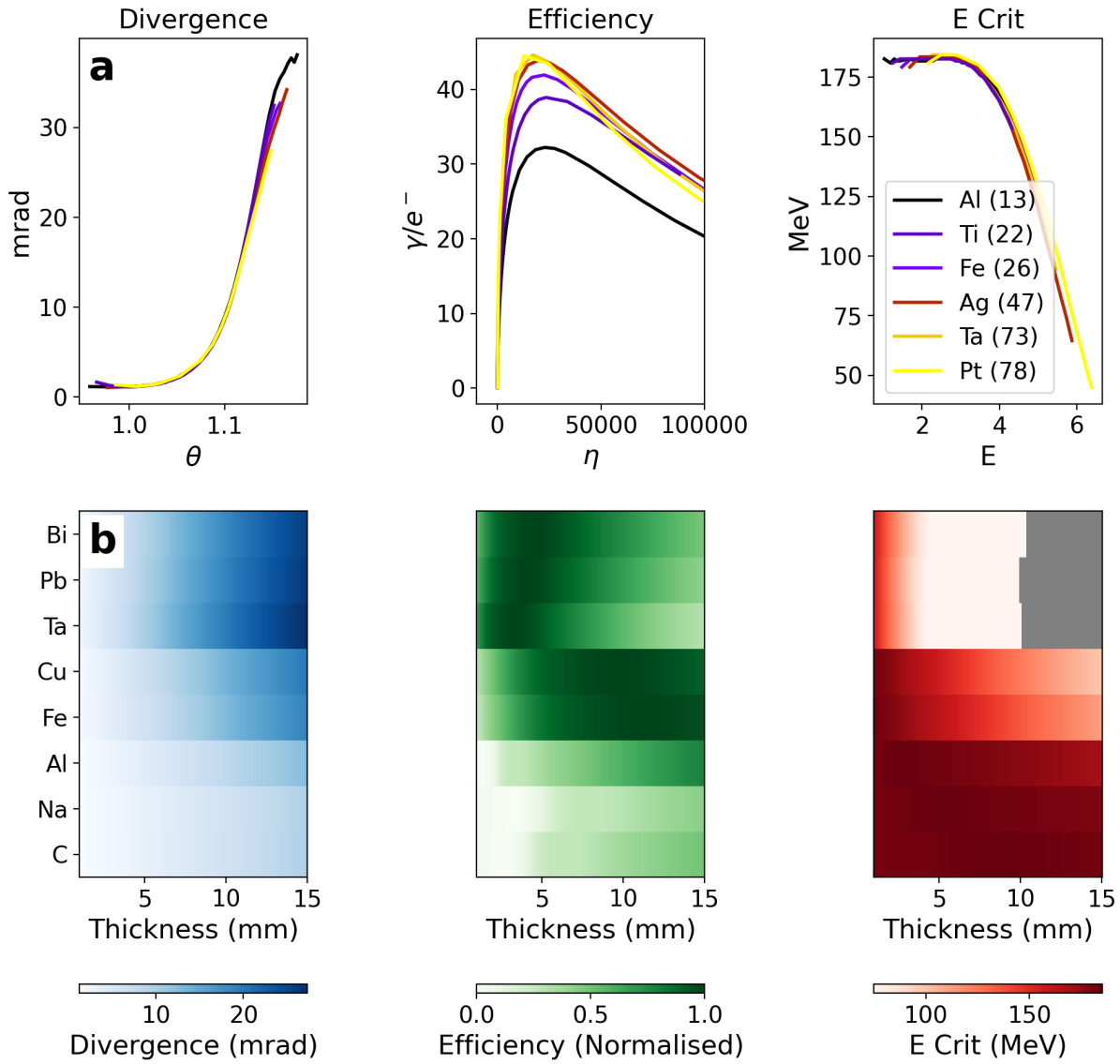

Figure 4.16: X-ray source scalings with converter parameters [35]. (a) Simulated X-ray source characteristics - divergence, conversion efficiency and E_{crit} - demonstrating similarity of behaviour across materials. Each characteristic scales at different rates of thickness, density and nuclear charge (Z) as shown in Eq (4.3). For divergence and E_{crit} the data from all the converter lies on the same line. The conversion efficiency data also has an amplitude scaling with Z of the converter. To create the scaling axis the flux data was normalised by the peak height. (b) Demonstration of this control for a range of materials at their standard densities [153]. (The grey region is outside the interpolation limits.)

4.9 Conclusions

A bremsstrahlung X-ray source has been create using a LWFA combined with converter targets. The measured X-ray spectrum is the highest energy reported from a LWFA driven bremsstrahlung source, with the maximum critical energy >150 MeV. The LWFA bremsstrahlung source was used to image high-density, industrially relevant materials with a resolution of $\lesssim$150 µm, currently limited by the detector used. The X-ray source size was measured experimentally to be $\lesssim$150 µm and simulations indicated a source size of ∼50→140 µm depending on the converter and electron bunch parameters. This small X-ray source size, required for single-shot high-resolution imaging, was shown to be characteristic of the LWFA bremsstrahlung X-ray source. This LWFA X-ray source size is significantly smaller than the industry-standard of ∼1 mm using linac beams.

Control of the X-ray source was shown by varying the electron density or the converter, both experimentally and in simulation, with results showing control was achieved over the brightness, divergence, and the characteristic energy of the X-ray beam.

The X-ray source properties were found to follow universal curves for changes to the converter target. The brightness, divergence, and the characteristic energy of the X-rays changed at different rates with respect to the converter density, atomic number and thickness. Using this information, the X-ray source can be modified to optimise these source parameters, through choice of converter, for the users requirements.

This laser produced source can provide a compact instrument for imaging of high areal density large objects and has the potential to become a valuable inspection tool in manufacturing. The tunability of the source presented here makes the X-ray source extremely versatile for industrial use. The detectors demonstrated here are capable of matching - and exceeding - the repetition rate of current laser systems, demonstrating a route to rapid tomographic imaging. This source, along with the high repetition rate (∼10 Hz) petawatt laser facilities coming on-line (ELI Beamlines [135], ELI-ALPS [24], EPAC [136]) will lead to the realisation of rapid high resolution MeV tomography for impact in high value manufacturing sectors.

5 | Controlling electron injection using a tailored density profile

In this chapter electron injection into the wakefield was controlled using a tailored plasma density profile, along the propagation length of the laser. Particle-in-cell (PIC) simulations were used to understand the effect of the density profile on the electron beam produced. Results from an experiment carried out in January 2019 at the CLF's Gemini Laser facility are presented showing ∼1.2 GeV electron beams produced with this method.

5.1 Background and motivation

Laser wakefield accelerators (LWFA) provide a compact way of producing high energy electron bunches [1], and since 2004 experiments have been able to create these bunches with a mono-energetic spectrum [3–5]. These first results were produced due to self-injection into the acceleration structure, an effect that is driven by the non-linear plasma waves created. This means that small changes in conditions can lead to a large fluctuation in electron beam parameters. Since these first results, there have been new injection methods developed which have been shown to improve control over the injection of mono-energetic electrons: ionisation injection [66]; dual laser beam [75, 76] and density profile [69]. See Section 2.8 for more details.

This chapter investigates the density profile method of injection with the aim of producing a LWFA suitable for applications (such as Chapter 4). For most applications, a stable, simple to set up and high repetition rate (kHz) LWFA will be required. Lasers

have intrinsic jitter, which means that their pointing, energy and pulse duration varies shot to shot. Lasers also have longer term performance drifts, which can be caused by the change of environmental conditions due to the time of day [7]. While technological solutions are being developed to mitigate such fluctuations on new laser system [24], an injection mechanisms with lower parameter dependence would be advantageous. The density transition injection occurs due to the changes in the plasma profile, resulting in an injection method that is less sensitive to the non-linear effects of the laser evolution, and hence, the laser fluctuations.

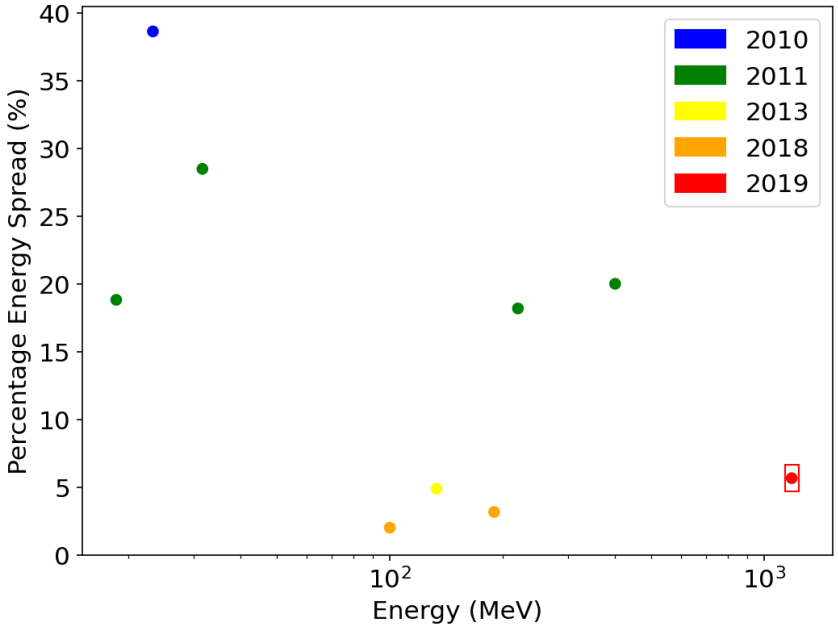

Figure 5.1: The progression of experimental produced electrons via density profile injection [59, 69, 71, 72, 158]. The data from this chapter is in the red box.

Density profile injection has been shown to produce low energy spread electron beams (Figure 5.1) and the experimental work presented here is the first GeV energy electrons produced using a density profile injection technique. This result was seen during the radiation reaction experimental run, using a density profile injection method, where mono-energetic electrons were produced with $\sim$1.2 GeV. In this chapter, to understand the experimental results, both experimental data and simulations are presented. Experimental measurements of the density profile were taken using interferometry, but as shown in this

chapter, it was not able to measure the transition region accurately. An accurate density profile, modelled using a fluid code (openFOAM [127]), is used in a PIC code (EPOCH [121]) to simulate the injection method. The shape of the transition is very important for the injection process.

5.2 Density injection mechanism

The density transition injection mechanism works by having a sharp ($\sim \lambda_p$) transition between a high plasma density (n_e) region into a lower density region [69]. Plasma wavelength scales with electron density, $\lambda_p \propto 1/\sqrt{n_e}$. The wake set up by the laser pulse has characteristic size of λ_p. When the wake propagates over the sharp density transition, the size of the wake suddenly changes (an increase with a drop in density). The electrons that were travelling in the background wake now end up in a position where they become trapped in the accelerating region of the lower density wake (Figure 5.2). Figure 5.2 (b) shows that the seperatrix (particles inside the line of the seperatrix are trapped by the wake) for the low density wake encloses a larger area of phase space.

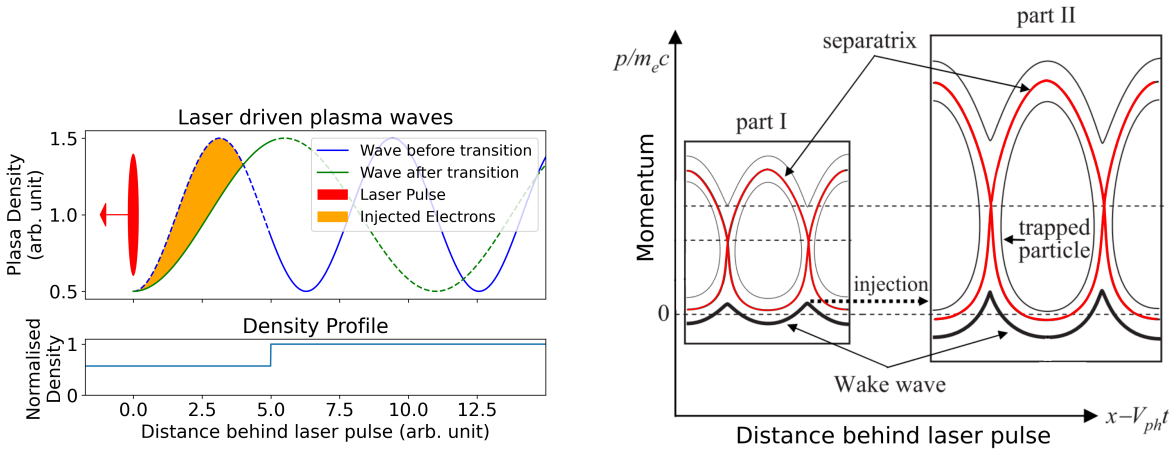

Figure 5.2: Density transition injection mechanism. (a) Schematic of density transition injection process. Electrons travelling in the high density wake get trapped in the low density wake. (b) Modified from [70], showing the injection process using a seperatrix diagram. The seperatrix is shown in red.

This enables a larger energy gain for particles in the second wake. It also shows that the momentum gained by particles in the oscillation of the first wake is higher than the minimum trapped momentum in the second wake. When the transition from the high density to low density region occurs, it is these electrons moving with the peak momentum in background oscillations that become trapped.

The electrons produced using this method have been found to have an order of magnitude decreases in transverse momentum spread, compared to using a homogeneous plasma [159].

5.3 Simulation parameter scans

The performance of the LWFA using a density profile injection method was investigated using the PIC code EPOCH in 2D [121]. The initial scans were conducted with a trapezoidal profile, Figure 5.3, with an initial density fixed so that no injection occurred at that density. For these simulations the potential variables were: laser pulse energy (E)

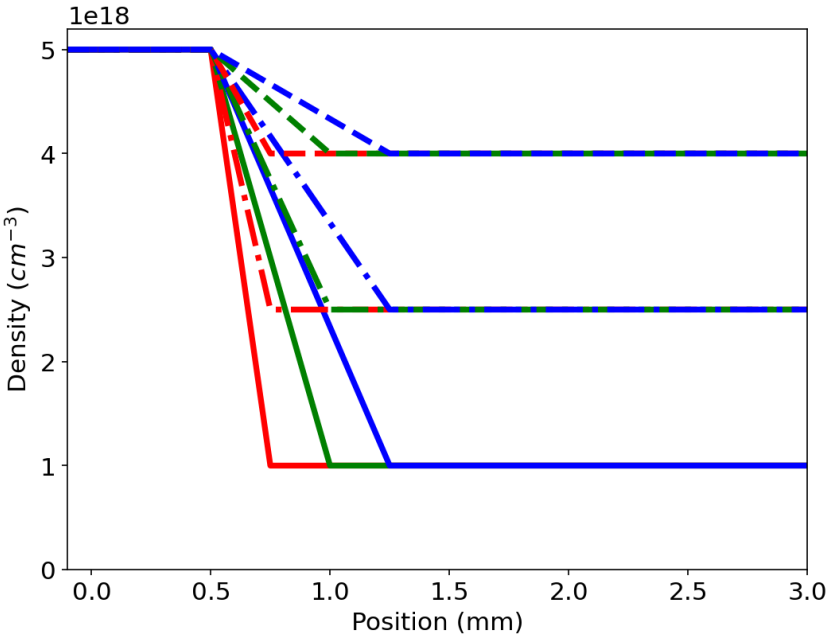

Figure 5.3: Examples of the plasma density profile variation for the EPOCH simulations parameter scans.

and duration (τ); initial and final plasma density ($n_{\text{Init}}, n_{\text{Accel}}$); position of the start of the transition (t_s); length of the transition from the initial to acceleration density (t_l). The simulation parameters that were kept constant are shown in Table 5.1.

Constant Parameter	Value
Laser focus spot size	20 µm
Laser focus plane position	0.5 mm
N_{cells} per wavelength	28
Initial particles per cell	16
Pulse duration	42 fs
n_{Init}	$5 \times 10^{18}\,\text{cm}^{-3}$
Duration of the simulation	10 ps
Length of the simulation	∼3 mm

Table 5.1: Constant simulation parameters for trapezoid profile PIC simulations. The resolution of the simulation was determined from convergence testing (Figure 5.4)

The simulations allowed the tracking of the electron's momentum and properties of the driving laser. This allowed investigation into: the electrons' peak energy and energy spread (calculated from the FWHM of the spectrum); the beam charge and energy (for electrons with an energy >5 MeV); and the beam divergence (for the electrons in the peak, defined as within the FWHM limits). The laser properties were tracked through the simulations measuring: where the focus occurred; the length over which the beam was tightly focused; the maximum intensity reached; and the intensity at the start of the density transition.

Convergence testing

Figure 5.4 shows the convergence testing for these simulations. For this a simulation of the density ramp was chosen to have the conditions shown in Table 5.2.

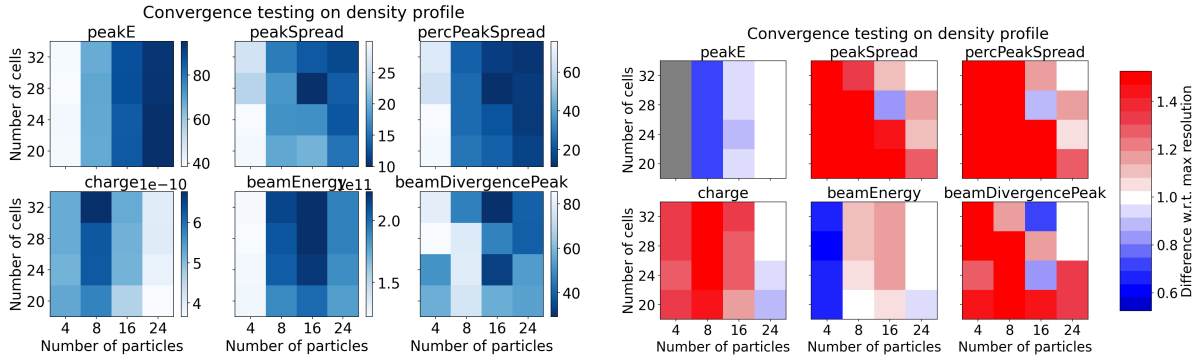

(a) (b)

Figure 5.4: Convergence testing for the EPOCH parameter scan. The number of particles that initially populates each cell is on the x axis, and the number of cells for each laser wavelength on the y. (a) The extracted results from the simulations. (b) The ratio of the results with respect to the highest resolution simulation.

Parameter	Value
n_{Init}	$5.0 \times 10^{18}\,\text{cm}^{-3}$
n_{Accel}	$3.0 \times 10^{18}\,\text{cm}^{-3}$
t_p	$500\,\mu\text{m}$
l_s	$10\,\mu\text{m}$
Laser energy	$500\,\text{mJ}$

Table 5.2: Simulation parameters for Figure 5.4.

As with all convergence testing some judgement on what resolution to use has to be exercised. For the simulations above, 16 particles per cell were used with 28 cells per laser wavelength. The data from this simulation is within 10 % of the highest resolution simulation run, and took around 2400 cpu-hours. Crucially this allowed each simulation to be run in one allowed time period on the University of York's supercomputer, Viking.

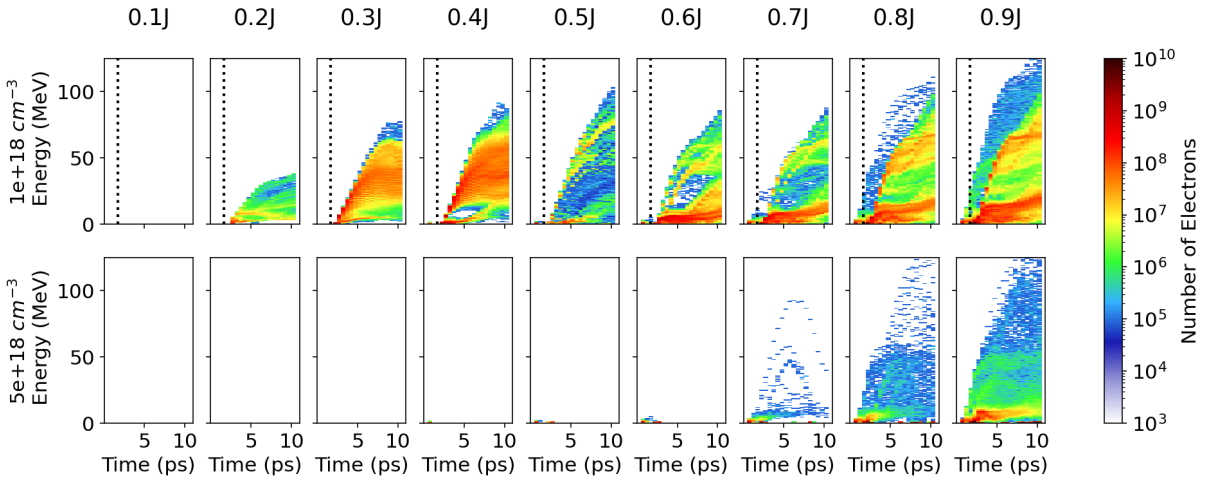

Figure 5.5: Varying laser power for the density profile injection (top row), and self-injection (bottom row). The density profile starts at $5 \times 10^{18}\,\mathrm{cm}^3$ and has a sharp drop to $1 \times 10^{18}\,\mathrm{cm}^3$ at 0.5 mm, corresponding to the laser focus. The transition is crossed at a time indicated with the vertical dashed black line.

5.3.1 Energy requirement

As with all multi-parameter scans, finding the starting position is important. To test the effectiveness of the profile, a comparison was made between a flat profile and a tailored profile. The choice of initial density was chosen to be in the range of experimentally used values, $n_{\mathrm{Init}} = 5 \times 10^{18}\,\mathrm{cm}^{-3}$.

The comparison is shown in Figure 5.5, where the evolution of electron energy is shown for each simulation. The x axis corresponds to time through the simulation going from left to right, and the energy of the particles is shown on the y axis. The colour corresponds to how many simulated particles are in each energy bin for each time stamp. This shows that the density profile (top row) has electron injected at lower laser energies (from 200 mJ) than the self injection (bottom row) simulation (from 700 mJ). This reduction in required energy for electron injection is important for realising applications. Applications required a high repetition rate, and building high repetition rate laser systems is easier with lower energy pulses as issues such as heat management are easier to manage. The petawatt

class lasers that are coming on-line shortly have a repetition rate of ∼Hz [24, 135, 136] whereas a terawatt laser can run at ∼kHz [160].

The top row of Figure 5.5 shows that as the energy increases, passed 0.5 J, the performance of the density transition injected accelerator degrades as fewer electrons are accelerated to higher energy (≈ 50 MeV), although more total charge is injected. This is likely to be due to beam loading, where a large number of electrons are injected which then disrupts the accelerating structure of the wake [148, 149].

5.3.2 2D scan: Acceleration density and length of transition.

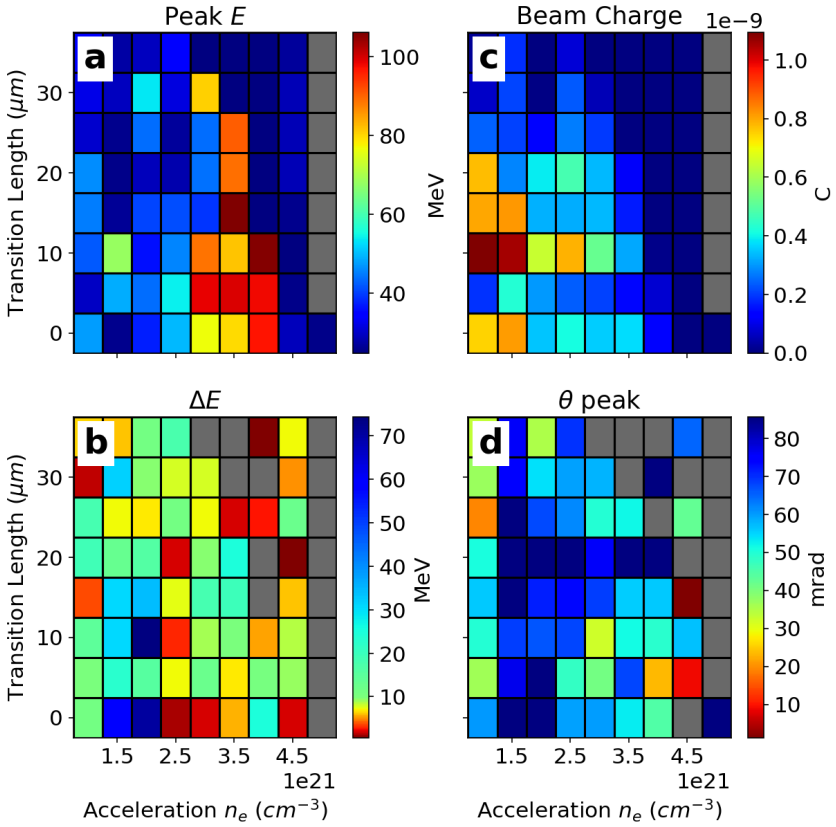

Figure 5.6: 2D simulation scan of the density profile transition length and acceleration density. A uniform profile of density 5×10^{18} cm^{-3} is included for comparison.

To explore how the density profile injection occurs, a 2 dimensional scan was conducted varying the length of the transition and the acceleration density (Figure 5.6). Previous

work shows that the sharpness of the transition needs to be of the order of the plasma wavelength [69, 70], which for these densities was of the order of 10 µm. The simulations showed that for t_l >100 µm, no electrons are accelerated to above 1 MeV.

Figure 5.6 (a) shows that there was a clear peak in electron energy for a transition down to $3.5 \times 10^{18}\,\mathrm{cm}^{-3}$. Increasing the size of the density difference increased the beam charge (Figure 5.6 (c)). The larger the beam charge the lower the energy (Figure 5.6 (a)) that the electron bunch is accelerated. Pathak *et al* explain this as the accelerator having a constant efficiency from the principle of conservation of energy [161]. The larger the accelerated charge the lower the energy gain. Beam loading could also describe this reduction in peak energy [148, 149], where the electric fields in the wake are reduced by the field of the injected charge. The energy spread (Figure 5.6 (b)) roughly remains <20 MeV, for most of the electron beams, indicating that the injection method may have an inherently low energy spread, with the median for (Figure 5.6 (b)) being 9.2 MeV.

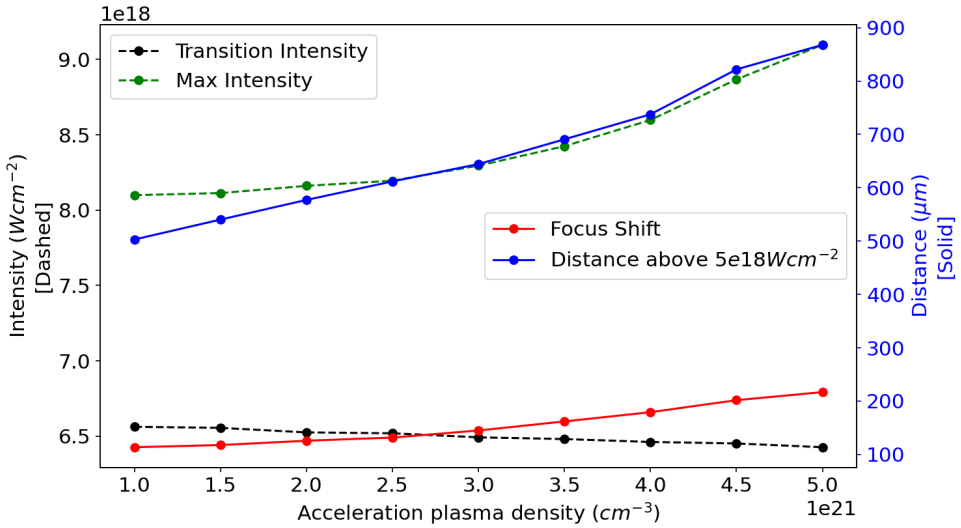

Figure 5.7: The laser pulse evolution for the 2D scan of transition length and acceleration density (Figure 5.6). The Rayleigh length for the laser pulse is 390 µm.

The evolution of the laser pulse is shown in Figure 5.7. Here the laser intensity on the transition is effectively constant, but the peak intensity increases with the acceleration density. This is expected as the self-focusing mechanism is stronger, with the acceleration

of the in spot width $\propto \frac{n_e}{n_c}$ [55]. Therefore, at higher densities result in a smaller focal spot. This means that the wake is driven by a higher a_0, which in turn means that the dephasing length has increased, allowing more energy gain [64]. The peak in electron energy (Figure 5.6 (a)) indicates there is an optimum between the density drop for injecting electron into the wake, and the evolution of the laser pulse to drive the electrons to a high energy.

The divergence of the beam (Figure 5.6 (d)) is far larger than expected with the average around 40 mrad. Schmid *et al.* experimentally measured a divergence of 9 mrad [69]. The simulation finished at 3 mm at the acceleration density. This larger than expected result maybe due to the simulation finishing with the full plasma density, instead of decreasing down to vacuum (Section 2.6.3 shows a decreasing density ramp damps the transverse oscillations).

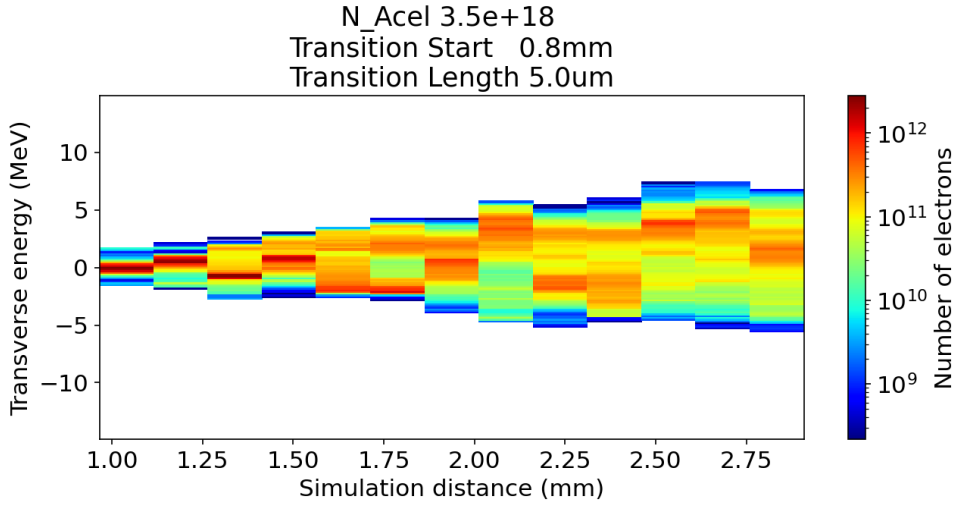

Figure 5.8: The evolution of the electrons' transverse energy through the simulation from the point of injection into the wake. Here the positive and negative energy are used to distinguish between the direction of the particles.

Figure 5.8 shows the evolution of the y momentum (p_y) from the point where the electrons were injected. The peak electron number is seen to oscillate indicative of the betatron oscillations. It also shows the p_y is increasing with propagation distance. If the

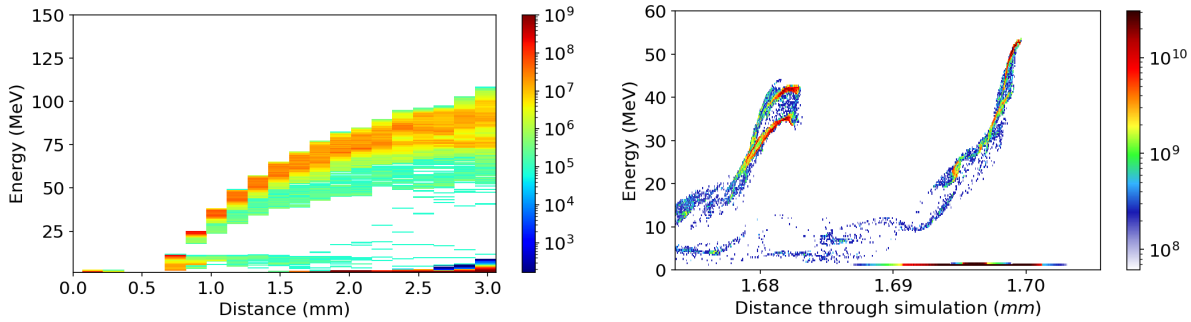

(a) (b)

Figure 5.9: Examples of an EPOCH simulation outputs for a LWFA with a density transition. (a) The evolution of the electron beam energy with respect to distance through the accelerator. (b) The x p_x plot for the final simulation time step. The two region of high numbers (x =1.68 mm and 1.7 mm) of electrons means the injection has occurred in two plasma buckets.

initial injection occurs on the laser beam axis, then p_y should remain ≈ 0 for the whole simulation as the bunch will not see transverse fields.

An example of the evolution of electron momentum from one of the individual simulations is shown in Figure 5.9 (a). This shows that the electrons are injected into the wake at the density transition, as expected. In the case of the largest density difference, the injected electrons do not all get uniformly accelerated from the initial injection leading to a large energy spread. The flattening of the curve in Figure 5.9 (a) indicates that the electrons are dephasing as the rate of acceleration is decreasing with distance through the simulation. The splitting of the curve at the end indicates that there are multiple electron bunches. Figure 5.9 (b) shows the energy of the electrons (from p_x) in each position bin (x). This shows that there are two wakefield buckets in which injection has occurred (only two were simulated) from the transition across the density profile. The second bucket (1.68 mm) also has two individual bunches in. This is detrimental to the production of mono-energetic electrons, as it is unlikely that each bunch is accelerated to the same energy.

5.3.3 2D scan: Position of transition and length of transition.

Looking at how the stability of the beam is effected by position of the transition with respect to the laser focus was investigated. The focus spot of the 800 nm light in vacuum was 20 µm, with a Rayleigh range of $\mathcal{Z}_R = 400\,\mu m$. The transition point was moved in the region $\pm\frac{1}{2}\mathcal{Z}_R$ about the focus position.

Figure 5.6 shows that there was an optimum density difference for accelerating to high energies for this system, 5×10^{18} to $3.5 \times 10^{18}\,cm^{-3}$, and this was used for this 2D parameter scan (Figure 5.10).

Figure 5.10 shows that moving the transition point to before the laser focus (-ve on x axis) increases the peak energy (Figure 5.10 (a)) of the beam. This increase is likely due to the following reasons. Firstly, moving the injection point before the laser focus increases the distance the electrons travel in the acceleration region. Secondly, the laser remains highly focused for a longer distance (∼730 µm from Figure 5.10 (h)), meaning that the wake was strongly driven for a longer distance compared with the transition occurring after the focus. The dephasing length for $a_0 > 1$ scales as quadratically with a_0: $4a_0^2\frac{n_c}{n_e}$ [64]. For the different peak intensities reached, the dephasing length would increase by 20% when changing from −200 µm to 350 µm. However, as the pulse was more intense for longer for a transition point −200 µm before focus, the dephasing length may be longer for this case. The peak in the electron energy (Figure 5.10 (a)) at −150 µm indicates that the longest dephasing length occurred for this length.

The shifts in position for this scan are of the order of a $\mathcal{Z}_R$. This means that in vacuum the laser will still be highly focused at the transition point (Figure 5.10 (f)). The self-focusing effect is stronger at higher plasma density, so the longer the region of high density the pulse has propagated through the smaller the focal spot, and therefore, the more intense the laser pulse is expected to be. This also couples with the vacuum focal position being at $t_p = 0$, so the pulses intensity will be increasing up to this point even without any self-focusing. Figure 5.10 (f) shows that the highest intensity occurs on the transition placed 200 µm after the vacuum focal plane. Figure 5.10 (g) shows that for the transition point before the vacuum focus (-ve) the focus does not occur until a

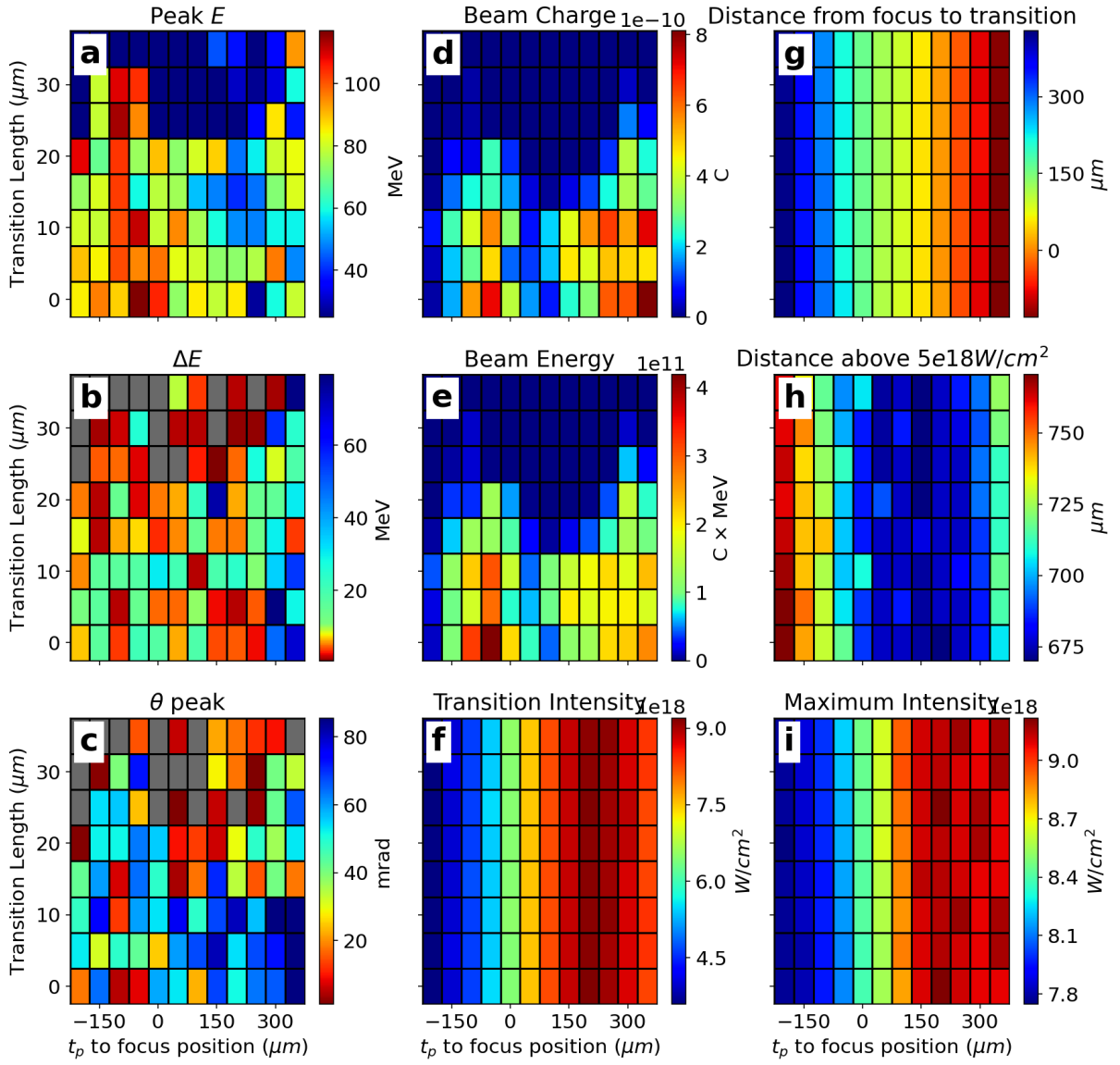

Figure 5.10: 2D simulation scan of the density profiles transition length and position Grey points are where the fitting did not succeed. Moving the transition point in the negative direction increases the length of the accelerating region.

few 100 µm after, meaning that the whole injection does not happen at peak intensity. However, Figure 5.10 (h) shows that the length of the high focus is longer for these shots too. The beam charge, Figure 5.10 (d), shows that there are two regions that produce high charge beams. The negative focus position peak occurs when the transition occurs at a lower intensity compared with the positive focus peak. This is indicating that for

charge there is some interplay between the transition intensity and the duration of the laser focus.

The energy spread of the injected electron beam is small when the transition length is >20 µm (Figure 5.10 (b)). However, when comparing the energy spread to the beam charge (Figure 5.10 (d)), this region does not have a large charge injected, indicating that this is not a useful region of space in which to operate. For a small energy spread of an electron beam with reasonable charge, this is seen from a sharp transition (<10 µm) with the density transition either occurring 50 µm before the vacuum laser focus, or 150 to 250 µm after. The median energy spread is 9.2 MeV.

5.3.4 Moving towards more realistic profiles

The initial simulations (Sections 5.3.2 and 5.3.3) show how the changes in a trapezoidal density profile effect the electrons. However, this is a profile shape that is unlikely to be found experimentally. Figure 5.11 shows the comparison of 4 different profiles. The trapezoidal and the sharp (an extreme case of the trapezoidal profile) have been examined in the previous section. The addition of the Gaussian and a fluid simulation (Section 5.5) of a density profile show a more realistic profile. The different profiles describe a similar shape, but a large effect is seen in the electron energies.

It is therefore, important to have a good method of understanding the profile that is produced and the laser properties around the transition region.

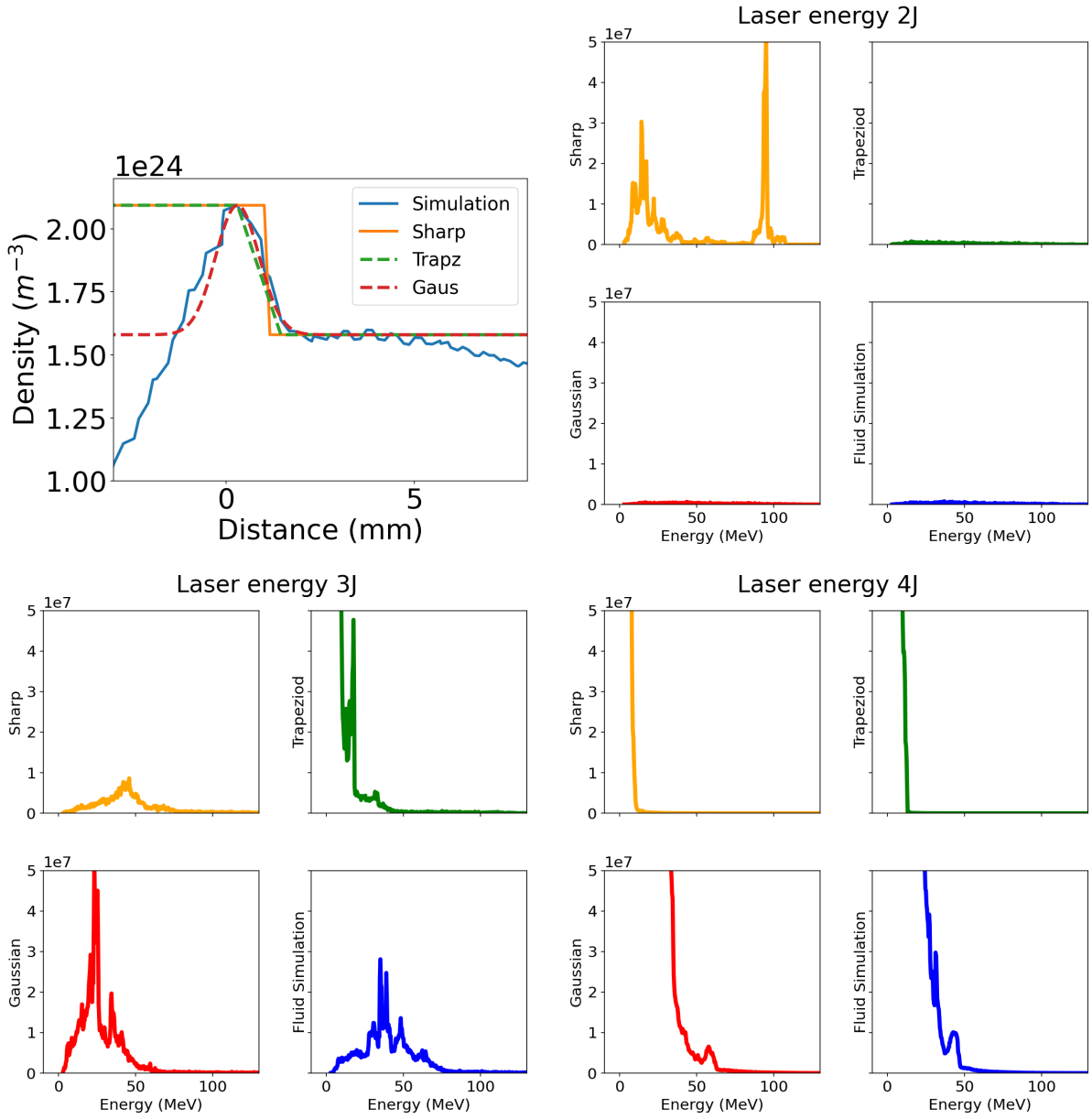

Figure 5.11: The effect of different shaped density profiles on the electron spectrum for different laser energies.

5.4 Experimental density profile injection

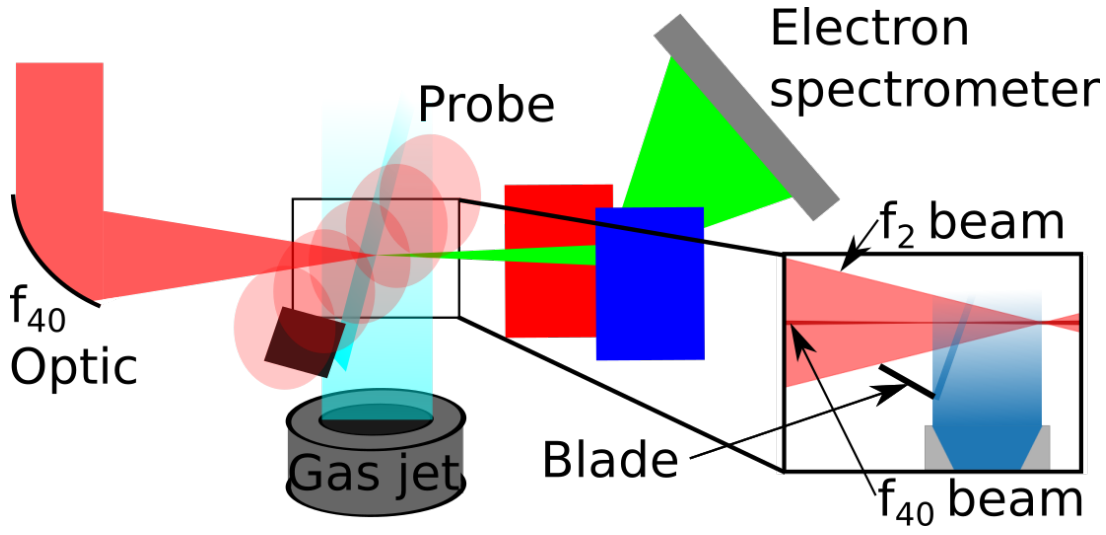

Figure 5.12: Experimental setup for density profile injection, with a transverse probe to measure the plasma density, and an electron spectrometer to measure the electron energy. The inset plot of the interaction point shows the spatial constraints caused by the second laser focused with an f_2 optic, which was required for the experimental aim of measuring radiation reaction. The gas jet had an opening diameter of 15 mm, with the blade at 14 mm above the nozzle.

The experiment was conducted in the Target Area 3 of the Gemini laser facility in the Central Laser Facility at the Rutherford Appleton Laboratory. The laser pulse (12.5 $\pm$ 0.2 J, 61 fs FWHM) with a peak power of 200 TW was focused using an f_{40} parabolic mirror into a gas jet inside the vacuum chamber. An adaptive optic was used to flatten the phase front and create an approximately Airy focal spot distribution with a spot width of 48.6 µm $\times$ 39.2 µm FWHM, resulting in a peak normalised vector potential of $a_0 \sim 2.5$ in vacuum.

A schematic of the experimental setup is shown in Figure 5.12. The density profile was created using a gas jet with a razor blade inserted into the flow. The supersonic gas jet was created using a conical nozzle, backed with a gas pressure of 100 bar, producing an approximately flat topped density profile for a horizontal laser path through an uninter-

rupted flow [162]. The conical nozzle had: an inlet diameter of 1 mm; a height of 23 mm; and an exit diameter of 15 mm. The aim of experiment was looking for radiation reaction, which to measurably occur requires $\gamma_e E \sim E_{cr}$, where $E_{cr} = m_e^2 c^3/\hbar e = 1.3 \times 10^{18}\,\mathrm{Vm}^{-1}$ is the critical field of quantum electrodynamics, m_e is the mass of an electron, e the charge of an electron, c the speed of light, $\hbar$ the reduced Planck constant, γ_e is the Lorentz factor of the electrons and E is the electric field [134]. To create a large electric field a second laser beam was focused using a f_2 optic, which created a spatial constrain on the blade position so the expanding beam after the interaction did not hit the blade. Therefore, the nozzle was positioned 14 mm below the laser beam height, allowing space for the blade mounted perpendicular to the laser axis 4 mm above the nozzle exit without being struck by the second laser beam. The blade was at fixed angle of $(32.4 \pm 0.3)^\circ$ to the horizontal plane, with the aim of having the shock normal to the laser propagation axis. The density transition occurs as the supersonic gas flow from the nozzle cannot adapt to the obstruction of the blade upstream. This creates a density build up with a transition width of the order of microns. An advantage of this method is that by moving the position of the blade the lengths of the two main regions, the high density initial region, and the low density accelerating region can be altered, which creates a tunable electron spectrum [72]. A disadvantage is the thin blade can be deformed by the force of the gas incident on it.

The energy of the electrons was measured with an electron spectrometer, Section 3.3.1. The plasma electron density was measured using a transverse probe, Section 3.3.2, with the light coming through a leakage mirror. The first lens after the interaction was 1000 mm focal length, and 100 mm diameter lens ($f_\# = 10$), putting a maximum resolution limit of 20 µm on the imaging system. The plasma was probed transversely, with both shadowgraphy and interferometry data collected. The interferogram had each fringe resolved with 15 pixels.

5.4.1 Results

A z scan of the blade found the highest peaked electrons with the blade inserted 1 mm into the gas flow, where the z axis is in the laser propagation direction. The electrons

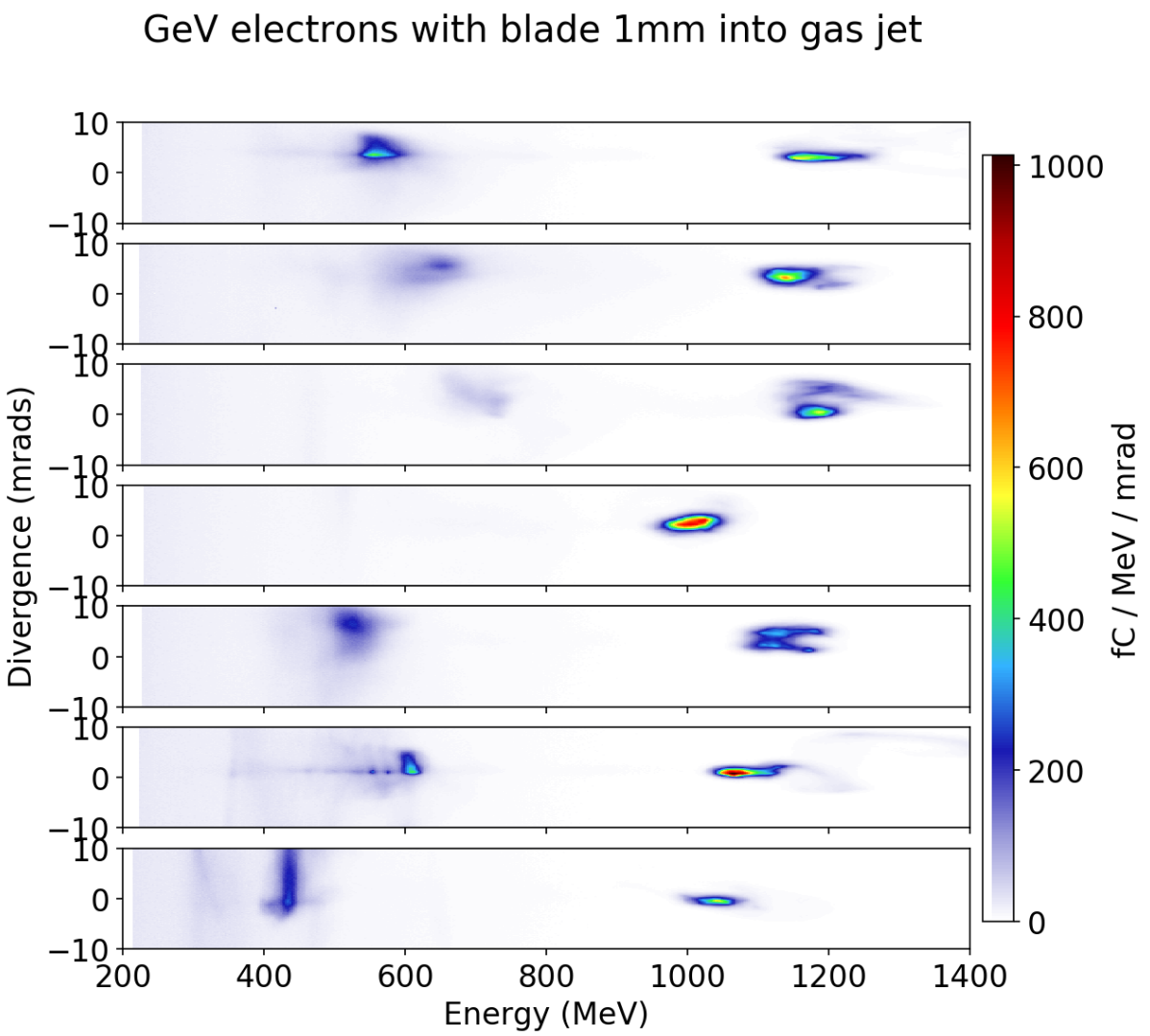

Figure 5.13: Experimental Electrons showing peaks at GeV level. Data extracted from electron spectrometer by Dominik Hollatz.

produced at this position are shown in Figure 5.13. The experimental conditions were kept constant for the data shots in Figure 5.13 and these shots show two characteristic electron bunches, one high energy 1-1.2 GeV and one lower energy 400-700 MeV. The average peak energy of the high energy bunch was 1.1 GeV, with an energy spread of 67 MeV or 6%. The highest energy bunch created had 1.185 GeV with an energy spread of 5%.

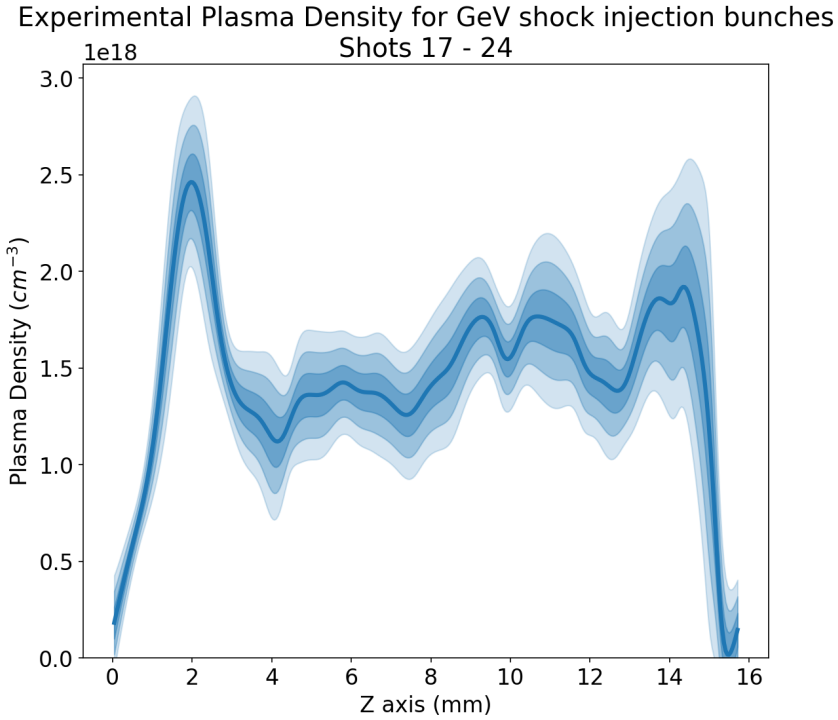

Figure 5.14: Interferometry density data, with each line being 1 standard deviation.

The experimentally measured electron density profile is shown in Figure 5.14. The method of extracting the density from the interferogram assumes symmetry, but this may not be true at the shock front. Therefore, the exact shape of the density transition is still unknown. The peak caused by the blade in the gas flow is seen at $z = 2\,\text{mm}$, and followed by a plateau region at $1.5 \times 10^{18}\,\text{cm}^{-3}$. The transition region (2 mm) from this figure is long in compared to the plasma wavelength at this density ($\sim$20 µm). The shock that forms close to the blade is a bow shock, but for more than glancing blade interception the shock the laser interacts with is an intercepting shock [163]. This is the shock formed from a pressure boundary between the plume and local ambient pressure. The insertion of the blade into the flow creates a virtual sonic nozzle, with a redirected angle [163]. This explains why the interferometry measurement increases towards the $z = 15\,\text{mm}$.

The simulation study presented in Section 5.3 indicates that Figure 5.14 cannot be the shape of the plasma around the shock location, as the transition length is too large.

Therefore, simulations of the density profile formation are required to fully understand this.

5.5 Fluid simulations of density profile

Fluid simulations of the formation of the density transition created by a knife blade in the supersonic gas flow were conducted. Figure 5.15 shows the comparison between the experimental, and the two simulation codes (openFOAM [127] by the author and FLASH [164] by Robbie Watt) used to model the system. In Figure 5.15 the width of the plasma

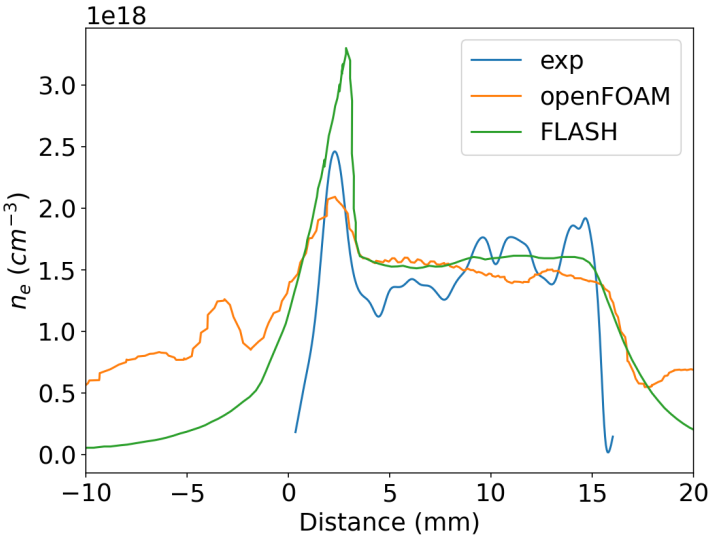

Figure 5.15: The different methods of calculating the density profile of the plasma. Experimental data was extracted from the interferometry, and two fluid codes (openFOAM and FLASH) simulation results. FLASH simulation data provide by Robbie Watt from Imperial College.

for all 3 methods is roughly the same, at 15 mm. This corresponds to the width of the nozzle and for supersonic gas jets with no blade produce a top hat profile with the width of the nozzle [162, 165]. The density profile created by openFOAM was scaled to the experimental data by matching the average plateau density for the openFOAM and the interferometry profile.

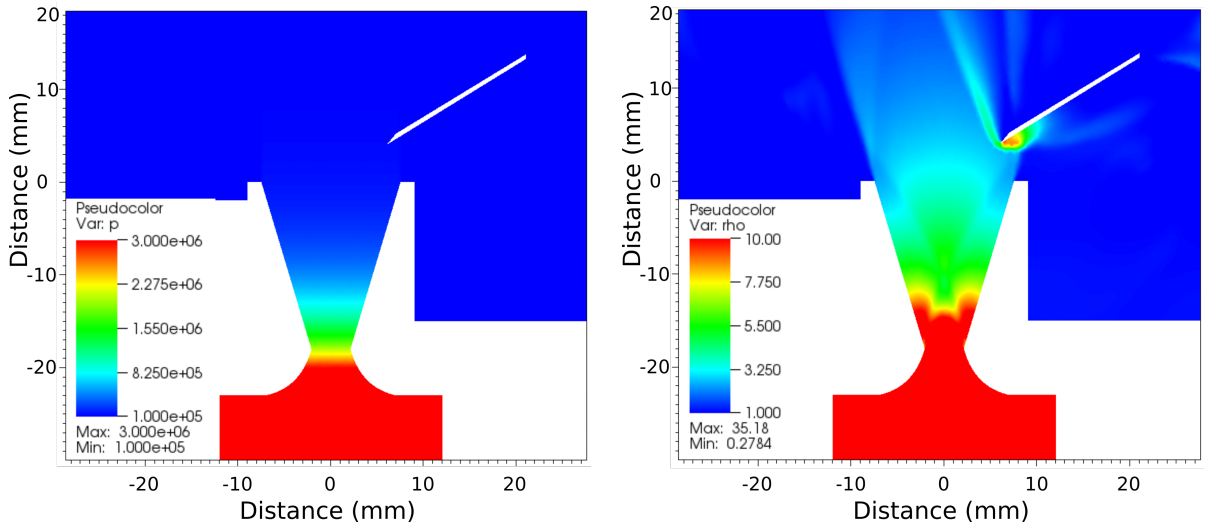

Figure 5.16: OpenFOAM gas jet and blade simulation. (a) The initial pressure profile in the gas nozzle. (b) The density profile produced by the blade in the supersonic flow.

5.5.1 OpenFOAM

The fluid code openFOAM was used by the author to model this set-up. OpenFOAM was chosen due to it being open source. The code was not completely suitable for the task, as it both struggled to simulate large pressure gradients and vacuum conditions. Experimentally the nozzle was backed with a pressure of 100 bar into a vacuum chamber of around 10^{-5} mbar. Figure 5.16 shows the input pressure into the simulations and the resulting density profile that is produced. These simulations of the nozzle and blade were performed in 2D slab geometry, as a 3D simulations was too computationally expensive. A comparison between 2D slab geometry and 2D cylindrically symmetric around the nozzle axis for a nozzle with no blade was performed (Figure 5.17). This showed that the shape of the density profile remained the same between the two geometries, although the density reached for the same inlet pressure was higher for the slab geometry case. This is expected as there is a larger surface area of nozzle to volume for the cylindrical (true) case. Simulations also showed a linear relation between input pressure and density profile

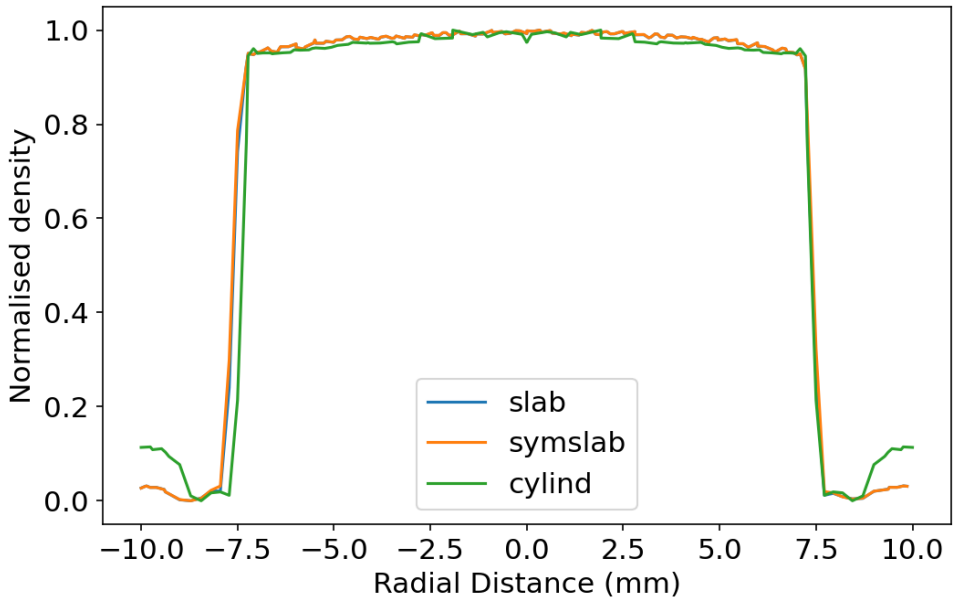

Figure 5.17: Comparison of the density profile created by different simulated geometry of the nozzle. The cylindrical geometry is the same as a 3D simulation for a symmetric nozzle around it's axis. 2D geometry was used for the nozzle blade simulations. The density line-out was taken at the same height horizontally across the nozzle.

formed. This allows scaling of a given profile created by a given backing pressure. For a backing pressure of 3×10^6 Pa the density profile was created in the order of 100 µs from the start of the simulation. The simulations show the density is then in an approximately steady state.

OpenFOAM has different solvers depending on the situation [127, 166]. The solver "rhoCentralFoam" was used, as the Mach number was between 0-4 in the simulations. The solver "sonicFoam" was also investigated, although this crashed at earlier time steps.

Mesh grids, boundary conditions and starting parameters were altered, but the largest pressure gradients that could be handled were around 30×. Therefore, to simulate the high backing pressure of the gas jet, the background pressure of the chamber had to be increased. The effect of the simulation code failure to simulate the experimental values was examined: Figure 5.18 shows a scan of background pressures on the simulated density

profile the laser interacts with for a fixed inlet pressure. Here is clearly shown that the

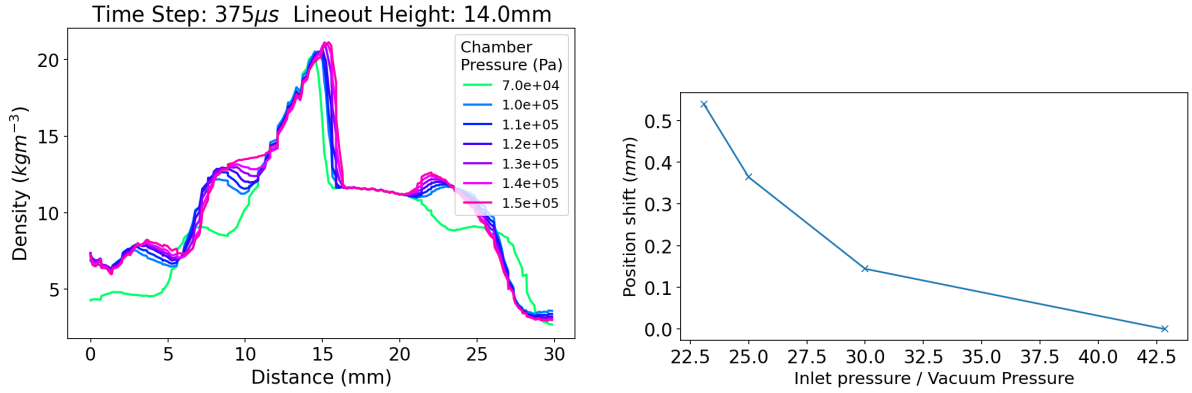

(a) (b)

Figure 5.18: The effect of the backing pressure of the openFOAM simulation with a blade at 0°. (a) The density profile produced with different "vacuum" pressures. (b) The amount of shift in shock position for different backing pressures.

effect of the chamber pressure is seen in the region below 10 mm and above 20 mm. The region between these points is the region of interest, and this does not show a large change with background pressure. The steepness of the transition is the same, although the point at which the transition occurs does move slightly. The Rayleigh length of the Gemini laser focused with an $f_{\#}40$ is 1.6 mm so the shift (Figure 5.18 (b)) is small in comparison. The peak height and the plateau region stays almost constant for the pressure ratios investigated. As only the region near the density transition is of interest, and this is not affected by the simulated chamber pressure, it is possible to continue with this code.

A study of how the input pressure changed the density profile was conducted. The results (Figure 5.19) show that the shape of the profile does not change with input pressure. For this data the pressure ratio between the inlet and background regions was kept constant 20 times larger than the background.

A 2D mesh of the nozzle was created (Figure 5.16). The simulations could not cope with the exact parameters of the nozzle (Section 5.4) so the input mesh was modified. The wall angle of the nozzle was kept constant, and the throat was moved up the nozzle

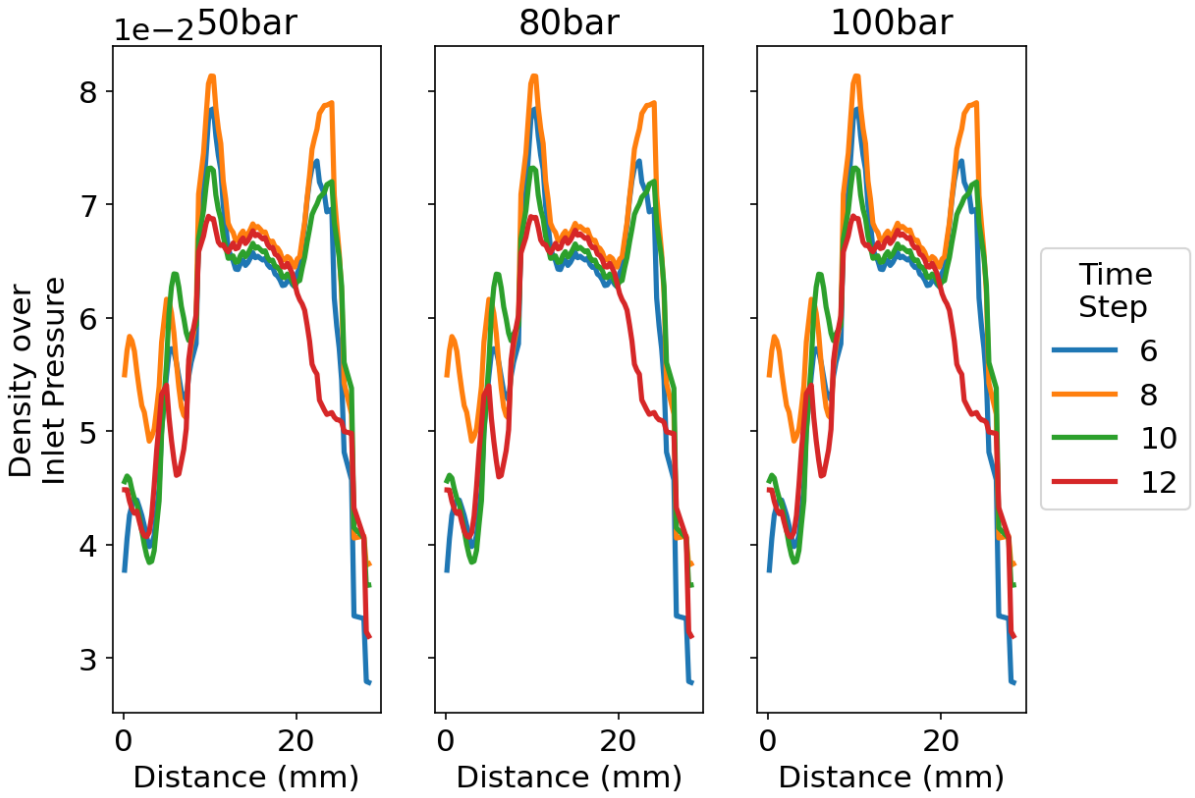

Figure 5.19: The simulated density profiles at the laser height for a range of input pressures. The density profile has been normalised by dividing by the input pressure. The normalised density profile remains the same across this pressure range.

making the entrance larger. This reduced the compression of the gas, and therefore the exit velocity of the gas. The nozzle that reached a steady state had an internal length of 18 mm, giving an internal radius of 2.1 mm instead of 0.5 mm.

Blade translation scans shows that there is a linear relation between the length of the high density and lower density acceleration region with blade translation over the nozzle.

5.5.2 Comments on difference between fluid codes

The problems with inputting the exact experimental parameters into openFOAM have been described above. The FLASH simulation shows a far sharper transition, and also smoother density down towards 0. The smoothness indicates that the resolution of the simulation was higher. The resolution of the openFOAM simulation mesh was set so

the density profile formed. Both an increase and decrease in resolution resulting in the simulation failing to run for long enough for the profile to form. The FLASH simulations was also conducted in 2D slab geometry, but had a higher backing pressure for the nozzle, of 100 bar.

The benefit of using openFOAM is it is an open-source code [127]. However, gas expansion into vacuum is problematic as the mean free path of the fluid particles tends to infinity as the density tends to zero, and the solvers available are not optimised for this problem. OpenFOAM uses an Eulerian mesh frame work and an extension to this work would be to add the adaptive mesh frame work. However, there is not currently a dynamic mesh solver for 'rhoCentralFoam', the solver that was deemed most applicable to this work. FLASH, an open radiation MHD simulation code [164], is not open-source and is computationally expensive due to its ability to solve far more complex processes than fluid dynamics. However, its adaptive mesh and Lagrangian framework mean it can resolve the sharp transition more effectively.

From the experience of this work, I would strongly recommend **not** using openFOAM to simulate gas flow from a nozzle onto a blade.

5.5.3 No moving parts density profile creation

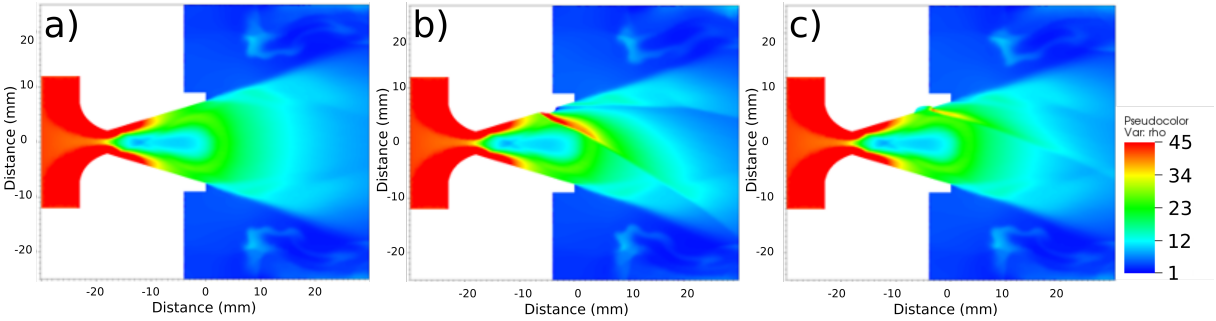

Figure 5.20: Density profiles created by nozzles with internal features in openFOAM. Simulations performed in 2D slab geometry. (a) Standard Nozzle, no feature. (b) Additional material feature. (c) Missing material feature.

Creating density profiles with a blade in the flow is problematic as the force of the gas on the thin blade causes it to deform. The deformation maybe either reversible, so the blade remains in the same final location for each shot, or irreversible leading to the blade position changing from shot to shot. If the latter is occurring, then the density profile will be changing and therefore, the electrons will not be as stable. If the laser is not at a normal incident angle to the shock, it will be steered [71], leading to a pointing shift of the produced electrons. Figure 5.20 shows a potential method of producing a density profile with no movable components. Here a sharp density profile is created from an internal feature in the nozzle. Both features, either the addition of material (b) or missing material (c), show the formation of a shock feature that is now inherent to the nozzle. Work is required to see whether in 3D this still has the same effect. If so, once a density profile is found that causes the electron beam features required, a static nozzle can be designed to create this profile. This would be advantageous over a gas cell as the nozzle would not degrade due to ablation of aperture material.

5.6 Examining GeV beams with PIC simulations

The FLASH, openFOAM and interferometry density profiles were used as the input to a 2D PIC (EPOCH [121]) laser wakefield simulation, with all other simulation parameters kept constant. The laser is focused at the start of the simulations, as experimentally the laser was focused on the front edge of the gas.

Convergence testing on these 15 mm simulations found that 28 cells per wavelength and 16 particles per cell were required, which allowed simulations to be run in sensible times (1-2 weeks). Increasing the resolution above this level changed the total number of electrons injected, but the shape of the spectrum produced was stable.

Figure 5.21 shows the 3 different profiles and the electron energy evolution through the simulation. In all 3 cases the injection occurs at the position relating to the start of the density plateau. In the PIC simulations using the fluid simulations' density profile (Figure 5.21 (b&c)) injection occurs from the beginning of the simulation, before the laser pulse has reached the density transition. This seems to be due to the higher plasma density at which the simulations starts. In all 3 cases the initial acceleration shows an energy gain of 150 MeV/mm, which over the remaining 13 mm this would provide enough acceleration to reach ∼2 GeV if no dephasing occurred.

The PIC simulations using the openFOAM and interferometry density profile show dephasing has occurred at a short distance into the simulation, ∼4 mm. At 6 mm for the openFOAM profile, and 7 mm for the interferometry profile, the electron bunch overlaps with the laser pulse, which scatters the electrons in phase space [3]. This interaction with the laser pulse increased the energy spread of the electron bunch. Therefore, the experimental electrons (Figure 5.13) cannot have dephased enough to interact with the laser pulse, as all the spectra produced have a $< 10\%$ energy spread.

The FLASH profile simulation, due to its higher initial density, has a stronger self-focusing effect on the laser pulse, increasing the a_0 of the pulse and hence the dephasing length [64]. The electron accelerated in the wake reach energies of ∼600 MeV, compared to

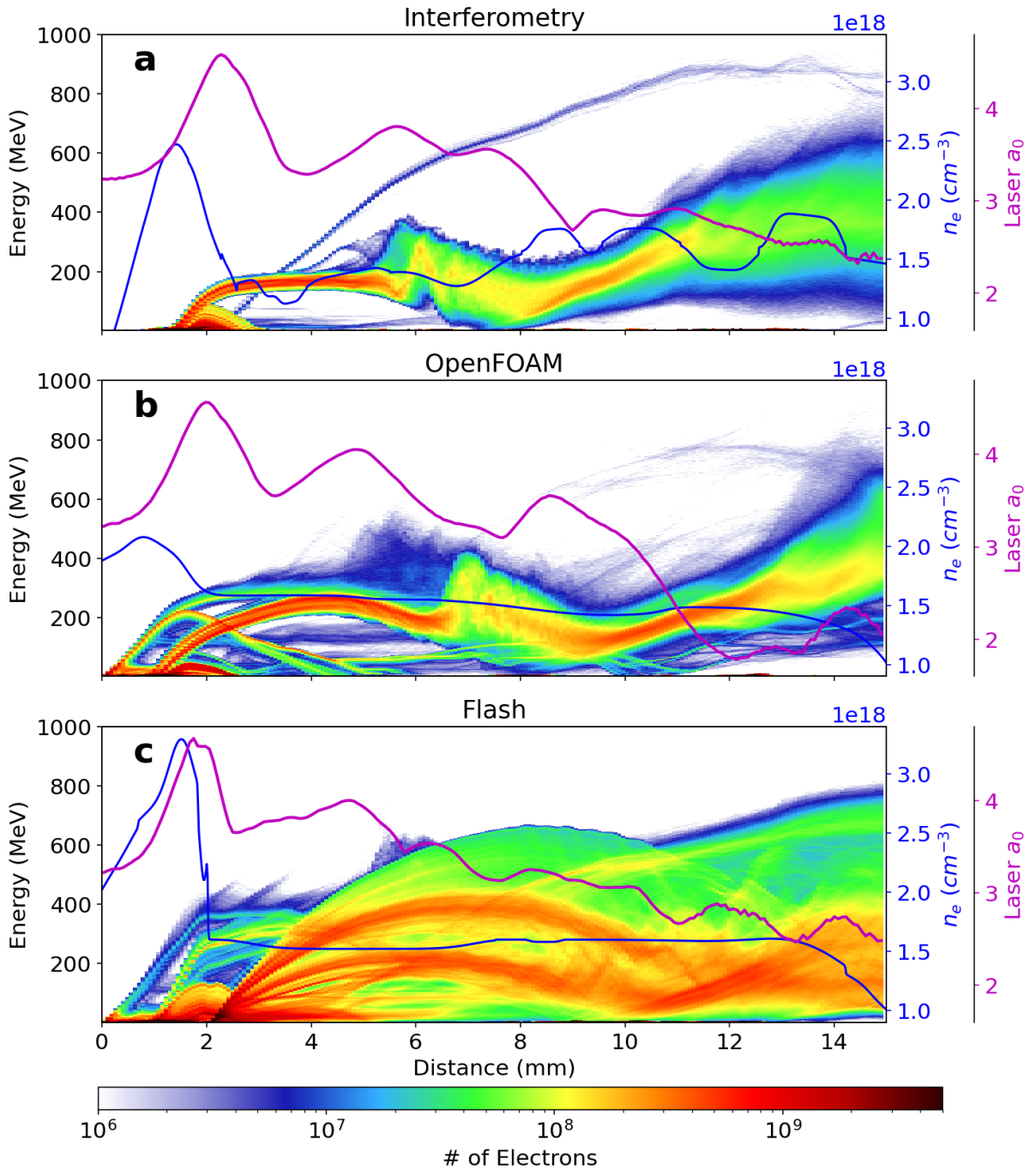

Figure 5.21: Comparison of the 3 different options for the density profile from the experiment. The non-perturbed plasma density (blue) is shown for each case. The laser field (purple) is extracted from the simulation, averaged over the central 20 µm of the wake.

200 to 300 MeV for the other profiles. However, the other profiles show that the injection leads to a far narrower energy spread electron beam.

Figure 5.21 (a & b) show the injection of electrons in with a narrow energy spread. Figure 5.21 (c) shows the acceleration to higher energies. The experimental electrons had both high energy and narrow energy spread. The high charge, but narrow energy spread, in the experimental high energy bunches indicates that the injection must have caused a lot of electrons to enter the same accelerating region of phase space at once. The FLASH profile simulation (Figure 5.21 (c)) shows a more continuous injection than occurred experimentally.

The simulations in Figure 5.21 were conducted in the 2D version of EPOCH. The self-focusing of the laser pulse in 2D will be less intense than in 3D, as it is only focusing in one dimension instead of two, meaning the laser evolution is weaker [167]. This means the 2D simulation will reached a lower overall a_0 compared to a 3D case, and hence the dephasing will occur at a shorted distance [64]. This effect cannot be compensated for just by increasing the a_0 of the laser pulse in the 2D simulation, as in 2D the power required for self-focusing is lower [167]. Tsung *et al.* [168] compared the results of a 2D and 3D PIC code, and found the rate of acceleration was much lower in 2D. They also show that the required a_0 for self-injection is lower in 3D than in 2D.

The laser pulse travelling in a plasma density of $1.5 \times 10^{18}\,\mathrm{cm}^{-3}$ should travel at $0.99956c$, where c is the speed of light [52]. The laser pulse in the simulations, over the whole 15 mm, travelled at an average velocity of $0.9963 \pm 0.0003c$. The decrease in velocity of the laser pulse was due to the discretisation of the fields in the PIC code. The numerical slowing of the laser pulse decreased the dephasing length by an order of magnitude. To correct this, the simulations would required a higher number of grid point per wavelength, which would increase the time required for the simulation. The dephasing length from Lu *et al.* [64] scaling law indicates that the electrons should not dephase in the 15 mm long LWFA.

5.7 Conclusions

Experimental results show that the density transition injection mechanism can be used to create electrons with energies of ∼1 GeV. Understanding the density profile that the laser interacts with is important for understanding the injection. Here PIC simulations have shown the sensitivity of the injected electrons to the profile's shape. Experimentally accurately measuring the density profile the laser interacts with is challenging. Fan-Chiang *et al.* [163] used planar laser-induced fluorescence measurements to compare with their simulations. However, this would not work for an on-shot measurement. Tomographic imaging of the density profile can also be conducted [169]. Tomography of the gas flow would require either the nozzle to be rotated, and therefore, not suitable for on-shot measurements, or for multiple probe laser pulses which due to the spatial constraints on the experiments this is often infeasible. As blade deformation can occur, characterising the plasma target before or after the experiment would still lead to uncertainties that would need to be quantified.

PIC simulations to reproduce the 1.2 GeV electrons seen experimentally did not recreate the narrow energy spread observed. This is likely due to the difference in dephasing length between experiment and 2D simulations, as the PIC code has not captured all the processes correctly. The resolution of the converged simulation in 2D EPOCH, when simulating the 15 mm plasma target took ∼48 000 cpu-hours. Running in 3D EPOCH is clearly infeasible due to the computational time that would be required. The long run time also prevented simple simulation scans occurring, such as increasing the laser a_0, to see whether 2D versus 3D effects could be compensated for. The 2D PIC simulations presented here have injection in the initial high density region, which was detrimental to the mono-energetic features of the spectrum. They also show the dephasing occurred when the electrons bunch had propagated only a fraction of the length of the plasma. A potential solution to this would be using a quasi-cylindrical PIC code, such as FBPIC [170] or QuickPIC [167]. FBPIC has been specifically designed for the simulation of accelerated particle beams and wakefield acceleration.

6 | Optimisation of electron beams using multiple input parameters

In this chapter the results are presented from a laser wakefield accelerator (LWFA) optimisation experiment at Target Area 2 (TA2) of the Astra-Gemini laser at the Central Laser Facility.

The aim of the experiment was to show that the performance of a LWFA could be improved by deploying a Bayesian optimisation algorithm. The experimental setup was automated, with computer control of six input parameters to the LWFA formed of: the laser pulse shape (three parameters); focus position (one parameter) and plasma target (two parameters). The diagnostics were setup such that some metric of success (extracted with a fitness function) of the resulting electron or X-ray beam could be measured as a single number. Using a Bayesian optimisation algorithm a multi-parameter space was efficiently explored to find the global optimum.

The data extraction routines from each diagnostic were written collectively by the experimental team. The author led the plasma density retrieval section of this code.

Elements of this work are published in Shalloo *et al.* [36].

6.1 Experimental setup

The experiment was conducted at TA2, with a setup shown in Figure 6.1. The laser (Ti:Sapphire) was focused with an $f/18$ off-axis parabola creating a minimum spot radius ($1/e^2$) of 16 µm, and a spectrum centred around a wavelength of 800 nm. To produce

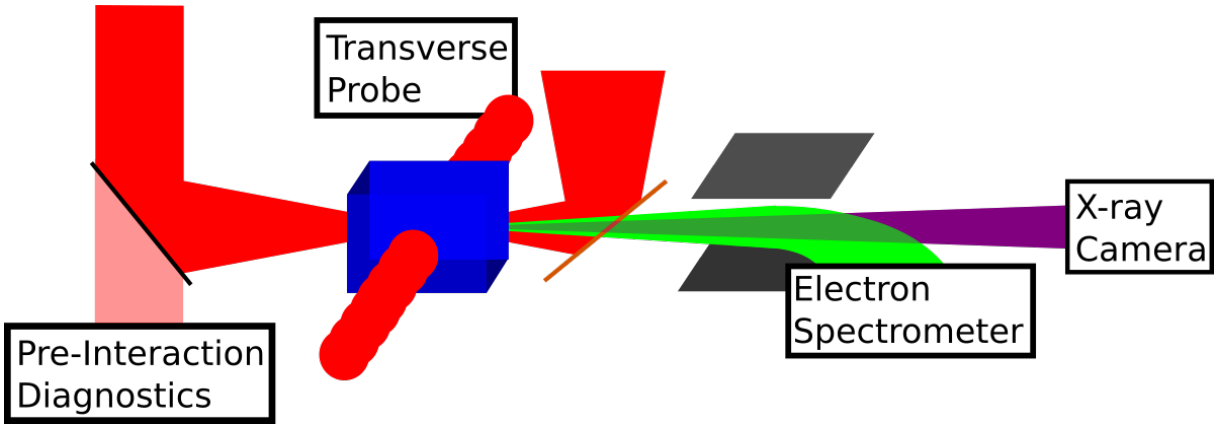

Figure 6.1: Experimental setup for the TA2 optimisation experiment. Here the red represents the laser pulses, the main pulse and the transverse probe. Prior to the interaction, through the leakage of a dielectric mirror, the main laser pulse was characterised. The plasma target (blue) was a gas cell with a variable length up to 5 mm. After the interaction there was a tape plasma mirror reflecting the remaining laser beam onto a beam dump. The electrons (green) and betatron X-rays (purple) were measured after the interaction. The electrons travelled between 75 and 93 cm from the plasma target to the Lanex screen of the electron spectrometer depending on their energy.

the best focal spot the laser wavefront was flattened using an adaptive optic (AO) and a wavefront sensor (HASO [100]) in an iterative loop. The laser energy varied over the course of the experiment between 200 to 400 mJ at the target, with a pulse duration of ~45 fs, giving the laser system a peak power of approximately 5 TW. The laser repetition rate was 1 Hz for this experiment. Obtaining data at 5 Hz was explored but the laser was found to be unstable operating in these conditions. This was thought to be because the laser pulse compression gratings suffering from heat-induced deformations due to the increased fluence of the 5 Hz laser beams.

The laser pulse was measured on-shot with pre-interaction diagnostics. These measured the wavefront (HASO [100]), the temporal pulse shape (APE Spider [103]) and the laser energy on target. A laser pulse originating from the main laser pulse was used as a transverse probe. This probe was used to measure the plasma density inside the gas

cell, using a folded wavefront interferometer, when the cell length was >1.7 mm. The gas cell length was changeable up to 10 mm, achieved by translating the rear aperture. The interaction occurred inside a differentially pumped chamber to allow the main chamber pressure to remain low ($\sim 10^{-5}$ mbar) while operating the gas cell at a high repetition rate. The remaining laser energy was extracted from the beam path using a thin tape, acting as a plasma mirror, directing the light onto a laser beam dump.

Control of the input parameters to the LWFA were automated, with control over the following six parameters. The plasma target had control over the inlet gas pressure, and the length of the cell (two parameters). The focal plane of the laser was altered using the AO (one parameter). The pulse shape was modified using an acousto-optic modulator (AOM) in the form of a Fastlite Dazzler [98], which is a form of acousto-optic programmable dispersive filter (three parameters). This gave control over the 2^{nd}, 3^{rd} and 4^{th} order spectral phase (β) of the laser pulse, which also changed the temporal shape.

The electron energy was measured using a magnetic spectrometer consisting of a permanent dipole magnet (Section 3.3.1), with a peak magnetic field of 558 mT and total length of 410 mm, and scintillating Lanex screen imaged with an optical camera (Allied Vision Manta [146]). The energy range of the spectrometer was 26 to 218 MeV. The second dimension on the Lanex screen gave information about the divergence in the non-dispersive direction (Section 3.3.1). The following beam characteristics were extracted from the spectrometer: electron beam charge (summing all counts on the Lanex); electron beam energy (multiplying counts by their energy); cut off energy (energy of beam below which 95% of the charge is measured); and divergence (divergence weighted by charge). These values were only calculated for the electrons in the range of the spectrometer. The X-rays created through betatron oscillations were diagnosed with a direct detection X-ray CCD (Andor iKon-M 934 [108]).

The data was taken in a format defined by shots, bursts and runs where an individual shot corresponds to the data from one laser pulse, a burst corresponds to 10 shots taken at the same input parameters to measure the fluctuation in the data, and a run corresponds to

a collection of bursts which are related in some-way, e.g. a pressure scan or an optimisation of a given output parameter such as electron beam charge.

6.2 Plasma density extraction during the experiment

The transverse probe allowed measurement of the plasma density with interferometry, using a Michelson interferometer (Section 3.3.2). This was chosen for ease of timing between the two arms and its compact nature. As the probe pulse had roughly the same pulse duration as the main pulse, ∼40 fs, the difference in the path length between the two interferometer arms has to be of the order of 10 µm. However, due to the Michelson interferometer's field of view it was unable to measure the plasma density when the gas cell length was less than 1.7 mm. The field of view was limited for two reasons. The first was the need to have fringes that are close to perpendicular to the plasma channel to measure the phase shift it induced. To create interference fringes there has to be an angle between the reference arm and the measurement arm (Equation 3.13) of the interferometer. The second was due to the folded wavefront setup, meaning that the plasma channel region in one arm must not overlap with the plasma channel region of another arm on the detector. The Michelson interferometer in this setup could only cause this offset by changing the angle of the one of the arms. The code to extract the density from the interferogram is described in Section 3.7.

The plasma target had two controls, the gas cell length and the inlet gas backing pressure. A two dimensional (2D) scan of the gas cell length and cell pressure showed the relation between plasma density and these parameters (Figure 6.2). The gas inlet to the cell was triggered 50 ms before the laser pulse arrived. The density data in Figure 6.2 is the average density of the first measurable 1 mm in the gas cell. The first measurable 1 mm was used in long cell lengths, as after this length at high backing pressures the measured density showed a significant decrease. The laser pulse depletion and diffraction were the likely cause of this drop. As the laser propagated the intensity decreased due to laser depletion. The diffraction of the laser pulse also decreased the intensity. For a laser pulse that has propagated 4 mm beyond the focal plan of the $f_{\#}18$ focusing optic,

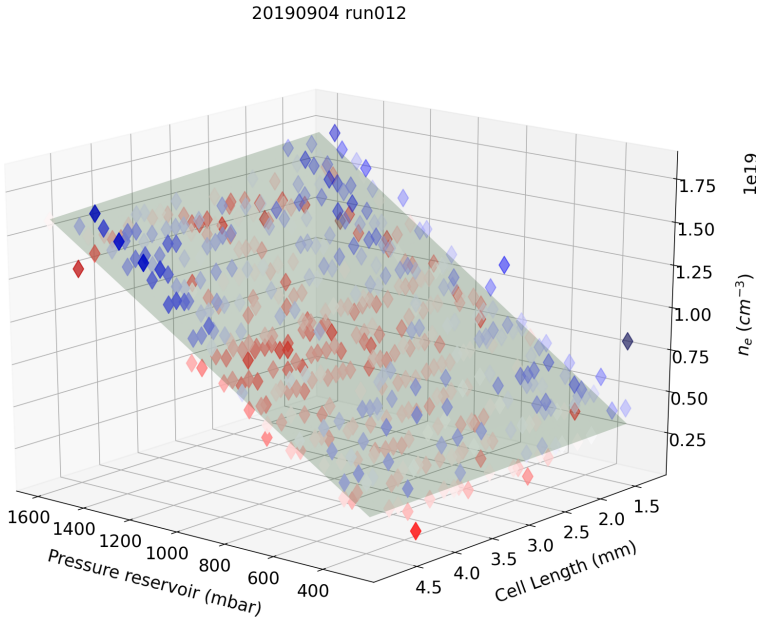

Figure 6.2: A 2D scan of cell backing pressure and cell length, and the plasma density produced. A plane fit has been applied and the colour of the diamonds shows whether they are above (red); below (blue) or on the plane (white).

the decrease in intensity will be two orders of magnitude. The drop in plasma density measured indicates that this decreased intensity can no longer fully ionise the plasma.

The planar fit showed in Figure 6.2 shows that the cell length did not have a significant effect on the plasma density, indicating that the cell fills to a steady state in the time before the laser arrives. There is a 4% difference in the plasma density between a cell length of 0 and 4 mm. The operating length of the cell was normally in the range of 1 to 2 mm, so this effect can be ignored compared to the error in the pressure to plasma density fit. For the experimental data of interest the plasma density was related to gas pressure by $n_e[\mathrm{cm}^{-3}] = (2.1 \pm 0.5) \times 10^{16}\ p[\mathrm{mbar}]$ unless stated otherwise.

6.3 Two dimensional input parameter scans on the LWFA

The performance of a LWFA can be controlled through the input parameters. To explore the parameter space and to show any coupled effects a series of 2D scans were performed.

The outputs of the LWFA were X-rays and electron beams, and the results are plotted in a heat-map style in Figures 6.3, 6.5 and 6.6.

6.3.1 The effect of changing the laser energy and cell pressure on the LWFA

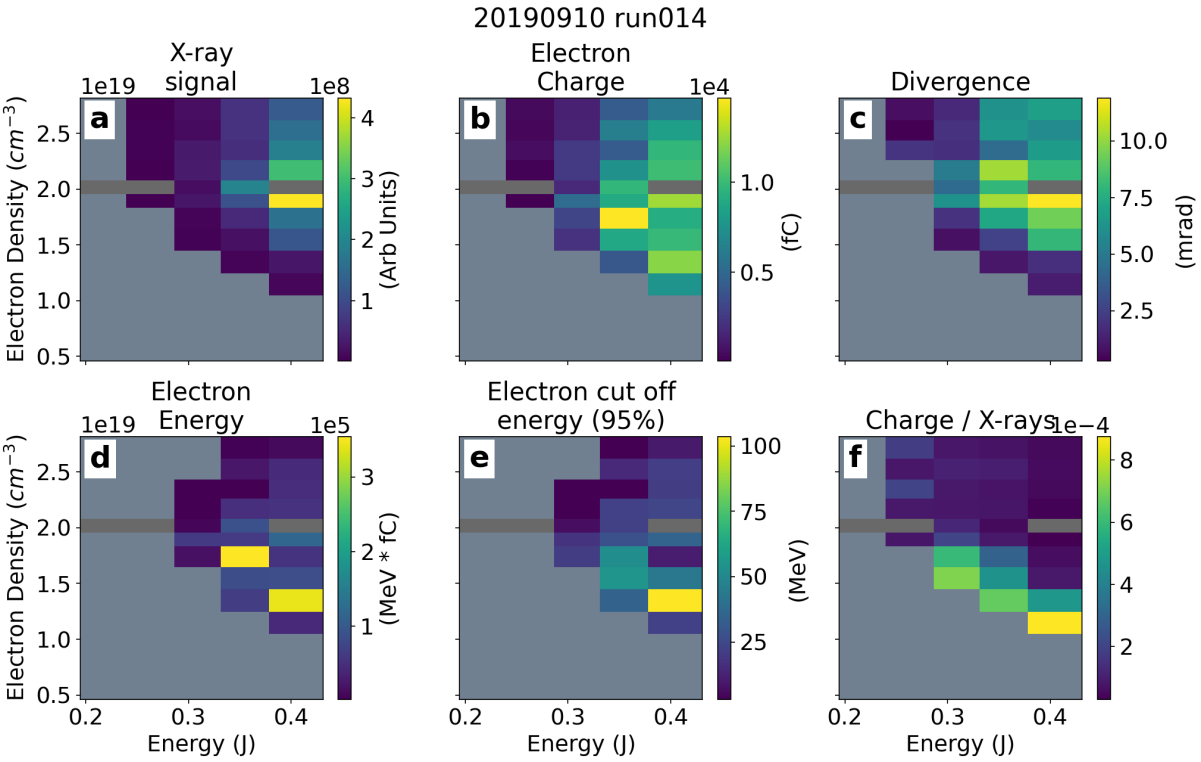

Figure 6.3: The effect of laser energy and cell pressure on LWFA performance. The plasma is formed from a doped gas, so the electrons are being injected through ionisation injection. Note that no electrons were produced in the bluey-grey regions. There was no data taken in the grey regions. The average standard error for this data is between 10 and 20%.

A 2D scan between energy and pressure was performed (Figure 6.3). The gas used to produce the plasma target consisted of 5% nitrogen in helium. For this data the plasma density was related to the pressure (p) by $n_e[\mathrm{cm}^{-3}] = (1.9 \pm 0.2) \times 10^{16}\ p[\mathrm{mbar}]$. Due to the presence of the nitrogen doping in the gas, injection of electrons into the wake was

triggered by ionisation [66]. The N^{6+} electrons are ionised, due to field ionisation [57], in one laser pulse cycle when $a_0 = 1.8$ [67]. Using the TA2 laser in this configuration, it was only possible to reach this intensity through self-focusing of the laser pulse in the plasma [52].

Figure 6.3 (b) and Figure 6.4 (b) show that for a given laser energy there was a minimum electron density below which no electrons were injected. This electron density decreased as the laser energy increased. The pulse duration was not measured for these data shots. However, for data taken before (and after) this run, the pulse duration was 30.9 fs (43.1 fs). The normalised vector potential of the laser (a_0) therefore, ranged from 0.51 to 0.70 (0.61 to 0.85) meaning the wake was in a linear regime ($a_0 < 1$). As the laser energy increased, so did the maximum energy electrons (Figure 6.3 (e)). The energy scaling for the linear regime is for maximum energy gain is [64]:

$$\Delta W \approx a_0^2 \frac{n_c}{n_e} \propto P \frac{n_c}{n_e} \tag{6.1}$$

where P is the laser power.

Figure 6.4 (a) compares the energy scaling shown in Equation 6.1 with the maximum experimental energy gain, and shows the latter roughly follows Equation 6.1, but with a decreased energy gain at the higher plasma densities. However, the scaling does not take account of whether electrons are injected (Figure 6.4 (b)), and therefore, there is a large mismatch at lower density. For ionisation injection to occur in this LWFA, the a_0 needed to be increased via the self-focusing mechanism. For the lower plasma densities and laser powers the self-focusing will not be strong enough to reach this value of a_0.

Figure 6.4 (a) shows that the peak value of each experimental curve lies above the scaling line, with the values at higher densities lying below the scaling line. The evolution of the laser pulse will be different in each LWFA corresponding to the different data points, as both a_0 and λ_p are changing which will change when the critical power for self-focusing is reached (Equation 2.47). For the peak energy seen at a plasma density of $1.35 \times 10^{19}\,\mathrm{cm}^{-3}$ for the $a_0 = 0.70$ pulse would occur at a predicted $a_0 = 0.91$ from the scaling law. This increase could have occurred experimentally due to the self-focusing of the laser pulse. Another reason for the differences between the scaling law and the data

points are the assumptions the scaling law is based upon not being met. The scaling law has been calculated assuming that the LWFA is operating in the blow-out regime, and that the focal spot size is matched to the blow-out radius.

Figure 6.4 (b) shows that that for the range of laser powers investigated, the required electron density monotonically decreases with increasing laser power. For self-injection the required laser power for injection is $P \propto \frac{n_c}{n_e}$ [171]. Figure 6.4 (b) shows that ionisation injection follows the same scaling over the range of the data, with a $R^2 = 0.96$.

Comparing the x-ray flux and the electron beam charge (Figure 6.3 (a & b)) shows that at the lowest density where electrons are injected for each laser energy, the produced beam has the highest ratio of charge to X-ray flux for that energy (Figure 6.3 (f)). A large ratio of electron charge to X-ray flux indicates the injection of the electrons is on the symmetric axis (on-axis) of the wake. When the injection occurs on-axis, the electrons do not experience the transverse focusing fields of the wake, only the accelerating field in the direction of the laser propagation (forward). Electrons that are injected into the

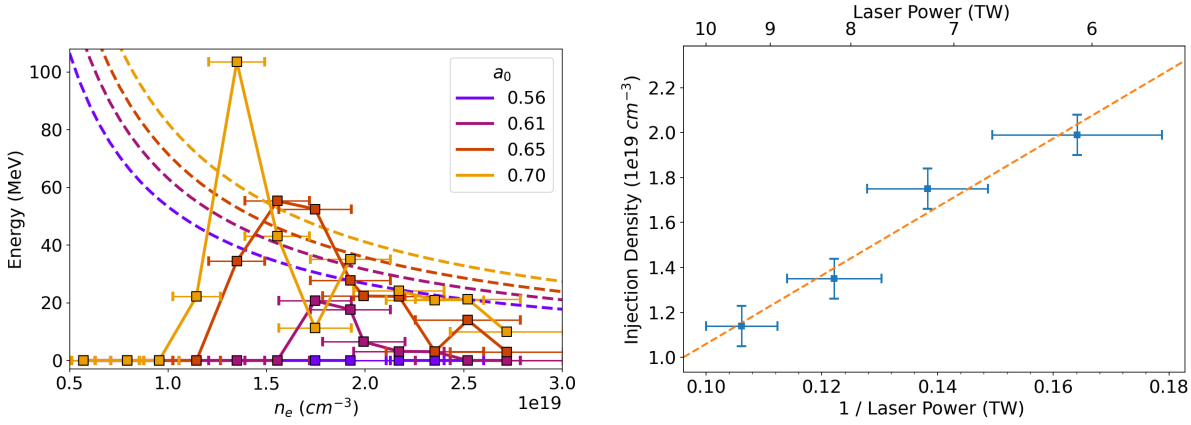

(a) (b)

Figure 6.4: The effect of laser power on the performance of the LWFA. (a) Intensity pressure scalings, showing the scaling lines (dashed) from Equation 6.1, and the experimental data (data points) for the maximum energy at the difference a_0 values. (b) The laser power versus the minimum density that electrons are injected into the wake, with the injection scaling (dashed line) $1/P \propto n_e$ fit having a $R^2 = 0.96$.

wake far from the symmetric axis will interact with a large transverse field as well as the forward accelerating field. This creates transverse oscillations which give rise to the betatron radiation. Another indicator that the electron beams created by the lowest electron density for each laser energy were being injected on-axis was the low electron beam divergence (Figure 6.3 (c)) of these beams, $\sim$2 mrad. A small divergence only could have occurred in this setup if the electrons experienced small transverse fields. The transverse fields tend to zero on the axis of the wake. Figure 6.3 (f) shows that for the ratio of charge to X-ray flux for the lowest electron density for each laser energy increases as the laser energy increases. This is because at a lower electron density the plasma wavelength is longer, which results in the transverse focusing fields of the wake being weaker. Less radiation is produced when the traverse oscillations are less intense [77].

6.3.2 The effect of changing cell length and plasma density on the LWFA

The effect of changing the cell length and the inlet pressure (plasma density) was explored. The plasma target for Figure 6.5 was a gas cell filled with pure helium, so the electron injection occurred via self-injection [172]. Figure 6.5 (a) shows that the beam charge was maximised for a plasma density around $1.2 \times 10^{19}\,\mathrm{cm}^{-3}$, once the length of the cell was above 0.8 mm long. Less than this cell length, the maximum beam charge occurred at higher densities. At higher densities the wave breaking is likely to be more extreme, injecting more electrons. When a large number of electrons are injected, the electric field of the accelerating electrons disrupts the accelerating structure of the wake, which is known as beam-loading [148, 149]. When the cell length is short, injection that causes beam-loading is acceptable in order to maximise the injected charge, as over the short distance all the charge gets accelerated. However, as the accelerator length increases, if the accelerated electrons are not in the correct phase space, or their transverse momentum is too great, they will no longer be trapped in the accelerating structure of the wake. Annular high charge electron beams are produced in a LWFA [173, 174], when the 'almost trapped' electrons gain forward momentum when travelling between the wakefield buckets.

The charge and the energy of these beams increases with plasma density [173]. If these angular beams are the cause of the increased charge, by lowering the plasma density the electrons accelerated in this way may no-longer have enough energy to be recorded using the spectrometer (measurable energy >26 MeV). The higher charge seen at the 0.8 mm long cell at the lower plasma density of $1.3 \times 10^{18}\,\mathrm{cm}^{-3}$, compared with a density of $1.5 \times 10^{18}\,\mathrm{cm}^{-3}$ for 0 mm long cell, was most likely due to the evolution of the laser pulse as it propagated through the plasma. When the cell length was increased, the laser pulse had more evolution time due to the longer propagation in the plasma. This means that the self-focusing effect increased the a_0 of the pulse. Therefore, a self-injecting wake

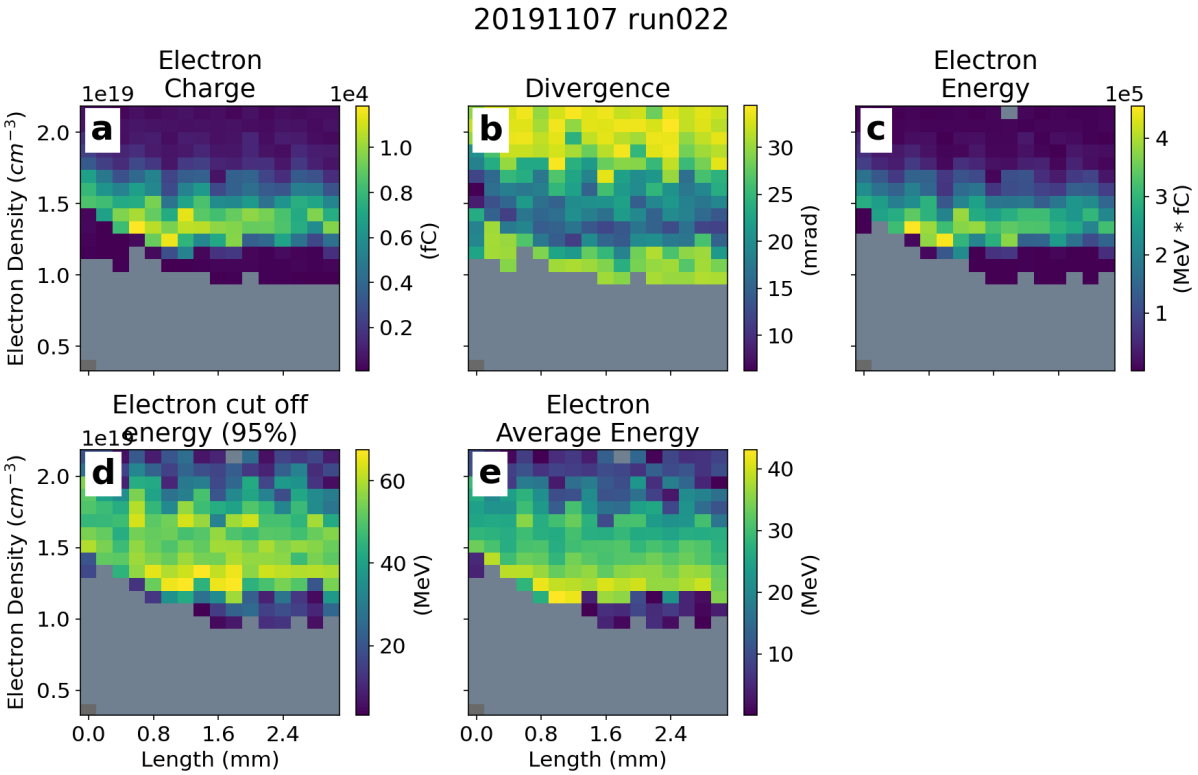

Figure 6.5: A 2D scan between cell length and plasma density for a pure helium plasma. The laser pulse conditions were: pulse duration (49.8 ± 1.3) fs and laser energy (0.251 ± 0.006) mJ. Note that no electrons were produced in the bluey-grey regions. There was no data taken in the grey regions.

can be driven by the same initial laser pulse at lower densities if pulse evolution occurs, as the laser's peak intensity increases.

Figure 6.5 (e) shows the average electron energy of the accelerated electrons. The high average energy relates to electron beams which have a non-Maxwellian, quasi mono-energetic spectrum [4]. This is because a quasi mono-energetic beam would have a high beam energy (Figure 6.5 (c)) in relation to the injected charge (Figure 6.5 (a)) as all electrons would have the same energy. Figure 6.5 (e) shows that the highest average energy occurs when the LWFA is operating just above the injection density threshold, with a cell length of ∼0.8mm. The peak electron energy of ∼60 MeV was seen at a length of 1.6 mm (Figure 6.5 (d)) showing that beyond this distance the electrons have dephased in the LWFA.

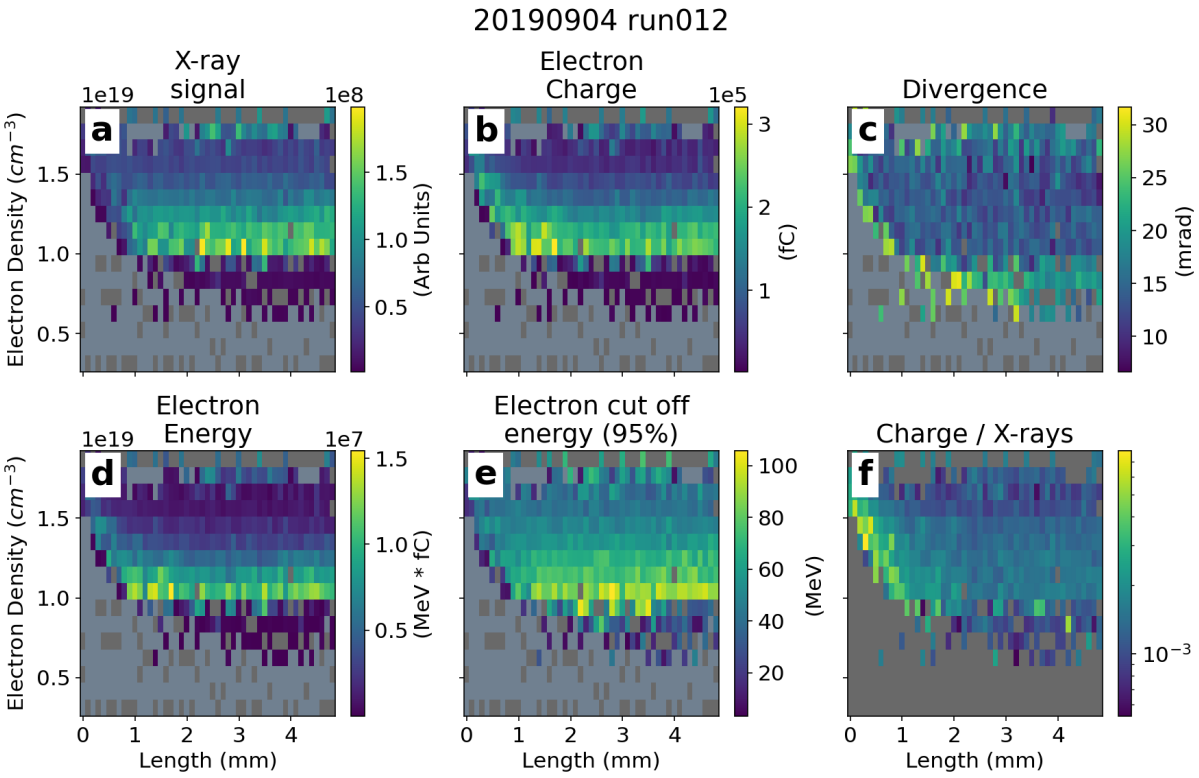

Figure 6.6: 2D scan between cell density and length at higher laser energy ((0.303 ± 0.033) mJ), and higher resolution. The plasma was formed from 5% nitrogen in helium. Note that no electrons were produced in the bluey-grey regions. There was no data taken in the grey regions.

In Figure 6.6, the plasma target was formed of 5% nitrogen in helium. Figure 6.6 (a) shows that the brightest X-ray signals occurred for cell lengths >2 mm at a cell density of $1.0 \times 10^{19}\,\mathrm{cm}^{-3}$. This does not correspond to the maximum injected charge (Figure 6.6 (b)), but more closely to the electron cut off energy (Figure 6.6 (e)). This indicates that more betatron radiation occurs with higher energy electrons, expected as $P \propto \gamma^2 F_\perp^2$, where P is the power radiated, γ the Lorentz factor of the electron beam, and $F_\perp$ the transverse force [77]. The peak in the electron spectrum's cut off energy (Figure 6.6 (e)) as the cell length was increased was likely due to the electrons reaching the dephasing length of the LWFA. The dephasing length in the linear regime [64] is $L_d \approx \frac{2}{3}\frac{n_c}{n_e}R$ where R is the blow-out radius. The fact that the electrons have dephased mean they will be interacting with the rear of the driving laser pulse. Interactions with the laser EM fields will increase the transverse momentum of the electrons in the wake [3], which then leads to an increased X-ray flux. As previously seen in the cell pressure and laser energy scan (Figure 6.3), the largest ratio of electron beam charge to X-ray flux (Figure 6.6 (f)) was seen at the lowest plasma density for each cell length that resulted in a measurable beam charge. In Figure 6.6 (e) the maximum energy was seen at a cell length of 2.8 mm and a plasma density of $1.0 \times 10^{19}\,\mathrm{cm}^{-3}$. Once the electrons dephase, they can start to drive their own wakes in the plasma, and this causes them to lose energy [175, 176]. The laser pulse will be depleting and diffracting over the laser propagation distance, so the strength with which the wake is being driven will decrease. The wake amplitude decreases with decreased driver strength, meaning that the maximum energy gain the accelerator can provide to an electron decreases with distance. Therefore, the accelerator cannot maintain electrons at the maximum energy as the accelerator length increases.

6.4 Convergence of the Bayesian optimisation method

The aim of the experiment was to show that the performance of LWFAs can be improved by deploying a Bayesian optimisation (BO) algorithm. One of the benefits of BO is that it can find a global optimum, instead of just local optima, in noisy data [128]. The surrogate model that the BO creates also allows exploration of the optimisation space, which is an advantage compared with other machine learning techniques that have been applied to LWFA in other experiments previously [177, 178].

The initial test of this algorithm was running 10 individual optimisations from the same starting parameters, optimising the electron beam charge. The optimisation process has to be able to deal with the random nature of the laser fluctuations (energy, pointing and pulse duration). Therefore, the optimum parameters found should relate to the global optimum, predicting the same value each time. Each data point comes from a burst of 10 shots, which enabled characterisation of the error in the measurement. For each optimisation run 35 bursts were taken for the algorithm to determine the optimum.

For the optimisation in the convergence test, four parameters were controlled; the second, third and fourth order of the AOM and the focus position controlled by the adaptive optic (AO). The inlet pressure was set to 1000 mbar and the cell length to 1 mm. The convergence of the model to find the highest charge beams is shown in Figure 6.7. The same starting point was used for each run in this convergence test, and the algorithm's predicted optimum is located within 20 bursts. This is an impressive feat, and although it is hard to compare to a human driven 1D scan approach in terms of shot numbers, as the number of points and the fidelity of the scan are changeable depending on the person searching, this is clearly an effective method at coming to this optimum. This BO method also required fewer data points than the genetic algorithm of Dann *et al.* [178]. Over the 10 data runs, 3500 shots were taken. The fluctuation in the experimental parameters that were kept nominally constant were: a laser energy of (210 ± 10) mJ and an input pressure of (1002 ± 2) mbar. These fluctuations, combined with beam profile fluctuations, are why the predicted optimum error is large.

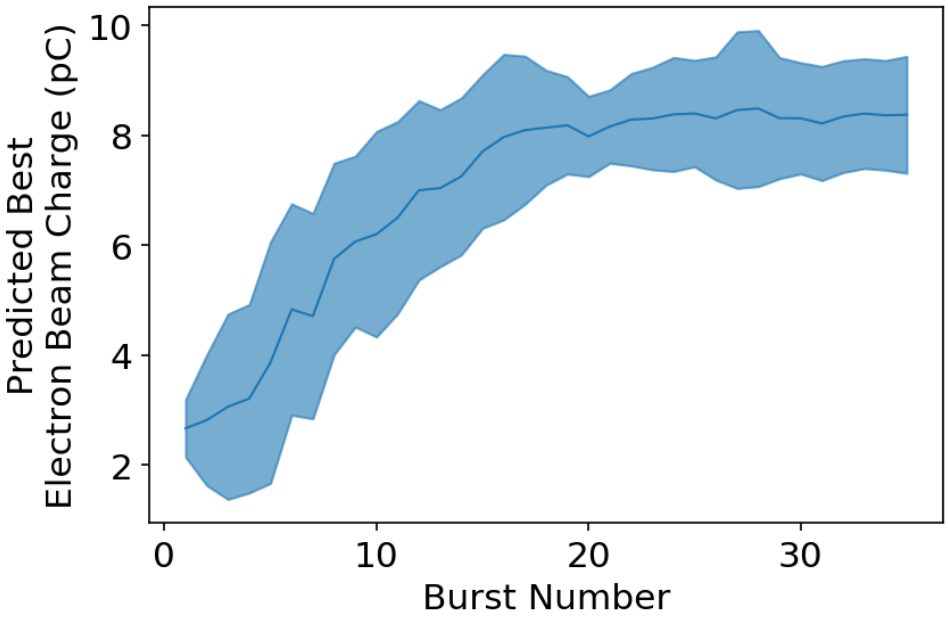

Figure 6.7: Convergence of the optimisation of the electron beam charge from 10 runs, starting at the same position. Here four parameters were optimised simultaneously, the 2^{nd}, 3^{rd}, 4^{th} orders of the AOM [98], and the focal plane. The error is the standard deviation of the 10 runs.

6.4.1 Experimentally extracted parameters and their relationship to the injected charge

During the experiment the control inputs were logged, and the effect of the inputs on the laser pulse were measured using the pre-interaction diagnostics. Pulse duration (FHWM) was extracted from the APE Spider [103] data, and the focal shift measured using the wavefront sensor (HASO, Section 3.2.1). The 3 AOM parameters all affected the pulse duration, reducing the dimensionality of the analysis to dependence on pulse duration and focal plane of the laser pulse. Figure 6.8 shows how the algorithm mainly investigates data points around the optimum, with less exploration of regions that it predicts of having a low probability for improvement (Section 3.6). The injected electron charge and energy increases with laser power [179], and therefore, one would expect to find the minimum pulse duration (τ) to maximise the laser pulse power, i.e. $\tau = \tau_{\text{min}}$. Here, the peak

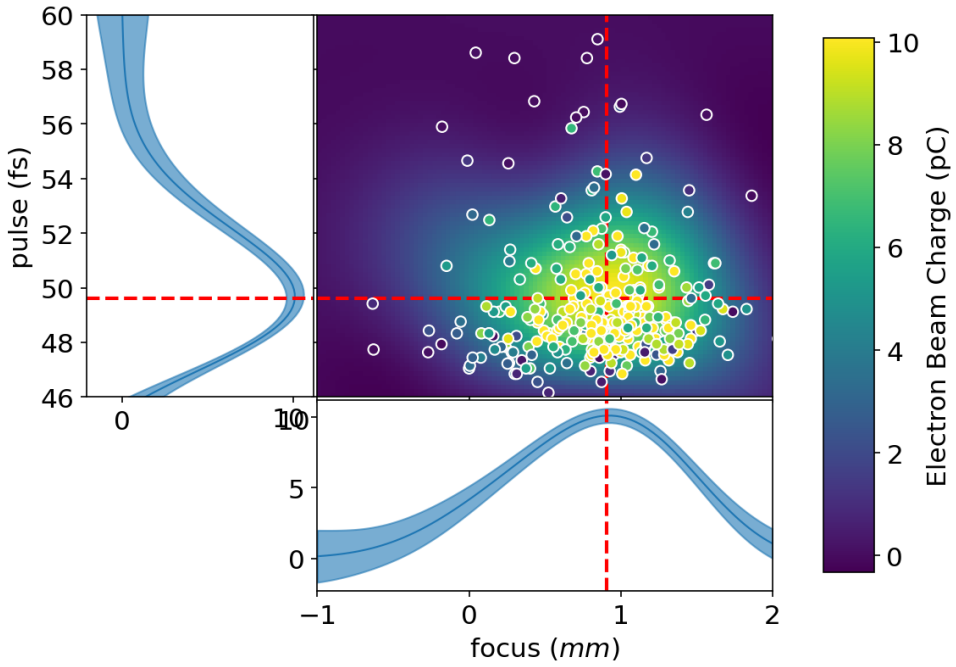

Figure 6.8: A Bayesian optimisation model from the data from the convergence runs, Figure 6.7, using the experimentally measured data as the input. The changes in the 3 AOM parameters changed the total pulse duration (FWHM), allowing representation in a 2D plot. The line-outs shows the prediction and error along the red dashed lines corresponding to the optimum.

electron charge was seen at an optimum pulse duration of (49.7 ± 0.1) fs. The minimum pulse duration produced by the laser during this scan was 46 fs.

The plasma density was $2 \times 10^{19}\,\mathrm{cm}^{-3}$ for the convergence runs and therefore, the plasma wavelength (λ_p) was 7.5 µm. For the τ=46 fs, $c\tau \simeq 14$ µm, the spatial length of the laser pulse was longer than the plasma wavelength. Therefore, the laser pulse was split over multiple plasma buckets for all of the pulse durations shown here. For the plasma to be resonantly driven, the pulse duration should be $c\tau \approx \lambda_p/2$ (From 1D theory the resonance length for a Gaussian pulse $= \lambda_p/(\pi\sqrt{2})$ Table 2.3). The peak charge was at a pulse duration of 49 fs where $c\tau \simeq 2\lambda_p$, indicating that the laser is being split into the two buckets in a specific case of the self-modulated laser wakefield accelerator (SM-LWFA) [2].

6.4.2 Testing the predictive capabilities of the model

To test the predictive capability of the model the dataset was randomly split into two parts (80% and 20%). For both parts, the 4D input values were used: the three AOM parameters and AO controlled focal plane. The larger portion was used to create the model, and the smaller was used to test the predictive power of the model against the real data. Figure 6.9 shows that the predicted results are a good match for the experimentally-measured results. The R^2 value for the test training data is $R^2 \sim 0.77$, showing there

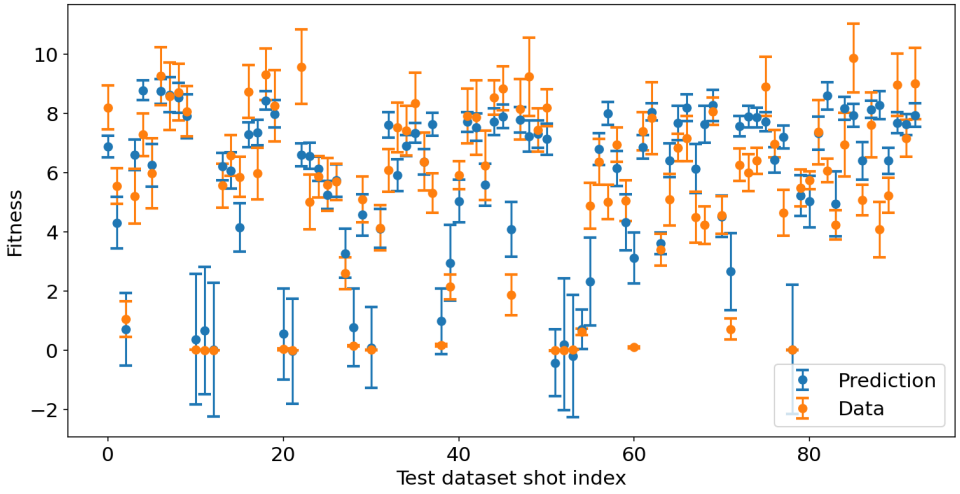

Figure 6.9: Showing the correlation between the surrogate model predictions and the test dataset. The model was created from 80% of the data, with the remaining 20% used to compare the predicted points from the surrogate model and the experimentally-measured data. The coefficient of determination was $R^2 \sim 0.77$.

is a strong correlation between the model prediction and the measured value. Therefore, the model produced can provide valuable insights into the physical processes behind the optimisation.

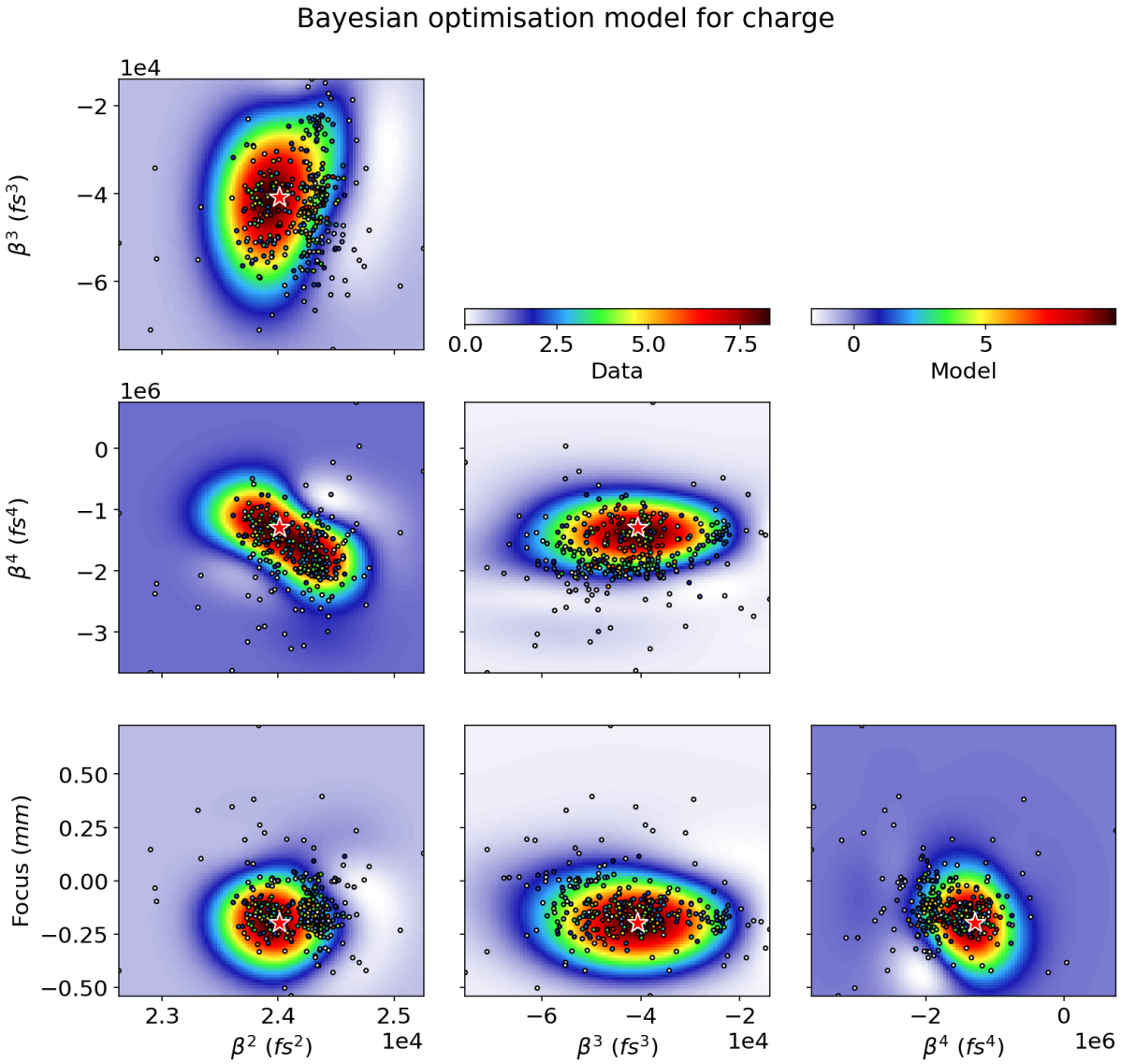

Figure 6.10: The surrogate model of the Bayesian optimisation algorithm for the optimisation of beam charge. Each plot is the 2D plane going through the optimum position (marked with a red star) in the other parameters. The data points are also projected onto this plane to show how well the space is sampled.

6.4.3 Investigating the 4D predicted charge model from AOM and focal plane inputs

Investigation of the models created using the four input parameters (focal plane and the 2nd, 3rd and 4th order of the spectral phase) showed that coupling effects occurred.

Figure 6.10 shows the predicted model in the optimum position in two of the parameters, and a 2D scan in the plane of the other two parameters. The model is most accurate near to the optimum value, as the BO algorithm searches the parameter space that most improves its prediction of the fitness function. In this case the fitness function is returning the total charge, along with an estimate of error for that data point. At a position in parameter space far away from the optimum the model is less accurate, but is predicting a value much less than the optimum and therefore, of less interest. This explains why there are fewer points in the purple regions of Figure 6.10.

The diagonal shape seen in the 2^{nd} and 4^{th} order on the AOM show a coupling. The diagonal shape suggests that a conventional search for the optimum by two 1D scans would not succeed (indicated by purple lines in Figure 6.11(a)) unless one of the parameters was already at the global optimum. The 1D scan data point is a likely end result of the 1D optimisations, and was deliberately chosen to be at the other end of the diagonal of peak charge (Figure 6.11(a)) to examine the coupled effect the BO algorithm has discovered.

The data from the APE Spider is examined in Figure 6.11. Figure 6.11 (b&c) use the data from the input values that are closest to the two optima, the BO optimum and the 1D scan optimum. Figure 6.11 (b) shows that the difference in input parameters of the two optima results in a small increases in pre-pulse, with the phase over the main duration of pulse remaining the same. Figure 6.11 (c) however, shows that the main difference is in the spectral phase, and this has caused the additional 9% increase in charge in the BO case. The 1D optimum has less negative spectral chirp than the BO optimum, where spectral chirp is defined so that a positively chirped pulse has lower frequency components at the front of the pulse and higher at the back [161].

The change in the spectral phase of the pulse, although maintaining a roughly constant FWHM pulse duration, did change the rise and fall times of the pulse. Looking at the half width at half maximum (HWHM) of the temporal shape of the pulse (Figure 6.11 (b)) the optimum has a rise time of 22.7 fs compared to the 1D case of 24.7 fs. The fall of the pulse is the same for both pulses at 25.7 fs, showing that the change in the pulse is a steepening of the leading edge. Mangles *et al.* found that a positive chirp injected

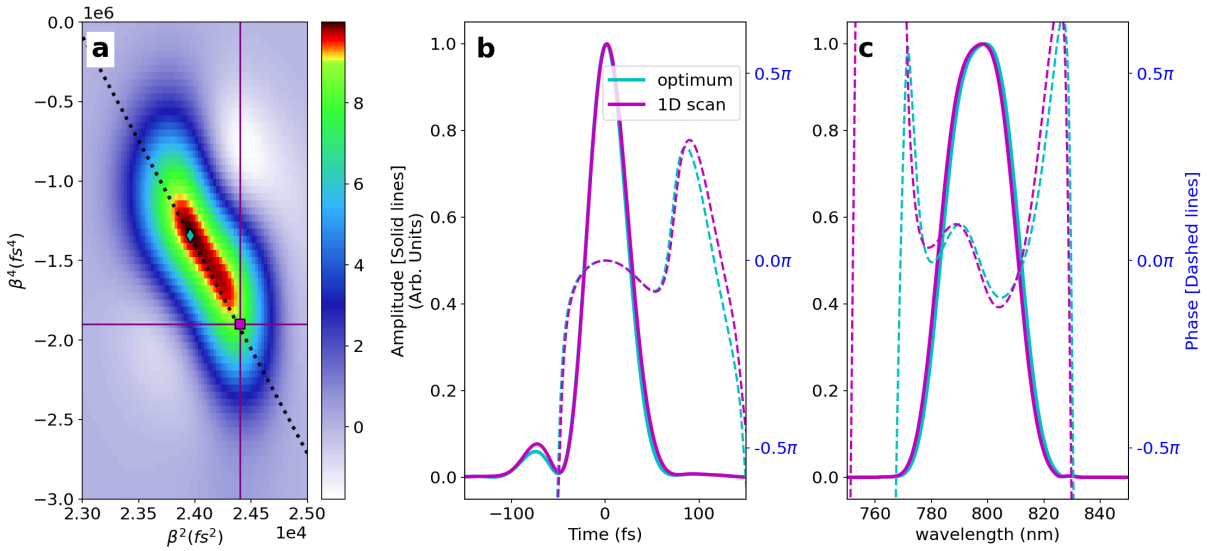

Figure 6.11: The effect of changing the 2nd and 4th order on the AOM has a coupled effect on injected charge. The optimum is shown in blue, and the 1D optimum shown in purple. (a) Zoomed in version of 2nd and 4th relation from BO model. The black dashed line indicates the slope that corresponds to an approximately constant total pulse duration [36, 180]. (b) The temporal trace of the two optima is shown in thick lines. The phase is shown in thin lines. (c) The spectral shape (thick lines) and phase (thin lines) for the two optima.

more charge, but the pulse shape was not measured [171]. Leemans *et al.* found that the change in the leading edge of the pulse, not the spectral chirp, is the main reason for the difference in the injected charge [181]. In this experiment, the 2 fs decrease in pulse rise time appears to be the reason for the increased charge of the true optimum the BO algorithm had found.

6.5 Five dimensional optimisation for different beam characteristics

The optimisation approach just outlined can also be used to search for different beam characteristics. For example, using this optimisation method, the input parameters that are required for the creation of small divergence angle electron beams can be found. These have uses such as making small source size bremsstrahlung sources (Chapter 4). The optimisations that were performed over the same five parameters looked for electron beams with: the maximum accelerated charge; the maximum beam energy and narrow beam divergence.

The experimental method of looking for narrow divergence beams was selecting a narrow band on the Lanex screen that corresponded to the laser axis. However, using a narrow band on the Lanex screen was found to miscategorise some of the electron beams where the beam pointing fluctuations resulted in the beam falling outside of the selection region. Hence the data was re-examined, converting the electron spectrometer Lanex image (which was in pixel position) to be in terms of the beam divergence and energy. The divergence was calculated around the centre of mass of the electron beam, to account for pointing fluctuations. This data was then put into bins of $\pm$ 1, 2, 3, 5, 10 and 20 mrad and corrected by the bin width. This allowed the total beam energy and charge to be compared with on-axis energy and charge. A figure of merit (FOM) was used to weight the results, such that the on-axis electrons were highly favourable and the electrons with high divergence were not. The FOM is calculated using the multiplier in Table 6.1. This FOM returned the highest value for narrow divergence beams, those with high electron counts on-axis and low electron counts off-axis.

Figure 6.12 shows the optimal electron beams for maximum beam energy (Figure 6.12 (a)) and narrow divergence (on-axis) beam energy (Figure 6.12 (b)). This clearly shows that the two optima are in different operating regimes. The pointing fluctuations of the on-axis beams can been seen in Figure 6.12 (b), with shots 2, 7 and 9 being above the central axis of the Lanex.

Divergence bands (mrad)	Signal Multiplier
0-1	20
1-2	8
2-3	1
3-5	-2
5-10	-10
10-20	-15

Table 6.1: The figure of merit (FOM) multiplier for the divergence bands. The FOM returns the highest values for beams with high charge/energy on-axis.

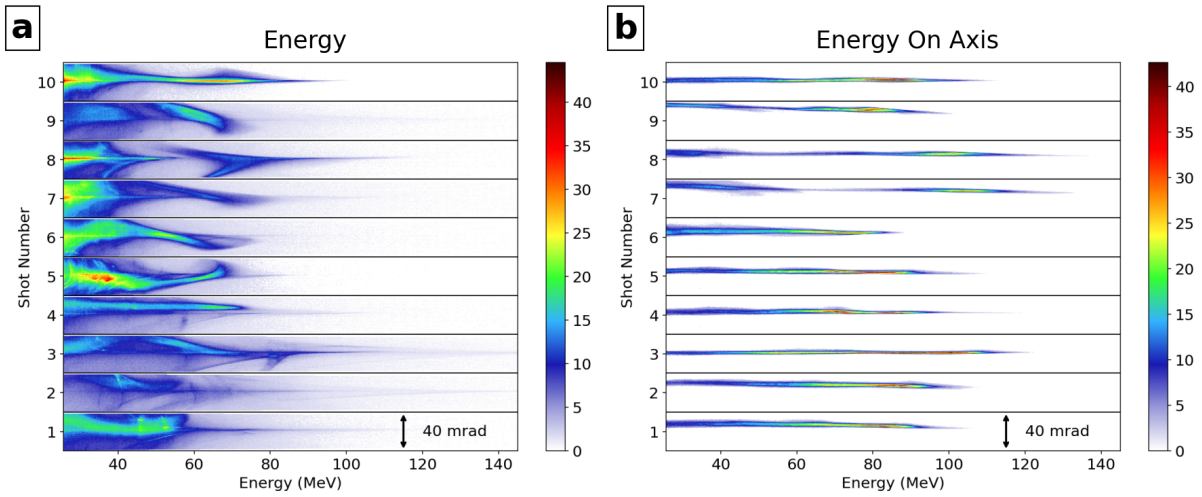

Figure 6.12: Comparison of the optimum burst for electron beams with different characteristics. The 10 angularly resolved electron spectra from each burst are shown stacked vertically with a total range of 40 mrad per shot. (a) Electron beam energy. (b) On-axis electron beam energy.

To investigate how the input parameters affect the output beams, the Gaussian process regression (GPR) model from the BO code (written in Scikit-learn [129]) was used to create a model of the 5D parameter space in which the optimisations were conducted.

To increase the size of the dataset, all data runs from a single day of shots have been combined.

Figure 6.13 shows the locations of the optimum position for the two different beam properties investigated: total energy and on-axis energy. Each sub-plot shows a 2D scan over the model in the plane assigned by the model optimum location in the other three parameters. The heat-map extracted from the model is displayed once the value is above 85% of the maximum. The total charge and on-axis charge were also investigated, with a strong correlation with the energy data. The optimum experimental burst for the on-axis energy and charge corresponded to the same shot, as did the optimum for total energy and total charge. The correlation is expected due to the shape of the electron spectra. This is because beam energy was calculated by summing the number of electrons per energy multiplied by that energy for each of the energies recorded on the spectrometer. While the energy spectrum is Maxwellian, to have an increase in the energy the charge also increases. This correlation indicates that the electron spectra of the energy optima did not have any quasi mono-energetic features.

The difference in the two optima was most apparent in the β^2, β^4 plot (Figure 6.13) where the highest 85% regions do not overlap between the FOM and the total energy. The values of the two optima lie on the line that corresponds to an approximately constant total pulse duration, as shown in Figure 6.11 [36, 180].

Input Parameter	Total energy	On-axis energy	Difference	BO length scale
β^2	23 600	24 300	−600	200
β^3	−34 200	−29 400	−4800	5×10^3
β^4	-6.54×10^5	-1.45×10^6	8.0×10^5	1×10^5
focus (µm)	−266	−190	−76.8	100
pressure (mbar)	968	921	47	100

Table 6.2: The input parameter optima from the BO surrogate model shown in Figure 6.13 (to 3 sig. fig). Comparing the difference to the length scale of the model, the changes to β^2 and β^4 are the largest ratio changes.

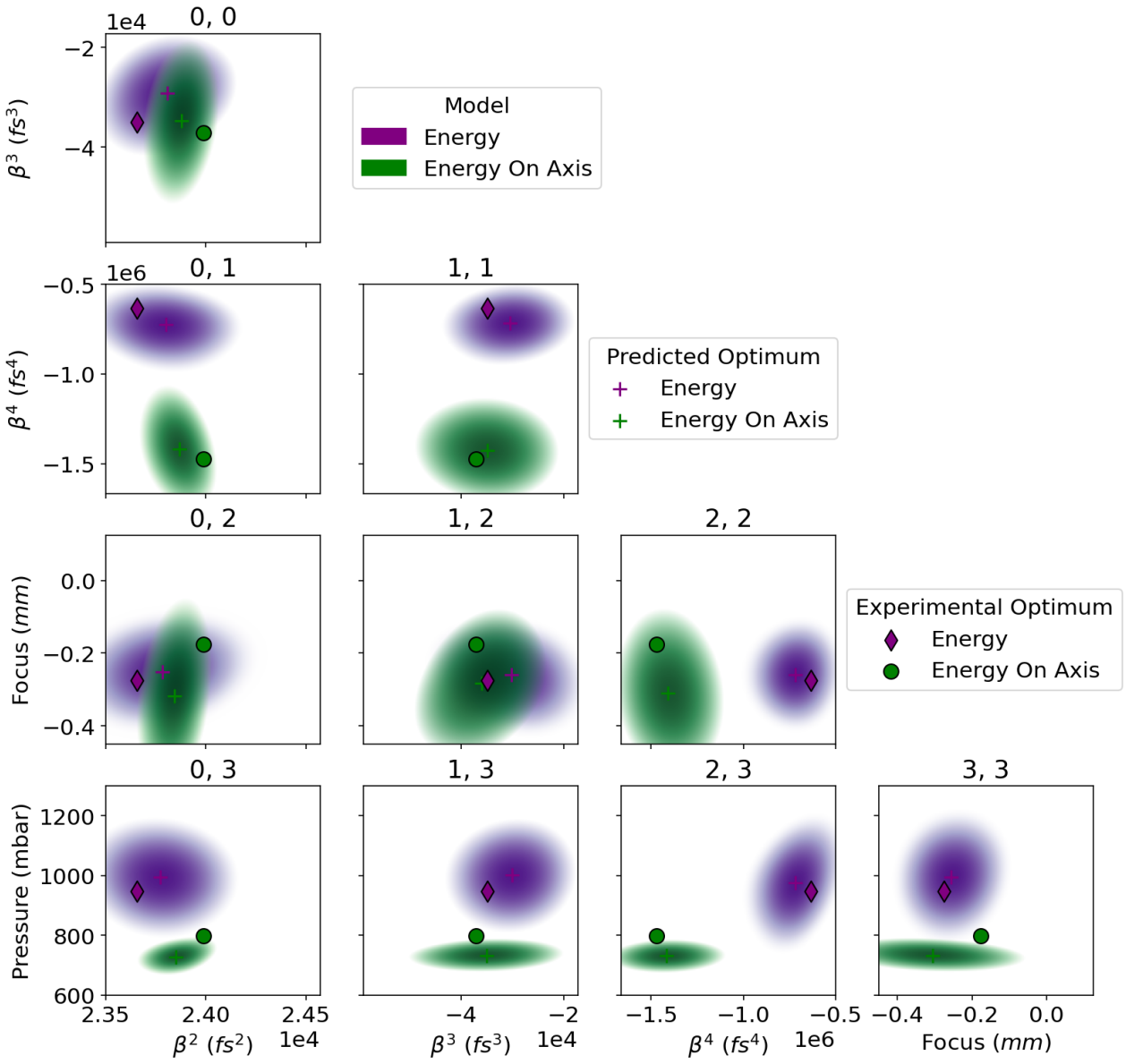

Figure 6.13: The predictive model, showing the predicted optimum (pluses) and the experimental optimum (shapes with black edge) for the different figures of merit: total energy and on-axis energy. The different coloured regions correspond to where the model predicts a result of greater than 85% of the maximum value. The optimum positions are shown in Table 6.2.

Parameter	Energy	On-axis energy	Difference
Focal Plane (µm)	0 ± 90	-190 ± 430	190
Pulse FWHM (fs)	50 ± 1	48 ± 1	2
Spectral Width (nm)	28.79 ± 0.03	28.77 ± 0.03	0.02
GDD (fs^2)	300 ± 70	280 ± 13	25
TOD (fs^3)	$(-2.1 \pm 0.6) \times 10^4$	$(-1.4 \pm 2.0) \times 10^4$	7400
FOD (fs^4)	$(2.3 \pm 4.0) \times 10^6$	$(2.1 \pm 1.0) \times 10^6$	2.2×10^5
Pressure (mbar)	940	910	30
Electron Density (cm^{-3})	$(2.0 \pm 0.5) \times 10^{19}$	$(1.9 \pm 0.5) \times 10^{19}$	1×10^{18}

Table 6.3: The experimentally measured parameters of the optimum electron beam energy and on-axis electron beam energy. Here the focal plane was set so the energy optimum was at zero and a negative number means that the focus has moved towards the back of the cell. The errors are the standard deviation of the burst (10 shots). The chromatic dispersion caused by the AOM was characterised by the group delay dispersion or second-order dispersion (GDD), the third-order dispersion (TOD) and the fourth-order dispersion (FOD).

For this LWFA setup, the optimum pressure only varied a small amount between the two optima, corresponding to a change in electron density of $7 \times 10^{17}\,\mathrm{cm}^{-3}$ (Figure 6.13 and Table 6.2) with λ_p=$(7.5 \pm 1.0)\,\mu\mathrm{m}$. The pulse duration for both optima was $c\tau \approx 2\lambda_p$, indicating a specific case of a SM-LWFA [2].

The shift of the focal plane towards the back of the cell will have resulted in the laser pulse losing more energy before it reaches its focal point. The extra distance travelled was input as a 77 µm shift, and experimentally measured as a 190 µm shift (Tables 6.2 and 6.3). The extra propagation distance means the laser pulse has lost more energy before reaching its focus and hence, a lower a_0 of the pulse. The reduction of a_0 will have effected the evolution of the pulse, and could have resulted in only the region around the symmetry axis of the pulse having a high enough intensity to cause ionisation injection.

This would have led to the injected electrons starting on-axis and mainly interact with the accelerating field, and not the transverse fields of the wake.

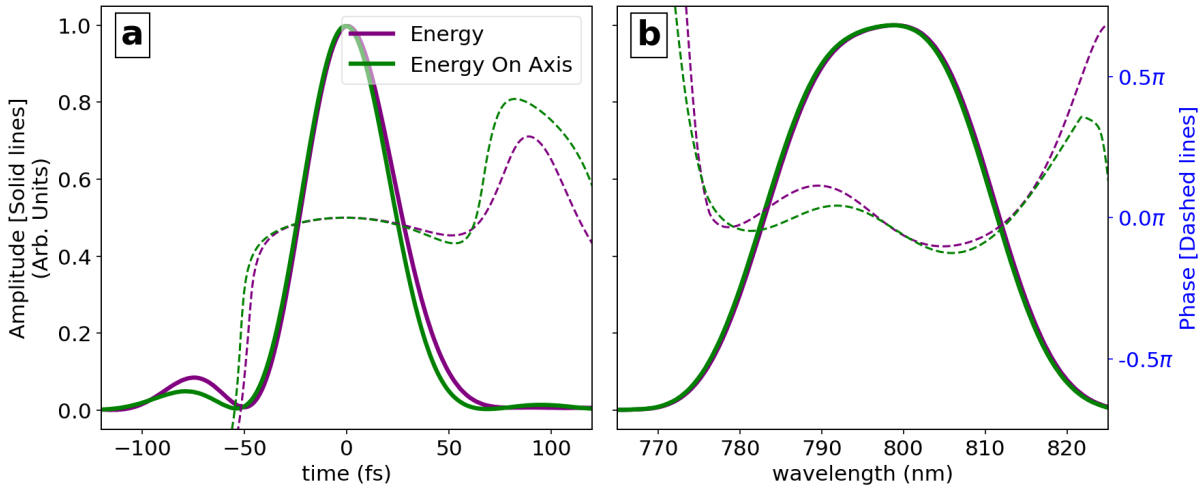

Figure 6.14: Comparison of the optimum electron beam's input laser pulses. (a) The pulse temporal shape (solid) and phase (dashed) measured with the Spider. (b) The spectral shape (solid) and phase (dashed) measured by the Spider. The FWHM pulse duration for the energy (on-axis) was 50.4 fs (48.4 fs). The FWHM spectral bandwidth was 28.7 nm for both spectra.

The optimal experimental electron beams for total energy and on-axis energy show that there was a clear difference between the two optima (Figure 6.12), with the on-axis optimisation successfully producing narrow divergence electron beams. The main difference in the input parameters was through changes to the AOM, affecting the spectral phase of the laser pulse. The effect on the measured laser pulse is shown in Figure 6.14 showing the temporal and spectral laser pulse data from the experimental shots.

Previous work looking at the effect of linear chirp on LWFA performance has found that a positive chirp increases the injected charge [161, 181–183]. This work did not examine the divergence of the accelerated electrons with respect to laser chirp. There are two explanations for the increase in charge from the chirp's effect are one, the ponderomotive force, and two, the effect on the steepness of the pulse. Due to the ponderomotive potential scaling $\propto \lambda^2$ (Equation 2.10), the force from the leading edge of the pulse is stronger from

a positively chirped pulse. This drives a larger amplitude wake in the plasma [182], which can accelerate more charge. The effect of changing the spectral phase of the pulse will not be fully compensated by the compressor gratings. The asymmetry between positive and negative chirp effect on charge arises due to uncompensated higher order phase non-linearity in the pulse compressor, leading to faster rise times of the leading edge for positively chirped pulses [183].

Figure 6.14 (b) shows the spectral phase, with the on-axis optimal pulse appearing flatter than the total energy. For the total energy, the part of the spectrum that arrives at the plasma first was centred around the 790 nm wavelength light, with a more prominent peak than the on-axis case. This indicates that a non-linearly negatively chirped pulse had driven the accelerator. The difference in the FWHM pulse duration was 2 fs (Figure 6.14 (a) and Table 6.3) but, as for the case of optimising beam charge (Section 6.4.3), the pulse rise and fall times had also changed. The total energy had a HWHM laser pulse rise time of 22.7 fs, 1 fs faster than the on-axis pulse with a rise time of 23.7 fs. The HWHM laser pulse fall time for the total energy was 27.7 fs and the on-axis 24.7 fs. Therefore, for the on-axis electrons the leading edge of the laser pulse was rising more slowly. A longer rise time may again reduce the a_0 of the pulse such that only the on-axis intensity becomes high enough to cause ionisation injection. Electrons that start on-axis will be accelerated only in the forward direction, creating a small divergence angle beam.

Dann *et al.* [178] found, using a genetic algorithm on the TA2 laser, to maximise the beam energy and charge the optimum pulse duration was longer and skewed compared to the fully compressed pulse. This change in the pulse was achieved through changing the β^2 and β^3 on the AOM. However, contrary to this work, they found that a slow rising leading edge to the laser pulse was optimum. Their result was found when the pulse duration, 40 fs compressed, had increased by a factor of ~ 2, which is far greater than the range of pulse durations examined here. Both the machine learning approaches to LWFA optimisation that have been deployed on TA2, a genetic [178] and BO algorithm [36], have located the global optimum with a pulse duration longer than the shortest pulse duration

the laser system can produce, indicating that the laser pulse shape is a more important parameter than peak laser intensity when optimising the beam charge from a LWFA.

6.6 Conclusions

The presented work shows the successful application of a Bayesian optimisation algorithm to the production of high energy electrons from a LWFA. This approach has been shown to converge quickly ($\lesssim 20$ data points required) when optimising for accelerated charge with experimental noise, and it has been shown to be able to optimise for different qualities in the electron beam. The algorithm's ability to optimise beams with a given quality, defined by a fitness function, will help LWFAs become a more versatile and accessible device for both science and industry.

The exploration of the BO surrogate model has identified a coupling between the group-delay dispersion (GDD) and the fourth-order dispersion (FOD) for all the optimisations presented. The effect on the experimental measured laser pulse indicated that the rise time of the pulse is a key parameter to a LWFA performance. Further work may discover more of these couplings, and the surrogate model produced will make these significantly easier to discover. The BO algorithm is a good approach to optimisation in a multi-parameter space with up to 20 dimensions [128].

An interesting extension would be to decouple the effect of spectral chirp and the rise time of the pulse to work out the mechanisms that causes the difference, either in total charge accelerated or for on-axis electron beams. However, the experimental methods deployed so far to change these have always been coupled.

Designing tools such as this algorithm is an important step towards realising applications. This Bayesian optimisation algorithm quickly locates the global optimum, allowing peak performance of the LWFA. It will also allow quicker re-optimisation of electron beams that occur when drifts in laser performance have changed the beam characteristics.

7 | High repetition rate plasma mirror

This chapter presents the characterisation of a design for a new high repetition rate (HRR) plasma mirror, which was undertaken in the Center for Ultrafast Optical Science (CUOS) at the University of Michigan, and is published in Underwood *et al.* [37]. The plasma mirror was created from of a flowing liquid film, creating a regenerative surface, that has the potential to run at kHz. The author took the experimental data for the thickness, stability and beam profile, and data was provided to the author for the high intensity reflection measurements.

7.1 Background and motivation

A plasma mirror is a device often used to improve the intensity contrast ratio (ICR) of a laser pulse. The ICR is the ratio between the intensity of the main pulse and the prepulse (energy that is delivered to the target before the main pulse). A poor ICR can be due to prepulses generated during amplification or amplified spontaneous emission (ASE) from the amplifier medium. Ultra-short pulses normally have a pulse pedestal [184] that starts of the order of picoseconds before the main pulse, which although several orders of magnitude smaller than the main pulse, due to the high intensities being achieved still cause severe perturbations to the target. High ICR is required for laser-solid interactions to prevent perturbations to the target before the main pulse arrives. For short pulse laser-solid interactions the effect of the pre-pulse is to perturb the target by ionisation. Field ionisation [57] occurs an intensity of the order $10^{14}\,\mathrm{Wcm}^{-2}$ [185] and two photon ionisation starts occurring at $10^{12}\,\mathrm{Wcm}^{-2}$ [56]. Therefore, a required ICR for the experiment can

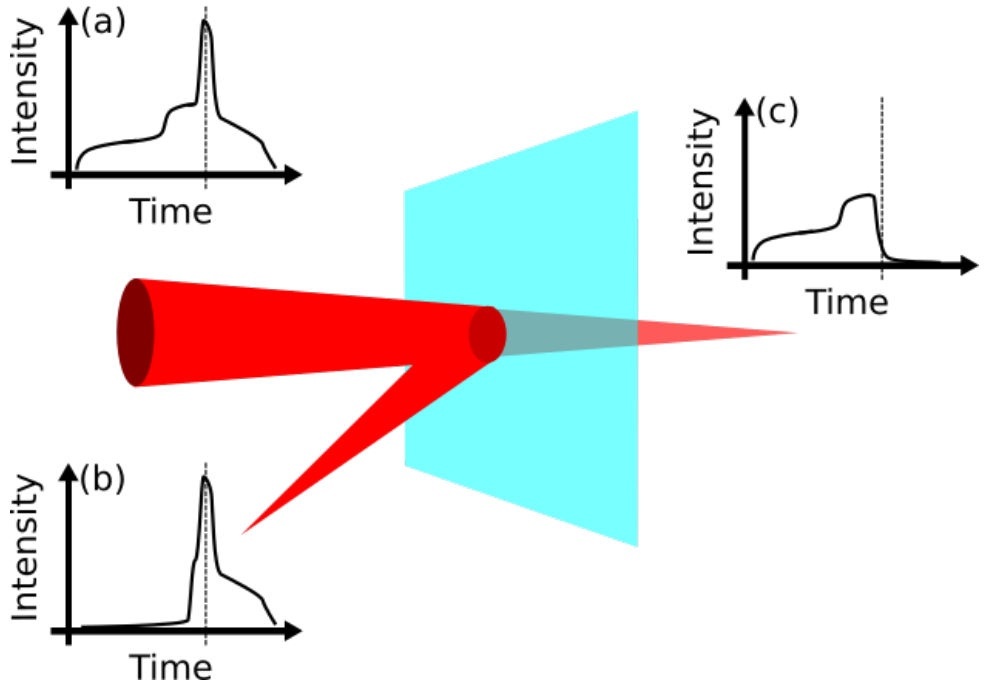

Figure 7.1: A plasma mirror (cyan) acting as a pulse cleaner, removing the pre-pulse from the laser. For the intensity against time plots, the time of the peak pulse is shown with the vertical dashed line. The laser spot size on the plasma mirror is chosen so the intensity is above the field ionisation limit for the main pulse. (a) The incident temporal shape on to the plasma mirror. (b) The temporal shape of the laser on the target. (c) The temporal shape of the pre-pulse that has propagated through the plasma.

be calculated by knowing the maximum intensity that should be achieved by a particular laser system. A high ICR is required for some sources based on laser-solid interactions, such as ion acceleration by radiation pressure [38].

Laser ICR can be improved by pulse cleaning in the laser chain itself (saturable absorbers, non-linear birefringence [186, 187]), but the pulse pedestal occurs too close in time to the main pulse for these options to work. To improve the contrast in the pico/femtoseconds leading up to the main pulse, a device called a plasma mirror can be implemented [185]. A plasma mirror works by having an anti-reflective (AR) surface, which allows almost all the light through it, until the intensity reaches the field ionisation

limit (Figure 7.1). At this limit, the surface gets ionised in less than one laser cycle [57], and the plasma density at the surface is greater than the critical density, resulting in the laser light now incident on this surface being reflected with an efficiency up to 90% [185]. In practice, the plasma mirror is positioned in the focusing laser such that the surface transmits the low intensity prepulse. As the main pulse approaches, the laser intensity surpasses the ionisation threshold for the material, transforming it into a thin and over-critical (highly-reflective) plasma layer which reflects the main pulse. When the position of the plasma mirror is optimised, the plasma will not have time to expand and thus the quality of the focus is preserved. Plasma mirrors tend to be made out of solid, highly engineered materials (anti-reflection dielectric-coated optic). The ICR is improved by a factor of 10→1000, depending on the efficacy of the AR coating.

Plasma mirrors are often used in laser wakefield accelerator (LWFA) experiments to insert/extracted the laser beam before or after an interaction. Due to dephasing, depletion and diffraction (Section 2.7) an individual accelerator stage, driven with a ∼PW laser, can reach $\lesssim$10 GeV [64]. To reach higher energies multiple acceleration stages can be combined together (Figure 7.2). Experimentally to insert the laser beams into subsequent stages, a thin tape has been used as a plasma mirror [39]. A potential use for this HRR plasma mirror would be in future staged accelerators, which due to its thinness should only cause small perturbations to the electron bunch, and would allow kHz operations.

The use of solid materials for plasma mirrors starts to become problematic as the repetition rate of the laser increases. Currently there are petawatt lasers are firing at a rate of the order 1 Hz [23], and terawatt lasers are approaching the order of kHz [188]. Plasma mirrors will also have to be able to function at these repetition rate to allow sources to be produced for real-world applications. Using solid plasma mirrors at kHz or higher repetition rates (using mechanical scanning stages) has been demonstrated, but debris is always generated during the formation of plasma mirrors. This debris causes the performance of the plasma mirror on the subsequent shots to be impaired, and can also cause damage to other optical components near the target [189]. Plasma mirrors made from liquid crystal films produced by a wiper [190] and liquid films running over a

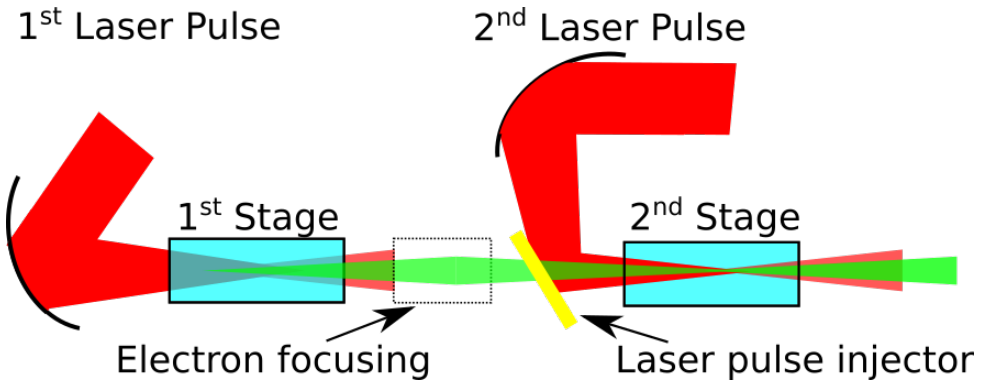

Figure 7.2: LWFA staging experiments use a plasma mirror as the injector for the second laser pulse [39]. The laser beamlines are shown in red, the plasma targets in cyan, and the accelerated electrons in green. The focusing optics for LWFA normally have an f-number > 10, resulting in beam paths on the order of 1 m, with plasma targets (stages) on the order of 1 cm. The pulse injection (plasma mirror) is shown in yellow.

mesh [191] have been investigated with promising results, but due to the rate at which they are refreshed are only suitable for a maximum repetition rate of the order of a 1 Hz. To the best of my knowledge, prior research into water plasma mirrors is as follows: laminar flowing water over a solid structure to aid the formation of thin films [191]; and liquid jets [192]. The flow rate of the water films over the solid structure cannot be high enough for kHz operation. Liquid jets used to form thin liquid gain medium and saturable absorber windows in ultrafast dye lasers of the 1980's [193] have shock related features that criss-cross their surfaces on intervals of tens of microns.

In this chapter a different method of creating a regenerating plasma mirror by using a thin film of water is presented, which is produced by impinging two equal cylindrical high flow rate water streams. It was first demonstrated by Felix Savart [194], and now has applications in industrial sprays [195, 196]. The film forms in the plane perpendicular to the two jets (Figure 7.3) and would be circular when the jets are coaxial and leaf shaped otherwise (Figure 7.4). This film is free of features over several millimetres, and the surface is continuously refreshed so does not need replacement. The higher flow rate

of the liquid optic enables operation at higher repetition rate, which will be required with kHz systems such as the ELI-Alps [24]. Measurement of the properties of these water films as plasma mirrors are presented here to evaluate their usefulness for applications.

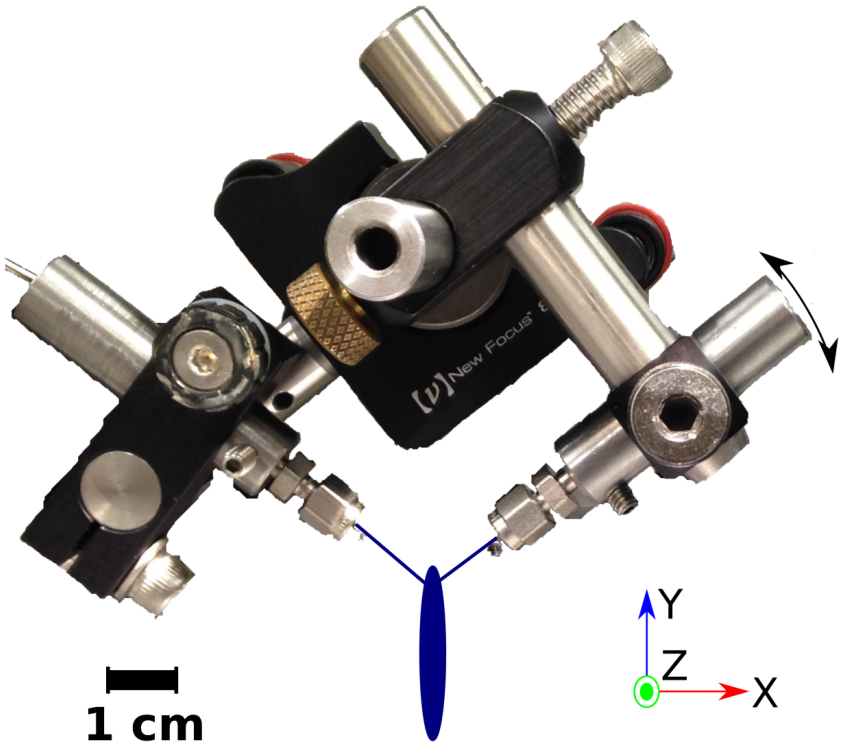

Figure 7.3: The experimental set-up to create the liquid films, showing the axes used when talking about the liquid window. The skew of the window was controlled by offsetting the nozzles in Z and the effect of changing the other axes is negligible in comparison [37].

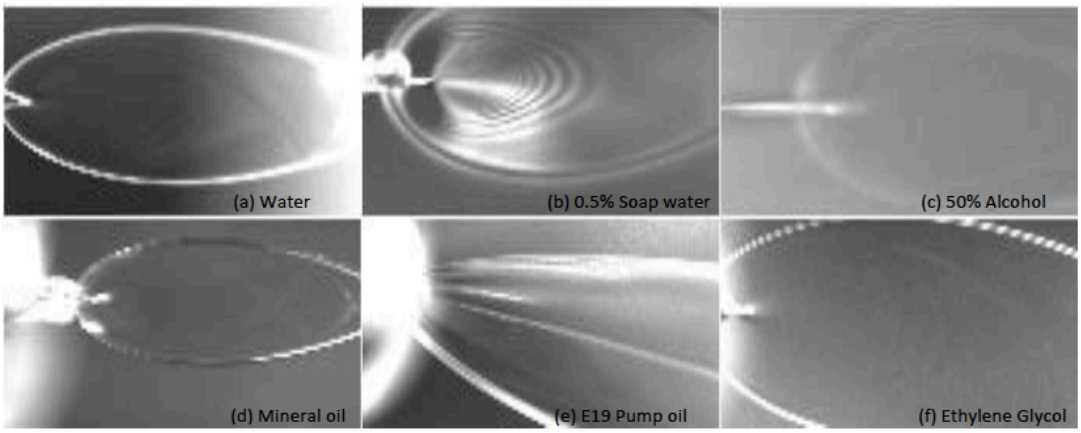

Figure 7.4: The liquid film images on the camera under the same conditions using either 20 µm and 50 µm inner diameter capillaries, 130° relative nozzle angle and gas pressure ranging from 600 to 1500 psi. Images provide by J. Nees. The film area is on the order of 1 cm^2. (c) and (e) have poor performance, (b) exhibits fluorescent light interference and (a) and (d) exhibit a single fish-tail shock pattern common to most flows. (a) and (f) are the best choices for liquid film, being both thin and stable [37].

7.2 Experimental methods and results

Generally, the thin water film target is formed by forcing liquid through two identical capillary nozzles, with an inner diameter ranging from 20 µm to 100 µm. Figure 7.3 shows the compact set-up to create the film. The two liquid jets collide, and a thin region of fluid film is formed at the interface. The collaborators from CUOS constructed a liquid film system in atmosphere using various nozzles with the fluid backed by a high-pressure gas as the pump. The films that were produced were imaged with an optical camera to look for a large region of laminar flow. The films that were produced were imaged with an optical camera to look for a large region of laminar flow. Several different liquid materials were tried at different gas pressures, with different angles of the intersecting jets. In Figure 7.4 the applied gas pressure to the liquid film system ranges from 600 to 1500 psi and the relative angle of two 20 µm or 50 µm nozzles is 130 degrees. In the experiments, water (a), soap water (b), mineral oil (d) and ethylene glycol (f) produced windows free of shock features on the scale of several millimetres. Thin films are required for AR properties, and an indication of their thinness was seen from interference fringes appear based on the fluorescent room lights. Pump oil (e) was not adequate for this application due to the non-uniformities generated in the flow. The mixture of 50% water and 50% alcohol (c) did not produce a flow stable enough to reveal fringes. The use of pure water or pure ethylene glycol as the flowing liquid produced the best results for generating a large region of thin uniform liquid film. The pressurising gas was replaced by a syringe pump to increase the control of the fluid flow rate. This also stopped additional gas dissolving into the liquid, which is important when using in a vacuum chamber.

7.2.1 Laminarity and reflecting surface size measurements

To work as a plasma mirror the water film must have a laminar area that is of the order 1 mm^2 for a terawatt laser, and 1 cm^2 for a petawatt. This region must be without droplets, or spray from other parts of the flow passing in front of the window and hence

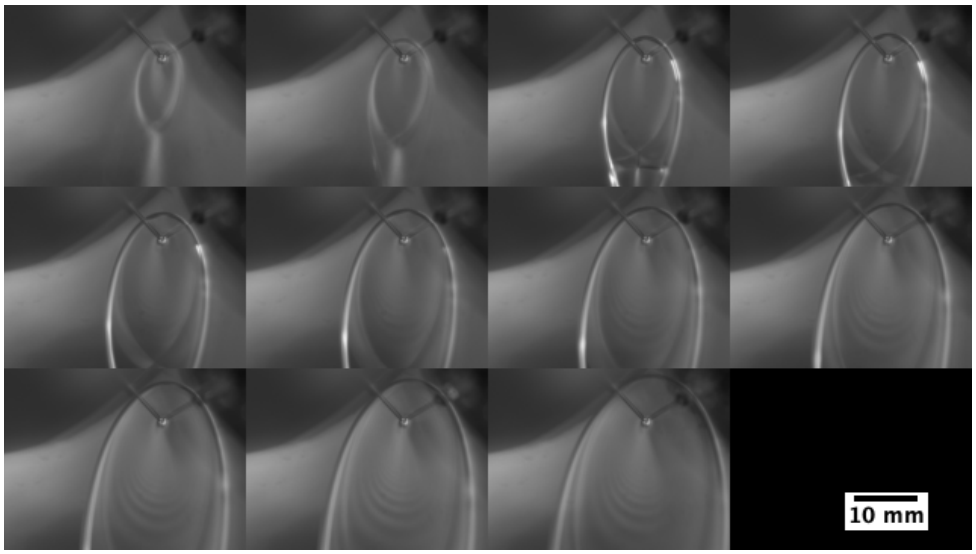

Figure 7.5: Size of the water window with a flow rate from the pump set from 6 to 11.5 mL min^{-1}. A montage of the water windows formed increasing in flow rate from left to right and top to bottom [37]. The film area is on the order of 1 cm^2 (Figure 7.6).

in the path of the laser. The collision dynamics (position, skew and impingement angle) were important for producing a stable window, as shown in Figure 7.5.

The stable regime had a characteristic rope of water around the edge of it, which stopped the edge breaking up into droplets. For some angles, skewing the film allowed the formation of a stable window, whereas a perpendicular film to the plane of the water stream was unstable. For 100 µm capillaries, an angle of $128.0 \pm 0.7°$ was chosen as it was stable for perpendicular and skewed water films. This angle and capillary size was used for the remaining work. The flow rate was important for defining the size of the window, shown in Figures 7.5 and 7.6. A linear relation between flow rate and area was found.

7.2.2 Measurements of surface thickness

The thickness of the pure water film through 100 µm nozzles was measured using the reflection of a white light emitting diode. The light that is reflected off the back surface (R_1) interferes with the light reflected off the front surface (R_0). The refractive index of

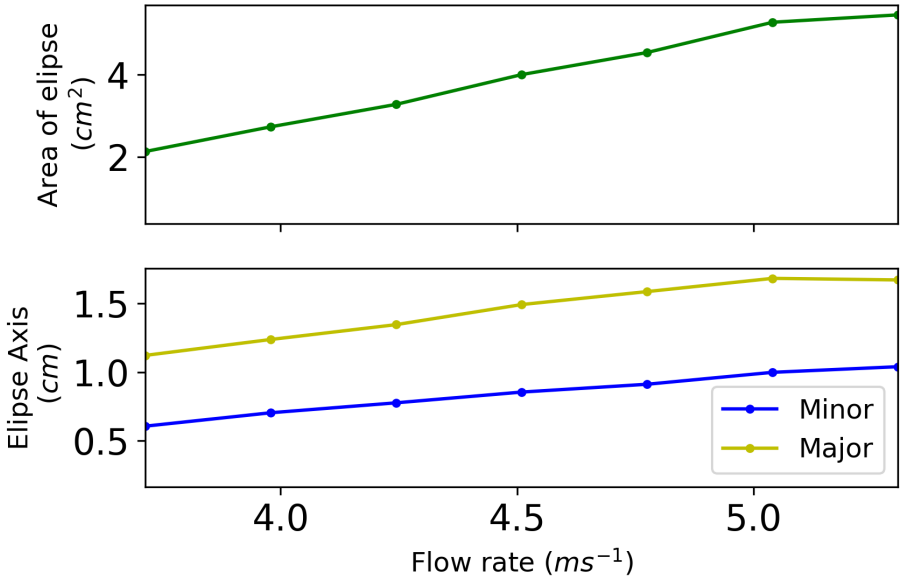

Figure 7.6: Size of the water window with a flow rate from the pump set from 6 to 11.5 mL min^{-1}. A linear relation between window size and flow rate was found over the range of exit velocities investigated [37].

air is $n_{air} = 1.0$ and of water $n_{water} = 1.33$.

$$R = \left| \frac{n_1 - n_2}{n_1 + n_2} \right|^2 \tag{7.1}$$

The reflections calculated from Equation 7.1 show the beam reflected from the front surface is 2% of the total incoming beam and from the back surface is 1.97%, giving the values of $R_0 = 2\%$ and $R_1 = 1.93\%$. Since most of the light is contained in the first transmission, T_1, successive reflections can be ignored. The film has AR properties if the reflection R_0 destructively interferes with R_1. The reflected light was measured with a spectrometer, and the thin film has the properties of an etalon, as the two surfaces of the film are neither fully reflective nor transmissive. The spectrum of the reflected light was modified with respect to the incoming spectrum, and the peaks are separated in frequency space by the free spectral range:

$$\nu_{\mathrm{FSR}} = \frac{c}{2dn} \tag{7.2}$$

c the speed of light, n is the refractive index and d is the path through the water, which then relates to the thickness:

$$t = d\cos(\theta) \tag{7.3}$$

where θ is the angle of incidence on the water film.

Figure 7.7 shows that the thickness of the water windows created by the 100 µm capillaries was not flow rate dependent for the range of flow rates examined, 3.5 to 5.5 ms^{-1}. When the film formed normal to the water jets (in the Z plane from Figure 7.3) its thickness was 2.10±0.06 µm, and a skewed window ($\sim 30°$ to normal) had a thickness of 1.6±0.3 µm. Further work could include changing the capillaries to see whether this leads to a change in film thickness. The thickness of a inviscid (having no or negligible viscosity) fluid film [196] is:

$$h_{\mathrm{inv}} = \frac{r_0}{2r_i} \tag{7.4}$$

where r_0 is the radius of the liquid jet and r_i is the radius of the impactor. This suggests that a change in the radius of the nozzles would have a linear change in film thickness.

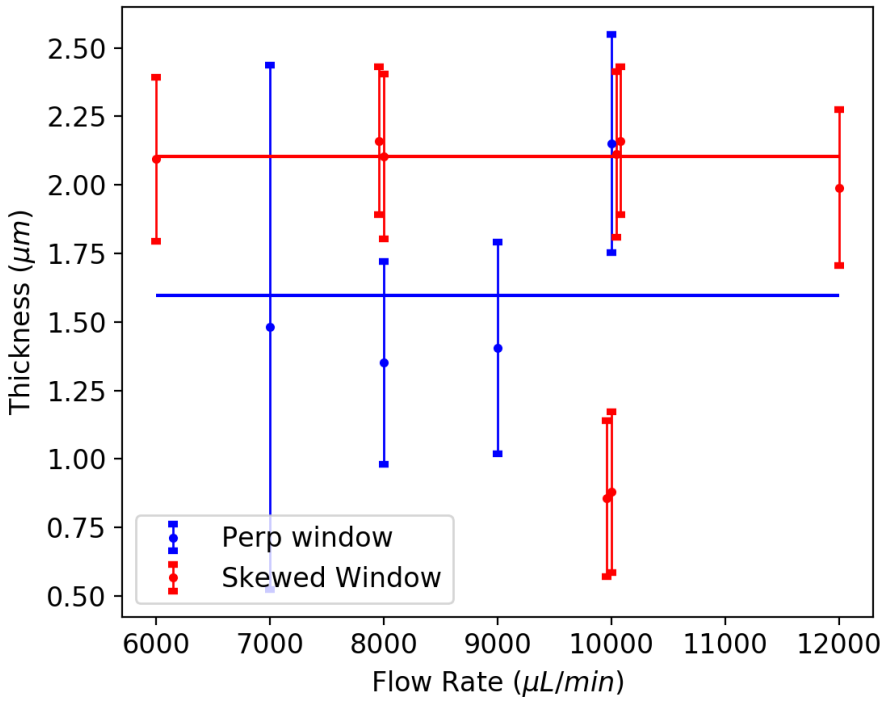

Figure 7.7: The thickness measurement of a stable window, showing that the thickness was constant for the different flow rates. The thickness of the skewed window was found to be (2.10 ± 0.06) µm (ignoring anomalous points at 10,000) and the normal window it was 1.59±0.32 µm. The capillaries were changed between these measurements from 10.46 mm and 10.15 mm long to 10.20 mm and 10.32 mm long, which allowed the formation of a stable perpendicular window [37].

7.2.3 Stability characterisation

The pointing stability of the laser after reflection from the plasma mirror is important. A measurement of how much the pointing was fluctuating was taken and is shown in Figure 7.8. The stability of the window was different in the two characteristic planes of the film. It was measured at 1.09±0.06 mrad around the y-axis as indicated in Figure 7.3, and 0.088±0.005 mrad around the z-axis. The stability is poorer around the y-axis as any motion of the order of µm in Z plane changes the skew angle of the window in this plane,

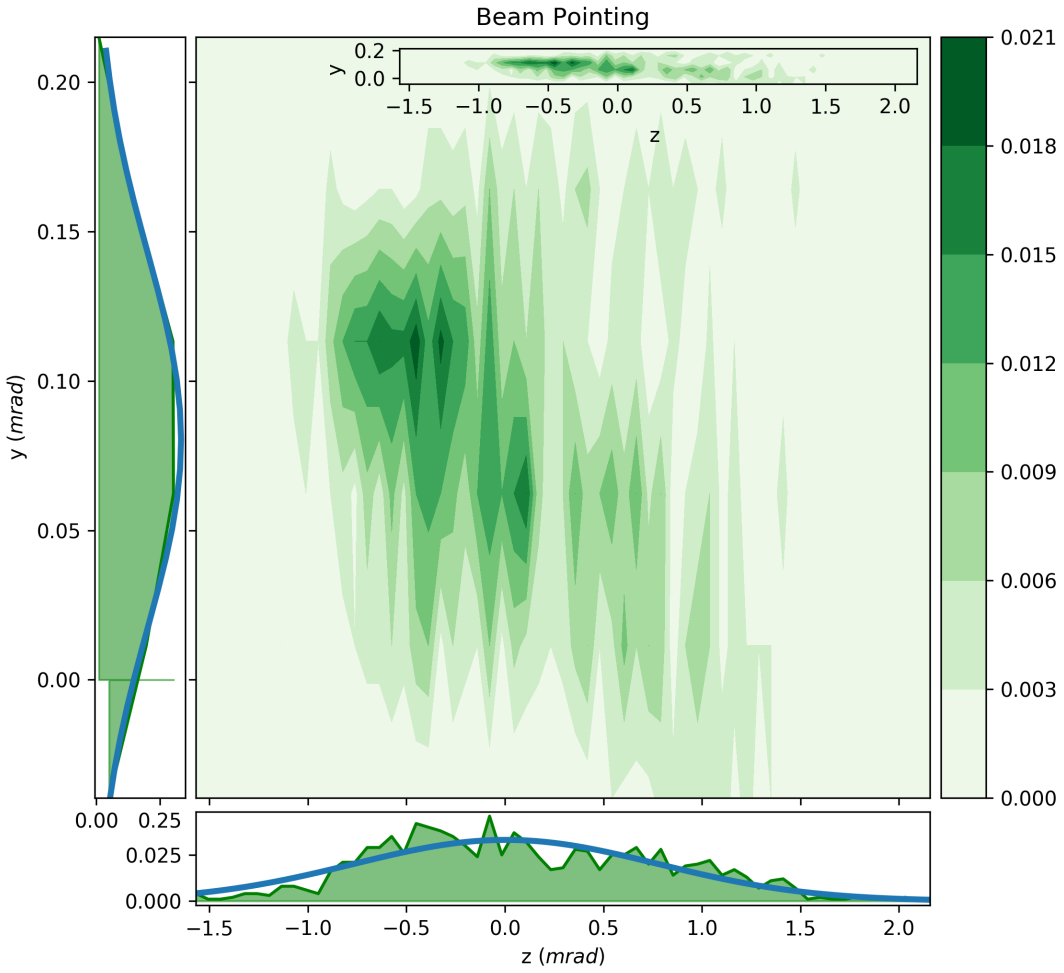

Figure 7.8: The pointing of the probe laser spot after reflecting off the water window. The stability measurement was created from a video with a exposure time of 1/83 s and tracking the main feature of the reflection. The stability is different in the two directions, the Z had a stability of 1.09±0.06 mrad and the Y: 0.088±0.005 mrad. The inset plot shows the data with equal aspect ratio.

as this motion was significant compared with the diameter of the liquid jets (100 µm). Therefore, any vibrations in the system will reduce the pointing stability in this axis. For a Y motion the collision point would move up or down on each stream which would only

have a small change in the angle of incidence. Hence, this angle is less sensitive to small changes caused by vibrations in the system.

Vibrations in the system were minimised by building the nozzle mounts out of one mirror mount (Figure 7.3). The metal tubing was attached to the optical table at regular points to damp vibrations, and the pump was not attached to the table. When operating in vacuum, the vacuum pumps may cause vibrations that would lead to an decrease in stability around the Y axis. Depending on the target, this pointing fluctuation may or may not be an issue.

7.2.4 High intensity reflection measurements

High intensity reflection measurement experiments were carried out under vacuum using the lambda-cubed (λ^3) laser at CUOS at the University of Michigan by previous researchers. This laser utilises chirped pulse amplification and delivers 800 nm wavelength laser pulses containing energies up to 20 mJ with a full-width-half-maximum (FWHM) pulse duration around 43 fs at a repetition rate of 500 Hz. Due to the limit of the optical diagnostic system, the system repetition rate was decreased to 83.3 Hz by using a chopper in the system. A half wave plate and polariser combination was mounted between the target and the laser system, which gave control of the incident intensity of the laser using a computer-controlled rotation stage.

The schematic set-up for generating the water film plasma mirror is shown in Figure 7.9. The incoming laser beam had a Gaussian beam diameter of 22 mm and was focused by a lens with a focal length of 650 mm, producing a focal spot around 30 µm diameter. The average power of the beam before focus was 3 W at the repetition frequency of 83.3 Hz. The maximum intensity on the target in this work was $\sim 5 \times 10^{16}\,\mathrm{Wcm^{-2}}$. The water film was positioned at the focus of the lens. When the intensity was great enough the surface of the film was ionised, generating a plasma mirror which reflected the remainder of the pulse. The reflected light was imaged onto a CCD camera (640 × 480 pixels each 5.6×5.6 µm) via a partially reflecting wedge, to decrease the delivered energy, and a lens. The nozzles were mounted on three-axis x-y-z stages, allowing the position

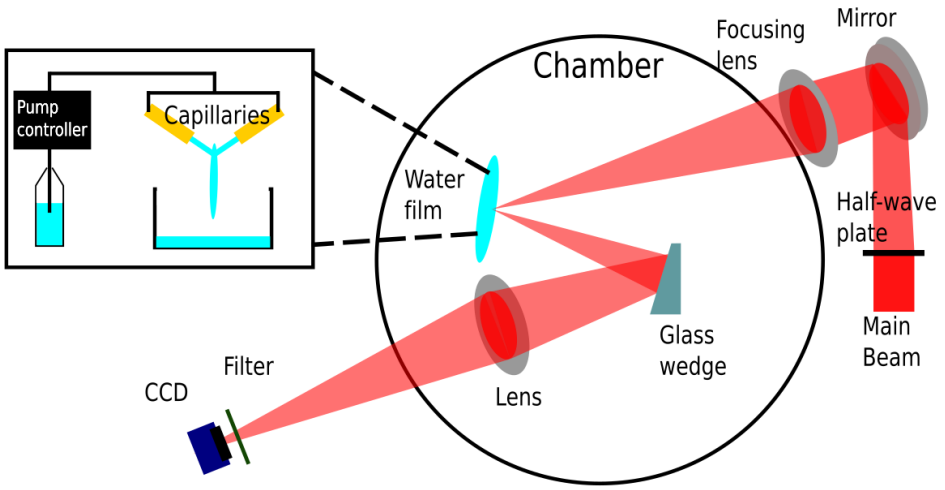

Figure 7.9: Schematic of the experimental set-up for a water film plasma mirror. The laser pulse was focused using a 650 mm focus length lens into a pure water film from two capillary water nozzles having an inner diameter of 100 µm. The reflection of the laser from the water film was attenuated by a wedge and passes through the lens to be imaged onto the CCD. The water film was controlled by a water pump and the capillaries were mounted on a x-y-z rotation stage [37]. The vacuum chamber had a diameter of ∼80 cm.

of the water film to be changed as well as the incident angles of the colliding jets. The inner diameter of the capillaries was 100 µm and the water flow rate was 6.5 mL min^{-1}. This corresponds to a flow rate of 6.9 ms^{-1} out of each nozzle so the liquid moves ∼80 mm between laser pulses. The chamber was under vacuum for the experiment, to avoid the generation of air plasma or laser filamentation. It should be noted that the vapour pressure of water is 30 mbar at room temperature, but the effect of the vacuum on the water film was uncharacterised for this work. Reducing the vacuum chamber pressure to below the vapour pressure of the liquid results in the liquid becoming gaseous and spreading around the chamber. This will limit the minimum chamber pressure reached, and the quality of the beam path could be degraded by depositing material on optics. Therefore, to mitigate the problems caused by the liquid in vacuum this optic would be best placed in a differentially pumped chamber or a different vacuum chamber to allow the rest of the experiment to be kept clean and at low pressure.

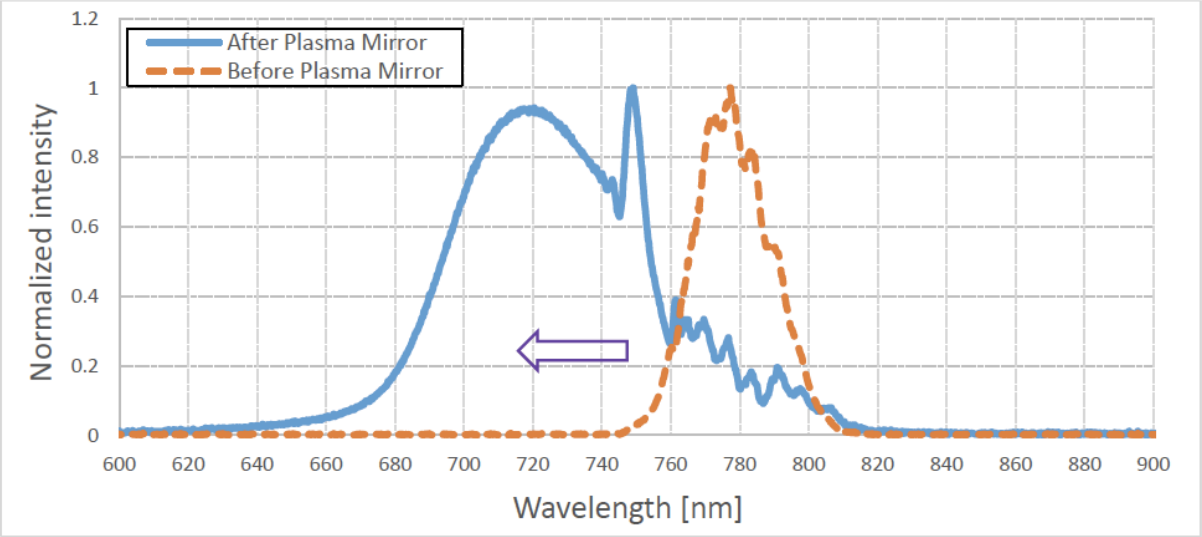

Figure 7.10: The spectrum of the laser before and after the plasma. The dotted curve shows the spectrum of the main laser beam, as a reference. The solid curve shows the spectrum after the water film plasma mirror. The FWHM of the spectra becomes wider after plasma mirror and there is also a blue shifting [37].

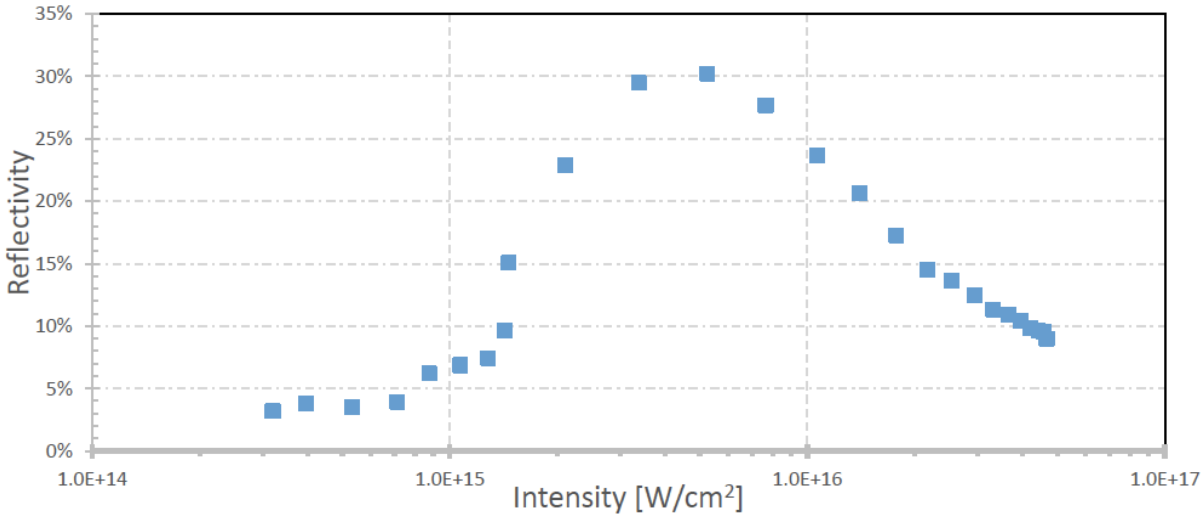

Figure 7.11: Assumed reflectivity of the pure water film using a pulse duration of 43 fs and repetition rate of 83.3 Hz. The intensity was varied by rotating the half wave plate [37].

The spectrum of the laser before and after the plasma is shown in Figure 7.10. It is clear that the centre wavelength has a blue shift of 60 nm following the plasma mirror. The FWHM of the laser pulse spectrum increases in reflection. However, it is unlikely that this indicates any additional pulse compression and rather, the presence of blue-shifting is likely attributable to ionization of the background water vapour (30 mbar) inside the chamber [197, 198]. This may also have reduced the transmitted energy measured in the experiments as the "neutral density" filters used were chosen for their spectral dependence in the range from 750 nm to 820 nm. The other viable liquid for stable films was ethylene glycol which has a lower vapour pressure. This would reduce the background vapour, and therefore the blue-shift. However, this was not investigated to avoid introduction of carbon into the vacuum system.

To characterise the reflectivity of the water plasma mirror the laser was operated at either 83.3 Hz or in single shot mode. The effective reflectivity of the water film as a function of the intensity is shown in Figure 7.11. The effective reflectivity was measured by taking the ratio of the integrated signal measured on a CCD camera directly

before and after the water film. In Figure 7.11, each data point represents an average result of 500 images obtained from the CCD camera. With the near-normal Fresnel intensity reflection being 2%, reflected by both surfaces of the water film, the total relative reflected power without plasma should be 4%. For future experiments the thickness of the film should be matched so its thickness is $\frac{n\lambda}{4}$, where n in an odd integer, the film should display AR properties and the reflectivity reduced [199]. At an intensity below $7 \times 10^{14}\,\mathrm{Wcm^{-2}}$, the reflectivity was 4%, matching the expected value. The threshold intensity of $7 \times 10^{14}\,\mathrm{Wcm^{-2}}$ is somewhat higher than the damage threshold measurements of a solid target ($10^{14}\,\mathrm{Wcm^{-2}}$) [200, 201]. Above this threshold the effective reflectivity rises up to 30% at an intensity of about $5 \times 10^{15}\,\mathrm{Wcm^{-2}}$, similar to the intensity with the laminar flow water film claimed by Panasenko *et al.* [191]. The measured maximum effective reflectivity was lower than previous liquid jet experiments.

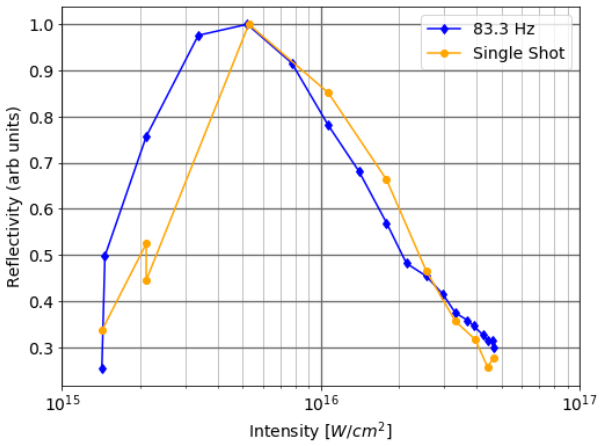

Figure 7.12: Comparison of repetition rate and plasma mirror material with water for single shot data and 83 Hz results [37].

The difference in reflection between single shot mode and high repetition rate was investigated. Figure 7.12 shows the reflectivity trend with intensity for the two operating regimes. This blue-shift modifies the laser to a spectral region where the CCD detector sensitivity is higher and throughput of the optical filter has increased, which compromises the quantitative nature of the measurement shown in Figure 7.10. However, since the

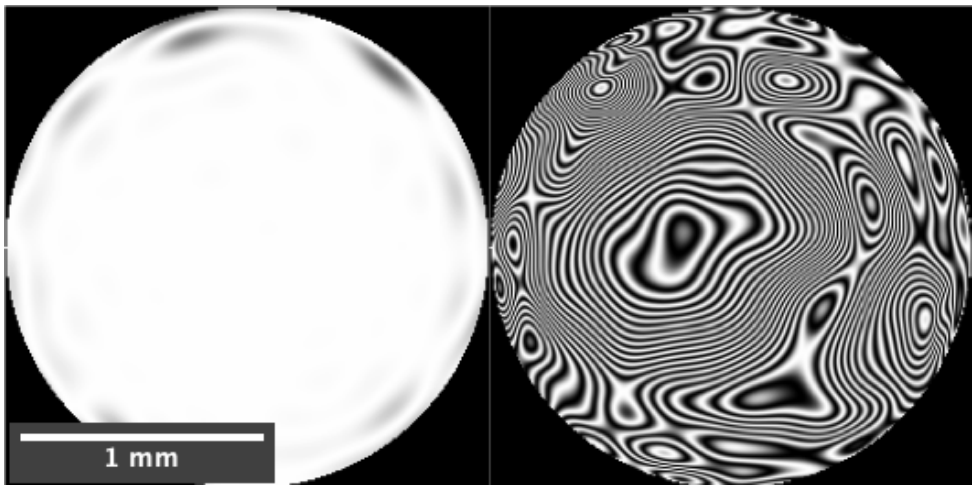

Figure 7.13: Reflected beam profile measurements of the liquid film with a low intensity beam. The film was in a liquid state, not a plasma. The unperturbed beam size was $\approx 0.5\,\mathrm{cm}^2$. The left hand image shows the phase of the incoming HeNe beam. The right hand image shows the phase measurement of the reflected beam. Each contour corresponds to a 2π phase shift.

general trend is consistent with single-shot operations, with the reflectivity for both cases normalised to its maximum value, it indicates that the water film studied may be suitable for use as a plasma mirror.

7.2.5 Reflected beam profile measurements

The beam profile reflected off the mirror is important. Ideally a spot would remain a spot after reflection, showing that the mirror does not deform the beam profile. A wavefront sensor (Shack-Hartmann design, Section 3.2.1) was used to measure the amount of distortion to the reflected wavefront.

The probing HeNe beam (λ =633 nm [49]) was measured to have an area of $\approx 0.5\,\mathrm{cm}^2$. An assumption made for this calculation was that the wavefront shape was not changing with respect to time. The stability measurements show an overall motion but no relative motion. This is a positive sign, as theoretically it will be possible to build an optic to correct for the distortion of the spot, therefore making a larger area of the plasma mirror

usable. Optics' surface flatness is measured in number of wavelength shifts per inch and for a good quality optic is less that $\lambda/4$ per inch, with high-flatness mirrors at $\lambda/20$ per inch. Measuring from the centre spot to the edge there is a flatness of $\approx 900\lambda$ per inch (Figure 7.13). The amount of wavefront distortion is too large to correct in one go for current adaptive optics, such as deformable mirrors. However, as this is an important problem to solve, it is not unreasonable to assume that an optic could be built to correct for this.

The reflected beam profile had what looked like a severe coma aberration, which might come from a slight curvature of the films surface. Unfortunately, there was not enough time to investigate this. The probe beam was reflected off the film about the Y axis, due to the lack of space in the Z plane. Therefore, reflecting in a different axis may improve the beam quality.

The main issue with this measurement was it was done at atmospheric pressure with a low intensity laser. This meant that the beam profile was measured with the reflection from the liquid, not the reflection of a plasma layer. Therefore, the beam will have been reflecting from both the front and back surfaces, and this will have also caused interference. This interference is likely to be the cause of the wavefront shifts. Further investigation of the reflected beam profile is required with a high intensity beam, creating a plasma mirror, under vacuum conditions.

7.3 Conclusion

This work has made measurements assessing the feasibility of a pure water film created by colliding liquid jets for use as a regenerating plasma mirror for high repetition rate systems (kHz). The flowing water-based plasma mirror has clear benefits, including refreshing the surface automatically and avoiding high-Z plasma debris. The maximum plasma mirror reflectivity was 30% which was less than that achieved by the water film produced by Panasenko *et al.* [191], but the flow rate is 2 orders of magnitude greater. There is a large flexibility in this water film system: the pressure of the water pump can be controlled,

and hence the size of the window; the diameter of the nozzles; the relatively angle of the two nozzles; and the film material can be replaced, ethylene glycol being a key candidate.

Comparisons between the regenerating water film in single shot mode and high repetition rate indicate the compatibility of this optic with high repetition-rate laser systems. The stability and thickness measurements show the current set-up is close to the required parameters. In addition to improvements of the reflectivity measurements, further work could be done to see if changing the capillary size alters the thickness of the film to give AR properties, and hence, improving the intensity contrast ratio.

8 | Conclusion

In this thesis, work on the development of laser wakefield accelerator (LWFA) sources has been presented, with the aim of enabling the deployment of LWFAs into industrial settings. The data chapters presented all add to the understanding required to make this step.

8.1 X-ray source development

Chapter 4 describes the characterisation of an X-ray beam created from a LWFA driven bremsstrahlung radiation source. X-ray source tunability has been shown by altering the properties of both the electron beam and the bremsstrahlung converter target. The produced X-ray source enables single-shot high-resolution imaging of dense objects due to its small source size (of the order of 50 µm), high flux and high photon energy (with over half the X-ray beam energy from photons over ∼100 MeV). This source had the highest recorded photon energy from a LWFA bremsstrahlung source.

The large experimental fluctuations measured in this X-ray source were due to the fluctuating electron beams. Methods of reducing these electron fluctuations are presented in Chapters 5 and 6, showing methods for improving the electron source. The electron fluctuations will also be reduced as the stability of laser systems improve. Therefore, it is expected that the stability of future LWFA bremsstrahlung sources can easily be increased.

8.2 Electron source development

Chapter 5 investigated the controlled injection of electrons into the wake using a sharp density transition. This injection method was found experimentally to create high energy electron bunches with a small energy spread. Fluid simulations of the density transition formation were performed, and a novel gas jet design with no moving parts was also proposed. Improving the stability of the electron injection will increase stability in the end source, whether that is the accelerated electrons or the X-rays created from the electrons (Chapter 4).

Chapter 6 showed the benefit of using a Bayesian optimisation algorithm when searching for different electron beam characteristics. The optimisation of charge showed that the global optimal position could be found in $\lesssim$ 20 laser bursts. All LWFAs require optimisation before data collection, as laser conditions are variable with time. When deployed on future accelerators, performing the optimisation in a reduced number of data points will increase the effective operational time of the LWFA. Another benefit is the global optimum found using the Bayesian optimisation algorithm. This is unlikely to be located via conventional optimisation, using 1D parameter scans, due to the 2D couplings discovered.

The power of this Bayesian optimisation technique is that any characteristic can be optimised, as long as a fitness function of the characteristic can be created. The fitness function returns a metric of the characteristic with one number and an error for each position in input parameter space. The Bayesian optimisation algorithm produces a surrogate model in the optimisation parameter space, which when explored allows understanding of the physical processes behind the optimisation. In the experiments performed, these surrogate models found that the rise time of the laser pulse was a key parameter for the optimisations. A short laser pulse rise time was seen at the optimal input parameters for accelerated charge and beam energy. A comparatively longer rise time was thought to be one of the key changes to create narrow divergence electron beams, compared to the maximum electron beam energy parameters.

Future work could combing the Bayesian optimisation technique (Chapter 6) with controlled injection methods (Chapter 5) with the optimisation parameter being for stability of the electrons produced. Bayesian optimisation was found to produce an 'electron source far exceeding that achieved manually with a 5 TW class laser system' [36] indicating that the combination of these two methods would produce an extremely stable electron source.

8.3 High repetition rate plasma mirror development

Chapter 7 describes the characterisation of a new high repetition rate plasma mirror. This plasma mirror, based on a flowing liquid, has the ability to work at the order of ∼kHz, a higher repetition rate than other liquid based plasma mirrors. This plasma mirror enables contrast enhancement for high repetition rate lasers, and one potential use would be the injection of subsequent laser pulses into a staged laser wakefield accelerator.

8.4 Summary

This work helps advance LWFAs from their current proof-of-principle research state to real life applications by furthering our understanding of the sources they can create. The Bayesian optimisation method has been shown to be an effective tool for optimising these sources, which can be optimised and controlled through adaptation of the injection mechanism and laser and plasma parameters. Injection methods such as the use of a tailored density profile can produced narrow energy spread electron bunches. The X-ray sources produced from a LWFA have clear industrial uses, and have been shown to be tunable using simple control parameters. The next generation of petawatt class lasers that are starting to come on-line now, operating repetition rates of $\gtrsim$1 Hz, combined with work such as this, will create sources which create active industrial involvement.

A | Derivations

A.1 Gaussian beam propagation

The beam propagation can be calculated from the paraxial wave equation [45]. The normal wave equation is:

$$\nabla^2 \vec{E} - \frac{n^2}{c^2}\frac{\partial^2}{\partial t^2}\vec{E} = 0 \tag{A.1}$$

where n is the refractive index ($n = 1$ for vacuum) and c is the speed of light. Assuming that the wave is propagating in the z direction, the solution takes the form:

$$E(x, y, z, t) = E_0 \psi(x, y, z) \exp(i(\omega t - kz)) \tag{A.2}$$

Splitting the Laplacian operator into the transverse Laplacian operator and the partial derivatives with respect to the direction of propagation, and then by assuming that the wave number k is a large number, ignoring the smallest term the paraxial equation is as follows:

$$\begin{aligned} 0 &= \nabla_t^2 \psi - 2ik\frac{\partial \psi}{\partial z} + \frac{\partial^2 \psi}{\partial z^2} \\ &\approx \nabla_t^2 \psi - 2ik\frac{\partial \psi}{\partial z} \\ 0 &= \frac{1}{r}\frac{\partial}{\partial r}\left(r\frac{\partial \psi}{\partial r}\right) - 2ik\frac{\partial \psi}{\partial z} \end{aligned} \tag{A.3}$$

The solutions to this equation are in the form:

$$\psi_0 = \exp\left(-i\left[P(z) + \frac{kr^2}{2q(z)}\right]\right) \tag{A.4}$$

Substituting in Equation A.4 into Equation A.3:

$$\left[\frac{k^2}{q(z)^2}\left(q\prime(z) - 1\right)r^2 - 2k\left(P\prime(z) + \frac{i}{q(z)}\right)\right]\psi_0 = 0 \tag{A.5}$$

Solutions exist when:

$$\begin{aligned} q\prime(z) &= 1 \\ P\prime(z) &= \frac{-i}{q(z)} \end{aligned} \tag{A.6}$$

$$\begin{aligned} q(z) &= z + iz_0 \\ q(z=0) &= iz_0 \end{aligned} \tag{A.7}$$

It turns out the additional term (z_0) is the Rayleigh length ($\mathcal{Z}_r$). The Rayleigh length describes the distance from the focus to the point where the beam electric field amplitude decreases to the $1/e$ of the maximum, and the intensity to $1/e^2$:

$$\mathcal{Z}_R = \frac{n\pi w_0^2}{\lambda_0} \tag{A.8}$$

The solutions to the paraxial wave equation now take the form:

$$\psi(z=0) = \exp\left(-\frac{kr^2}{2\mathcal{Z}_r}\right)\exp\left(-iP(z=0)\right) \tag{A.9}$$

The first term (exponential) is real, and shows that with an increasing r there is a decrease in amplitude of the electric field. The $\frac{1}{e}E_0$ value is reached when $r = \sqrt{(2\mathcal{Z}_r)/k}$. The minimum size of the beam can be calculated by re-arranging Equation A.8:

$$w_0^2 = \frac{2\mathcal{Z}_r}{k} = \frac{\lambda_0 \mathcal{Z}_r}{n\pi} \tag{A.10}$$

The $1/q(z)$ term from Equation A.4, using Equation A.7 becomes:

$$\frac{1}{q(z)} = \frac{z}{z^2 + \mathcal{Z}_r^2} - i\frac{\mathcal{Z}_r}{z^2 + \mathcal{Z}_r^2} \tag{A.11}$$

To work out the waist at $z \neq 0$ by substituting in Equation A.10 and Equation A.11, the solution to the paraxial wave equation Equation A.4 becomes:

$$\psi_0 = \exp\left(-\frac{k\mathcal{Z}_r r^2}{2(z^2 + \mathcal{Z}_r^2)}\right)\exp\left(-i\frac{kzr^2}{2(z^2 + \mathcal{Z}_r^2)}\right)\exp(-iP(z)) \tag{A.12}$$

The first exponential term describes amplitude decrease with r. A decrease by $1/e$ occurs at $r = \frac{2(z^2+\mathcal{Z}_r^2)}{k\mathcal{Z}_r}^{0.5}$. Hence the width of the beam is:

$$\begin{aligned} w^2(z) &= \frac{2}{k\mathcal{Z}_r}(z^2 + \mathcal{Z}_r^2) = \frac{2\mathcal{Z}_r}{k}\left(1 + \left(\frac{z}{\mathcal{Z}_r}\right)^2\right) \\ &= w_0^2\left(1 + \left(\frac{\lambda_0 z}{\pi n w_0^2}\right)^2\right) = w_0^2\left(1 + \left(\frac{z}{\mathcal{Z}_r}\right)^2\right) \end{aligned} \tag{A.13}$$

Equation A.11 is rewritten as:

$$\frac{1}{q(z)} = \frac{1}{R(z)} - i\frac{\lambda_0}{\pi n w(z)^2} R(z) \tag{A.14}$$

where the radius of curvature is:

$$\begin{aligned} R(z) &= \frac{1}{z}\left(z^2 + \mathcal{Z}_r^2\right) \\ &= z\left(1 + \left(\frac{\mathcal{Z}_r}{z}\right)^2\right) \end{aligned} \tag{A.15}$$

For completeness the $P(z)$ term is as follows, which allows the plotting of the electric field in Figure 2.3:

$$iP(z) = \ln\left(\left(1 + \frac{z}{\mathcal{Z}_r}^2\right)^{0.5}\right) - i\arctan\left(\frac{z}{\mathcal{Z}_r}\right) \tag{A.16}$$

The electric field is:

$$\begin{aligned} E(z,r) = E_0 &\left(\frac{w_0}{w(z)}\exp\left(-\frac{r^2}{w^2(z)}\right)\right) \\ &\times \exp\left(-i\left(kz - \arctan\left(\frac{z}{z_0}\right)\right)\right) \\ &\times \exp\left(-i\frac{kr^2}{2R(z)}\right) \\ &\times \exp(i\omega t) \end{aligned} \tag{A.17}$$

Here each line of the equation corresponds to the: amplitude factor, longitudinal phase, radial phase and temporal phase.

A.2 1D Plasma potential

Following the method in [60], the 1D plasma potential can be calculated from the following the starting information and assumptions: one fluid, cold relativistic hydrodynamics; Maxwell's equations; and the quasi-static approximation.

Equation of motion:

$$\frac{D\vec{p}}{Dt} = m_e\left(\frac{\partial\vec{v}}{\partial t} + (\vec{v}\cdot\nabla)\vec{v}\right) = -e(\vec{E} + \vec{v}\times\vec{B}) \tag{A.18}$$

Continuity equation:

$$\frac{\partial n_e}{\partial t} + \nabla\cdot(n_e\vec{v}) = 0 \tag{A.19}$$

Gauss' Law:

$$\nabla \cdot \vec{E} = \frac{-e(n_e - n_i)}{\epsilon_0} \tag{A.20}$$

where n_e is the plasma density, n_i the ion density, m_e the mass of the electron, ϵ_0 the vacuum permittivity, $\vec{E}$ the electric field and $\vec{B}$ the magnetic field.

The change in momentum comes from the force applied, using $\vec{E} = -\frac{\partial \vec{A}}{\partial t}$:

$$\Delta(m\vec{v}) = \int \vec{F} dt = \int q\vec{E} dt = -q \int \frac{\partial \vec{A}}{\partial t} dt \tag{A.21}$$

As $t \to 0$ the position is constant, so:

$$\begin{aligned} \Delta(m\vec{v}) &= -q \int \frac{\partial \vec{A}}{\partial t} dt \\ &= -q \int \frac{d\vec{A}}{dt} dt = q\Delta\vec{A} \\ \Delta(m\vec{v} + q\vec{A}) &= \text{ constant} \end{aligned} \tag{A.22}$$

Therefore:

$$\begin{aligned} \vec{p} &= e\vec{A} \\ \vec{v} &= \frac{e}{m}\vec{A} \end{aligned} \tag{A.23}$$

Using vector identity $(\vec{A}\cdot\nabla)\vec{A} + \vec{A}\times(\nabla\times\vec{A}) = \frac{1}{2}\nabla(\vec{A}\times\vec{A}) = \frac{1}{2}\nabla|\vec{A}|^2$ then Equation A.18 is rearranged to:

$$\begin{aligned} m_e\frac{\partial \vec{v}}{\partial t} + e\vec{E} &= -e\vec{v}\times\vec{B} - m_e(\vec{v}\cdot\nabla)\vec{v} \\ &= -e\left(\frac{e\vec{A}}{m_e}\times\nabla\times\vec{A}\right) - m_e\left(\frac{e\vec{A}}{m_e}\cdot\nabla\right)\frac{e\vec{A}}{m_e} \\ &= -\frac{e^2}{2m_e}\nabla|\vec{A}|^2 \end{aligned} \tag{A.24}$$

Linearising the equation of motion (EOM), continuity and Gauss's law by using $n_e = n_0 + \delta n_e$, $n_i = n_0$, and $a_0 = \frac{eA_0}{m_e c}$. Take only the first order terms. The EOM (Equation A.24) becomes:

$$m\frac{\partial v}{\partial t} + eE = -\frac{mc^2}{2}\frac{\partial a_0^2}{\partial x} \tag{A.25}$$

The continuity equation (Equation A.19) becomes:

$$\begin{aligned} \frac{\partial \delta n_e}{\partial t} + n_0\nabla\vec{v} + \nabla\cdot(\delta n\vec{v}) &= 0 \\ \frac{\partial \delta n_e}{\partial t} + n_0\nabla\vec{v} &\simeq 0 \end{aligned} \tag{A.26}$$

Gauss's Law (Equation A.20) becomes:

$$\frac{\partial}{\partial x}\vec{E} = -e\frac{\delta n_e}{\epsilon_0} \tag{A.27}$$

The EOM for small electron density perturbations is produced by substituting the linearised results in. Using ∂_x of Equation A.24, ∂_t of Equation A.26:

$$\begin{aligned}\frac{\partial^2 a^2}{\partial x^2} &= \frac{2}{m_e c^2}\left(m_e\frac{\partial^2 v}{\partial x \partial t} + e\frac{\partial E}{\partial x}\right) \\ &= \frac{2}{c^2}\frac{\partial^2 v}{\partial x \partial t} + \frac{2}{m_e c}\frac{\partial E}{\partial x} \\ &= \frac{2}{n_0 c^2}\frac{\partial^2 \delta n_e}{\partial t^2} + \frac{2}{n_0 c^2}\omega_p^2 \delta n_e\end{aligned} \tag{A.28}$$

which uses $\omega_p = \sqrt{\frac{n_e e}{m_e \epsilon_0}}$.

Giving the EOM:

$$\left(\frac{\partial^2}{\partial t^2} + \omega_p^2\right)\delta n_e = \frac{n_0 c^2}{2}\frac{\partial^2 a^2}{\partial x^2} \tag{A.29}$$

This equation can be used to work out the maximum electric field, as shown by Dawson [202]:

$$E_{\max} = \frac{\omega_p^2 m_e}{e}\frac{\lambda_E}{2\pi} \tag{A.30}$$

Once fields exceed this limit then the fluid approximation breaks down [18, 202]. From this the maximum energy is also calculated:

$$E_{\max} = \frac{m_e \omega_p v_g}{e} = \frac{v_g}{c}E_0 \tag{A.31}$$

where $E_0 = (m_e c\omega_p)/e$, and ω_p scales with $\sqrt{n_e}$. The maximum energy an electron gains is:

$$W_{\max} = 2\gamma_p^2 m_e c^2 = 2\left(\frac{\omega}{\omega_p}\right)^2 m_e c^2 \tag{A.32}$$

as $\gamma_p = \frac{\omega}{\omega_p}$. This means that at lower densities electron can get to higher energies, which is because dephasing is more detrimental than getting larger acceleration fields at the higher plasma densities.

A.2.1 Relativistic coordinate transform

The plasma oscillations are travelling in the wake of the driving laser pulse. Transforming into the coordinates of the co-moving frame so the laser is static is done with the following transforms.

Position:

$$\begin{aligned} x - ct &= \zeta \\ \partial_x &= \partial_\zeta \end{aligned} \tag{A.33}$$

Time:

$$\begin{aligned} t &= \tau \\ \partial_t &= -c\partial_\zeta + \partial_t \end{aligned} \tag{A.34}$$

The quasi-static approximation means that quantities vary spatially faster than they do temporally, which results in $\partial_\tau \to -c\partial_\zeta$.

The equations in the co-moving frame are now the following.

Equation of motion (Equation A.29) becomes:

$$\left[\frac{\partial^2}{\partial\zeta^2} + k_p^2\right]\delta n_e = \frac{n_0}{2}\frac{\partial^2 a^2}{\partial\zeta^2} \tag{A.35}$$

Continuity equation (Equation A.26) becomes:

$$\frac{\partial^2 v}{\partial\zeta^2} = \frac{c}{n_0}\frac{\partial^2\delta n_e}{\partial\zeta^2} \tag{A.36}$$

Gauss' law (Equation A.27) becomes:

$$\begin{aligned} \frac{\partial E}{\partial\zeta} &= -\frac{e\delta n_e}{\epsilon_0} \\ \frac{\partial^2\phi}{\partial\zeta^2} &= \frac{e\delta n_e}{\epsilon_0} \end{aligned} \tag{A.37}$$

Bibliography

[1] T. Tajima and J. M. Dawson. "Laser electron accelerator". *Physical Review Letters* 43.4 (1979), pp. 267–270. DOI: 10.1103/PhysRevLett.43.267.

[2] S. M. Hooker. "Developments in laser-driven plasma accelerators". *Nature Photonics* 7.10 (2013), pp. 775–782. DOI: 10.1038/nphoton.2013.234.

[3] J Faure et al. "A laser-plasma accelerator producing monoenergetic electron beams." *Nature* 431.7008 (2004), pp. 541–544. DOI: 10.1038/nature02963.

[4] S. P. D. Mangles et al. "Monoenergetic beams of relativistic electrons from intense laser-plasma interactions". *Nature* 431.7008 (2004), pp. 535–538. DOI: 10.1038/nature02939.

[5] C. G. R. Geddes et al. "High-quality electron beams from a laser wakefield accelerator using plasma-channel guiding." *Nature* 431.7008 (2004), pp. 538–41. DOI: 10.1038/nature02900.

[6] A. J. Gonsalves et al. "Petawatt Laser Guiding and Electron Beam Acceleration to 8 GeV in a Laser-Heated Capillary Discharge Waveguide". *Physical Review Letters* 122.8 (2019), p. 084801. DOI: 10.1103/PhysRevLett.122.084801.

[7] A. R. Maier et al. "Decoding Sources of Energy Variability in a Laser-Plasma Accelerator". *Physical Review X* 10.3 (2020), p. 31039. DOI: 10.1103/physrevx.10.031039.

[8] A. P. Chernyaev and S. M. Varzar. "Particle accelerators in modern world". *Physics of Atomic Nuclei* 77.10 (2014), pp. 1203–1215. DOI: 10.1134/S1063778814100032.

[9] W. N. Association. *Radioisotopes in Medicine*. data retrieved: June 2020, https://www.world-nuclear.org/information-library/non-power-nuclear-applications/radioisotopes-research/radioisotopes-in-medicine.aspx. 2020.

[10] R. W. Hamm. "Linacs for medical and industrial applications". *Proceedings of the 1986 International Linac Conference, Stanford, California, USA* (1986), pp. 33–36.

[11] energy.gov. *How particle accelerators work*. data retrieved: Feburary 2020, https://www.energy.gov/articles/how-particle-accelerators-work/. 2019.

[12] G. Aad et al. "Observation of a new particle in the search for the Standard Model Higgs boson with the ATLAS detector at the LHC". *Physics Letters, Section B: Nuclear, Elementary Particle and High-Energy Physics* 716.1 (2012), pp. 1–29. DOI: 10.1016/j.physletb.2012.08.020.

[13] E Rutherford. "The Scattering of α and β Particles by Matter and the Structure of the Atom". *Philosophical Magazine* 6.21 (1911).

[14] B. J. Holzer. "Introduction to Particle Accelerators and their Limitations". *Proceedings of the CAS-CERN Accelerator School: PlasmaWake Acceleration* 1.November 2014 (2016), p. 29. DOI: 10.5170/CERN-2016-001.29.

[15] R. J.V. D. Graaff. "A 15 000 000 Volt Electrostatic Generator". *Phys Rev* 38 (1931), p. 1919.

[16] A. R. Steere. "A Timeline of Particle Accelerators". *A Timeline of Particle Accelerators* (2005), pp. 1–82.

[17] home.cern. *LHC Facts and Figures*. data retrieved: January 2020, https://home.cern/sites/home.web.cern.ch/files/2018-07/factsandfigures-en_0.pdf. 2019.

[18] J. M. Cole. "Diagnosis and Application of Laser Wakefield Accelerators". PhD thesis. Imperial College London, 2016.

[19] M. Weiss. *Introduction to RF Linear Accelerators*. Tech. rep. CERN, 1994.

[20] European XFEL. *Facility Comparison*. data retrieved: June 2020, https://www.xfel.eu/facility/comparison/index_eng.html. 2020.

[21] F. F. Chen. "Erratum to: Introduction to Plasma Physics and Controlled Fusion". *Introduction to Plasma Physics and Controlled Fusion*. Cham: Springer International Publishing, 2018, E1–E1. DOI: 10.1007/978-3-319-22309-4_11.

[22] B. Hidding et al. "Plasma Wakefield Accelerator Research 2019 - 2040: A community-driven UK roadmap compiled by the Plasma Wakefield Accelerator Steering Committee (PWASC)". March (2019).

[23] C. Danson et al. "Petawatt class lasers worldwide". *High Power Laser Science and Engineering* 3 (2015), e3. DOI: 10.1017/hpl.2014.52.

[24] S. Kühn et al. "The ELI-ALPS facility: The next generation of attosecond sources". *Journal of Physics B: Atomic, Molecular and Optical Physics* 50.13 (2017). DOI: 10.1088/1361-6455/aa6ee8.

[25] D. Gustas et al. "High-charge relativistic electron bunches from a kHz laser-plasma accelerator". *Physical Review Accelerators and Beams* 21.1 (2018), pp. 1–7. DOI: 10.1103/PhysRevAccelBeams.21.013401.

[26] nobelprize.org. *The Nobel Prize in Physics 2018*. data retrieved: Feburary 2020, https://www.nobelprize.org/prizes/physics/2018/press-release/. 2018.

[27] R Brinkmann and Others. "Accelerator Layout of the XFEL". *XXII International Linear Accelerator Conference* 1 (2004), pp. 2–7.

[28] W. Decking and H. Weise. "Commissioning of the European XFEL Accelerator". *Proceedings of the 8th International Particle Accelerator Conference (IPAC2017)* 8 (2017), pp. 1–6.

[29] O. Lundh et al. "Few femtosecond, few kiloampere electron bunch produced by a laser-plasma accelerator". *Nature Physics* 7.3 (2011), pp. 219–222. DOI: 10.1038/nphys1872.

[30] A. Rousse et al. "Production of a keV X-Ray Beam from Synchrotron Radiation in Relativistic Laser-Plasma Interaction". *Physical Review Letters* 93.13 (2004), p. 135005. DOI: 10.1103/PhysRevLett.93.135005.

[31] K. Ta Phuoc et al. "All-optical Compton gamma-ray source". *Nature Photonics* 6.5 (2012), pp. 308–311. DOI: 10.1038/nphoton.2012.82.

[32] B. R. Wheaton. "Bremsstrahlung". *Compendium of Quantum Physics*. Ed. by D. Greenberger, K. Hentschel, and F. Weinert. Berlin, Heidelberg: Springer Berlin Heidelberg, 2009, pp. 78–81. DOI: 10.1007/978-3-540-70626-7_23.

[33] S Chen et al. "MeV-Energy X Rays from Inverse Compton Scattering with Laser-Wakefield Accelerated Electrons". *Physical Review Letters* 110.15 (2013), p. 155003. DOI: 10.1103/PhysRevLett.110.155003.

[34] N. D. Powers et al. "Quasi-monoenergetic and tunable X-rays from a laser-driven Compton light source". *Nature Photonics* 8.1 (2014), pp. 28–31. DOI: 10.1038/nphoton.2013.314.

[35] C. I. D. Underwood et al. "Development of control mechanisms for a laser wakefield accelerator-driven bremsstrahlung x-ray source for advanced radiographic imaging". *Plasma Physics and Controlled Fusion* 62.12 (2020), p. 124002. DOI: 10.1088/1361-6587/abbebe.

[36] R. J. Shalloo et al. "Automation and control of laser wakefield accelerators using Bayesian optimization". *Nature Communications* 11.1 (2020), p. 6355. DOI: 10.1038/s41467-020-20245-6.

[37] C. I. D. Underwood et al. "Characterization of flowing liquid films as a regenerating plasma mirror for high repetition-rate laser contrast enhancement". *Laser and Particle Beams* May (2020), pp. 1–7. DOI: 10.1017/S0263034620000129.

[38] S. Steinke et al. "Stable laser-ion acceleration in the light sail regime". *Physical Review Special Topics - Accelerators and Beams* 16.1 (2013), pp. 1–5. DOI: 10.1103/PhysRevSTAB.16.011303.

[39] S. Steinke et al. "Multistage coupling of independent laser-plasma accelerators". *Nature* 530.7589 (2016), pp. 190–193. DOI: 10.1038/nature16525.

[40] C. D. Murphy. "Diagnosis of High Energy Electron Beams Produced by Laser Wakefield Accelerators". PhD thesis. 2007, p. 144.

[41] D. J. Griffiths. *Introduction to electrodynamics*. 3rd ed. Pearson Education Inc, 2008.

[42] G. Tallents. *Laser-plasma interactions*. 2016.

[43] P. Jameson and A. Khvedelidze. "Classical dynamics of a charged particle in a laser field beyond the dipole approximation". *Physical Review A - Atomic, Molecular, and Optical Physics* 77.5 (2008), pp. 1–13. DOI: 10.1103/PhysRevA.77.053403.

[44] A Einstein. *On the quantum theory of radiation [in] Laser Theory, ed. FA Barnes*. 1972.

[45] G. Tallents and E. Wagenaars. *Radiation and Matter*. 2017.

[46] A. L. Schawlow and C. H. Townes. "Infrared and optical masers". *Physical Review* 112.6 (1958), pp. 1940–1949. DOI: 10.1103/PhysRev.112.1940.

[47] T. H. Maiman. "Stimulated optical radiation in Ruby". *Nature* 187.4736 (1960), pp. 493–494. DOI: 10.1038/187493a0.

[48] F. J. McClung and R. W. Hellwarth. "Giant optical pulsations from ruby". *Journal of Applied Physics* 33.3 (1962), pp. 828–829. DOI: 10.1063/1.1777174.

[49] K. F. Renk. *Basics of Laser Physics. Graduate Texts in Physics*. 2012, pp. 75–80. DOI: 10.1007/s00436-002-0802-5.

[50] D. Strickland and G. Mourou. "Compression of amplified chirped optical pulses". *Optics Communications* 56.3 (1985), pp. 219–221. DOI: 10.1016/0030-4018(85)90120-8.

[51] M. D. Perry and G. Mourou. "Terawatt to petawatt subpicosecond lasers". *Science* 264.5161 (1994), pp. 917–924. DOI: 10.1126/science.264.5161.917.

[52] W. B. Mori. "The physics of the nonlinear optics of plasmas at relativistic intensities for short-pulse lasers". *IEEE Journal of Quantum Electronics* 33.11 (1997), pp. 1942–1953. DOI: 10.1109/3.641309.

[53] C. D. Murphy et al. "Evidence of photon acceleration by laser wake fields". *Physics of Plasmas* 13.3 (2006). DOI: 10.1063/1.2178650.

[54] A. I. Rae. *Quantum Mechanics 5th Edition*. 5th ed. Taylor and Francis Group, 2008.

[55] E Esarey, C. B. Schroeder, and W. P. Leemans. "Physics of laser-driven plasma-based electron accelerators". *Reviews of Modern Physics* 81.3 (2009), pp. 1229–1285. DOI: 10.1103/RevModPhys.81.1229.

[56] K. Ishikawa. "Photoemission and Ionization of He+ under Simultaneous Irradiation of Fundamental Laser and High-Order Harmonic Pulses". *Physical Review Letters* 91.4 (2003), p. 043002. DOI: 10.1103/PhysRevLett.91.043002.

[57] Keldysh L. V. "Ionization in the field of a strong electromagnetic wave". *J. Exp. Theor. Phys.* 20.5 (1965), pp. 1307–1314. DOI: 10.1234/12345678.

[58] A. Kramida et al. *NIST Atomic Spectra Database*. NIST Atomic Spectra Database (ver. 5.8), [Online]. Available: `https://physics.nist.gov/asd` [2020, October 30]. National Institute of Standards and Technology, Gaithersburg, MD. 2020.

[59] A. Buck. "Advanced characterization and control of laser wakefield acceleration". PhD thesis. Max-Planck-Gesellschaft, 2011.

[60] R. Bingham and R. Trines. "Introduction to plasma accelerators: The basics". *CAS-CERN Accelerator School: Plasma Wake Acceleration 2014, Proceedings* 001.November 2014 (2014), pp. 67–77. DOI: 10.5170/CERN-2016-001.67.

[61] L. M. Gorbunov and V. I. Kirsanov. "Excitation of plasma waves by an electromagnetic wave packet". *Sov. Phys. JETP* 66.2 (1987), p. 290.

[62] C. Arran. personal communication. Mar. 16, 2020.

[63] E. Esarey and M. Pilloff. "Trapping and acceleration in nonlinear plasma waves". *Physics of Plasmas* 2.5 (1995), pp. 1432–1436. DOI: 10.1063/1.871358.

[64] W Lu et al. "Generating multi-GeV electron bunches using single stage laser wakefield acceleration in a 3D nonlinear regime". *Physical Review Special Topics - Accelerators and Beams* 10.6 (2007), pp. 1–12. DOI: 10.1103/PhysRevSTAB.10.061301.

[65] K. Nakamura et al. "GeV electron beams from a centimeter-scale channel guided laser wakefield accelerator". *Physics of Plasmas* 14.5 (2007). DOI: 10.1063/1.2718524.

[66] C. McGuffey et al. "Ionization induced trapping in a laser wakefield accelerator". *Physical Review Letters* 104.2 (2010), pp. 1–4. DOI: 10.1103/PhysRevLett.104.025004.

[67] A. Pak et al. "Injection and Trapping of Tunnel-Ionized Electrons into Laser-Produced Wakes". *Physical Review Letters* 104.2 (2010), p. 025003. DOI: 10.1103/PhysRevLett.104.025003.

[68] B. B. Pollock et al. "Demonstration of a narrow energy spread, âĹij0.5GeV electron beam from a two-stage laser wakefield accelerator". *Physical Review Letters* 107.4 (2011). DOI: 10.1103/PhysRevLett.107.045001.

[69] K. Schmid et al. "Density-transition based electron injector for laser driven wakefield accelerators". *Physical Review Special Topics - Accelerators and Beams* 13.9 (2010), pp. 1–5. DOI: 10.1103/PhysRevSTAB.13.091301.

[70] A. V. Brantov et al. "Controlled electron injection into the wake wave using plasma density inhomogeneity". *Physics of Plasmas* 15.7 (2008). DOI: 10.1063/1.2956989.

[71] K. K. Swanson et al. "Control of tunable, monoenergetic laser-plasma-accelerated electron beams using a shock-induced density downramp injector". *Physical Review Accelerators and Beams* 20.5 (2017), pp. 1–6. DOI: 10.1103/PhysRevAccelBeams.20.051301.

[72] A. J. Gonsalves et al. "Tunable laser plasma accelerator based on longitudinal density tailoring". *Nature Physics* 7.11 (2011), pp. 862–866. DOI: 10.1038/nphys2071.

[73] O. Kononenko et al. "2D hydrodynamic simulations of a variable length gas target for density down-ramp injection of electrons into a laser wakefield accelerator". *Nuclear Instruments and Methods in Physics Research, Section A: Accelerators, Spectrometers, Detectors and Associated Equipment* 829 (2016), pp. 125–129. DOI: 10.1016/j.nima.2016.03.104.

[74] M. Vargas et al. "Improvements to laser wakefield accelerated electron beam stability, divergence, and energy spread using three-dimensional printed two-stage gas cell targets". *Applied Physics Letters* 104.17 (2014), pp. 3–8. DOI: 10.1063/1.4874981.

[75] J. Faure et al. "Controlled injection and acceleration of electrons in plasma wakefields by colliding laser pulses". *Nature* 444.7120 (2006), pp. 737–739. DOI: 10.1038/nature05393.

[76] A. G. R. Thomas et al. "Monoenergetic electronic beam production using dual collinear laser pulses". *Physical Review Letters* 100.25 (2008), pp. 16–19. DOI: 10.1103/PhysRevLett.100.255002.

[77] S. Corde et al. "Femtosecond x rays from laser-plasma accelerators". *Reviews of Modern Physics* 85.1 (2013). DOI: 10.1103/RevModPhys.85.1.

[78] F. Albert and A. G. Thomas. "Applications of laser wakefield accelerator-based light sources". *Plasma Physics and Controlled Fusion* 58.10 (2016). DOI: 10.1088/0741-3335/58/10/103001.

[79] S. Fourmaux et al. "Single shot phase contrast imaging using laser-produced Betatron x-ray beams". *Optics Letters* 36.13 (2011), p. 2426. DOI: 10.1364/ol.36.002426.

[80] S. Kneip et al. "X-ray phase contrast imaging of biological specimens with femtosecond pulses of betatron radiation from a compact laser plasma wakefield accelerator". *Applied Physics Letters* 99.9 (2011), pp. 1–4. DOI: 10.1063/1.3627216.

[81] J. Wenz et al. "Quantitative X-ray phase-contrast microtomography from a compact laser-driven betatron source". *Nature Communications* 6.May (2015), pp. 1–6. DOI: 10.1038/ncomms8568.

[82] A. E. Hussein et al. "Laser-wakefield accelerators for high-resolution X-ray imaging of complex microstructures". *Scientific Reports* 9.1 (2019), pp. 1–13. DOI: 10.1038/s41598-019-39845-4.

[83] F Albert et al. "Laser wakefield accelerator based light sources: potential applications and requirements". *Plasma Physics and Controlled Fusion* 56.8 (2014), p. 084015. DOI: 10.1088/0741-3335/56/8/084015.

[84] R. D. Edwards et al. "Characterization of a gamma-ray source based on a laser-plasma accelerator with applications to radiography". *Applied Physics Letters* 80.12 (2002), pp. 2129–2131. DOI: 10.1063/1.1464221.

[85] Y. Glinec et al. "High-resolution γ-ray radiography produced by a laser-plasma driven electron source". *Physical Review Letters* 94.2 (2005), pp. 1–4. DOI: 10.1103/PhysRevLett.94.025003.

[86] A. Döpp et al. "A bremsstrahlung gamma-ray source based on stable ionization injection of electrons into a laser wakefield accelerator". *Nuclear Instruments and Methods in Physics Research, Section A: Accelerators, Spectrometers, Detectors and Associated Equipment* 830 (2016), pp. 515–519. DOI: 10.1016/j.nima.2016.01.086.

[87] K. Dong et al. "Micro-spot gamma-ray generation based on laser wakefield acceleration". *Journal of Applied Physics* 123.24 (2018). DOI: 10.1063/1.4997142.

[88] P. Reimers et al. "Some aspects of industrial non-destructive evaluation by X- and γ-ray computed tomography". *Nuclear Instruments and Methods in Physics Research* 221.1 (1984), pp. 201–206. DOI: 10.1016/0167-5087(84)90200-X.

[89] J.-N. Gruse et al. "Application of compact laser-driven accelerator X-ray sources for industrial imaging". *Nuclear Instruments and Methods in Physics Research Section A: Accelerators, Spectrometers, Detectors and Associated Equipment* 983.July (2020), p. 164369. DOI: 10.1016/j.nima.2020.164369.

[90] L. Antonelli et al. "X-ray phase-contrast imaging for laser-induced shock waves". *Epl* 125.3 (2019). DOI: 10.1209/0295-5075/125/35002.

[91] Varex Imaging. *Linear Accelerators*. data retrieved: March 2019, https://www.vareximaging.com/products/security-industrial/linear-accelerators. 2019.

[92] R. Van Noorden. "Radioisotopes: The medical testing crisis". *Nature* 504.7479 (2013), pp. 202–204. DOI: 10.1038/504202a.

[93] P. F. Moulton. "Spectroscopic and laser characteristics of Ti:Al_2O_3". *JOSA B* 3.1 (1986), pp. 125–133.

[94] A Wall, K F and Sanchez. "Titanium sapphire laser." *Lincoln Laboratory Journal; (USA)* 3.3 (1990), pp. 447–462.

[95] C. Le Blanc, P. Curley, and F. Salin. "Gain-narrowing and gain-shifting of ultra-short pulses in Ti: Sapphire amplifiers". *Optics Communications* 131.4-6 (1996), pp. 391–398. DOI: 10.1016/0030-4018(96)00262-3.

[96] E. Cartlidge. "The Light Fantastic". *Science Mag* 359.6374 (2018), pp. 382–385.

[97] P. Tournois. "Acousto-optic programmable dispersive filter for adaptive compensation of group delay time dispersion in laser systems". *Optics Communications* 140.4-6 (1997), pp. 245–249. DOI: 10.1016/S0030-4018(97)00153-3.

[98] Fastlite. *Dazzler ultrafast pulse shaper*. data retrieved: Oct 2020, https://fastlite.com/produits/dazzler-ultrafast-pulse-shaper/. 2020.

[99] RP-Photonics. *Acousto-optic Modulators*. data retrieved: July 2020, https://www.rp-photonics.com/acousto_optic_modulators.html. 2020.

[100] I. Optic. *HASO Wavefront sensors*. data retrieved: Oct 2020, https://www.imagine-optic.com/products/wavefront-sensors-and-optical-metrology-tools/haso-wavefront-sensors/. 2020.

[101] R Shack and B. Platt. "History and principles of Shack-Hartmann wavefront sensing". *Journal of Refractive Surgery* 17.October 2001 (2001), pp. 573–577.

[102] C. Iaconis and I. A. Walmsley. "Spectral phase interferometry for direct electric-field reconstruction of ultrashort optical pulses". *Opt. Lett.* 23.10 (1998), pp. 792–794. DOI: 10.1364/OL.23.000792.

[103] APE. *LX Spider*. data retrieved: Oct 2020, https://www.ape-berlin.de/en/spider-spectral-phase-interferometry-for-direct-electric-field-reconstruction/compact-lx-spider/. 2020.

[104] Y. Glinec et al. "Absolute calibration for a broad range single shot electron spectrometer". *Review of Scientific Instruments* 77.10 (2006), pp. 1–7. DOI: 10.1063/1.2360988.

[105] H. D. Young, R. A. Freedman, and A. L. Ford. *Sears and Zemansky's university physics*. Vol. 1. Pearson education, 2006.

[106] I. H. Hutchinson. *Principles of plasma diagnostics*. Vol. 44. 12. IOP Publishing, 2002, p. 2603.

[107] R. J. Shalloo. "Hydrodynamic Optical-Field-Ionized Plasma Waveguides for Laser Plasma Accelerators". PhD thesis. University of Oxford, 2018.

[108] A. O. Instruments. *Andor iKon-M 934 Camera Specifications*. data retrieved: Sept 2020, https://andor.oxinst.com/products/ikon-xl-and-ikon-large-ccd-series/ikon-m-934. 2020.

[109] J. Hubbell and S. Seltzer. *NIST Standard Reference Database Number 126, National Institute of Standards and Technology*. data retrieved: Oct 2019, https://www.nist.gov/pml/x-ray-mass-attenuation-coefficients. 2004.

[110] B. Henke, E. Gullikson, and J. Davis. *X-ray interactions: photoabsorption, scattering, transmission, and reflection at E=50-30000 eV, Z=1-92, Atomic Data and Nuclear Data Tables Vol. 54 (no.2), 181-342*. data retrieved: Nov 2019, http://henke.lbl.gov/optical_constants/. 1993.

[111] S. Kneip et al. "Bright spatially coherent synchrotron X-rays from a table-top source". *Nature Physics* 6.12 (2010), pp. 980–983. DOI: 10.1038/nphys1789.

[112] D. J. Corvan, G. Sarri, and M. Zepf. "Design of a compact spectrometer for high-flux MeV gamma-ray beams". *Review of Scientific Instruments* 85.6 (2014). DOI: 10.1063/1.4884643.

[113] W. P. Leemans et al. "Gamma-neutron activation experiments using laser wakefield accelerators". *Physics of Plasmas* 8.5 II (2001), pp. 2510–2516. DOI: 10.1063/1.1352617.

[114] G. A. Carlson, D. L. Fehl, and L. J. Lorence. "A differential absorption spectrometer for determining flash X-ray spectra". *Nuclear Inst. and Methods in Physics Research, B* 62.2 (1991), pp. 264–274. DOI: 10.1016/0168-583X(91)95910-6.

[115] M. Thoms. "The quantum efficiency of radiographic imaging with image plates". *Nuclear Instruments and Methods in Physics Research, Section A: Accelerators, Spectrometers, Detectors and Associated Equipment* 378.3 (1996), pp. 598–611. DOI: 10.1016/0168-9002(96)00530-X.

[116] W. R. Leo. *Techniques for nuclear and particle physics experiments: a how-to approach.* Springer Science & Business Media, 2012.

[117] Saint-Gobain. *CsI(Tl) Data sheet https://www.crystals.saint-gobain.com/sites/imdf.crystals.com/files/documents/csitl-and-na-material-data-sheet.pdf*. 2020.

[118] Saint-Gobain. *LYSO Data sheet https://www.crystals.saint-gobain.com/sites/imdf.crystals.com/files/documents/lyso-material-data-sheet.pdf*. 2020.

[119] P. Schotanus, R. Kamermans, and P. Dorenbos. "Scintillation characteristics of pure and T1-doped CsI crystals". *IEEE Transactions on Nuclear Science* 37.2 (1990), pp. 177–182. DOI: 10.1109/23.106614.

[120] E. Frlež et al. "Cosmic muon tomography of pure cesium iodide calorimeter crystals". *Nuclear Instruments and Methods in Physics Research, Section A: Accelerators, Spectrometers, Detectors and Associated Equipment* 440.1 (2000), pp. 57–85. DOI: 10.1016/S0168-9002(99)00886-4.

[121] T. D. Arber et al. "Contemporary particle-in-cell approach to laser-plasma modelling". *Plasma Physics and Controlled Fusion* 57.11 (2015), p. 113001. DOI: 10.1088/0741-3335/57/11/113001.

[122] C. Shannon. "Communication in the Presence of Noise". *Proceedings of the IRE* 37.1 (1949), pp. 10–21. DOI: 10.1109/jrproc.1949.232969.

[123] C. Arran. "Techniques for High Repetition Rate Laser Wakefield Acceleration". PhD thesis. University of Oxford, 2018.

[124] S. et al. Agostinelli. "GEANT4 - a simulation toolkit." *Nuclear Instruments and Methods in Physics Research Section A: Accelerators, Spectrometers, Detectors and Associated Equipment* 506.3 (2003), pp. 250–303.

[125] B. R. Martin. *Nuclear and particle physics: an introduction*. Wiley, 2009.

[126] M. Novak. *Physics I.: Physics Lists. Geant4 Tutorial at Lund University, Lund (Sweden), 3-7 September 2018, http://indico.lucas.lu.se/event/932/session/0/contribution/7/material/slides/0.pdf*. data retrieved: Jun 2020. 2018.

[127] H. G. Weller et al. "A tensorial approach to computational continuum mechanics using object-oriented techniques". *Computers in Physics* 12.6 (1998), p. 620. DOI: 10.1063/1.168744.

[128] P. I. Frazier. "A Tutorial on Bayesian Optimization". Section 5 (2018), pp. 1–22.

[129] G. Varoquaux et al. "Scikit-learn". *GetMobile: Mobile Computing and Communications* 19.1 (2015), pp. 29–33. DOI: 10.1145/2786984.2786995.

[130] M. Takeda, H. Ina, and S. Kobayashi. "Computer-Based Topography and Interferometry". *J. Opt. Soc. Am. A* 72.1 (1982), pp. 156–160.

[131] S. van der Walt et al. "scikit-image: image processing in Python". *PeerJ* 2 (June 2014), e453. DOI: 10.7717/peerj.453.

[132] PyAbel. *PyAbel*. data retrieved: Oct 2020, github.com/PyAbel/PyAbel. 2020.

[133] K. T. Behm et al. "A spectrometer for ultrashort gamma-ray pulses with photon energies greater than 10 MeV". *Review of Scientific Instruments* 89.11 (2018). DOI: 10.1063/1.5056248.

[134] J. M. Cole et al. "Experimental Evidence of Radiation Reaction in the Collision of a High-Intensity Laser Pulse with a Laser-Wakefield Accelerated Electron Beam". *Physical Review X* 8.1 (2018), p. 11020. DOI: 10.1103/PhysRevX.8.011020.

[135] B. Rus et al. "Outline of the ELI-Beamlines facility". *Diode-Pumped High Energy and High Power Lasers; ELI: Ultrarelativistic Laser-Matter Interactions and Petawatt Photonics; and HiPER: the European Pathway to Laser Energy* 8080 (2011), p. 808010. DOI: 10.1117/12.890392.

[136] Central Laser Facility. *Introducing The Extreme Photonics Applications Centre*. data retrieved: June 2020, https://www.clf.stfc.ac.uk/Pages/EPAC-introduction-page.aspx. 2020.

[137] J. Osterhoff et al. "Generation of stable, low-divergence electron beams by laser-wakefield acceleration in a steady-state-flow gas cell". *Physical Review Letters* 101.8 (2008), pp. 1–4. DOI: 10.1103/PhysRevLett.101.085002.

[138] M. J. Streeter et al. "Temporal feedback control of high-intensity laser pulses to optimize ultrafast heating of atomic clusters". *Applied Physics Letters* 112.24 (2018). DOI: 10.1063/1.5027297.

[139] A. O. Instruments. *Andor Neo Camera Specifications*. data retrieved: June 2020, https://andor.oxinst.com/products/scmos-camera-series/neo-5-5-scmos. 2012.

[140] C. D. Armstrong et al. "Bremsstrahlung emission profile from intense laser-solid interactions as a function of laser focal spot size". *Plasma Physics and Controlled Fusion* 61.3 (2019). DOI: 10.1088/1361-6587/aaf596.

[141] A. Ben-Ismaïl et al. "Compact and high-quality gamma-ray source applied to 10 μm-range resolution radiography". *Applied Physics Letters* 98.26 (2011), pp. 98–101. DOI: 10.1063/1.3604013.

[142] Y. C. Wu et al. "Towards high-energy, high-resolution computed tomography via a laser driven micro-spot gamma-ray source". *Scientific Reports* 8.1 (2018), pp. 1–7. DOI: 10.1038/s41598-018-33844-7.

[143] S. W. Wilkins et al. "Phase-contrast imaging using polychromatic hard X-rays". *Nature* 384.6607 (1996), pp. 335–338. DOI: 10.1038/384335a0.

[144] S. Li et al. "Ultrafast multi-MeV gamma-ray beam produced by laser-accelerated electrons". *Physics of Plasmas* 24.9 (2017). DOI: 10.1063/1.4996020.

[145] O. J. Finlay et al. "Characterisation of a Laser Plasma Betatron Source for High Resolution X-ray Imaging" (2020), pp. 1–6.

[146] A. Vision. *GigE Manta Vision camera*. data retrieved: June 2020, https://www.alliedvision.com/en/products/cameras/detail/Manta/G-033.html. 2020.

[147] J. Arends et al. "The tagged photon beam facility at the Bonn 500 MeV synchrotron". *Nuclear Instruments and Methods in Physics Research* 201.2-3 (1982), pp. 361–369. DOI: 10.1016/0167-5087(82)90565-8.

[148] S. Wilks et al. "Beam loading in plasma waves". *IEEE Transactions on Plasma Science* 15.2 (1987), pp. 210–217. DOI: 10.1109/TPS.1987.4316687.

[149] P. Lee et al. "Optimization of laser-plasma injector via beam loading effects using ionization-induced injection". *Physical Review Accelerators and Beams* 21.5 (2018), p. 52802. DOI: 10.1103/PhysRevAccelBeams.21.052802.

[150] C. McGuffey et al. "Experimental laser wakefield acceleration scalings exceeding 100 TW". *Physics of Plasmas* 19.6 (2012). DOI: 10.1063/1.4729659.

[151] S. Cipiccia et al. "A tuneable ultra-compact high-power, ultra-short pulsed, bright gamma-ray source based on bremsstrahlung radiation from laser-plasma accelerated electrons". *Journal of Applied Physics* 111.6 (2012), p. 063302. DOI: 10.1063/1.3693537.

[152] D. J. S. Findlay. "Analytic representation of bremsstrahlung spectra from thick radiators as a function of photon energy and angle". *Nuclear Inst. and Methods in Physics Research, A* 276.3 (1989), pp. 598–601. DOI: 10.1016/0168-9002(89)90591-3.

[153] R. S. of Chemistry. *Periodic Tabel*. data retrieved: Jan 2020, https://www.rsc.org/periodic-table/trends. 2020.

[154] H. Eberhard and N. Werner. *The Elementary Process Of Bremsstrahlung*. World Scientific Lecture Notes In Physics. World Scientific Publishing Company, 2004.

[155] G. Gillman and I. Macleod. "Reconstruction of X-ray sources from penumbral images". *Computer Graphics and Image Processing* 11.3 (1979), pp. 227–241. DOI: 10.1016/0146-664X(79)90090-X.

[156] K. Kosako et al. "Angular Distribution of Bremsstrahlung from Copper and Tungsten Targets Bombarded by 18, 28, and 38MeV Electrons". *Journal of Nuclear Science and Technology* 47.3 (2010), pp. 286–294. DOI: 10.1080/18811248.2010.9711956.

[157] M. A. Aegerter, N. Leventis, and M. M. Koebel. *Aerogels handbook*. Springer Science & Business Media, 2011.

[158] A. Buck et al. "Shock-front injector for high-quality laser-plasma acceleration". *Physical Review Letters* 110.18 (2013), pp. 1–5. DOI: 10.1103/PhysRevLett.110.185006.

[159] C. G. R. Geddes et al. "Plasma-density-gradient injection of low absolute-momentum-spread electron bunches". *Physical Review Letters* 100.21 (2008), pp. 1–4. DOI: 10.1103/PhysRevLett.100.215004.

[160] ELI Beamlines. *Laser 1 Allegra*. data retrieved: Oct 2020, https://www.eli-beams.eu/facility/lasers/laser-1-allegra-100-mj-1-khz/. 2020.

[161] N. Pathak et al. "Spectral effects in the propagation of chirped laser pulses in uniform underdense plasma". *Physics of Plasmas* 25.1 (2018). DOI: 10.1063/1.5011081.

[162] S. Semushin and V. Malka. "High density gas jet nozzle design for laser target production". *Review of Scientific Instruments* 72.7 (2001), pp. 2961–2965. DOI: 10.1063/1.1380393.

[163] L Fan-Chiang et al. "Gas density structure of supersonic flows impinged on by thin blades for laser–plasma accelerator targets". *Physics of Fluids* 32.6 (2020), p. 066108.

[164] B. Fryxell et al. "FLASH: An Adaptive Mesh Hydrodynamics Code for Modeling Astrophysical Thermonuclear Flashes". *The Astrophysical Journal Supplement Series* 131.1 (2000), pp. 273–334. DOI: 10.1086/317361.

[165] K. Schmid and L. Veisz. "Supersonic gas jets for laser-plasma experiments". *Review of Scientific Instruments* 83.5 (2012). DOI: 10.1063/1.4719915.

[166] openfoam. *OpenFOAM Standard solvers*. data retrieved: July 2020, https://www.openfoam.com/documentation/user-guide/standard-solvers.php. 2020.

[167] J. Vieira et al. "One-to-one full-scale simulations of laser-wakefield acceleration using QuickPIC". *IEEE Transactions on Plasma Science* 36.4 PART 4 (2008), pp. 1722–1727. DOI: 10.1109/TPS.2008.927429.

[168] F. S. Tsung et al. "Near-GeV-energy laser-wakefield acceleration of self-injected electrons in a centimeter-scale plasma channel". *Physical Review Letters* 93.18 (2004), pp. 1–4. DOI: 10.1103/PhysRevLett.93.185002.

[169] J. P. Couperus et al. "Tomographic characterisation of gas-jet targets for laser wakefield acceleration". *Nuclear Instruments and Methods in Physics Research, Section A: Accelerators, Spectrometers, Detectors and Associated Equipment* 830 (2016), pp. 504–509. DOI: 10.1016/j.nima.2016.02.099.

[170] R. Lehe et al. "A spectral, quasi-cylindrical and dispersion-free Particle-In-Cell algorithm". *Computer Physics Communications* 203 (2016), pp. 66–82. DOI: 10.1016/j.cpc.2016.02.007.

[171] S. P. Mangles et al. "Self-injection threshold in self-guided laser wakefield accelerators". *Physical Review Special Topics - Accelerators and Beams* 15.1 (2012), pp. 2–7. DOI: 10.1103/PhysRevSTAB.15.011302.

[172] A. Akhiezer and R. Polovin. "Theory of Wave Motion of an Electron Plasma". *Soviet Phys. JETP* Vol: 3 (1956), pp. 696–705.

[173] X. Yang et al. "Three electron beams from a laser-plasma wakefield accelerator and the energy apportioning question". *Scientific Reports* 7 (2017), pp. 1–10. DOI: 10.1038/srep43910.

[174] K. Behm et al. "Measurements of electron beam ring structures from laser wakefield accelerators". *Plasma Physics and Controlled Fusion* 61.6 (2019). DOI: 10.1088/1361-6587/ab0622.

[175] P. E. Masson-Laborde et al. "Giga-electronvolt electrons due to a transition from laser wakefield acceleration to plasma wakefield acceleration". *Physics of Plasmas* 21.12 (2014). DOI: 10.1063/1.4903851.

[176] K. H. Pae, I. W. Choi, and J. Lee. "Self-mode-transition from laser wakefield accelerator to plasma wakefield accelerator of laser-driven plasma-based electron acceleration". *Physics of Plasmas* 17.12 (2010), pp. 1–6. DOI: 10.1063/1.3522757.

[177] Z. H. He et al. "Coherent control of plasma dynamics". *Nature Communications* 6.May (2015), pp. 1–7. DOI: 10.1038/ncomms8156.

[178] S. J. D. Dann et al. "Laser wakefield acceleration with active feedback at 5 Hz". *Physical Review Accelerators and Beams* 22.4 (2019), p. 041303. DOI: 10.1103/PhysRevAccelBeams.22.041303.

[179] S. P. Mangles. "An overview of recent progress in laser wakefield acceleration experiments". *CAS-CERN Accelerator School: Plasma Wake Acceleration 2014, Proceedings* 001.November 2014 (2014), pp. 289–300. DOI: 10.5170/CERN-2016-001.289.

[180] M. Streeter. personal communication.

[181] W. P. Leemans et al. "Electron-yield enhancement in a laser-wakefield accelerator driven by asymmetric laser pulses". *Physical Review Letters* 89.17 (2002), pp. 174802/1–174802/4. DOI: 10.1103/PhysRevLett.89.174802.

[182] V. B. Pathak et al. "Effect of the frequency chirp on laser wakefield acceleration". *New Journal of Physics* 14 (2012). DOI: 10.1088/1367-2630/14/2/023057.

[183] B. S. Rao et al. "Effect of chirp on self-modulation and laser wakefield electron acceleration in the regime of quasimonoenergetic electron beam generation". *Physical Review Special Topics - Accelerators and Beams* 16.9 (2013), pp. 1–6. DOI: 10.1103/PhysRevSTAB.16.091301.

[184] G. Doumy et al. "Complete characterization of a plasma mirror for the production of high-contrast ultraintense laser pulses". *Physical Review E - Statistical, Nonlinear, and Soft Matter Physics* 69.2 2 (2004), pp. 1–12. DOI: 10.1103/PhysRevE.69.026402.

[185] H. C. Kapteyn et al. "Prepulse suppression for high-energy ultrashort pulses using self-induced plasma shuttering from a fluid target". *Optics Letters* 16.7 (1991), p. 490. DOI: 10.1364/OL.18.000134.

[186] L. P. Ramirez et al. "Efficient cross polarized wave generation for compact, energy-scalable, ultrashort laser sources". *Optics Express* 19.1 (2011), p. 93. DOI: 10.1364/OE.19.000093.

[187] S. Fourmaux et al. "Pedestal cleaning for high laser pulse contrast ratio with a 100 TW class laser system". *Optics Express* 19.9 (2011), p. 8486. DOI: 10.1364/OE.19.008486.

[188] M. Perry and G. Atomics. "Terawatt to Petawatt Sub-Picosecond Lasers". June 1994 (2016). DOI: 10.1126/science.264.5161.917.

[189] R Bobkowski and R Fedosejevs. "Particle emission debris from a KrF laser–plasma x-ray source". *Journal of Vacuum Science & Technology A: Vacuum, Surfaces, and Films* 14.4 (1996), pp. 1973–1980.

[190] P. L. Poole et al. "Experiment and simulation of novel liquid crystal plasma mirrors for high contrast, intense laser pulses". *Scientific Reports* 6.August (2016), pp. 1–8. DOI: 10.1038/srep32041.

[191] D. Panasenko et al. "Demonstration of a plasma mirror based on a laminar flow water film". *Journal of Applied Physics* 108.4 (2010). DOI: 10.1063/1.3460627.

[192] S. Backus et al. "Prepulse suppression for high-energy ultrashort pulses using self-induced plasma shuttering from a fluid target". *Optics Letters* 18.2 (1993), p. 134. DOI: 10.1364/ol.18.000134.

[193] R. L. Fork, B. I. Greene, and C. V. Shank. "Generation of optical pulses shorter than 0.1 psec by colliding pulse mode locking". *Applied Physics Letters* 38.9 (1981), pp. 671–672. DOI: 10.1063/1.92500.

[194] F. Arago, J. L. Gay-Lussac, et al. *Annales de chimie et de physique*. Vol. 2. Crochard, 1841.

[195] R. Li and N. Ashgriz. "Characteristics of liquid sheets formed by two impinging jets". *Physics of Fluids* 18.8 (2006). DOI: 10.1063/1.2338064.

[196] E. Villermaux, V. Pistre, and H. Lhuissier. "The viscous Savart sheet". *Journal of Fluid Mechanics* 730 (2013), pp. 607–625. DOI: 10.1017/jfm.2013.354.

[197] W. M. Wood, C. W. Siders, and M. C. Downer. "Femtosecond Growth Dynamics of an Underdense Ionization Front Measured by Spectral Blueshifting". *IEEE Transactions on Plasma Science* 21.1 (1993), pp. 20–33. DOI: 10.1109/27.221098.

[198] J. K. Koga et al. "Fixed blueshift of high intensity short pulse lasers propagating in gas chambers". *Physics of Plasmas* 7.12 (2000), pp. 5223–5231. DOI: 10.1063/1.1320469.

[199] J. Hecht and A. Street. "A short history of laser development Short history of laser development". *Optical Engineering* 49.September 2010 (2010), pp. 99–122. DOI: 10.1117/1.3483597.

[200] C. H. Ziener et al. "Specular reflectivity of plasma mirrors as a function of intensity, pulse duration, and angle of incidence". *Journal of applied physics* 93.1 (2003), pp. 768–770.

[201] W. Kautek et al. "Laser ablation of dielectrics with pulse durations between 20 fs and 3 ps". *Applied physics letters* 69.21 (1996), pp. 3146–3148.

[202] J. M. Dawson. "Nonlinear electron oscillations in a cold plasma". *Physical Review* 113.2 (1959), pp. 383–387. DOI: 10.1103/PhysRev.113.383.